8-9-2014

ULTRASONICS TRANSDUCTION IN METALLIC AND COMPOSITE STRUCTURES FOR STRUCTURAL HEALTH MONITORING USING EXTENSIONAL AND SHEAR HORIZONTAL PIEZOELECTRIC WAFER ACTIVE SENSORS

Ayman Kamal Abdelrahman
University of South Carolina - Columbia

ULTRASONICS TRANSDUCTION IN METALLIC AND COMPOSITE STRUCTURES FOR STRUCTURAL HEALTH MONITORING USING EXTENSIONAL AND SHEAR HORIZONTAL PIEZOELECTRIC WAFER ACTIVE SENSORS

by

Ayman Kamal Abdelrahman

Bachelor of Science
Ain Shams University, 2008

Master of Engineering
University of South Carolina, 2014

Submitted in Partial Fulfillment of the Requirements

For the Degree of Doctor of Philosophy in

Mechanical Engineering

College of Engineering & Computing

University of South Carolina

2014

Accepted by:

Victor Giurgiutiu, Major Professor

Yuh Chao, Committee Member

Lingyu Yu, Committee Member

Bin Lin, Committee Member

Matthieu Gresil, Committee Member

Paul Ziehl, Committee Member

Lacy Ford, Vice Provost and Dean of Graduate Studies

DEDICATION

I would like to dedicate this work to my family and thank my father, Mohammed Kamal, my mother, Bahira Mohammed, and my sister, Eman Kamal, for their support, praying, and their valuable advice both in my life and my research. I would like to dedicate this dissertation to my wife, Nour Habib, for her love and support and to our families.

ACKNOWLEDGEMENTS

I would like to thank my advisor Dr. Victor Giurgiutiu for his great support, giving me the opportunity to join the Laboratory of Active Materials and Smart Structures (LAMSS), and his support of advising me throughout my course work and research. I would like also to thank Dr. Yuh Chao, Dr. Paul Ziehl, Dr. Lingyu Yu, Dr. Bin Lin, and Dr. Matthieu Gresil for being part of my Dissertation Committee. I would like to thank Dr. Lingyu Yu for working in her lab and using laser vibrometer equipment, Zhenhua Tian for his help with the experiments, Dr Bin Lin for his great tips in MATLAB and writing nice papers, Dr. Jingjing Bao for all his programming advice, and Dr Mohammed Elkholy for his help producing efficient MATLAB programs.

I would like to thank all my smart colleagues working in LAMSS for their friendship and support. Last but not least thanks to Dr. Mike Lowe from Imperial College of London, Dr. Ivan Bartoli from Drexel University, and Dr. Alessandro Marzani from The University of Bologna for their help in providing some dispersion curves simulations using computer packages they developed. Thanks to Dr. Stanislav Rokhlin, Dr. Evgeny Glushkov, and Dr Natalia Glushkova for their invaluable comments. I would like to thank Ashley Valovcin, Nour Habib and Dr. Victor Giurgiutiu for proof reading my dissertation.

Funding supports from Dr Giurgiutiu's research assistantship, the National Science Foundation # CMS-0925466; Office of Naval Research # N00014-11-1-0271, Dr. Ignacio Perez, Program manager; Air Force Office of Scientific Research #FA9550-11-1-0133, Dr. David Stargel, Program Manager are thankfully acknowledged.

ABSTRACT

Structural health monitoring (SHM) is crucial for monitoring structures performance, detecting the initiation of flaws and damages, and predicting structural life span. The dissertation emphasizes on developing analytical and numerical models for ultrasonics transduction between piezoelectric wafer active sensors (PWAS), and metallic and composite structures.

The first objective of this research is studying the power and energy transduction between PWAS and structure for the aim of optimizing guided waves mode tuning and PWAS electromechanical (E/M) impedance for power-efficient SHM systems. Analytical models for power and energy were developed based on exact Lamb wave solution with application on multimodal Lamb wave situations that exist at high excitation frequencies and/or relatively thick structures. Experimental validation was conducted using Scanning Laser Doppler Vibrometer. The second objective of this work focuses on shear horizontal (SH) PWAS which are poled in the thickness-shear direction (d_{35} mode). Analytical and finite element predictive models of the E/M impedance of the free and bonded SH-PWAS were developed. Next, the wave propagation method has been considered for isotropic materials. Finally, the power and energy of SH waves were analytically modeled and a MATLAB graphical user interface (GUI) was developed for determining the phase and group velocities, modeshapes, and the energy of SH waves.

The third objective focuses on guided wave propagation in composites. The transfer matrix method (TMM) has been used to calculate dispersion curves of guided waves in composites. TMM suffers numerical instability at high frequency-thickness values, especially in multilayered composites. A method of using stiffness matrix method was investigated to overcome instability. A procedure of using combined stiffness transfer matrix method (STMM) was presented and coded in MATLAB. This was followed by a comparative study between commonly used methods for the calculation of ultrasonic guided waves in composites, e.g. global matrix method (GMM), semi–analytical finite element (SAFE).

The last part of this dissertation addresses three SHM applications: (1) using the SH-PWAS for case studies on composites, (2) testing of SHM industrial system for damage detection in an aluminum aerospace-like structure panel, and (3) measuring dispersion wave propagation speeds in a variable stiffness CFRP plate.

TABLE OF CONTENTS

LIST OF TABLES

LIST OF FIGURES

CHAPTER 1: BACKGROUND AND RESEARCH OBJECTIVES

Structural health monitoring (SHM) is a fast-growing field that is extending into many industries. SHM uses a set of sensing elements permanently attached to or embedded in the structure in order to effectively monitor its structural integrity, detect, and quantify damage that develops during the entirety of its life. Effective SHM will not only increase the safety of structures, it will also limit the amount of manual error prone inspections that currently dominate the field. Over the past several decades, much work has been done in developing SHM methods.

1.1. BACKGROUND

1.1.1. Wave Propagation Theory

Lamb waves are elastic waves, propagating in solid plates, whose particle motion lies in the plane that contains the direction of wave propagation and the direction perpendicular to the plate. In 1917, Sir Horace Lamb published his classic analysis and description of acoustic waves of this type; these waves were therefore called Lamb waves. An infinite medium supports two wave modes traveling at unique velocities, pressure and shear waves, whereas plates support two infinite sets of Lamb waves modes whose properties depend on various parameters such as plate elastic properties, thickness, and frequency, etc.

A comprehensive mathematical description of the problem of Lamb waves propagation in solids can be found in various textbooks, such as: Viktorov (1967); Graff (1991); Rose (1999); Giurgiutiu (2008). Lamb waves can exist in two basic types: symmetric and antisymmetric, and for each of these types, various modes appear as solutions of the Rayleigh-Lamb equations.

The speeds at which Rayleigh-Lamb waves propagate are referred to as dispersion wave speeds. The term "dispersion" in wave propagation context means that the wave packet stretches out as it travels through the medium; dispersion happens because the frequency components of the wave travel at different wave speeds. Lamb waves are dispersive by nature. This can be exemplified as shown in **Figure 1.1**. A structure was excited by 20-volt amplitude, 3.5-count tone burst signal using a transducer. The received signal was picked up at a point farther on the structure by another transducer. The received signal would contain S0 and A0 Lamb-type waves. S0 is the fundamental symmetric mode; as shown in **Figure 1.1**, S0 is almost non-dispersive: it resembles the excitation signal (at this particular excitation frequency). However, A0, the fundamental antisymmetric mode is dispersive: it has spread from 3.5 to almost 5-count tone burst signal; this is what the "dispersion" word refers to. A0 wave in this illustration is referred to as a wave packet that contains different wave components (or individual waves at each frequency.)

This dispersion nature allows the wave propagation to be characterized by two wave velocities: (1) phase velocity: which is the velocity at which every frequency component travels, and (2) group velocity: the velocity with which the whole packet travels.

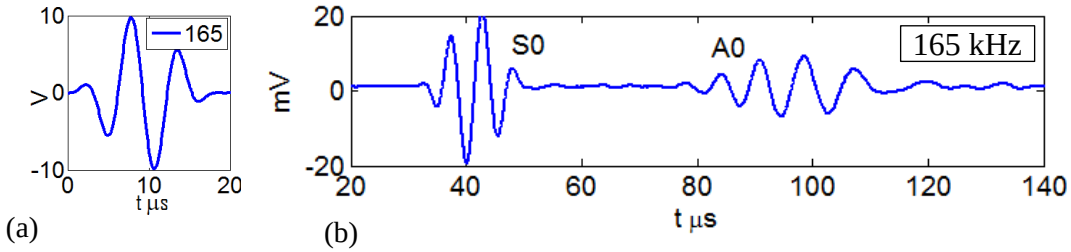

Figure 1.1. (a) Excitation signal, (b) Sensing after traveling through the plate: dispersion Lamb wave signals S0: symmetric Lamb wave, A0: antisymmetric Lamb wave.

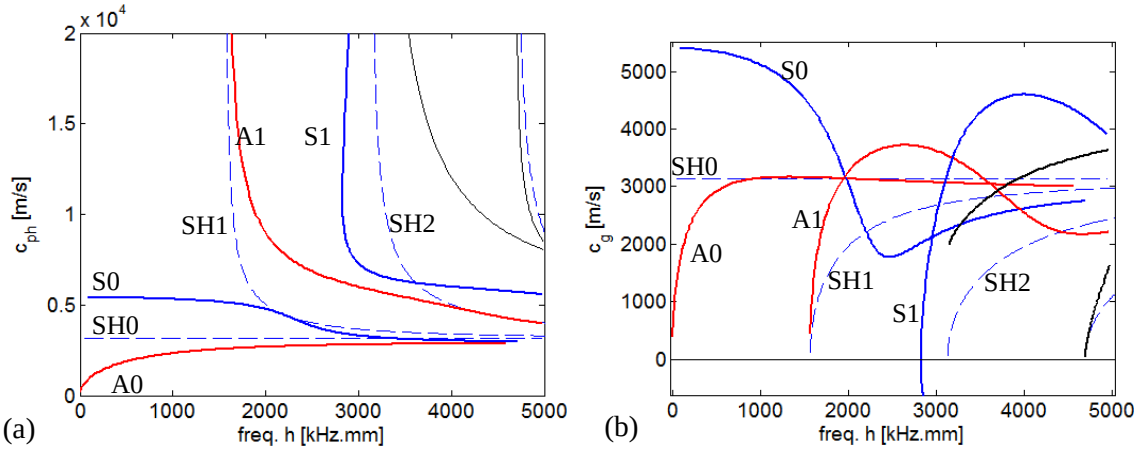

Figure 1.2. Dispersion curves for an aluminum plate, (a) phase velocities, (b) group velocities

The phase and group velocities of Lamb waves propagating in aluminum plates are shown in **Figure 1.2**. We can see the strong dependence of the wave speeds on the frequency. The zero order modes: S0, A0 are present at all the frequencies, while higher modes appear at certain "cut-off" frequencies. Lamb waves by definition have the particle motion in the plane containing: (a) wave propagation direction and (b) the out-of-plane direction, which is perpendicular to the plate's plane. Hence, the S0 and A0 mode, especially at low frequencies, are sometimes called axial (pressure P-wave) and flexural wave respectively. At relatively low frequencies, S0 mode shape resembles axial vibrations, and A0 mode shape resembles flexural vibrations. As the frequency increases, the mode shapes form complex shapes and lose their simple linear approximation of axial

and flexural modes (**Figure 1.3**). At very high frequencies, both modes S0 and A0 approach the speed of each other, and the structure vibrates with Rayleigh waves, where the waves travel near the structure surface, and the particle motion decreases rapidly with the depth.

Particle motion could be in the third direction, inplane but perpendicular to the wave propagation direction, these waves are called SH-waves or shear horizontal waves. They are complementary to Lamb wave modes. **Figure 1.2** also shows phase and group velocities of SH waves, e.g. SH0, SH1, SH2… In isotropic materials, guided waves are decoupled into (1) symmetric and antisymmetric Lamb waves, in addition to (2) shear horizontal (SH) waves. However, in anisotropic materials, e.g., composites, the three modes of particle motion are coupled, and they have to be solved together. Lamb and SH waves are particularly advantageous because they can propagate at large distances as guided waves in plates and shells. This qualifies Lamb and SH waves to be used in the SHM applications.

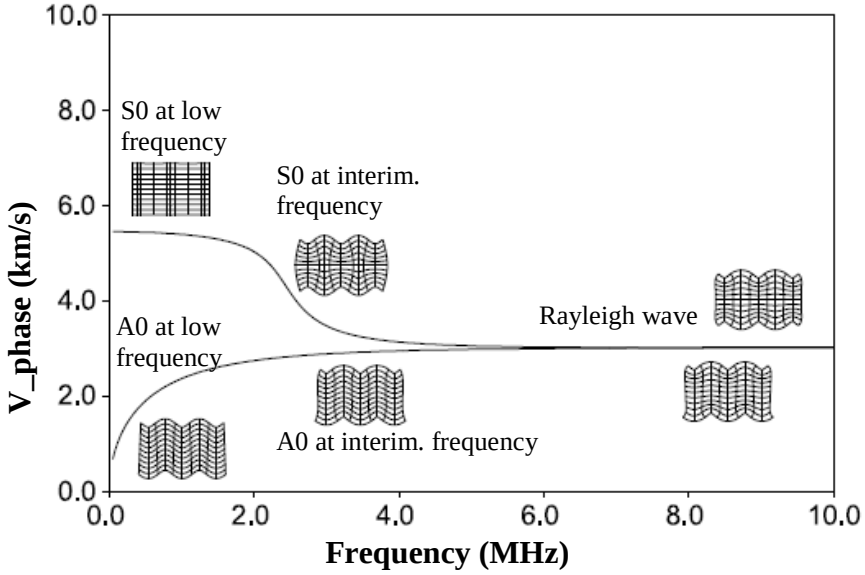

Figure 1.3. Mode shapes of Lamb waves at different excitation frequencies (Pavlakovic and Lowe, 2003)

1.1.2. Piezoelectric Wafer Active Sensor (PWAS)

PWAS transducers utilize the piezoelectric principle to convert electric energy to mechanical energy or mechanical energy back to electrical energy. PWAS transducers are a type of ultrasonic transducers. PWAS are bonded to the structure and can be left on the structure for its remaining life. These transducers have been used under various names for embedded ultrasonic testing for structural health monitoring.

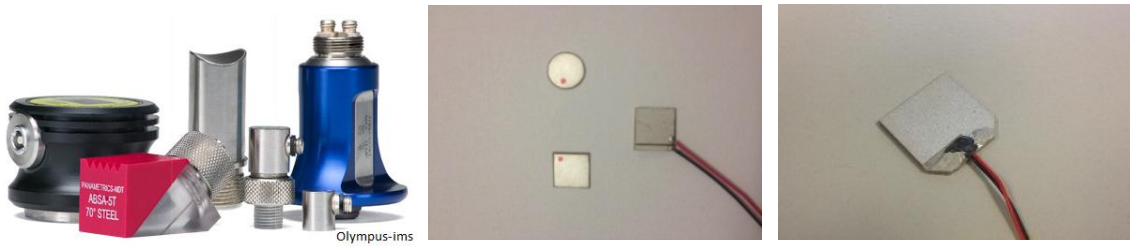

(a) (b) (c)

Figure 1.4. (a) Conventional ultrasonic transducers, (b) Rectangular and circular PWAS, (c) SH-PWAS

These transducers have certain advantages: (1) they are less expensive than conventional ultrasonic transducers, (2) their ability to act as passive sensors, i.e. without interacting with the structure, and/or (3) active sensors, where they interact with the structure to detect the presence and intensity of damage. PWAS transducers are good candidates for exciting guided waves for structural health monitoring (SHM) techniques, like pitch-catch, pulse-echo, and phased array (**Figure 1.7**). PWAS transducers operate on the piezoelectric principle coupling between electrical and mechanical variables. The piezoelectric constitutive equations are

$$S_{ij} = s^{E}_{ijkl} T_{kl} + d_{kij} E_k \tag{1.1}$$

$$D_j = d_{jkl} T_{kl} + \varepsilon^{T}_{jk} E_k \tag{1.2}$$

Equations (1.1) and (1.2) define how the mechanical strain S_{ij}, stress T_{kl}, the electrical field E_k, and electric displacement D_j, relate, where s^{E}_{ijkl} is the mechanical compliance of the material at zero electrical field $(E = 0)$, ε^{T}_{jk} is the dielectric constant at zero stress $(T = 0)$, and d_{jkl} is the induced strain coefficient (mechanical strain per unit electric field). In order to create in-plane strain from a transverse electric field or vice versa, the d_{31} property is utilized by the PWAS.

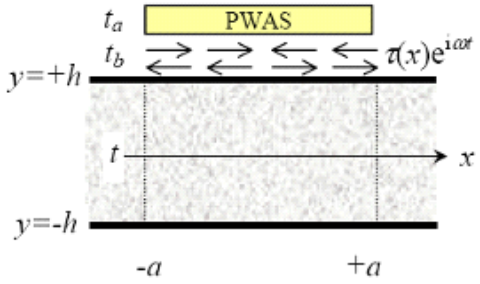

Figure 1.5. Schematic of the PWAS shows the coupling of the in-plane shear stress (Giurgiutiu, 2008)

Depending on the poling direction (**Figure 1.6**) of the PWAS transducer, Eqs. (1.1), (1.2) can be further expanded as follows:

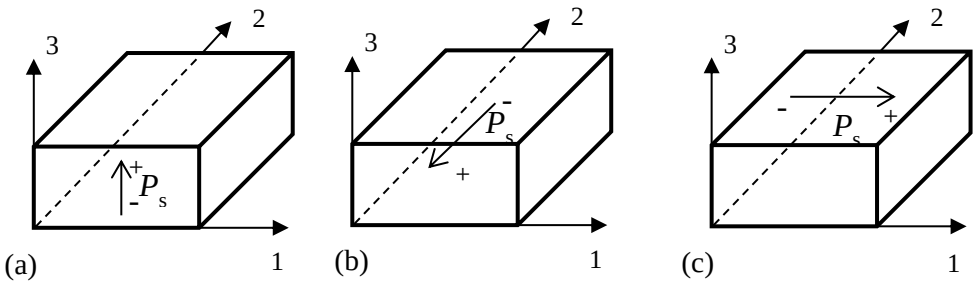

Figure 1.6. Different PWAS poling directions

Case A, where the poling is along 3-direction, the strain equation becomes

$$\begin{Bmatrix} S_1 \\ S_2 \\ S_3 \\ S_4 \\ S_5 \\ S_6 \end{Bmatrix} = \begin{bmatrix} s_{11}^E & s_{12}^E & s_{13}^E & & & \\ s_{21}^E & s_{22}^E & s_{23}^E & & & \\ s_{31}^E & s_{32}^E & s_{33}^E & & & \\ & & & s_{44}^E & & \\ & & & & s_{55}^E & \\ & & & & & s_{66}^E \end{bmatrix} \begin{Bmatrix} T_1 \\ T_2 \\ T_3 \\ T_4 \\ T_5 \\ T_6 \end{Bmatrix} + \begin{bmatrix} & & d_{31} \\ & & d_{32} \\ & & d_{33} \\ & d_{24} & \\ d_{15} & & \\ & & \end{bmatrix} \begin{Bmatrix} E_1 \\ E_2 \\ E_3 \end{Bmatrix} \tag{1.3}$$

And the electric displacement becomes

$$\begin{Bmatrix} D_1 \\ D_2 \\ D_3 \end{Bmatrix} = \begin{bmatrix} & & & & d_{15} & \\ & & & d_{24} & & \\ d_{31} & d_{32} & d_{33} & & & \end{bmatrix} \begin{Bmatrix} T_1 \\ T_2 \\ T_3 \\ T_4 \\ T_5 \\ T_6 \end{Bmatrix} + \begin{bmatrix} \varepsilon_{11}^T & & \\ & \varepsilon_{22}^T & \\ & & \varepsilon_{33}^T \end{bmatrix} \begin{Bmatrix} E_1 \\ E_2 \\ E_3 \end{Bmatrix} \tag{1.4}$$

Case B: the constitutive equations become

$$\begin{Bmatrix} S_1 \\ S_2 \\ S_3 \\ S_4 \\ S_5 \\ S_6 \end{Bmatrix} = \begin{bmatrix} s_{11}^E & s_{12}^E & s_{13}^E & & & \\ s_{21}^E & s_{22}^E & s_{23}^E & & & \\ s_{31}^E & s_{32}^E & s_{33}^E & & & \\ & & & s_{44}^E & & \\ & & & & s_{55}^E & \\ & & & & & s_{66}^E \end{bmatrix} \begin{Bmatrix} T_1 \\ T_2 \\ T_3 \\ T_4 \\ T_5 \\ T_6 \end{Bmatrix} + \begin{bmatrix} & d_{21} & \\ & d_{22} & \\ & d_{23} & \\ & & d_{34} \\ d_{16} & & \end{bmatrix} \begin{Bmatrix} E_1 \\ E_2 \\ E_3 \end{Bmatrix} \tag{1.5}$$

$$\begin{Bmatrix} D_1 \\ D_2 \\ D_3 \end{Bmatrix} = \begin{bmatrix} & & & & & d_{16} \\ d_{21} & d_{22} & d_{23} & & & \\ & & & d_{34} & & \end{bmatrix} \begin{Bmatrix} T_1 \\ T_2 \\ T_3 \\ T_4 \\ T_5 \\ T_6 \end{Bmatrix} + \begin{bmatrix} \varepsilon_{11}^T & & \\ & \varepsilon_{22}^T & \\ & & \varepsilon_{33}^T \end{bmatrix} \begin{Bmatrix} E_1 \\ E_2 \\ E_3 \end{Bmatrix} \tag{1.6}$$

In the inplane mode of case A, applying an electric field in the thickness direction E_3 causes the transducer's lateral dimensions to increase or decrease, a longitudinal strain

will occur $\varepsilon_1 = d_{31}E_3$, where d_{13} is the piezoelectric coupling coefficient measured in [m/V]. Thickness mode is a mode that occurs simultaneously with extension mode, but dominates at higher frequencies in MHz, in which strain in the thickness direction will occur $\varepsilon_3 = d_{33}E_3$, where d_{33} is the piezoelectric coupling coefficient in thickness direction. A different mode of oscillation can be achieved when the applied electric field is applied perpendicular to the poling direction; and it is referred to as shear mode. This shear mode can occur for all the three cases of **Figure 1.6**. The corresponding piezoelectric coupling coefficients for shear mode are d_{24} or d_{15} for case A; d_{34} or d_{16} for case B; and d_{35} or d_{26} for case C. The constitutive equations for case C are

$$\begin{Bmatrix} S_1 \\ S_2 \\ S_3 \\ S_4 \\ S_5 \\ S_6 \end{Bmatrix} = \begin{bmatrix} s_{11}^E & s_{12}^E & s_{13}^E & & & \\ s_{21}^E & s_{22}^E & s_{23}^E & & & \\ s_{31}^E & s_{32}^E & s_{33}^E & & & \\ & & & s_{44}^E & & \\ & & & & s_{55}^E & \\ & & & & & s_{66}^E \end{bmatrix} \begin{Bmatrix} T_1 \\ T_2 \\ T_3 \\ T_4 \\ T_5 \\ T_6 \end{Bmatrix} + \begin{bmatrix} d_{11} & & \\ d_{12} & & \\ d_{13} & & \\ & & d_{35} \\ & d_{26} & \end{bmatrix} \begin{Bmatrix} E_1 \\ E_2 \\ E_3 \end{Bmatrix} \tag{1.7}$$

$$\begin{Bmatrix} D_1 \\ D_2 \\ D_3 \end{Bmatrix} = \begin{bmatrix} d_{11} & d_{12} & d_{13} & & & d_{26} \\ & & & & d_{35} & \end{bmatrix} \begin{Bmatrix} T_1 \\ T_2 \\ T_3 \\ T_4 \\ T_5 \\ T_6 \end{Bmatrix} + \begin{bmatrix} \varepsilon_{11}^T & & \\ & \varepsilon_{22}^T & \\ & & \varepsilon_{33}^T \end{bmatrix} \begin{Bmatrix} E_1 \\ E_2 \\ E_3 \end{Bmatrix} \tag{1.8}$$

The transducer shown in **Figure 1.4**c is called SH-PWAS that is shear-horizontally coupled PWAS. SH-PWAS has electrodes on the top and bottom surfaces; it utilizes the d_{35} coupling coefficient in which electric current is applied across thickness (i.e. in the x_3 direction) and the poling is in the x_1 direction.

1.1.2.1. PWAS for guided wave propagation and wave tuning

Figure 1.7 shows various ways to use PWAS in SHM. There are two methods of using the PWAS as an active sensor. The first is through the use of wave propagation, and is capable of sensing far-field damage. The second method is through standing waves and uses high-frequency electro-mechanical impedance to find damage in the near-field damage (Giurgiutiu, 2008). PWAS can be used as a passive sensor, e.g. acoustic emission.

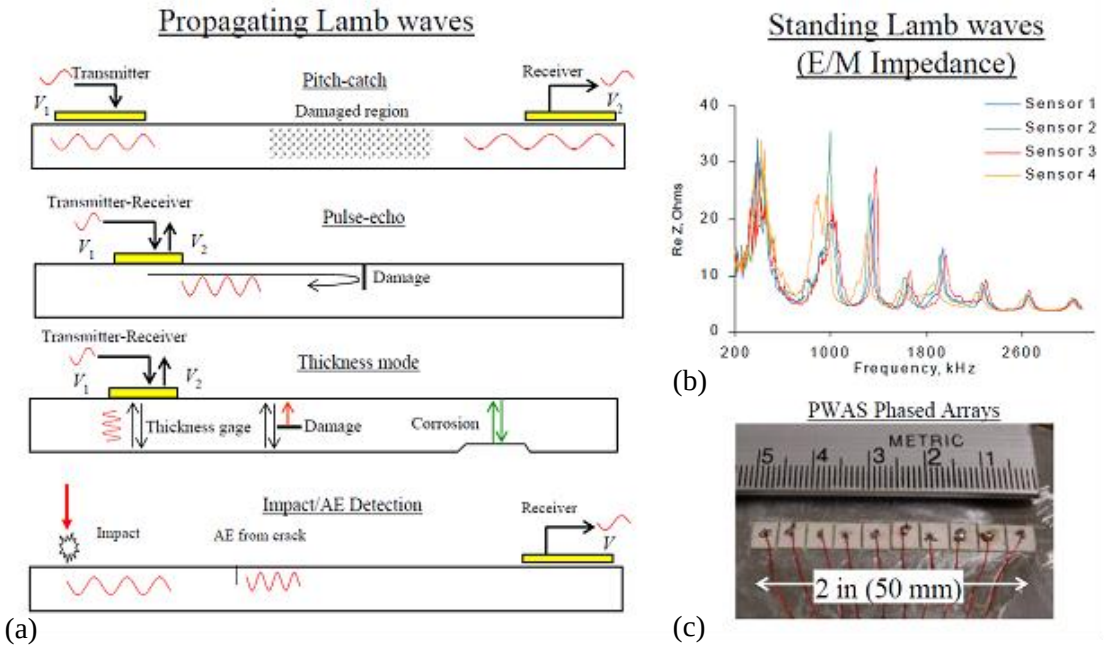

Figure 1.7. The various ways in which PWAS are used for structural sensing includes (a) propagating Lamb waves, (b) standing Lamb waves and (c) phased arrays. The propagating waves methods include: pitch-catch; pulse-echo; thickness mode; and passive detection of impacts and acoustic emission (Giurgiutiu, 2008).

In recent years, an increasing number of investigators are using PZT transducers for ultrasonic waves generation and sensing (Lee and Staszewski, 2003; Giurgiutiu, 2005; Banerjee et al., 2008; Chang, 1998; Giurgiutiu and Santoni, 2011). The central concept of these studies is the characterization of stress waves induced by PWAS transducers inside the plate during their operating modes. It was shown that various Lamb wave modes, i.e.

S0, A0 can be excited by tuning the frequency such that the amplitude of one mode is greater or smaller than the other modes amplitudes, also a situation where one mode is totally "rejected" can be attained. This process is called wave tuning (Giurgiutiu, 2005). The function linking wave amplitude with frequency presents some maxima and minima respectively corresponding to the following two conditions

$$\begin{cases} l_a = (2n-1)\dfrac{\lambda(f)}{2} \\ l_a = (2n)\dfrac{\lambda(f)}{2} \end{cases} \tag{1.9}$$

where l_a is the PWAS dimension (the length for a rectangular or square PWAS, and the diameter for a circular one), λ is the wavelength of the wave, and n =1,2,3… .**Figure 1.8** shows that Lamb waves tuning can be achieved by controlling the frequency. PWAS excites S0 and A0, and the amplitudes of received signals are different at different frequencies. If it is desired to excite only A0; then, a good frequency to use is ≈200 kHz. When PWAS excites S0 and A0 modes, it causes the structure particles to oscillate in typical mode shapes (**Figure 1.3**).

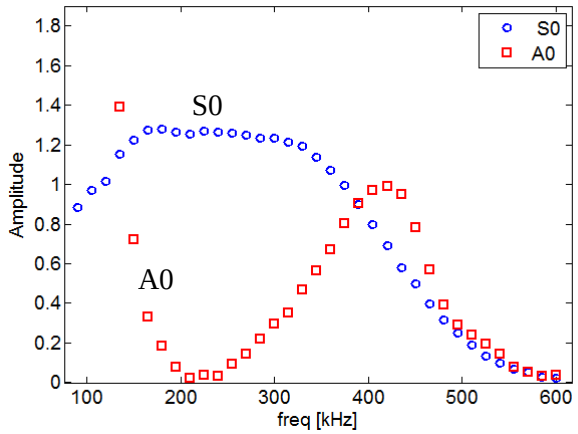

Figure 1.8. Lamb wave experimental tuning curves for 1-mm aluminum plate using 7 mm x 7 mm x 0.2 mm PWAS

1.1.2.2. Electromechanical (E/M) Impedance method for PWAS

The electromechanical (E/M) impedance method is a technique that can be used to detect damage in structures. For a given structure, the ratio between the resultant particle velocity and applied force is the mechanical impedance. The E/M impedance method is based on the electro-mechanical coupling between the active PWAS transducer and the structure. The measured electrical impedance is a direct reflection of the structural impedance and is an assessment method for the local structural dynamics. A good comprehensive study of the analytical modeling and characterization of E/M impedance with PWAS can be found in Giurgiutiu and Zagrai (2000). PWAS transducers can be used to excite mechanical vibrations in a structure. The measured E/M impedance response is primarily a function of the dynamics of the structure. During a frequency sweep, the measured real part of the E/M impedance follows the up and down variation as the structural impedance as it goes through the peaks and valleys of structural resonances and anti-resonances.

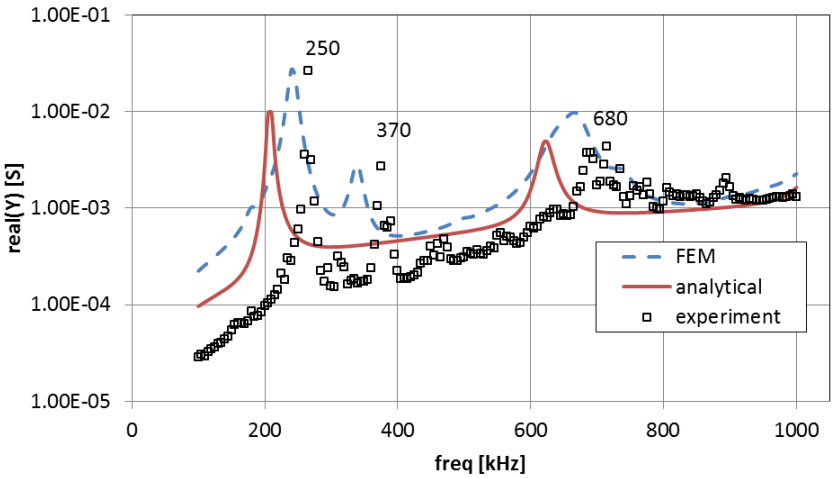

Figure 1.9. Electromechanical admittance of a free 7 mm x 7 mm x 0.2 mm PWAS

Figure 1.9 shows the admittance (the inverse of the impedance) of a free 7 mm x 7 mm x 0.2 mm STEMiNC PWAS. The method itself is usually called E/M impedance spectroscopy (EMIS), but the admittance quantity represents the resonance situations. Free PWAS EMIS is needed to identify the transducer resonant frequencies. Whereas the E/M impedance of the bonded PWAS to the structure is the method used for SHM applications. E/M impedance of the bonded PWAS infers the structural resonances at low frequencies (**Figure 1.10**). High-frequency E/M impedance method can detect localized small damages that is undetectable with conventional vibration methods (Giurgiutiu, 2008).

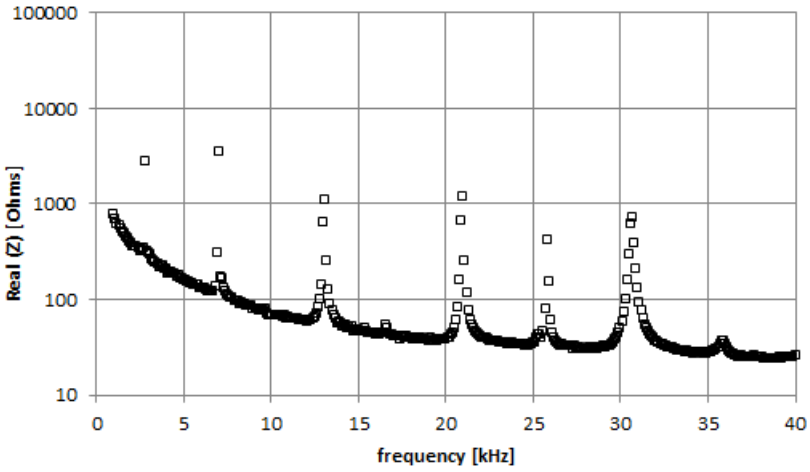

Figure 1.10. Low frequency E/M impedance of bonded 7 mm x 7 mm x 0.2 mm PWAS on 1-mm thick aluminum beam

1.1.3. Composite Materials

The term “composite” can be used to describe any material that is comprised of a homogeneous matrix reinforced by material with higher strength and stiffness properties. When designing a structure for an application, material selection is an essential process. The properties of materials are analyzed, often with a metric to assist in the process, and a material is selected based on trade-offs between its desirable and undesirable properties. Because simple mechanical properties like stiffness and strength are not the only traits that need to be taken into account, the process of material selection can be complicated.

For aerospace, automotive, and naval applications, materials with a high strength to weight ratio offer desirable performance. Composite materials offer such properties along with other desirable properties, thus placing composite material use at the leading edge of material selection for many types of structures. A composite material can have a strength-to-weight ratio in certain directions around 5 times that of aluminum or steel. This is especially useful in the aerospace industry, where weight is at a premium. Another unique and beneficial trait of composite materials is the ability to customize their properties in different directions, creating an anisotropic material; however, composite material can be very costly compared to metals and hard to predict in terms of behavior due to their complex structure.

One of the most important definitions that will be used frequently when we treat the composite materials is the anisotropy and the level of anisotropy, so it will be covered here briefly.

The isotropic material is the one that has the same material properties in every direction at a point in the body (Jones, 1999). Anisotropic material is the opposite and

there are levels of anisotropy. If there is not any plane of material symmetry that exists, then the material experiences the most general case of anisotropy (also called triclinic), and the material stiffness coefficients are 21 independent constants, i.e.,

$$[C]=\begin{bmatrix} C_{11} & C_{12} & C_{13} & C_{14} & C_{15} & C_{16} \\ & C_{22} & C_{23} & C_{24} & C_{25} & C_{26} \\ & & C_{33} & C_{34} & C_{35} & C_{36} \\ & & & C_{44} & C_{45} & C_{46} \\ & (\text{Sym}) & & & C_{55} & C_{56} \\ & & & & & C_{66} \end{bmatrix} \tag{1.10}$$

Note that the matrix in Eq. (1.10) is symmetric because stiffness and compliance matrices are symmetric; hence we have only 21 independent constants. If the material has one plane of material symmetry, it is called monoclinic and [C] will be

$$[C]=\begin{bmatrix} C_{11} & C_{12} & C_{13} & 0 & 0 & C_{16} \\ & C_{22} & C_{23} & 0 & 0 & C_{26} \\ & & C_{33} & 0 & 0 & C_{36} \\ & & & C_{44} & C_{45} & 0 \\ & (\text{Sym}) & & & C_{55} & 0 \\ & & & & & C_{66} \end{bmatrix} \tag{1.11}$$

For the monoclinic case, there are 13 independent material constants. If the material has three planes of material symmetry, then the case of anisotropy is called orthotropic. Usually any composite lamina or layer with fibers along 0 or 90 degrees is considered orthotropic, i.e.,

$$[C]=\begin{bmatrix} C_{11} & C_{12} & C_{13} & 0 & 0 & 0 \\ & C_{22} & C_{23} & 0 & 0 & 0 \\ & & C_{33} & 0 & 0 & 0 \\ & & & C_{44} & 0 & 0 \\ & \text{(Sym)} & & & C_{55} & 0 \\ & & & & & C_{66} \end{bmatrix} \tag{1.12}$$

The orthotropic material has only 9 independent material constants.

Further, we have a transversely isotropic case, where three planes of material symmetry exist and, in addition, material properties are the same in two directions (e.g. 2 and 3); hence directions 2 and 3 are interchangeable. In this case we have only 5 independent material constants, i.e.,

$$[C]=\begin{bmatrix} C_{11} & C_{12} & C_{12} & 0 & 0 & 0 \\ & C_{22} & C_{23} & 0 & 0 & 0 \\ & & C_{32} & 0 & 0 & 0 \\ & & & \frac{C_{11}-C_{12}}{2} & 0 & 0 \\ & \text{(Sym)} & & & C_{55} & 0 \\ & & & & & C_{55} \end{bmatrix} \tag{1.13}$$

A good illustration about the differences between anisotropic, orthotropic and isotropic is shown in **Figure 1.11**.

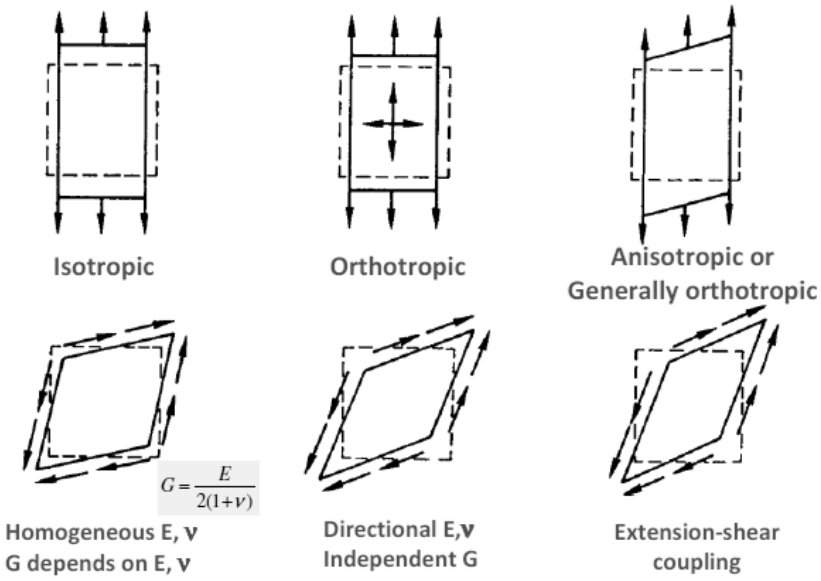

Figure 1.11. Differences in the deformation of isotropic, orthotropic and anisotropic materials subjected to uniaxial tension and pure shear stresses, (Jones, 1999)

Finally, in the isotropic case, we have three planes of material symmetry and the material properties are the same in all the three directions; this is typically for metallic structures. In this case, we have

$$[C] = \begin{bmatrix} C_{11} & C_{12} & C_{12} & 0 & 0 & 0 \\ & C_{11} & C_{12} & 0 & 0 & 0 \\ & & C_{11} & 0 & 0 & 0 \\ & & & C_{44} & 0 & 0 \\ & (\text{Sym}) & & & C_{44} & 0 \\ & & & & & C_{44} \end{bmatrix} \tag{1.14}$$

$$C_{44} = (C_{11} - C_{12})/2$$

We have 2 independent material constants, because the three shear moduli are all the same and are related to the Young's Modulus and Poisson ratio by $G = E/(2(1+\nu))$.

1.1.4. Guided Waves in Polymer Composite Materials

The benefits of using composites come at the cost of a more complicated mechanical response to the applied loads, static or dynamic. The anisotropic nature of the composite material introduces many interesting wave phenomena that are not observed in isotropic bodies; for example, the directional dependence of wave speeds. An understanding of the nature of waves in anisotropic materials is required if we want to use these materials effectively in structural design, or if we want to inspect them using ultrasonic methods, which is one of the goals of our present work.

The type of waves we investigate within the scope of this study are guided elastic waves in free-anisotropic plates, i.e. plates with traction-free surfaces, where the waves are confined within plate surfaces.

State of the art textbooks that treat ultrasonic wave propagation in anisotropic composites are several, they include: Auld (1990); Nayfeh (1995); Rose (1999); and Rokhlin et al. (2011). Some useful tips for obtaining dispersion wave propagation curves can be found in Lowe (1995); Glushkov et al. (2011); Su et al. (2006). There are different methods to calculate dispersion curves in multilayered composite materials (a) transfer matrix method (TMM); (b) global matrix method (GMM); (c) semi-analytical finite element method (SAFE); (d) local interaction simulation approach (LISA); and (e) equivalent matrix method (EMM). Mathematical formulations of these techniques are presented, along with highlighting key features. GMM was studied comprehensively by Lowe (1995), and there is a commercial software that has been developed based on GMM, which is called DISPERSE (Pavlakovic and Lowe, 2003).

1.2. MOTIVATION

A previous study by Lin and Giurgiutiu (2012) had considered the axial and flexural approximation of S0 and A0 Lamb waves to develop power and energy transduction between PWAS and metallic structure. But, this model is only applicable at low frequencies. **Figure 1.12** shows that the axial wave speed is constant along the frequency variations. It only approximates S0 mode at relatively low frequencies, same for flexural mode, only approximating A0 mode only at relatively low frequencies. Hence it was important to consider modeling power and energy transduction between PWAS and host structure based on exact Lamb wave modes.

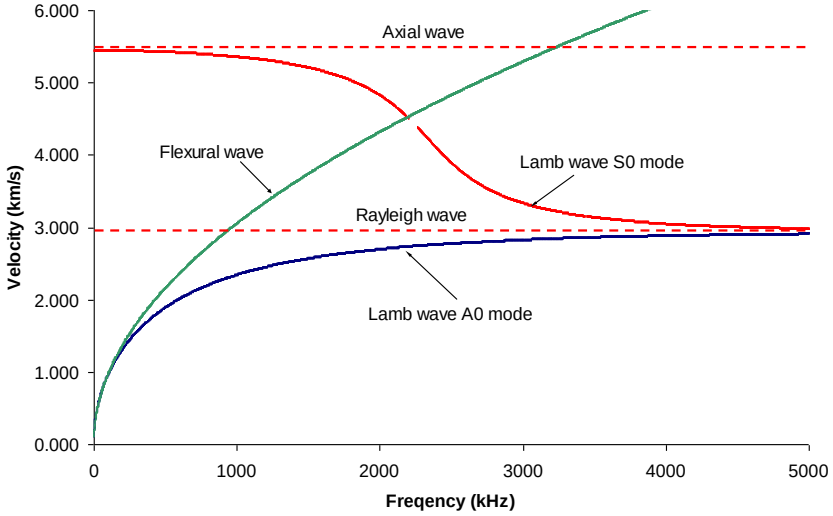

Figure 1.12. Axial and flexural approximation of S0 and A0 Lamb wave modes for aluminum plate

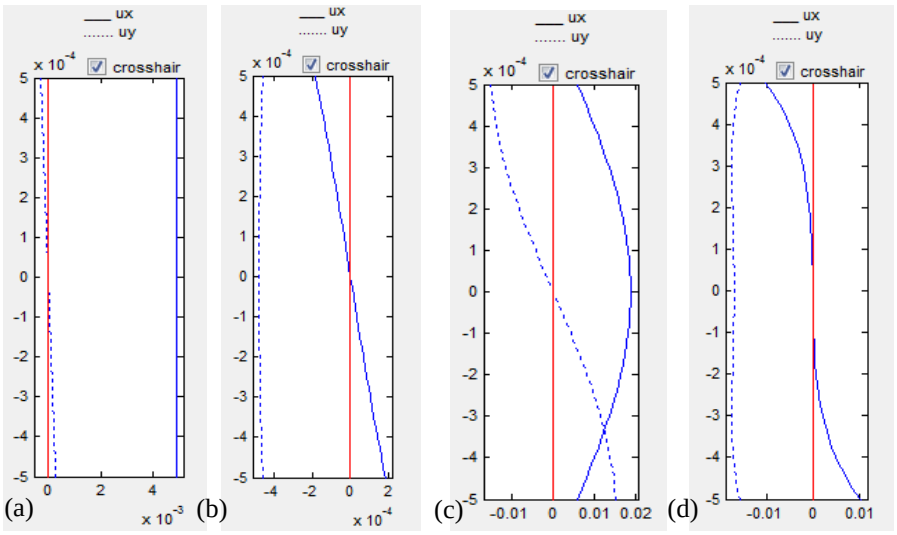

Figure 1.13. Mode shapes across 1-mm thick aluminum beam, (a) S0 at 200 kHz, (b) A0 at 200 kHz, (c) S0 at 2000 kHz, (d) A0 at 2000 kHz

If we look at mode shapes at 200 and 2000 kHz (**Figure 1.13**), we can see that S0 and A0 modes at 2000 kHz can no longer be represented by the simple constant and linear u_x across thickness, i.e., axial and flexural respectively. Cases of thick structures (e.g. $\frac{1}{2}$"-thick steel plates) are often considered in ultrasonics, even up to 500 kHz (a relatively small frequency in ultrasonics). This requires models of power and energy based on exact "multi" modal Lamb waves; therefore, this study considers the case of thick structures too.

To consider power and energy models in anisotropic multilayered composites; first dispersion curves of wave propagation speeds in composites need to be well established and understood. Second, we need to consider shear horizontal waves, because in composite materials, SH and Lamb waves are coupled and exist in most cases.

To be able to get dispersion curves, we conducted a literature review of commercially available software codes that have been developed in the past few years. Some provide the dispersion curves as figures without actually providing the data; others

frequently miss one of the modes we wanted to predict their speed (namely SH0). Hence, for more flexibility and to integrate dispersion wave speeds in composites with power and energy models, we considered developing a predictive tool based on transfer matrix method (TMM). TMM was described in details in Nayfeh (1995). A software, "LAMSS Guided Waves in Composites" based on TMM has been developed in our group (Santoni, 2010). Two key issues need to be highlighted, (1) Nayfeh approach leads to a singular situation if the material is isotropic or quasi-isotropic, and (2) TMM suffers instability at higher frequencies, or as layers of the composite laminate increase. Our study tries to eliminate these issues by combining Nayfeh approach (TMM) with the stiffness matrix method (SMM) by Rokhlin et al. (2011). A combined stiffness transfer matrix method (STMM) is proposed to obtain correct and stable results over the entire domain of interest. STMM procedure is coded in a MATLAB graphical user interface that also allows displaying modeshapes at any selected root of interest.

To experimentally validate our SH waves prediction in metallic and composite materials, we needed to understand, to model, and to characterize SH-PWAS. It is shown in Chapter-3 that SH waves are good candidates for SHM, e.g., capturing delaminatons in composites; and inferring the shear stiffness of bonding layers, which is a vital role for adhesive bonded layers. For these reasons, it was very promising and worthwhile to work on predictive models of SH-PWAS behavior, including free SH-PWAS predictive models for admittance and impedance, in addition to the bonded SH-PWAS case, which contributes to the advancement of knowledge beyond the state of the art.

1.3. RESEARCH GOAL, SCOPE, AND OBJECTIVES

The **goals** of this research are (1) to understand, model, and predict the power and energy transduction mechanism between piezoelectric wafer active sensor (PWAS) and the host structure and (2) to characterize and model shear horizontal-coupled piezoelectric wafer active sensor and to study the impedance spectroscopy and wave propagation methods associated with this transducer.

In terms of materials, the **scope** of this study is to develop analytical and finite element predictive models for (1) isotropic metallic structures and (2) anisotropic polymer composites. In terms of type and number of guided waves excited in the structure, the study covers: (1) single symmetric and antisymmetric Lamb wave modes, which typically exist in thin structures; (2) multimodal Lamb waves that typically exist in thick structures and at high excitation frequencies; and (3) coupled shear horizontal and Lamb waves in anisotropic composite laminates.

The **objectives** of this research are defined as follows:

1. To develop analytical equations for power and energy transduction between the PWAS and hosted structure based on exact Lamb wave modes and normal mode expansion (NME) method and to identify model assumptions, limitations, and the range of applicability.
2. To characterize SH-PWAS, including the impedance, wave propagation, and power and energy of SH waves.
3. To develop analytically the electromechanical impedance and admittance of the constrained SH-PWAS (which is bonded to a host structure) based on normal

mode expansion method and elasticity solution of the structural displacement response.

4. To develop a graphical user interface by MATLAB for SH-waves analysis in the common isotropic materials. This will complement existing developed software in our group for Lamb waves, e.g. WAVESCOPE and MODESHAPE.
5. To solve dispersion wave propagation speeds in multilayered composites based on the transfer matrix method (TMM) and to develop stable and robust predictive tool for predicting dispersion curves and modeshapes in composite materials.
6. To demonstrate experiments of SH waves propagation in composites and, in general, the coupled guided waves in composites. In addition, to demonstrate FEM predictions of wave propagation and impedance spectroscopy methods in composites.
7. To perform application studies on complex aerospace-like structures and composite plates and to identify challenges of SHM of complex metallic and composite structures.

1.3.1. Dissertation Layout and Research Topics

To accomplish the objectives set forth in the preceding section, the dissertation is organized in six chapters divided into two parts.

In **part I**, we address theoretical developments and validation experiments.

Chapter-2 presents power and energy studies, and these cover the following topics:

Topic-1 Exact Lamb waves' power and energy, based on the normal mode expansion theory (NME) and harmonic waves.

Topic-2 Multimodal Lamb waves case in thick structures.

Topic -3 Power partitioning based on constant voltage.

Topic -4 Experiments using laser vibrometer for measuring actual amplitudes and validating analytical tuning curves based on (a) signal amplitude values and (b) signal energy content.

Topic -5 Experiments and FEM of impedance spectroscopy.

Chapter-3 presents the SH-PWAS, as a candidate for SHM compared to other state-of-the-art transducers. Characterization of the SH-PWAS includes the analytical development of the free transducer (in d_{35} mode). We developed the E/M impedance and admittance of the free transducer based on the constant electric field assumption and based on the constant electric displacement assumption. Analytical models were compared with experiments and FEM results. Furthermore, we extended the analytical development to find closed-form expressions for the E/M impedance and admittance of the constrained (bonded) SH-PWAS. We studied the power and energy of multimodal SH-waves based on NME, and we developed a MATLAB graphical user interface (GUI) for calculating SH waves dispersion phase and group velocities, mode shapes, and wave energies. The research topics of this chapter are summarized as:

Topic -1 Analytical modeling of the E/M impedance and admittance of the free SH-PWAS, as well as experimental and FEM validations.

Topic -2 Analytical modeling of the E/M impedance and admittance for the bonded SH-PWAS, based on NME and structural elasticity solution.

Topic -3 Performed experiments of the bonded SH-PWAS on structures at low frequencies to capture structural resonances.

Topic -4 Performed wave propagation experiments between different combinations of PWAS and SH-PWAS to study the generation and reception of SH waves by SH-PWAS and to study the effect of SH-PWAS poling.

Topic -5 Development of the power and energy models of SH waves analytically.

Topic -6 Building a GUI on MATLAB for SH waves' analysis.

Chapter-4 presents guided wave propagation in composites. We developed analytically the equations of TMM, based on Nayfeh (1995) and the equations of SMM, based on Rokhlin, et al. (2011). Then, we integrated TMM and SMM as a combined stable stiffness transfer matrix method (STMM). We presented in detail the procedure needed to code this method in a way to avoid numerical instability and to be applicable on an isotropic plate; a multi-layered isotropic plate; a unidirectional fiber composite lamina with fibers along 0 or 90 degrees w.r.t. wave propagation direction; a unidirectional fiber composite lamina with arbitrary fiber angles; multilayered unidirectional composite with fibers along 0 direction; and cross-ply composites. For each of the preceding cases, we obtained phase velocities, group velocities, and wavenumber-frequency domain solutions. Afterwards, a comparable study was established between the STMM results and results from commercially available software,

e.g. DISPERSE based on GMM, and GUIGUW based on SAFE. This is followed by experimental and FEM studies. The research topics of this chapter are:

Topic -1a Understanding TMM and SMM, identifying instability and singularity issues

Topic -1b Obtaining stable results based on the stable combined stiffness transfer matrix method (STMM): (a) $\xi - f$ (b) c_{ph} (c) c_g .

Topic -2 Analyzing a multilayered isotropic case (a) $\xi - f$ (b) c_{ph} (c) c_g .

Topic -3 Analyzing a unidirectional composite case with fibers angle along 0 or 90 degree directions w.r.t wave propagation direction: (a) $\xi - f$ (b) c_{ph} (c) c_g .

Topic -4 Analyzing a unidirectional composite case with arbitrary fibers angle, e.g. 30, 45, 60: (a) $\xi - f$ (b) c_{ph} (c) c_g .

Topic -5 Developing cross ply solutions based on equivalent matrix method:
(a) $\xi - f$ (b) c_{ph} (c) c_g .

Topic -6 Developing multilayered unidirectional and cross ply solutions based on STMM: (a) $\xi - f$ (b) c_{ph} (c) c_g .

Topic -7 Comparative study between different methods, GMM, STMM, and SAFE for (a) unidirectional, (b) cross ply, and (c) quasi- isotropic laminates.

Topic -8 Experimental validation.

Topic-9 Performing FEM on a cross-ply situation and showing the directional dependence of wave propagation on composites.

Part II addresses some SHM applications and related issues

In Chapter 5, we performed a case study of using SH-PWAS on composites, we exemplified the case studies by a 1-mm thick woven GFRP and a 2-mm thick [0/45/45/0]s CFRP plate with woven prepreg layers. We studied impedance spectroscopy and wave propagation methods on both materials. Then, we built predictive finite element models and addressed the challenges and limitations. The research topics of this chapter are:

Topic-1 Experimental and FEM studies of E/M impedance and admittance for the SH-PWAS bonded on GFRP and CFRP plates.

Topic -2 Combination of pitch catch experiments between PWAS and SH-PWAS on both GFRP and CFRP plates.

Topic -3 Finite element models for 2-D wave propagation for the following cases

(a) The SH-PWAS is the transmitter transducer (both GFRP, CFRP).

(b) The regular PWAS is the transmitter in GFRP case.

In Chapter 6, we studied a commercial SHM system for damage detection in aerospace-like structure. The research topics of this chapter are:

Topic -1 Sensors installation and the equipment setup (contribution: this task was done by Dr. Bin Lin, research PostDoc, USC.)

Topic -2 Performing experiments on pristine complex structure.

Topic -3 Inducing different damage cases and testing the system for damage detection.

Topic -4 Modeling includes (1) building CAD files for such plates, (2) meshing by ANSYS, meshing was done by Dr. Bin Lin, and (3) input of the mesh to the software.

In Chapter 7, we studied wave propagation in a variable stiffness CFRP plate that was designed as a buckling resistance plate. We performed pitch catch experiments between PWAS transducers at different angles and at different locations of the plate. We addressed the possible data analysis procedures to measure dispersion group velocities. The research topics of this chapter are:

Topic -1 Design of experiment for installation locations of PWAS transducers.

Topic -2 Performing pitch catch experiments.

Topic -3 Analyzing the results using time of flight (TOF) method by using (1) Hilbert envelop method and (2) short time Fourier transform (STFT).

PART I THEORETICAL DEVELOPMENTS & VALIDATION EXPERIMENTS

CHAPTER 2: POWER AND ENERGY

This chapter presents an analytical model for the power and energy transfer between the excited piezoelectric wafer active sensors (PWAS) and a host structure. This model is based on exact multi-modal Lamb waves, normal mode expansion technique, and the orthogonality of Lamb waves. Modal participation factors were presented to show the contribution of every mode to the total energy transfer. The model assumptions included: (a) waves are of straight-crested multimodal harmonic type; (b) evanescent (non-propagating) waves were ignored; and (c) ideal bonding (pin-force) connection between the PWAS and structure. The admittance of the constrained PWAS (bonded PWAS to the structure) was reviewed. Electrical active power; mechanical converted power; and Lamb waves kinetic and potential energies were derived in closed form formulae. Numerical simulations were performed for both the symmetric and antisymmetric excitation of thin aluminum structures. The simulation results were compared with the axial and flexural approximation for the case of low frequency Lamb waves. In addition, a thick steel structure example was considered to illustrate the case of multimodal guided waves. A parametric study for different excitation frequencies and different transducer sizes was performed to show the best match of the PWAS size and the excitation frequency to achieve maximum energy transfer into the excited structure. Finally, experimental study was performed to validate Lamb wave tuning (using a scanning laser vibrometer) and to validate the PWAS E/M impedance (using an impedance analyzer). This chapter is based on the 2014 Article: *J. Int. Mat. Syst. Struct* **25**, 4 Sage: doi:10.1177/1045389X13498310

NOMENCLATURE

A_n	=	amplitude of nth antisymmetric mode
A0, A1, A2	=	antisymmetric Lamb-wave modes
a	=	half-length of the piezoelectric-wafer transducer, m
$a_n(x)$	=	modal-participation factor
B_n	=	amplitude of nth symmetric mode
b	=	width, m
C	=	mode contribution factor
C_0	=	capacitance, F
c	=	wave speed, m/s
c_p	=	pressure (longitudinal) wave speed m/s
c_s	=	shear(transverse) wave speed m/s
d	=	plate half thickness, m
d_{31}	=	piezoelectric coupling coefficient in *31*, m/V
E	=	Young's modulus, GPa
$\langle e_e \rangle$	=	time-averaged total Lamb wave energy
F	=	force vector
$F_0(\omega)$	=	pin-force at PWAS ends
f	=	frequency, Hz
g_n	=	coefficient to simplify modal participation factor
h	=	plate thickness = $2d$, m
I	=	electric current, Ampere
i	=	$\sqrt{-1}$

Im	=	imaginary part of a complex quantity
k_e	=	kinetic energy
$\langle k_e \rangle$	=	time-averaged kinetic energy
k_{PWAS}	=	PWAS stiffness, N/m
k_{str}	=	dynamic stiffness, N/m
k_{31}	=	electromechanical cross-coupling coefficient
l, l_a	=	PWAS length = $2a$
P_{mn}	=	power factor. Measure of average power flow
p	=	power, W
$\langle p \rangle$	=	time-averaged power
R	=	eigen coefficients
$r(\omega)$	=	dynamic stiffness ratio
Re	=	real part of a complex quantity
S_{ij}	=	mechanical strains
S0, S1, S2	=	symmetric Lamb-wave modes
s_{11}^E	=	mechanical compliance under constant electric field, m^2/N
T	=	period time, s
T_{ij}	=	stress in tensor notation
$\mathbf{T_n}$	=	stress tensor for nth guided-wave mode, Pa
t	=	time, s
t_a	=	PWAS thickness, m
$t_x(x)$	=	traction in x direction
U	=	displacement amplitudes, m. Also orthogonal modes

u	=	displacement, m
u_{ISA}	=	induced strain actuation PWAS displacement
V	=	voltage
v	=	velocity
$\mathbf{v}$	=	velocity vector
v_{e}	=	potential energy
$\langle v_e \rangle$	=	time-averaged potential energy
W	=	parameter to simplify normalized modes formula, unit: m^{-2}
x,y,z	=	global coordinates, m
x_1,x_2,x_3	=	material polarization directions
Y	=	admittance (simens)
$\lvert Y \rvert$	=	absolute of admittance
Y_{I}	=	imaginary part of admittance
Y_{R}	=	real part of admittance
α, β	=	wave numbers, m^{-1}
δ	=	kronecker delta
ε_{jk}^{T}	=	dielectric permittivity measured at zero mechanical stress, T = 0
λ	=	Lame constant, Pa
μ	=	Material shear modulus,quivalent to the engineering constant G), Pa
ν	=	poisson ratio
ξ	=	wave numbers, m^{-1}
ρ	=	material density kg/m^3

τ, τ_a	=	shear stress at PWAS tip $x = a$
ϕ	=	Lamb-wave longitudinal potential function
$\phi(\omega)$	=	dynamic
ψ	=	Lamb-wave shear potential function
Ω	=	domain
ω	=	angular frequency, rad/s

Subscripts

A	=	antisymmetric modes
i, j	=	indices = 1,2,3
m, n	=	different normal modes
n	=	nth guided wave mode
S	=	symmetric modes
x, y, z	=	global coordinates, m
1	=	solution due to source excitation
2	=	solution due to homogeneous solution (free mode shapes)

Superscripts

A	=	antisymmetric modes
m, n	=	different normal modes
S	=	symmetric modes
1	=	solution due to source excitation
2	=	solution due to homogeneous solution (free mode shapes)

$\tilde{a}$ = conjugate of a

$\hat{a}$ = amplitude of a

2.1. LITERATURE REVIEW

Ultrasonic Lamb waves are used to find damage and flaws in plates, pipes, rails, thin-wall structures, multi-layered structures, and composite materials. The advantage of Lamb waves over other common ultrasonic techniques is that they travel large distances along the structure. Lamb waves can be 'tuned' to excite certain modes; some modes are more sensitive to certain types of defects.

Chinthalapudi and Hassan (2005) showed that energy loss of guided waves may be due to multiple reasons, such as existing flaws in the structure. Impedance mismatch is considered as an "energy-stealing" agent that results from flaws like delamination, splits, and cavities. In practice, the sensitivity to most simple defects, such as notches and cracks, is adequate and of similar magnitude due to the fairly uniform distribution of energy through the thickness of the plate. The sensitivity considerations become much more important in anisotropic materials. Wilcox, et al. (2001) showed an example of delamination detection in composites where certain modes were found to be blind to delamination at certain depths. Other studies (Alleyne and Cawley, 1992; Koh et al., 2002) gave more insights on how different defects interact with Lamb waves, and how the severity of impact damages can be predicted from the transmitted power. Generally, the failure theories based on energy methods are more robust in predicting failure. Hence, it is very important to model Lamb wave power and energy transduction between PWAS and host structures. Other applications that have attracted more interest recently are

energy harvesting applications. The need of optimizing energy transfer (Park et al., 2007; Kural et al., 2011) requires accurate models for Lamb waves energy, rather than simplified axial and flexural approximation that is only at low frequencies.

Excitation at frequencies beyond the cut off frequency of A1, S1 modes will generate multimodal Lamb waves. This phenomenon appears also for relatively thick structures. In these cases, every mode shares parts of the supplied power and energy. Our analytical model was developed based on the "normal modes." Normal modes represent the possible vibration characteristics of the structure and are independent of the loading scheme (Rose, 1999). The method of normal mode expansion (NME) is described in this study. It is worth mentioning that there are other methods that can be used to solve the forced loading of a structure, e.g. the integral transform techniques (ITT). Some of the most popular transforms are Laplace, Fourier, Hankel and Mellin. Various integral transforms are used to transform a given function into another. These transformations are done via integration (over some domain) of the original function multiplied by a known kernel function. This is followed by either solving for the exact solution, e.g. with residue theorem, or by numerically evaluating the integral in the case of complicated problems.

The solution of Lamb waves propagation in a plate that is excited with surface PWAS was done by Giurgiutiu (2008) with the integral transform technique of the exact solution. The NME method determines the expanded amplitudes. NME can be used for isotropic or generally anisotropic layers. The difference between isotropic or anisotropic cases is in evaluating the quantities appearing in the solution. Therefore, the NME method can be considered more general because the physical nature of the excitation process is clear and independent of the material. The ITT method does have extensive

algebra and Viktorov (1967) discussed it in details. It was also shown by Viktorov (1967) how the solution is different between isotropic and generally anisotropic layers.

A previous study was done by Lin and Giurgiutiu (2012), where they investigated the power and energy transduction in pitch catch PWAS configuration, but that study was based on axial and flexural wave approximation of S0 and A0 Lamb waves. Frequency response functions were developed for voltage, current, complex power, and active power. It was shown (**Figure 2.1**) that increasing the transmitter PWAS size and frequency of excitation requires the input of more electrical power; however, this may not increase the power transducted to waves, as shown in **Figure 2.1**b.

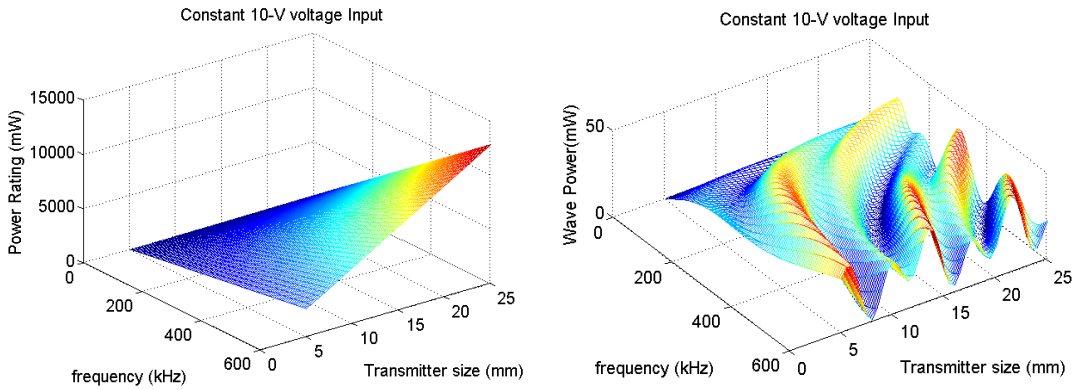

(a) (b)

Figure 2.1. PWAS transmitter under constant voltage excitation (a) power rating, (b) wave power (Lin and Giurgiutiu, 2012)

Other similar studies were performed by Glushkov et al. (2006) and Glushkov et al. (2007) where the energy supplied to the waveguide versus the transducer size was addressed (**Figure 2.2**). The first study (Glushkov et al., 2006) was based on the Green matrix and the study showed that flexural approximation of A0 mode is only valid at low frequencies. In the second study, Glushkov et al. (2007) have studied the multimodal case

and energy partitioning, along with a comparison between integral equation based modeling and FEM.

In our work, we show the analytical development based on the NME method. This method is straight forward when needed for anisotropic composite material cases, which involve studying the energy transduction between the PWAS and hosted anisotropic layers.

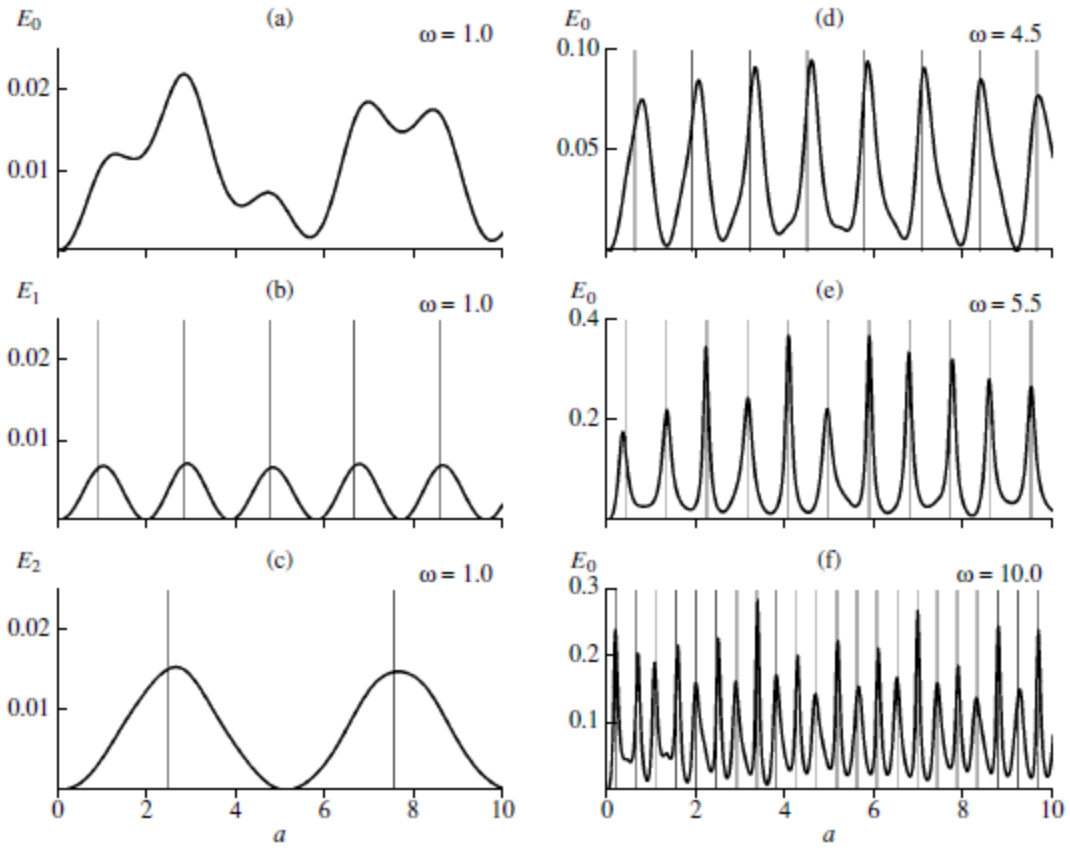

Figure 2.2. Energy supplied to the waveguide versus the patch size (Glushkov et al., 2006)

2.2. ANALYTICAL DEVELOPMENT

2.2.1. Lamb Waves Normal Mode Expansion

The normal mode expansion method is used to (a) directly find the amplitudes of a given mode in terms of loading parameters and (b) evaluate the contribution factor of every mode to the total wave power and energy. Normal modes of the guided waves in the structure serve as the eigenfunctions. The method assumes that the desired solution can be written in the form of a series of known functions, each with unknown amplitudes. Then, those amplitudes are to be determined either numerically or by finding a general expression that is valid for all modes.

Normal modes (eigenfunctions) of the analyzed structure are assumed 'complete,' meaning that any function can be represented exactly in terms of a finite or infinite number of functions in the set of 'normal modes.' The second condition for the NME method is the orthogonality of the base functions (Rose, 1999). The NME of the displacement can be written as a summation of mode functions:

$$u(x,y,t) = \sum_{j=1}^{\infty} C_j U_j(x,y) e^{i\omega t} \tag{2.1}$$

where C_j is the contribution factor for each mode and U_j is mode shape. This solution is assumed for the particular case of time harmonic with angular frequency ω.

Lamb waves (guided plate waves) are fully analyzed in a number of textbooks: Graff (1991); Rose (1999); Giurgiutiu (2008). Here, we reproduce the essentials for power and energy models. The wave equations are:

$$\frac{\partial^2\phi}{\partial x^2}+\frac{\partial^2\phi}{\partial y^2}+\frac{\omega^2}{c_P^2}\phi=0$$
$$\frac{\partial^2\psi}{\partial x^2}+\frac{\partial^2\psi}{\partial y^2}+\frac{\omega^2}{c_S^2}\psi=0 \qquad (2.2)$$

where ϕ , ψ are two potential functions, $c_p=\sqrt{(\lambda+2\mu)/\rho}$ and $c_s=\sqrt{\mu/\rho}$ are the pressure (longitudinal) and shear (transverse) wavespeeds; λ and μ are the Lame constants; and ρ is the mass density. The time dependence is assumed harmonic, the displacement solution for symmetric and antisymmetric wave propagation (**Figure 2.3**), and can be obtained as:

$$\begin{cases} u_x(x,y,t)=-B_n\left(\xi_{Sn}\cos\alpha_{Sn}y-R_{Sn}\beta_{Sn}\cos\beta_{Sn}y\right)e^{-i(\xi_{Sn}x-\omega t)} \\ u_y(x,y,t)=iB_n\left(\alpha_{Sn}\sin\alpha_{Sn}y+R_{Sn}\xi_{Sn}\sin\beta_{Sn}y\right)e^{-i(\xi_{Sn}x-\omega t)} \end{cases} \quad (\text{Symmetric}) \quad (2.3)$$

$$\begin{cases} u_x(x,y,t)=-A_n\left(\xi_{An}\sin\alpha_{An}y-R_{An}\beta_{An}\sin\beta_{An}y\right)e^{-i(\xi_{An}x-\omega t)} \\ u_y(x,y,t)=-iA_n\left(\alpha_{An}\cos\alpha_{An}y+R_{An}\xi_{An}\cos\beta_{An}y\right)e^{-i(\xi_{An}x-\omega t)} \end{cases} \quad (\text{Antisymmetric}) \quad (2.4)$$

where subscript *n* denotes the values for each mode; B_n , A_n are the amplitudes to be determined using normal mode expansion method, ξ_{Sn} , ξ_{An} are wave numbers evaluated using the relation $\xi=\frac{\omega}{c}$,where *c* is wave speed; α and β are functions given by $\alpha^2=\frac{\omega^2}{c_p^2}-\xi^2$ and $\beta^2=\frac{\omega^2}{c_s^2}-\xi^2$; R_{Sn} , R_{An} are the symmetric and antisymmetric eigen-coefficients calculated from the solution of the Rayleigh-Lamb equation for symmetric and antisymmetric modes:

$$\frac{\tan\alpha d}{\tan\beta d}=-\left[\frac{\left(\xi^2-\beta^2\right)^2}{4\xi^2\alpha\beta}\right]^{\pm1} \qquad (2.5)$$

For free wave motion, the homogeneous solution is derived by applying the stress-free boundary conditions at the upper and lower surfaces ($y = \pm d$, where d is the plate half thickness)

$$R_S = \frac{\left(\xi_S{}^2 - \beta_S{}^2\right)\cos\alpha_S d}{2\xi_S\beta_S\cos\beta_S d} \qquad R_A = \frac{\left(\xi_A{}^2 - \beta_A{}^2\right)\sin\alpha_A d}{2\xi_A\beta_A\sin\beta_A d} \tag{2.6}$$

Power flow normalization is used to determine a closed form for expanded amplitudes B_n , A_n . This method is based on the complex reciprocity relation and orthogonal modes (Auld, 1990; Santoni, 2010).

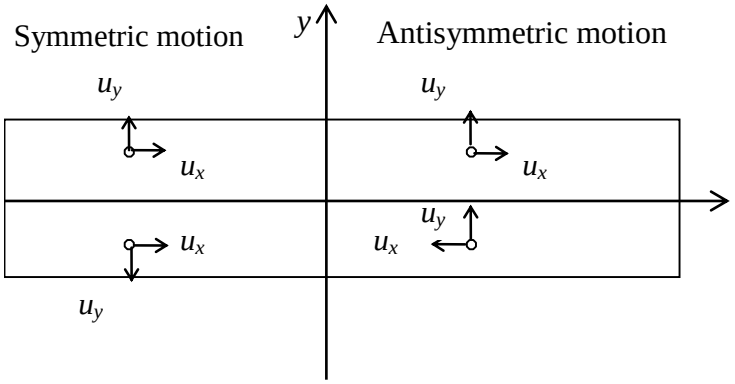

Figure 2.3. Symmetric and antisymmetric particle motion across the plate thickness.

2.2.2. Reciprocity Relation for Lamb waves

Reciprocity relation is essentially an extension of Newton's third law of motion, where action and reaction are equivalent. Assume $\mathbf{u}_{12}$ is the displacement of point P_1 due to force $\mathbf{F}_2$, and $\mathbf{u}_{21}$ is the displacement of point P_2 due to force $\mathbf{F}_1$. In its most elementary form, the *mechanics reciprocity principle* states that (Santoni, 2010): the work done at point P_1 by force $\mathbf{F}_1$ upon the displacement induced by force $\mathbf{F}_2$ is the

same as the work done at point P_2 by force $\mathbf{F}_2$ upon the displacement induced by force $\mathbf{F}_1$, i.e., $\mathbf{F}_1 \cdot \mathbf{u}_{12} = \mathbf{F}_2 \cdot \mathbf{u}_{21}$

For Lamb waves, we have real reciprocity and complex reciprocity; we focus on complex reciprocity following Auld (1990).

Considering a generic body Ω, and two sources $\mathbf{F}_1$ and $\mathbf{F}_2$ applied at points P_1 and P_2 (**Figure 2.4**); the two force sources produce two wave fields with velocity and stress $\mathbf{v}_1, \mathbf{T}_1$ and $\mathbf{v}_2, \mathbf{T}_2$. Using equation of motion and applying the two different sources (1) and (2) and adding the two field equations together, we can prove the complex reciprocity form that relates the velocity responses, tractions and applied sources for harmonic excitation, i.e.,

$$\nabla\left(\tilde{\mathbf{v}}_2 \cdot \mathbf{T}_1 + \mathbf{v}_1 \cdot \tilde{\mathbf{T}}_2\right) = -\left(\tilde{\mathbf{v}}_2 \cdot \mathbf{F}_1 + \mathbf{v}_1 \cdot \tilde{\mathbf{F}}_2\right) \tag{2.7}$$

For Lamb waves, a similar relation has been derived in Santoni (2010), with the assumption of time harmonic solution. One important assumption considered throughout the analysis is that Lamb waves fields are *z-invariant*. Hence, the only surviving stresses are normal stresses, T_{xx}, T_{yy} and shear stress T_{xy}; velocity fields are v_x, v_y; superscript ^{1,2} indicate fields due to sources ^{1,2}.

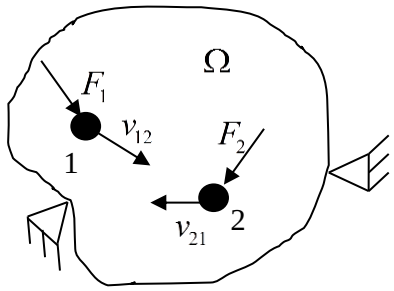

Figure 2.4. Reciprocity relation, (Santoni, 2010)

The complex reciprocity relation for Lamb waves takes the form:

$$\begin{aligned}&\frac{\partial}{\partial x}\left(\tilde{v}_x^2 T_{xx}^1 + \tilde{v}_y^2 T_{xy}^1 + v_x^1 \tilde{T}_{xx}^2 + v_y^1 \tilde{T}_{xy}^2\right) + \frac{\partial}{\partial y}\left(\tilde{v}_x^2 T_{xy}^1 + \tilde{v}_y^2 T_{yy}^1 + v_x^1 \tilde{T}_{xy}^2 + v_y^1 \tilde{T}_{yy}^2\right) \\ &= -\tilde{v}_x^2 F_x^1 - v_x^1 \tilde{F}_x^2 - \tilde{v}_y^2 F_y^1 - v_y^1 \tilde{F}_y^2\end{aligned} \tag{2.8}$$

This reciprocity relation is the basic formula used to derive orthogonality condition; in addition, the source influence (PWAS excitation) determines modal-contribution factors for each mode.

2.2.3. Orthogonality of Lamb waves

The definition of orthogonal functions *U* over given domain [*a*,*b*] can be defined as

$$\int_a^b U_m U_n dy = 0 \quad \text{for } m \neq n \tag{2.9}$$

Recalling the complex reciprocity relation of Eq. (2.7), with the source forces F_x, $F_y = 0$ and assuming 1 and 2 are two solutions for time-harmonic-propagating Lamb waves, we get

$$\begin{aligned}\mathbf{v}_1(x,y,z,t) &= \left(v_x^n(y)\hat{\mathbf{x}} + v_y^n(y)\hat{\mathbf{y}}\right)e^{-i\xi_n x}e^{i\omega t} \\ \tilde{\mathbf{v}}_2(x,y,z,t) &= \left(\tilde{v}_x^m(y)\hat{\mathbf{x}} + \tilde{v}_y^m(y)\hat{\mathbf{y}}\right)e^{i\tilde{\xi}_m x}e^{-i\omega t}\end{aligned} \tag{2.10}$$

$$\begin{aligned}\mathbf{T}_1(x,y,z,t) &= \begin{bmatrix} T_{xx}^n(y) & T_{yx}^n(y) & 0 \\ T_{yx}^n(y) & T_{yy}^n(y) & 0 \\ 0 & 0 & T_{zz}^n(y) \end{bmatrix} e^{-i\xi_n x}e^{i\omega t} \\ \tilde{\mathbf{T}}_2(x,y,z,t) &= \begin{bmatrix} \tilde{T}_{xx}^m(y) & \tilde{T}_{yx}^m(y) & 0 \\ \tilde{T}_{yx}^m(y) & \tilde{T}_{yy}^m(y) & 0 \\ 0 & 0 & \tilde{T}_{zz}^m(y) \end{bmatrix} e^{i\tilde{\xi}_m x}e^{-i\omega t}\end{aligned} \tag{2.11}$$

Substituting Eqs. (2.10) and (2.11) in the reciprocity Eq. (2.7) with F_x, $F_y = 0$ and integrating over plate thickness, we get

$$-i\left(\xi_n-\tilde{\xi}_m\right)\int_{-d}^{d}\left(v_y^n(y)\tilde{T}_{xy}^m(y)+\tilde{v}_y^m(y)T_{xy}^n(y)+v_x^n(y)\tilde{T}_{xx}^m(y)+\tilde{v}_x^m(y)T_{xx}^n(y)\right)dy= \\ -\left(v_y^n(y)\tilde{T}_{yy}^m(y)+\tilde{v}_y^m(y)T_{yy}^n(y)+v_x^n(y)\tilde{T}_{xy}^m(y)+\tilde{v}_x^m(y)T_{xy}^n(y)\right)\Big|_{-d}^{d} \tag{2.12}$$

Using the assumption of traction free boundary condition, $T_{xy}=T_{yy}=0$, at the top and bottom surfaces, Eq. (2.12) yields

$$-i\left(\xi_n-\tilde{\xi}_m\right)\int_{-d}^{d}\left(v_y^n(y)\tilde{T}_{xy}^m(y)+\tilde{v}_y^m(y)T_{xy}^n(y)+v_x^n(y)\tilde{T}_{xx}^m(y)+\tilde{v}_x^m(y)T_{xx}^n(y)\right)dy=0 \tag{2.13}$$

Alternatively, in short form:

$$i\left(\xi_n-\tilde{\xi}_m\right)4P_{mn}=0 \tag{2.14}$$

where

$$P_{nm}=-\frac{1}{4}\int_{-d}^{d}\left(v_y^n(y)\tilde{T}_{xy}^m(y)+\tilde{v}_y^m(y)T_{xy}^n(y)+v_x^n(y)\tilde{T}_{xx}^m(y)+\tilde{v}_x^m(y)T_{xx}^n(y)\right)dy \tag{2.15}$$

Recall our assumption of considering only propagating waves (evanescent waves, which die out away from the source, are ignored); consequently, ξ_m,ξ_n are real, and $\tilde{\xi}_m=\xi_m$. Since $\mathrm{Re}(\tilde{a}\cdot b)=\mathrm{Re}(a\cdot\tilde{b})$, the orthogonality condition can be further simplified to

$$P_{mn}=\begin{cases}0 & \text{if } m\neq n\\ \mathrm{Re}\left[-\frac{1}{2}\int_{-d}^{d}\left(\tilde{v}_x^n(y)T_{xx}^n(y)+\tilde{v}_y^n(y)T_{xy}^n(y)\right)dy\right] & \text{if } m=n\end{cases} \tag{2.16}$$

P_{mn} is a measure of average power flow through the plate, and is used to determine Lamb waves amplitudes, through normalization.

2.2.4. Normalization of Wave Amplitudes

To apply orthogonality of Lamb waves of Eq. (2.16), velocity fields v_x^n, v_y^n and stresses T_{xx}^n, T_{xy}^n are required. In addition, stresses are needed to evaluate potential energy and wave power. From elasticity equations, stresses are related to strains by Lame constants as

$$\begin{aligned} T_{xx} &= (\lambda + 2\mu) S_{xx} + \lambda S_{yy} \\ T_{yy} &= \lambda S_{xx} + (\lambda + 2\mu) S_{yy} \\ T_{xy} &= 2\mu S_{xy} \end{aligned} \tag{2.17}$$

where S_{xx}, S_{yy} and S_{xy} are normal and shear strains; they can be derived by differentiating Eqs. (2.3), (2.4)

For symmetric waves *(superscript S)*

$$\begin{cases} S_{xx}^S = iB_n \xi_{Sn} \left(\xi_{Sn} \cos \alpha_{Sn} y - R_{Sn} \beta_{Sn} \cos \beta_{Sn} y \right) e^{-i(\xi_{Sn} x - \omega t)} \\ S_{yy}^S = iB_n \left(\alpha_{Sn}^2 \cos \alpha_{Sn} y + R_{Sn} \xi_{Sn} \beta_{Sn} \cos \beta_{Sn} y \right) e^{-i(\xi_{Sn} x - \omega t)} \\ 2S_{xy}^S = B_n \left(2\xi_{Sn} \alpha_{Sn} \sin \alpha_{Sn} y + R_{Sn} \left(\xi_{Sn}^2 - \beta_{Sn}^2 \right) \sin \beta_{Sn} y \right) e^{-i(\xi_{Sn} x - \omega t)} \end{cases} \tag{2.18}$$

Substituting the strains in Hooke's law, Eq. (2.17) becomes

$$\begin{cases} T_{xx}^S = iB_n \left[\left((\lambda + 2\mu) \xi_{Sn}^2 + \lambda \alpha_{Sn}^2 \right) \cos \alpha_{Sn} y - 2\mu R_{Sn} \xi_{Sn} \beta_{Sn} \cos \beta_{Sn} y \right] e^{-i(\xi_{Sn} x - \omega t)} \\ T_{yy}^S = iB_n \left[\left(\lambda \xi_{Sn}^2 + (\lambda + 2\mu) \alpha_{Sn}^2 \right) \cos \alpha_{Sn} y + 2\mu R_{Sn} \xi_{Sn} \beta_{Sn} \cos \beta_{Sn} y \right] e^{-i(\xi_{Sn} x - \omega t)} \\ T_{xy}^S = \mu B_n \left[2\xi_{Sn} \alpha_{Sn} \sin \alpha_{Sn} y + R_{Sn} \left(\xi_{Sn}^2 - \beta_{Sn}^2 \right) \sin \beta_{Sn} y \right] e^{-i(\xi_{Sn} x - \omega t)} \end{cases} \tag{2.19}$$

Equations (2.19) can be rearranged using the relations

$$\begin{aligned} (\lambda + 2\mu) \xi^2 + \lambda \alpha^2 &= \mu \left(\xi^2 + \beta^2 - 2\alpha^2 \right) \\ \lambda \xi^2 + (\lambda + 2\mu) \alpha^2 &= -\mu \left(\xi^2 - \beta^2 \right) \end{aligned} \tag{2.20}$$

The stresses for symmetric case become

$$\begin{cases} T_{xx}^{S} = i\mu B_n \left[\left(\xi_{Sn}^2 + \beta_{Sn}^2 - 2\alpha_{Sn}^2 \right) \cos \alpha_{Sn} y - 2R_{Sn} \xi_{Sn} \beta_{Sn} \cos \beta_{Sn} y \right] e^{-i(\xi_{Sn} x - \omega t)} \\ T_{yy}^{S} = i\mu B_n \left[-\left(\xi_{Sn}^2 - \beta_{Sn}^2 \right) \cos \alpha_{Sn} y + 2R_{Sn} \xi_{Sn} \beta_{Sn} \cos \beta_{Sn} y \right] e^{-i(\xi_{Sn} x - \omega t)} \\ T_{xy}^{S} = \mu B_n \left[2\xi_{Sn} \alpha_{Sn} \sin \alpha_{Sn} y + R_{Sn} \left(\xi_{Sn}^2 - \beta_{Sn}^2 \right) \sin \beta_{Sn} y \right] e^{-i(\xi_{Sn} x - \omega t)} \end{cases} \quad (2.21)$$

Similarly for antisymmetric waves, *(superscript A)* for the sake of completeness

$$\begin{cases} S_{xx}^{A} = iA_n \left(\xi_{An}^2 \sin \alpha_{An} y - R_{An} \xi_{An} \beta_{An} \sin \beta_{An} y \right) e^{-i(\xi_{An} x - \omega t)} \\ S_{yy}^{A} = iA_n \left(\alpha_{An}^2 \sin \alpha_{An} y + R_{An} \xi_{An} \beta_{An} \sin \beta_{An} y \right) e^{-i(\xi_{An} x - \omega t)} \\ 2S_{xy}^{A} = -A_n \left(2\xi_{An} \alpha_{An} \cos \alpha_{An} y + R_{An} \left(\xi_{An}^2 - \beta_{An}^2 \right) \cos \beta_{An} y \right) e^{-i(\xi_{An} x - \omega t)} \end{cases} \quad (2.22)$$

The stresses for antisymmetric case are

$$\begin{cases} T_{xx}^{A} = i\mu A_n \left[\left(\xi_{An}^2 + \beta_{An}^2 - 2\alpha_{An}^2 \right) \sin \alpha_{An} y - 2R_{An} \xi_{An} \beta_{An} \sin \beta_{An} y \right] e^{-i(\xi_{An} x - \omega t)} \\ T_{yy}^{A} = i\mu A_n \left[-\left(\xi_{An}^2 - \beta_{An}^2 \right) \sin \alpha_{An} y + 2R_{An} \xi_{An} \beta_{An} \sin \beta_{An} y \right] e^{-i(\xi_{An} x - \omega t)} \\ T_{xy}^{A} = -\mu A_n \left[2\xi_{An} \alpha_{An} \cos \alpha_{An} y + R_{An} \left(\xi_{An}^2 - \beta_{An}^2 \right) \cos \beta_{An} y \right] e^{-i(\xi_{An} x - \omega t)} \end{cases} \quad (2.23)$$

Velocity fields are evaluated by taking time derivative of displacements in Eqs. (2.3) and (2.4)

$$\begin{cases} v_x^{S} = \dfrac{\partial u_x^{S}}{\partial t} = -i\omega B \left(\xi_S \cos \alpha_S y - R_S \beta_S \cos \beta_S y \right) e^{-i(\xi_S x - \omega t)} \\ v_y^{S} = \dfrac{\partial u_y^{S}}{\partial t} = -\omega B \left(\alpha_S \sin \alpha_S y + R_S \xi_S \sin \beta_S y \right) e^{-i(\xi_S x - \omega t)} \end{cases} \quad (2.24)$$

$$\begin{cases} v_x^{A} = \dfrac{\partial u_x^{A}}{\partial t} = -i\omega A \left(\xi_A \sin \alpha_A y - \beta_A R_A \sin \beta_A y \right) e^{-i(\xi_A x - \omega t)} \\ v_y^{A} = \dfrac{\partial u_y^{A}}{\partial t} = \omega A \left(\alpha_A \cos \alpha_A y + \xi_A R_A \cos \beta_A y \right) e^{-i(\xi_A x - \omega t)} \end{cases} \quad (2.25)$$

Substituting Eqs. (2.21),(2.23),(2.24) and (2.25) in Eq. (2.16) and performing the integration yields

$$P_{nn} = \frac{\omega \mu B_n^{\,2}}{2} W_S \quad \text{(Symmetric)} \qquad P_{nn} = \frac{\omega \mu A_n^{\,2}}{2} W_A \quad \text{(Antisymmetric)} \quad (2.26)$$

where

$$W_S = \begin{bmatrix} \xi_S d\left(R_S^2+1\right)\left(\xi_S^2+\beta_S^2\right) - R_S^2\xi_S\left(\xi_S^2-3\beta_S^2\right)\dfrac{\sin\beta_S d\cos\beta_S d}{\beta_S} \\ +\xi_S\left(\xi_S^2+\beta_S^2-4\alpha_S^2\right)\dfrac{\sin\alpha_S d\cos\alpha_S d}{\alpha_S} \\ +4R_S\alpha_S\beta_S\sin\alpha_S d\cos\beta_S d - 2R_S\left(3\xi_S^2+\beta_S{}^2\right)\cos\alpha_S d\sin\beta_S d \end{bmatrix} \tag{2.27}$$

$$W_A = -\begin{bmatrix} -\xi_A d\left(R_A^2+1\right)\left(\xi_A^2+\beta_A^2\right) - R_A^2\xi_A\left(\xi_A^2-3\beta_A^2\right)\dfrac{\sin\beta_A d\cos\beta_A d}{\beta_A} \\ +\xi_A\left(\xi_A^2+\beta_A^2-4\alpha_A^2\right)\dfrac{\sin\alpha_A d\cos\alpha_A d}{\alpha_A} \\ +4R_A\alpha_A\beta_A\cos\alpha_A d\sin\beta_A d - 2R_A\left(3\xi_A^2+\beta_A^2\right)\sin\alpha_A d\cos\beta_A d \end{bmatrix} \tag{2.28}$$

The symmetric mode coefficient B_n and the antisymmetric mode coefficient A_n can be resolved as

$$B_n = \sqrt{\frac{2P_{nn}}{\omega\mu W_{Sn}}} \quad \text{(symmetric)} \qquad A_n = \sqrt{\frac{2P_{nn}}{\omega\mu W_{An}}} \quad \text{(antisymmetric)} \tag{2.29}$$

For normal modes, we may assume $P_{nn}=1$; hence,

$$B_n = \sqrt{\frac{2}{\omega\mu W_{Sn}}} \quad \text{(symmetric)} \qquad A_n = \sqrt{\frac{2}{\omega\mu W_{An}}} \quad \text{(antisymmetric)} \tag{2.30}$$

2.2.5. Modal Contribution Factors and PWAS Excitation

Basic assumptions used in this study are: (1) straight crested Lamb waves, i.e., z-invariant, and (2) ideal bonding (pin-force) connection between PWAS and structure (**Figure 2.5**). After consideration of the orthogonality of Lamb wave modes and after the normalization of modes amplitudes with respect to the power, modal-participation factor

for each mode needs to be evaluated (i.e. how much a particular mode contributes to the total wave power and energy). This uses the reciprocity relation with consideration of excitation forces from the source (e.g. a PWAS on the excited structure).

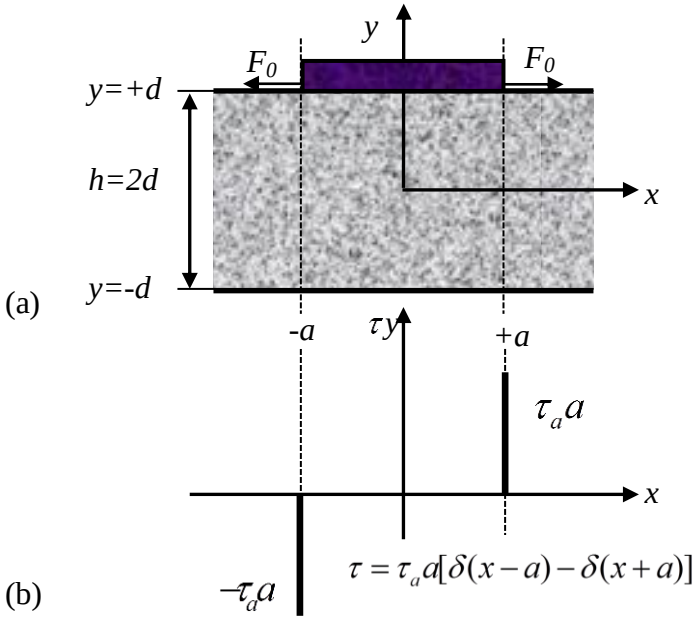

Figure 2.5. Pin force model for structurally- bonded PWAS, reproduced from Giurgiutiu (2008); (a) PWAS pin forces at the ends on the upper surface; (b) shear stresses developed.

Recalling the complex reciprocity Eq. (2.7), multiplying by -1, and upon expansion of the del operator, we get

$$\frac{\partial}{\partial y}\left(-\tilde{\mathbf{v}}_2 \cdot \mathbf{T}_1 - \mathbf{v}_1 \cdot \tilde{\mathbf{T}}_2\right) \cdot \hat{\mathbf{y}} + \frac{\partial}{\partial x}\left(-\tilde{\mathbf{v}}_2 \cdot \mathbf{T}_1 - \mathbf{v}_1 \cdot \tilde{\mathbf{T}}_2\right) \cdot \hat{\mathbf{x}} = \tilde{\mathbf{v}}_2 \mathbf{F}_1 + \mathbf{v}_1 \tilde{\mathbf{F}}_2 \qquad (2.31)$$

where $\mathbf{F}$ is a volume source; $\mathbf{T} \cdot \hat{\mathbf{y}}$ are traction forces and $\mathbf{v}$ are velocity sources.

A solution denoted by '1' such as $\mathbf{T}_1$ indicates traction due to source excitation (e.g. by PWAS) while a solution denoted by '2' is representing normal modes, i.e. a homogeneous solution of eigenfunctions of the free mode shapes of the structure – without considering excitation from the source. Fields due to the excitation source can be

represented as normal modes summation over all possible modes (Rose, 1999; Santoni, 2010), i.e.

$$\begin{aligned}\mathbf{v}_1 &= \mathbf{v}_1(x,y) = \sum_m a_m(x)\mathbf{v}_m(y) \\ \mathbf{T}_1 &= \mathbf{T}_1(x,y) = \sum_m a_m(x)\mathbf{T}_m(y)\end{aligned} \tag{2.32}$$

where $a_m(x)$ are the modal-participation factors that must be determined.

Homogeneous solution '2' can be represented as

$$\begin{aligned}\mathbf{v}_2(x,y) &= \mathbf{v}_n(y)e^{-i\xi_n x} \\ \mathbf{T}_2(x,y) &= \mathbf{T}_n(y)e^{-i\xi_n x}\end{aligned} \tag{2.33}$$

Integrate Eq. (2.31) with respect to the plate thickness y from ($y=-d$ to $y=+d$) to get

$$\left(-\tilde{\mathbf{v}}_2\cdot\mathbf{T}_1-\mathbf{v}_1\cdot\tilde{\mathbf{T}}_2\right)\cdot\hat{\mathbf{y}}\Big|_{-d}^{d}+\int_{-d}^{d}\frac{\partial}{\partial x}\left(-\tilde{\mathbf{v}}_2\cdot\mathbf{T}_1-\mathbf{v}_1\cdot\tilde{\mathbf{T}}_2\right)\cdot\hat{\mathbf{x}}\,dy=\int_{-d}^{d}\tilde{\mathbf{v}}_2\mathbf{F}_1\,dy \tag{2.34}$$

Substitution of Eqs. (2.32) and (2.33) ,and rearrangement yields

$$\begin{aligned}&\left(-\tilde{\mathbf{v}}_n(y)\cdot\mathbf{T}_1-\mathbf{v}_1\cdot\tilde{\mathbf{T}}_n(y)\right)\cdot\hat{\mathbf{y}}\Big|_{-d}^{d}\,e^{i\tilde{\xi}_n x} \\ &+\frac{\partial}{\partial x}\left[e^{i\tilde{\xi}_n x}\sum_m a_m(x)\int_{-d}^{d}\left(-\tilde{\mathbf{v}}_n(y)\cdot\mathbf{T}_m(y)-\mathbf{v}_m(y)\cdot\tilde{\mathbf{T}}_n(y)\right)\cdot\hat{\mathbf{x}}dy\right]=e^{i\tilde{\xi}_n x}\int_{-d}^{d}\tilde{\mathbf{v}}_n(y)\mathbf{F}_1\,dy\end{aligned} \tag{2.35}$$

Recall the orthogonality relation in its general form

$$P_{mn}=-\frac{1}{4}\int_{-d}^{d}\left(\tilde{\mathbf{v}}_m(y)\cdot\mathbf{T}_n(y)+\mathbf{v}_n(y)\cdot\tilde{\mathbf{T}}_m(y)\right)\cdot\hat{\mathbf{x}}\,dy \tag{2.36}$$

In the absence of a volume force source term $\mathbf{F}_1$, Eq. (2.35) yields

$$\left(-\tilde{\mathbf{v}}_n\cdot\mathbf{T}_1-\mathbf{v}_1\cdot\tilde{\mathbf{T}}_n\right)\cdot\hat{\mathbf{y}}\Big|_{-d}^{d}\,e^{i\tilde{\xi}_n x}+\frac{\partial}{\partial x}e^{i\tilde{\xi}_n x}\sum_m 4a_m(x)P_{mn}=0 \tag{2.37}$$

Since the modes are orthogonal, the summation in (2.37) has only one nonzero term corresponding to the propagating mode n (ξ_n real) for which $P_{nn} \neq 0$. Hence, Eq. (2.37) becomes

$$4P_{nn}\left(\frac{\partial}{\partial x} + i\tilde{\xi}_n\right)a_n(x) = \left(\tilde{\mathbf{v}}_n \cdot \mathbf{T}_1 + \mathbf{v}_1 \cdot \tilde{\mathbf{T}}_n\right) \cdot \hat{\mathbf{y}}\Big|_{-d}^{d} \tag{2.38}$$

This is a general ordinary differential equation, which needs to be solved to get the modal participation factor $a_n(x)$.

$\tilde{\mathbf{T}}_n$ is the traction force; it must satisfy the traction free boundary condition for Lamb waves, $T_{xy}^n\big|_{\pm d} = 0$ and $T_{yy}^n\big|_{\pm d} = 0$. $\mathbf{T}_1$ is the excitation shear. We have $T_{xy}\big|_{d} = t_x(x)$ at the upper surface, and $T_{xy}\big|_{-d} = 0$ on the lower surface, since PWAS excitation is only on the upper surface (**Figure 2.5**).

For Lamb waves, Eq. (2.38) takes the form

$$4P_{nn}\left(\frac{\partial}{\partial x} + i\tilde{\xi}_n\right)a_n(x) = \begin{pmatrix} v_y^1(y)\tilde{T}_{yy}^n(y) + \tilde{v}_y^n(y)T_{yy}^1(y) \\ +v_x^1(y)\tilde{T}_{xy}^n(y) + \tilde{v}_x^n(y)T_{xy}^1(y) \end{pmatrix}_{-d}^{d} \tag{2.39}$$

Applying traction free conditions and PWAS excitation, then solving the ODE, yields

$$a_n^+(x) = \left[\frac{\tilde{v}_x^n(d)}{4P_{nn}}\int_{-a}^{a} e^{i\tilde{\xi}_n\bar{x}}t_x(\bar{x})d\bar{x}\right]e^{-i\tilde{\xi}_n x} \quad \text{for } x > a \tag{2.40}$$

It should be noted that this formula is only for the forward wave solution and outside the excitation region, i.e. for $x > a$.

The total particle velocity using NME can be written as

$$\mathbf{v}(x,y) = \sum_n a_n(x)\mathbf{v}_n(y) \tag{2.41}$$

where $\mathbf{v}_n(y)$ is the velocity modeshape of the n^{th} mode, i.e., $\mathbf{v}_n(y) = \begin{Bmatrix} v_x^n(y) \\ v_y^n(y) \end{Bmatrix}$. $\mathbf{v}_n(y)$ can be derived using the combination of the symmetric particle velocity in Eq. (2.24) with the symmetric normalization coefficient of Eq. (2.30) and the antisymmetric particle velocity Eq. (2.25) and antisymmetric normalization coefficient of Eq. (2.30).

We exemplify the NME method for velocity fields with two examples: (a) 1-mm thick aluminum plate, up to 2000 kHz where only S0, A0 modes exist; (b) 2.6-mm thick steel plate, with excitation up to 500 kHz. **Figure 2.6** shows the particle velocity at the plate's surface in the *x*-axis and y-axis for the two plates. Note that the values of NME velocities are not multiplied yet by PWAS excitation. The displayed results are only for the first symmetric S0 and antisymmetric A0 modes; the multi-modes demonstration will be shown in a later section.

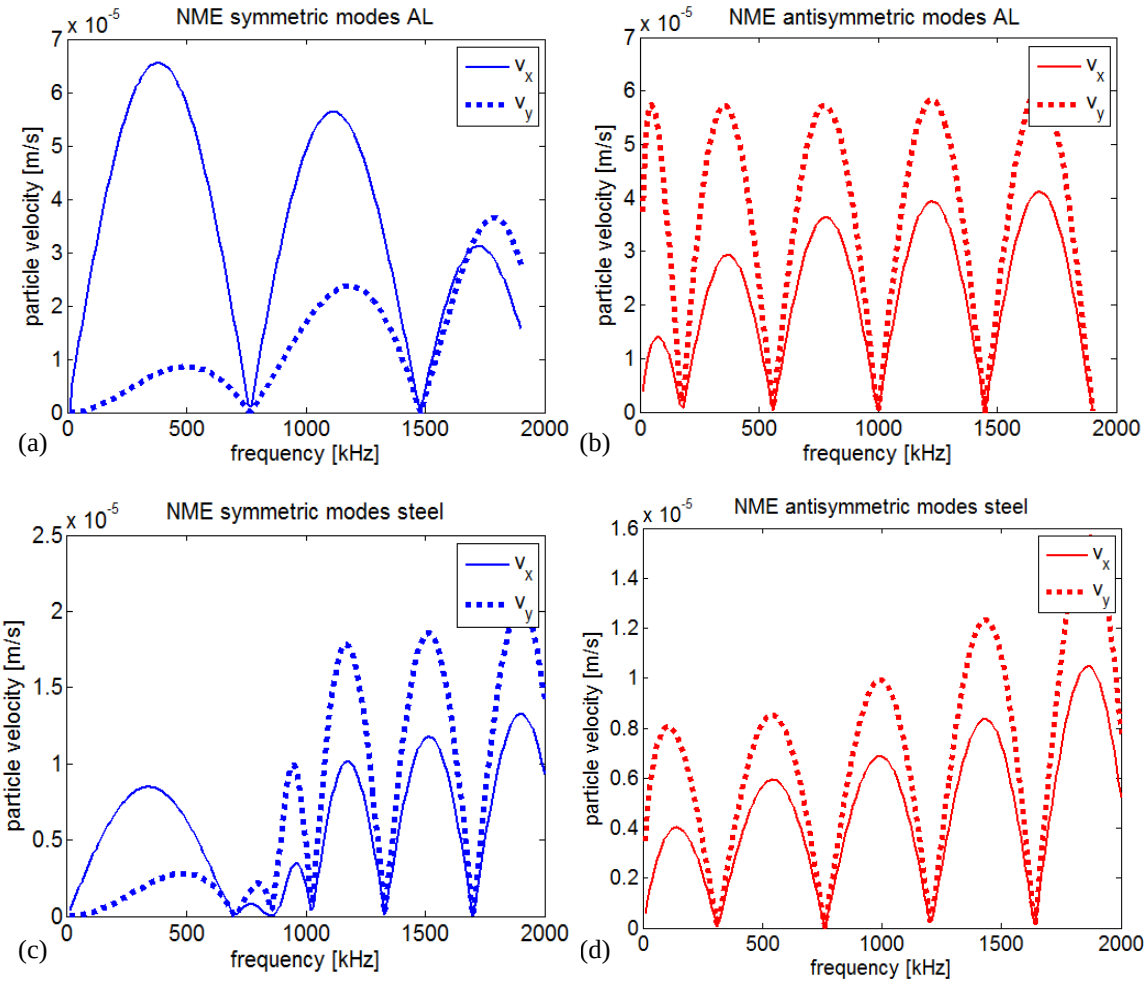

Figure 2.6. Normal mode expansion for particle velocity fields (a) aluminum S0, (b) aluminum A0, (c) steel S0, and (d) steel A0 mode.

Considering the ideal bonding assumption (pin-force model), the load transfer takes place over an infinitesimal region at the ends of the PWAS. Assuming a PWAS with a center at $x_0 = 0$ and length $l_a = 2a$, the traction on the plate surface can be written as

$$t_x(x)=a\tau_0[\delta(x-a)-\delta(x+a)] = F_0(\omega)[\delta(x-a)-\delta(x+a)] \tag{2.42}$$

Here F_0 is the pin- force per unit width. Substitution of Eq. (2.42) into Eq. (2.40) gives the mode participation factor under PWAS excitation as

$$a_n^{PWAS}(x) = \frac{\tilde{v}_x^n(d)}{4P_{nn}} F_0(\omega)[e^{i\xi_n a} - e^{-i\xi_n a}]e^{-i\xi_n x} = g_n F_0(\omega)_0 e^{-i\xi_n x} \tag{2.43}$$

where g_n is the coefficient $g_n = \frac{\tilde{v}_x^n(d)}{4P_{nn}}[e^{i\xi_n a} - e^{-i\xi_n a}]$

The Lamb wave NME of the particle displacement under PWAS excitation is

$$u(x,y) = \frac{1}{i\omega}\sum_n g_n F_0(\omega) e^{-i\xi_n x}\mathbf{v}_n(y) \tag{2.44}$$

The displacement in x-direction at the PWAS end ($x = a,\ y = d$) is

$$u_x(a,d) = \frac{1}{i\omega}\sum_n \frac{\tilde{v}_x^n(d)}{4P_{nn}} v_x^n(d)[e^{i\xi_n a} - e^{-i\xi_n a}]F_0(\omega)e^{-i\xi_n a} \tag{2.45}$$

2.2.6. PWAS – Structure Interaction

Consider a PWAS of length $l = 2a$, width b and thickness t_a; the relation between the PWAS pin-force applied to the structure and the particle displacement is through the structural dynamic stiffness. The structures as well as the PWAS stiffness are now analyzed. When the PWAS transmitter is excited by an oscillatory voltage, its volume expands in phase with the voltage in accordance with the piezoelectric effect, (**Figure 2.7**). Expansion of the PWAS mounted on the surface of the structure induces a surface reaction from the structure in the form of a force at the PWAS end. The PWAS end displacement is constrained by the plate and is equal to the plate displacement at $x = a$. The reaction force along the PWAS edge, $F_{.0}(\omega)b$, depends on the PWAS displacement, u_{PWAS}, and on the frequency-dependent dynamic stiffness, $k_{str}(\omega)$, presented by the structure to the PWAS.

$$F_0(\omega)b = k_{str}(\omega)u_x(a,d) \tag{2.46}$$

The two stiffness elements on the right and the left of PWAS are selected to be $2k_{str}$; hence the overall structure stiffness is k_{str} (**Figure 2.7**). Under harmonic excitation, the dynamic stiffness $k_{str}(\omega)$ is obtained by dividing the force by the displacement given by Eq. (2.44), i.e.

$$k_{str}(\omega) = \frac{F_0(\omega)b}{\hat{u}_x(a,d)} = i\omega b\left[\sum_n g_n e^{-i\xi_n a}\mathbf{v}_n(d)\right]^{-1} \tag{2.47}$$

Define the static stiffness k_{PWAS} of a free PWAS as

$$k_{PWAS} = \frac{t_a b}{s_{11}^E a} \tag{2.48}$$

The dynamic stiffness ratio is defined as the ratio between $k_{str}(\omega)$ and k_{PWAS}, i.e.,

$$r(\omega) = \frac{k_{str}(\omega)}{k_{PWAS}} \tag{2.49}$$

The relation between pin-force force per unit width and the static stiffness of the PWAS is

$$F_0(\omega)b = k_{PWAS}\left(u_x(a,d) - \frac{1}{2}u_{ISA}\right) \tag{2.50}$$

where u_{ISA} is the "induced strain actuation" displacement (Giurgiutiu, 2008), defined as, $u_{ISA} = ld_{31}\hat{V}/t_a$ and the quantity $u_x(a,d) - \frac{1}{2}u_{ISA}$ represents the total x-direction displacement at the right tip of the PWAS (because of symmetry, only the forward propagating wave needs to be considered.)

Substitute $u_x(a,d)$ from Eq. (2.45) into Eq. (2.50) and solve for F_0 using k_{str} from Eq. (2.47) to get

$$F_0(\omega) = \frac{1}{b}\left(\frac{r(\omega)}{1-r(\omega)}\right)\frac{k_{PWAS}u_{ISA}}{2} \tag{2.51}$$

The excitation pin-force $F_0(\omega)$ can now be used to determine the NME fields (displacements – strains – velocities), the modal participation factors $a_n^{PWAS}(x)$ and the coefficients g_n; then the power and energy can be analyzed.

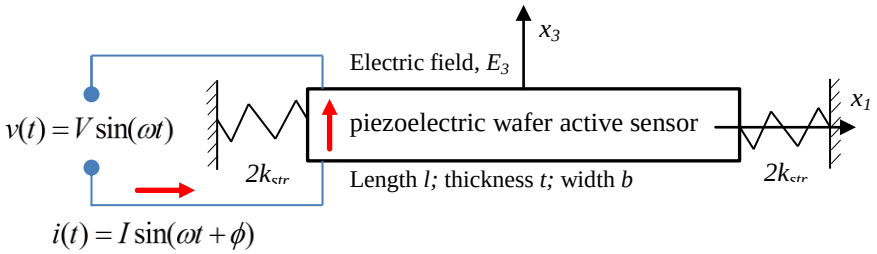

Figure 2.7. PWAS constrained by an overall structural stiffness k_{str}.

2.2.7. Power Transduction between PWAS and Structure

The power and energy transduction flow chart for a PWAS transmitter on a structure is shown in **Figure 2.8** (Lin et al., 2012). The electrical energy due to the input voltage applied at the PWAS terminals is converted, through piezoelectric transduction, into mechanical energy that activates the expansion-contraction motion of the PWAS transducer. This motion is transmitted to the underlying structure through the shear stress in the adhesive layer at the PWAS-structure interface. As a result, ultrasonic guided waves are excited into the underlying structure. The mechanical power at the interface becomes the acoustic wave power and the generated Lamb waves propagate in the structure.

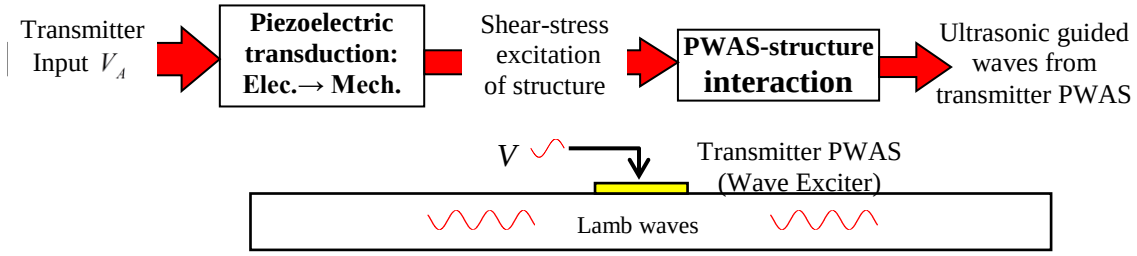

Figure 2.8. PWAS transmitter power flow (Lin et al., 2012)

2.2.8. PWAS Admittance and Electrical Active Power

To calculate the transmitter electrical power and energy, we need to calculate the input electrical power by using input admittance of the PWAS when attached to the structure. Because of the electromechanical coupling, the impedance is strongly influenced by the dynamic behavior of the structure and is substantially different from the free-PWAS impedance.

Under harmonic excitation, the time-averaged power is the average amount of energy converted per unit time under continuous harmonic excitation. The time-averaged product of the two harmonic variables is one half the product of one variable times the conjugate of the other. When a harmonic voltage is applied to the transmitter PWAS, the current is

$$I = Y\hat{V} \tag{2.52}$$

The constrained PWAS admittance can be expressed (Giurgiutiu, 2008) using the frequency dependent stiffness ratio of equation(2.49), i.e.,

$$Y(\omega) = i\omega C_0 \left[1 - k_{31}^2 \left(1 - \frac{1}{r(\omega) + \phi(\omega)\cot\phi(\omega)} \right) \right] \tag{2.53}$$

where $\phi(\omega) = \xi(\omega)a$. A simplified form of Eq. (2.53) can be obtained under the quasi-static assumption in which the PWAS dynamics are assumed to happen at much higher frequencies than the Lamb-wave propagation ($\phi(\omega) \to 0, \phi(\omega)\cot\phi(\omega) \to 1$), i.e.,

$$Y(\omega) = i\omega C_0 \left[1 - k_{31}^2 \frac{r(\omega)}{1 + r(\omega)} \right] \tag{2.54}$$

This simplified model of admittance was used in Lin and Giurgiutiu (2012); it was used for axial and flexural wave propagation at low frequency excitation. Here we use a new definition of $r(\omega)$ in Eq. (2.49) and $k_{str}(\omega)$ in Eq. (2.47) based on NME for multi-modal Lamb waves propagation.

The power rating, time-averaged active power, and reactive power are

$$P_{rating} = \frac{1}{2}|Y|\hat{V}^2 = \sqrt{P_{active}^2 + P_{reactive}^2} \qquad P_{active} = \frac{1}{2}Y_R\hat{V}^2 \qquad P_{reactive} = \frac{1}{2}Y_I\hat{V}^2 \tag{2.55}$$

where Y_R is the real part of admittance and Y_I is the imaginary part of admittance.

The active power is the power that is converted to the mechanical power at the interface. The reactive power is the imaginary part of the complex power that is not consumed and is recirculated to the power supply. The power rating is the power requirement of the power supply without distortion. In induced-strain transmitter applications, the reactive power is the dominant factor, since the transmitter impedance is dominated by its capacitive behavior (Lin et al., 2012). Managing high reactive power requirements is one of the challenges of using piezoelectric induced-strain actuators.

2.2.9. Mechanical Power

Due to the electro-mechanical transduction in the PWAS, the electrical active power is converted into the mechanical power; through shear effects in the adhesive layer between the PWAS and the structure. The mechanical power transfers into the structure and excites the guided wave. Santoni (2010) studied shear lag solution for the case of multiple Lamb wave modes. This solution can be simplified by considering that the shear stress transfer is concentrated over some infinitesimal distances at the ends of the PWAS actuator (**Figure 2.5**). The concept of ideal bonding (also known as the pin-force model) assumed that all the load transfer takes place over an infinitesimal region at the PWAS ends; the generated mechanical power is the multplication of this load times the structure particle velocity at the PWAS tip. The time-averaged power is defined as

$$\langle p \rangle = \frac{1}{T}\int_0^T p(t)\,dt \tag{2.56}$$

The time-averaged product of two harmonic variables is one half the product of one variable times the conjugate of the other. The time-averaged mechanical power at PWAS-structure interface is

$$\langle p_0 \rangle = -\frac{1}{2}\tilde{F}_0(\omega)\hat{v}_0(\omega) \tag{2.57}$$

Mechanical power excites both forward and backward propagating waves initiating from the two end tips at $x = a$ and $x = -a$. Due to symmetry, we only need to consider the forward wave, which will contain only half of the mechanical power converted from the electrical active power.

2.2.10. Lamb waves Power and Energy

The mechanically converted power is in turn transferred into the power of the propagating forward wave. It is important to mention that evanescent (non-propagating) waves are not considered in this study. The time averaged wave power is:

$$\langle p \rangle = -\frac{1}{2}\int_A \left(\tilde{T}_{xx} v_x + \tilde{T}_{xy} v_y\right) dA \tag{2.58}$$

where v denotes particle velocity either in x or y directions, T denotes stress, $\tilde{T}$ is the conjugate. These values are determined from Eqs. (2.17), (2.24) ,and (2.25). **Figure 2.9** shows all associated stresses and velocities.

The time-averaged wave power can be determined for a given section x by integration over the cross section area. Under the *z-invariant* assumption, the width b is taken outside the integration; Eq. (2.58) can be further simplified as

$$\langle p \rangle = -\frac{b}{2}\int_{-d}^{d} \left\{\left((\lambda + 2\mu)\tilde{S}_{xx} + \lambda \tilde{S}_{yy}\right) v_x + \left(2\mu \tilde{S}_{xy}\right) v_y\right\} dy \tag{2.59}$$

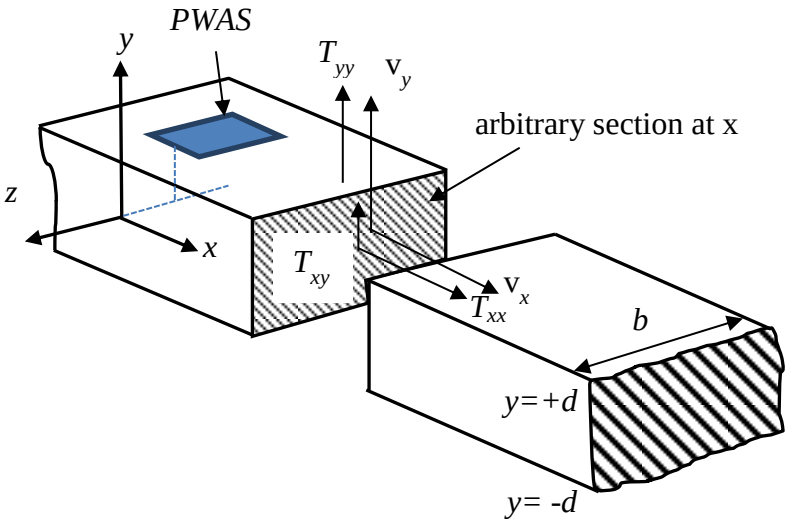

Figure 2.9. Representation of the stresses and velocities at an arbitrary section of the structure.

Orthogonality of Lamb waves can be used during the expansion of Eq. (2.59); because all the quantities are defined as summation of the symmetric solution plus the antisymmetric solution, e.g. v_x is the summation of v_x parts of Eqs. (2.24) and (2.25) . The same is true for strains.

When evaluating the multiplication of $\tilde{S}_{xx}$ times v_x , and integrating the quantities generated from multiplying the symmetric part times the antisymmetric part, it ended up as integration of sine times cosine terms and the integration vanished due to orthogonality of Lamb waves. On the other hand,'$\cos^2$' and '$\sin^2$' terms are retained. The time-averaged wave power takes the closed form:

$$\langle p \rangle = \sum_n \langle p_n^S \rangle + \sum_n \langle p_n^A \rangle \tag{2.60}$$

where $\langle p_n^S \rangle$ and $\langle p_n^A \rangle$ are the time-averaged wave powers for the symmetric mode S_n and antisymmetric mode A_n respectively.

$$\langle p_n^S \rangle = -\frac{b}{2}\left[g_n^S B_n F(\omega) \right]^2 \left(\begin{array}{l} -(\lambda+2\mu)\omega\xi_{Sn} \int_{-d}^{d} \left\{ \begin{array}{l} \xi_{Sn}^2 \cos^2 \alpha_{Sn} y + R_{Sn}^2 \beta_{Sn}^2 \cos^2 \beta_{Sn} y \\ -2R_{Sn}\beta_{Sn}\xi_{Sn} \cos\alpha_{Sn} y \cos\beta_{Sn} y \end{array} \right\} dy \\ -\lambda(\omega/\xi_{Sn}) \int_{-d}^{d} \left\{ \begin{array}{l} \xi_{Sn}^2 \alpha_{Sn}^2 \cos^2 \alpha_{Sn} y - R_{Sn}^2 \beta_{Sn}^2 \xi_{Sn}^2 \cos^2 \beta_{Sn} y \\ +R_{Sn}\beta_{Sn}\xi_{Sn}(\xi_{Sn}^2 - \alpha_{Sn}^2) \cos\alpha_{Sn} y \cos\beta_{Sn} y \end{array} \right\} dy \\ -\mu\omega \int_{-d}^{d} \left\{ \begin{array}{l} 2\xi_{Sn}\alpha_{Sn}^2 \sin^2 \alpha_{Sn} y + R_{Sn}^2 \xi_{Sn} \left(\xi_{Sn}^2 - \beta_{Sn}^2 \right) \sin^2 \beta_{Sn} y \\ +R_{Sn}\alpha_{Sn} \left(3\xi_{Sn}^2 - \beta_{Sn}^2 \right) \sin\alpha_{Sn} y \sin\beta_{Sn} y \end{array} \right\} dy \end{array} \right) \tag{2.61}$$

$$\left\langle p_n^A \right\rangle = -\frac{b}{2}\left[g_n^A A_n F(\omega) \right]^2 \left(\begin{array}{l} -(\lambda+2\mu)\omega\xi_{An} \int_{-d}^{d} \left\{ \begin{array}{l} \xi_{An}^2 \sin^2 \alpha_{An} y + R_{An}^2 \beta_{An}^2 \sin^2 \beta_{An} y \\ -2R_{An}\beta_{An}\xi_{An} \sin\alpha_{An} y \sin\beta_{An} y \end{array} \right\} dy \\ -\lambda(\omega/\xi_{An}) \int_{-d}^{d} \left\{ \begin{array}{l} \xi_{An}^2 \alpha_{An}^2 \sin^2 \alpha_{An} y - R_{An}^2 \beta_{An}^2 \xi_{An}^2 \sin^2 \beta_{Sn} y \\ +R_{An}\beta_{An}\xi_{An}(\xi_{An}^2 - \alpha_{An}^2) \sin\alpha_{An} y \sin\beta_{An} y \end{array} \right\} dy \\ -\mu\omega \int_{-d}^{d} \left\{ \begin{array}{l} 2\xi_{An}\alpha_{An}^2 \cos^2 \alpha_{An} y + R_{An}^2 \xi_{An}\left(\xi_{An}^2 - \beta_{An}^2\right) c\cos^2 \beta_{An} y \\ +R_{An}\alpha_{An}\left(3\xi_{An}^2 - \beta_{An}^2\right) \cos\alpha_{An} y \cos\beta_{An} y \end{array} \right\} dy \end{array} \right) \tag{2.62}$$

The terms $g_n^{S_n}$ and $g_n^{A_n}$ represent the coefficients in Eq. (2.43) for symmetric and antisymmetric modes.

Kinetic energy for Lamb waves is defined as

$$k_e(x,t) = \frac{1}{2}\rho \int_A \left(v_x^2 + v_y^2 \right) dA \tag{2.63}$$

The time-averaged kinetic energy associated with velocity components can be calculated as half the velocity times the conjugate of itself.

$$\left\langle k_e \right\rangle = \frac{1}{4}\rho \int_A \left(v_x . \tilde{v}_x + v_y . \tilde{v}_y \right) dA \tag{2.64}$$

The kinetic energy contains both symmetric and antisymmetric wave energy. Upon rearrangement, the time-averaged kinetic energy takes the form

$$\left\langle k_e \right\rangle = \sum_n \left\langle k_e^{S_n} \right\rangle + \sum_n \left\langle k_e^{A_n} \right\rangle \tag{2.65}$$

where $\left\langle k_e^{S_n} \right\rangle$ and $\left\langle k_e^{A_n} \right\rangle$ are the time-average kinetic energies for the symmetric mode S_n and antisymmetric mode A_n. Upon multiplication and then integration over thickness, kinetic energy can be expressed in closed form as

$$\left\langle k_e^{S_n} \right\rangle = \frac{b}{4}\left[g_n^{S_n} B_n F(\omega) \right]^2 \left(\begin{array}{l} \rho\omega^2 \int_{-d}^{d} \left\{ \xi_{Sn}^2 \cos^2 \alpha_{Sn} y + R_{Sn}^2 \beta_{Sn}^2 \cos^2 \beta_{Sn} y - 2R_{Sn}\beta_{Sn}\xi_{Sn} \cos\alpha_{Sn} y \cos\beta_{Sn} y \right\} dy \\ +\rho\omega^2 \int_{-d}^{d} \left\{ \alpha_{Sn}^2 \sin^2 \alpha_{Sn} y + R_{Sn}^2 \xi_{Sn}^2 \sin^2 \beta_{Sn} y + 2R_{Sn}\xi_{Sn}\alpha_{Sn} \sin\alpha_{Sn} y \sin\beta_{Sn} y \right\} dy \end{array} \right) \tag{2.66}$$

$$\left\langle k_e^{A_n} \right\rangle = \frac{b}{4}\left[g_n^{A_n} A_n F(\omega) \right]^2 \left(\begin{array}{l} \rho\omega^2 \int_{-d}^{d} \left\{ \xi_{An}^2 \sin^2 \alpha_{An} y + R_{An}^2 \beta_{An}^2 \sin^2 \beta_{An} y - 2R_{An}\beta_{An}\xi_{An} \sin\alpha_{An} y \sin\beta_{An} y \right\} dy \\ +\rho\omega^2 \int_{-d}^{d} \left\{ \alpha_{An}^2 \cos^2 \alpha_{An} y + R_{An}^2 \xi_{An}^2 c\cos^2 \beta_{An} y + 2R_{An}\xi_{An}\alpha_{An} \cos\alpha_{An} y \cos\beta_{An} y \right\} dy \end{array} \right) \tag{2.67}$$

Equations (2.66), (2.67) can be further simplified as

$$\left\langle k_e^{S_n} \right\rangle = \frac{b}{4}\left[g_n^{S_n} B_n F(\omega) \right]^2 \rho\omega^2 \int_{-d}^{d} \left[\left(\xi_{Sn} \cos\alpha_{Sn} y - R_{Sn}\beta_{Sn} \cos\beta_{Sn} y \right)^2 + \left(\alpha_{Sn} \sin\alpha_{Sn} y + R_{Sn}\xi_{Sn} \sin\beta_{Sn} y \right)^2 \right] dy \tag{2.68}$$

$$\left\langle k_e^{A_n} \right\rangle = \frac{b}{4}\left[g_n^{A_n} A_n F(\omega) \right]^2 \rho\omega^2 \int_{-d}^{d} \left[\left(\xi_{An} \sin\alpha_{An} y - R_{An}\beta_{An} \sin\beta_{An} y \right)^2 + \left(\alpha_{An} \cos\alpha_{An} y + R_{An}\xi_{An} \cos\beta_{An} y \right)^2 \right] dy \tag{2.69}$$

Potential energy of the wave can be evaluated by the double inner (double dot) product between stress and strain

$$v_e(x,t) = \frac{1}{2}\int_A \mathbf{T} : \mathbf{S}\, dA \tag{2.70}$$

$$v_e(x,t) = \frac{1}{2}\int_A \begin{pmatrix} T_{xx} & T_{xy} & T_{xz} \\ T_{yx} & T_{yy} & T_{yz} \\ T_{zx} & T_{zy} & T_{zz} \end{pmatrix} : \begin{pmatrix} S_{xx} & S_{xy} & S_{xz} \\ S_{yx} & S_{yy} & S_{yz} \\ S_{zx} & S_{zy} & S_{zz} \end{pmatrix} dA \tag{2.71}$$

T_{zz} and S_{zz} are ignored due to the *z-invariant* assumption. Also $T_{yx} = T_{xy}$, $T_{zx} = T_{xz}$, $T_{zy} = T_{yz}$ due to symmetry of both stress and strain tensors; Eq. (2.71) yields

$$v_e(x,t) = \frac{1}{2}\int_A \left(T_{xx}S_{xx} + T_{yy}S_{yy} + 2T_{xy}S_{xy} + 2T_{xz}S_{xz} + 2T_{yz}S_{yz} \right) dA \tag{2.72}$$

The stresses and strains associated with Lamb waves are T_{xx}, T_{xy}, T_{yy} and S_{xx}, S_{xy}, S_{yy}; then Lamb wave potential energy reduces to

$$v_e(x,t) = \frac{1}{2}\int_A \left(T_{xx}S_{xx} + T_{yy}S_{yy} + 2T_{xy}S_{xy} \right) dA \tag{2.73}$$

The time-averaged potential energy is

$$\langle v_e \rangle = \frac{1}{4}\int_A \left\{ (\lambda + 2\mu) S_{xx}\tilde{S}_{xx} + 2\lambda S_{yy}\tilde{S}_{xx} + (\lambda + 2\mu) S_{yy}\tilde{S}_{yy} + 2\left(2\mu S_{xy}\right)\tilde{S}_{xy} \right\} dA \tag{2.74}$$

Similar to the kinetic energy, the time-averaged potential energy is the summation of the potential energy of all modes, i.e.

$$\langle v_e \rangle = \sum_n \langle v_e^{S_n} \rangle + \sum_n \langle v_e^{A_n} \rangle \tag{2.75}$$

where $\langle v_e^{S_n} \rangle$ and $\langle v_e^{A_n} \rangle$ are the time-averaged potential energy for symmetric mode S_n and antisymmetric mode A_n respectively, i.e.,

$$\langle v_e^{S_n} \rangle = \frac{b}{4}\left[g_n^{S_n} B_n F_0(\omega) \right]^2 \begin{pmatrix} (\lambda + 2\mu)\xi_{Sn}^2 \int_{-d}^{d} \left(\xi_{Sn}\cos\alpha_{Sn}y - R_{Sn}\beta_{Sn}\cos\beta_{Sn}y \right)^2 dy + \\ (2\lambda) \int_{-d}^{d} \begin{Bmatrix} \xi_{Sn}^2\alpha_{Sn}^2\cos^2\alpha_{Sn}y - R_{Sn}^2\beta_{Sn}^2\xi_{Sn}^2\cos^2\beta_{Sn}y + \\ R_{Sn}\beta_{Sn}\xi_{Sn}(\xi_{Sn}^2 - \alpha_{Sn}^2)\cos\alpha_{Sn}y\cos\beta_{Sn}y \end{Bmatrix} dy + \\ (\lambda + 2\mu) \int_{-d}^{d} \left(\alpha_{Sn}^2\cos\alpha_{Sn}y + R_{Sn}\beta_{Sn}\xi_{Sn}\cos\beta_{Sn}y \right)^2 dy + \\ \mu \int_{-d}^{d} \left(2\xi_{Sn}\alpha_{Sn}\sin\alpha_{Sn}y + R_{Sn}\left(\xi_{Sn}^2 - \beta_{Sn}^2\right)\sin\beta_{Sn}y \right)^2 dy \end{pmatrix} \tag{2.76}$$

$$\left\langle v_e^{A_n} \right\rangle = \frac{b}{4}\left[g_n^{A_n} A_n F_0(\omega) \right]^2 \left(\begin{array}{l} (\lambda+2\mu)\xi_{An}^2 \int_{-d}^{d} \left(\xi_{An}\sin\alpha_{An}y - R_{An}\beta_{An}\sin\beta_{An}y\right)^2 dy + \\ (2\lambda)\int_{-d}^{d} \left\{ \begin{array}{l} \xi_{An}^2\alpha_{An}^2\sin^2\alpha_{An}y - R_{An}^2\beta_{An}^2\xi_{An}^2\sin^2\beta_{An}y + \\ R_{An}\beta_{An}\xi_{An}(\xi_{An}^2-\alpha_{An}^2)\sin\alpha_{An}y\sin\beta_{An}y \end{array} \right\} dy + \\ (\lambda+2\mu)\int_{-d}^{d} \left(\alpha_{An}^2\sin\alpha_{An}y + R_{An}\beta_{An}\xi_{An}\sin\beta_{An}y\right)^2 dy + \\ \mu\int_{-d}^{d} \left(2\xi_{An}\alpha_{An}\cos\alpha_{An}y + R_{An}\left(\xi_{An}^2-\beta_{An}^2\right)\cos\beta_{An}y\right)^2 dy \end{array} \right) \quad (2.77)$$

The total energy for Lamb waves per unit length is the summation of the kinetic and potential energy. The total time-averaged Lamb wave energy at the plate cross section corresponding to the PWAS end is

$$\left\langle e_e \right\rangle = \left\langle k_e \right\rangle + \left\langle v_e \right\rangle \quad (2.78)$$

2.3. SIMULATION RESULTS

This section gives results of the simulation of power and energy transduction between the PWAS and structure using the exact Lamb waves model. Comparison was performed between the exact Lamb waves model results were presented here, and the simplified axial and flexural waves model results of Lin and Giurgiutiu (2012). This was followed by a parametric study to show how wave power and energy were changed with different PWAS-sizes and excitation frequencies. The last part of this section shows the applicability of our model for the case of multi-modal Lamb waves, which happens either at higher frequency or in thicker structures. We examplify with the simulation of two plates: (a) 1-mm aluminum up to 2000 kHz, and (b) 12.7-mm (½ in) steel up to 500 kHz

frequency. **Figure 2.10**a,b shows dispersion curves for the two plates. **Figure 2.10**a also shows how the simplified axial and flexural waves compare with S0 and A0 Lamb waves at low frequencies.

For the 1-mm aluminum plate, harmonic excitation of 10-volts was applied on a 7- mm PWAS with a frequency sweep from 1-2000 kHz such that only S0 and A0 Lamb waves exist. However, the 12.7-mm steel plate (**Figure 2.10**b) was excited up to 500 kHz, such that three symmetric modes (S0, S1, S2) and three antisymmetric modes (A0, A1, A2) exist. Complete simulation parameters are given in Table 2.1 and Table 2.2.

2.3.1. Thin Plate Structure (One Symmetric and one Antisymmetric mode)

The simulation results for the 1-mm aluminum structure are given in **Figure 2.11**. As expected, the reactive electrical power required for PWAS excitation was orders of magnitude larger than the active electrical power. Hence, the power rating of the PWAS transmitter was dominated by the reactive power, i.e., by the capacitive behavior of the PWAS. We noted that the transmitter reactive power was directly proportional to the transmitter admittance ($Y = i\omega C$), whereas the transmitter active power was the power converted into the ultrasonic acoustic waves generated into the structure from the transmitter. A remarkable variation of active power with frequency is shown in **Figure 2.11**a: we noticed that the active power (i.e., the power converted into the ultrasonic waves) was not monotonic with frequency, but manifested peaks and valleys. As a result, the ratio between the reactive and active powers was not constant, but presented the peaks and valleys. The increase and decrease of active power with frequency corresponds to the PWAS tuning in and out of various ultrasonic waves traveling into the structure.

The maximum active power seemed to be ~ 8 mWatt at 340 kHz. At ~1460 kHz, the PWAS was not transmitting any power; hence no power was delivered into a wave power at this frequency. This is because the rejection of Lamb waves at this particular frequency for both S0 and A0. **Figure 2.6**a,b, show that v_x and v_y vanish for both S1 and A1 at ~ 1460 kHz. Since the electrical active power is equally divided into forward and backward waves, the Lamb wave power plot of **Figure 2.11**c is the half of the electrical active power plot of **Figure 2.11**a. **Figure 2.11**d shows the simulation results for Lamb waves kinetic energies, Eqs. (2.68), (2.69), and potential energies, Eqs. (2.76), (2.77).

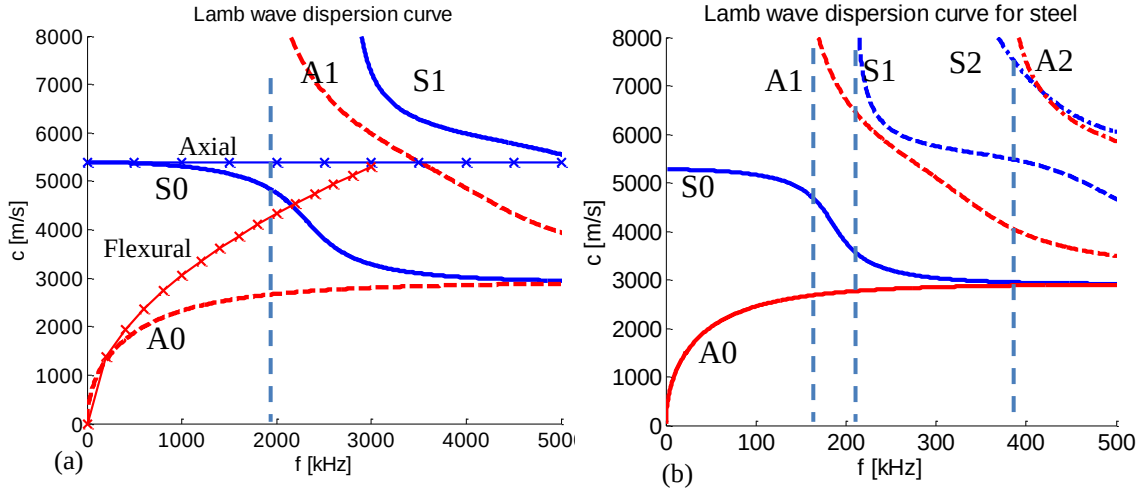

Figure 2.10. Dispersion curves (a) aluminum 1 mm, (b) steel 12.7 mm (1/2 in).

Table 2.1. Structure simulation parameters.

	symbol	2024 AL alloy	steel-AISI-4340
Length	L	∞	∞
thickness	h	1 mm	12.7 mm (½ in)
Width	b	7 mm	7mm
Young's Modulus	E	72.4 GPa	200 GPa
Poisson ratio	ν	0.33	0.29
density	ρ	2780	7850
Harmonic input voltage amplitude	$\hat{V}$	10 V	10 V
Frequency	f	sweep 1-2000 kHz	1-500 kHz

Table 2.2. Transmitter PWAS (PZT850) properties
(as from the company website www.americanpiezo.com).

	symbol	PZT850
Length	l	5-25 mm
thickness	t_a	0.2 mm
Width	b	7 mm
Young's Modulus	E	63 GPa
Elastic compliance	s_{11}^E	15.8e-12 m^2/N
Relative dielectric constant	$\varepsilon_{33}^T / \varepsilon_0$	1750
Coupling coefficient	k_{31}	0.353
Piezoelectric coefficient	d_{31}	-175e-12 m/V

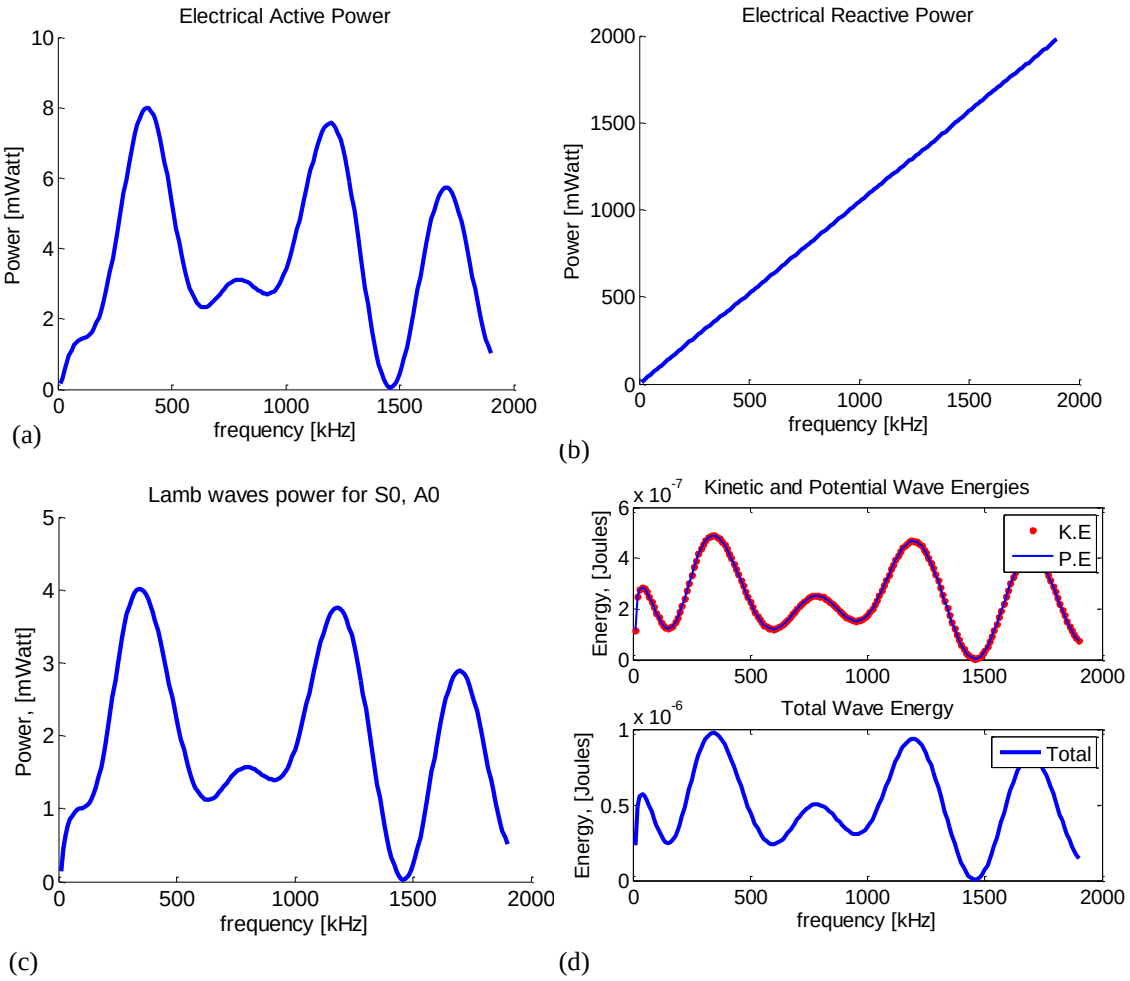

Figure 2.11. Simulation results for 1-mm aluminum plate, (a) electrical active power, (b) reactive power, (c) Lamb wave power, (d) Lamb wave kinetic and potential energy.

2.3.2. Comparison with Low Frequency (Axial and Flexural) Approximation

Figure 2.10a shows that an axial wave can be approximate to S0 mode up to ~ 700 kHz for this particular case of excited 1-mm aluminum plate. A flexural wave can approximate A0 for up to ~100 kHz. The axial and flexural model of Lin and Giurgiutiu (2012) compared with our exact Lamb wave model shows good agreement at relatively low frequencies excitation (**Figure 2.12**). At higher frequencies, i.e., beyond 700 kHz for

S0 and 100 kHz for A0, the differences between exact and approximate models are very significant.

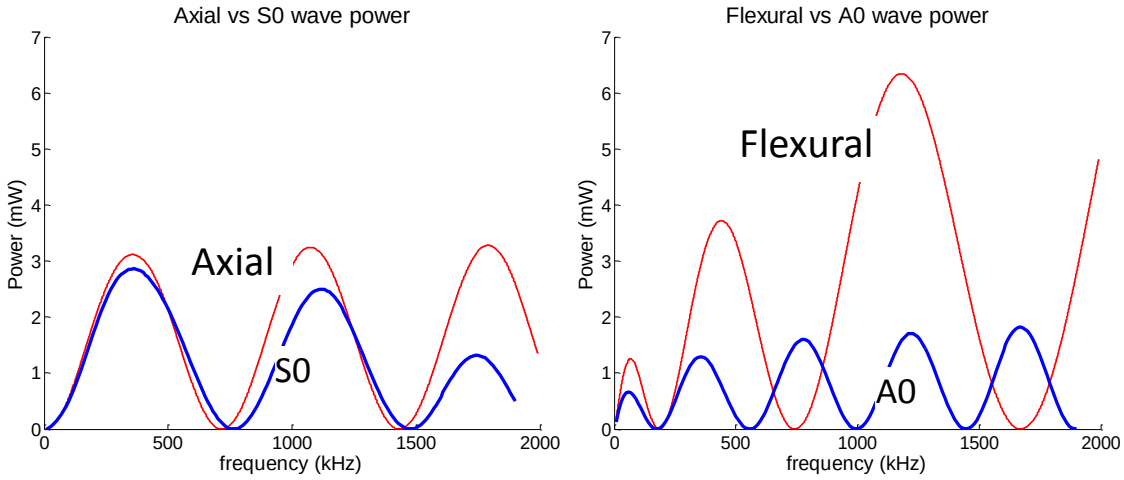

Figure 2.12. Comparison between axial and flexural wave powers and S0/A0 Lamb wave powers.

2.3.3. Parametric Study

Figure 2.13 presents the results of a parametric study for various PWAS sizes (5-25 mm) and frequencies (1-1000 kHz). The resulting parametric plots are presented as 3D mesh plots. It indicates that active power generated from the PWAS to the structure contains the tuning effect of transmitter size and excitation frequency. A larger PWAS does not necessarily produce more wave power at a given frequency. The maximum active power in the simulation is ~ 8.3 mW. This can be achieved by different combinations of PWAS and excitation frequencies, e.g. (5mm PWAS size and 610 kHz, 9-mm PWAS and 890 kHz, 20-mm PWAS and 680 kHz, or 23-mm PWAS and 820 kHz). These combinations provide guidelines for the design of transmitter size and excitation frequency in order to obtain maximum wave power into the SHM structure. Similarly, the

total Lamb wave energy shows the same tuning trend in relation to the PWAS size and excitation frequency as shown in **Figure 2.14**.

2.4. EXPANDING TO MULTIMODE LAMB WAVE

2.4.1. Thick Plate Structure (multi-mode Lamb waves)

A multi-modal Lamb waves simulation was performed on a 12.7-mm thick steel plate for up to 500 kHz excitation frequency and 10V harmonic voltage applied to PWAS. All structural simulation parameters are listed in Table 2.1 and PWAS parameters are listed in Table 2.2.

The objective is to evaluate electrical active power, reactive power and show how the active power part is converted to Lamb wave power in the presence of multi-modal Lamb waves. Dispersion curves plots in **Figure 2.10**b show that the S1 mode starts ~ 215 kHz, S2 starts at ~ 370 kHz, while A1 starts at ~ 170 kHz, and A2 starts at 390 kHz. Due to the sudden appearance of Lamb wave modes at *cut-off frequencies*, the normal mode expansion solution encounters sudden jumps. This is due to the appearance of new components caused by the new modes. For that reason, a smoothing function is applied as described in the next section.

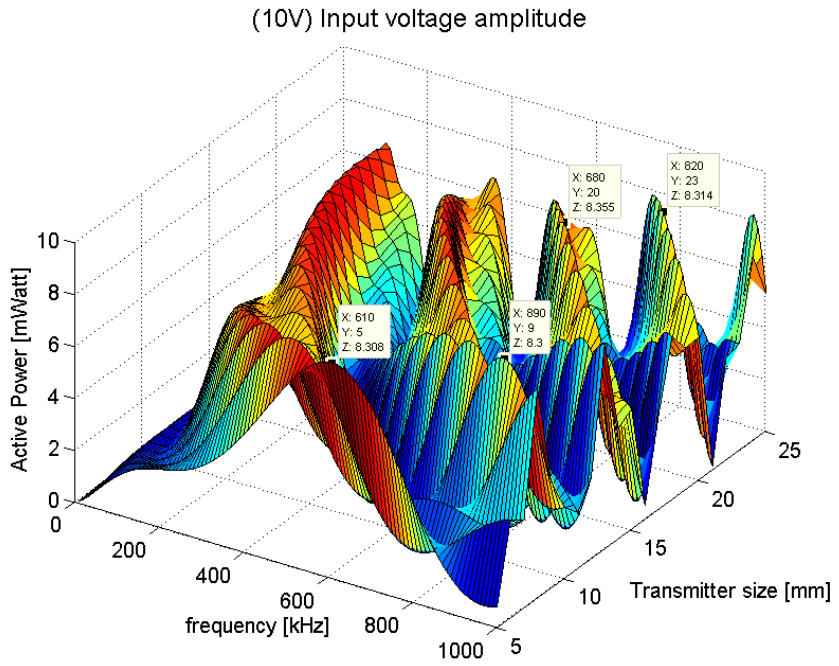

Figure 2.13. Parametric study for Active power for 1-mm aluminum simulation.

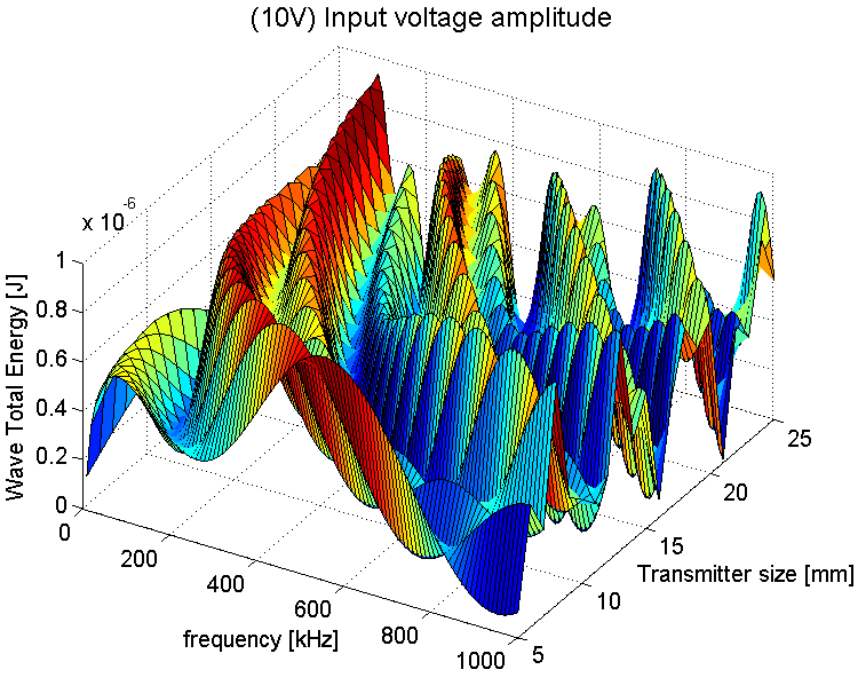

Figure 2.14. Parametric study for total Lamb wave energy for 1-mm aluminum simulation.

Smoothing function

The smoothing function is a smoothed step function, (Sohoni, 1995) as shown in **Figure 2.15**. The mathematical formula is

$$f(x) = \begin{cases} h_1 & x < X_1 \\ f(x, X_1, h_1, X_2, h_2) & X_1 \le x \le X_2 \\ h_2 & x > X_2 \end{cases} \tag{2.79}$$

$$f(x) = h_1 + [\Delta h / \Delta x] * (x - X_1) - [\Delta h / 2\pi] * \sin\{(2\pi / \Delta x) * (x - X_1)\} \tag{2.80}$$

This is implemented in our NME solution by setting X_1 to the cut-off frequency of the selected mode and h_1 to zero; hence the mode is forced to start from zero, and consequently its contribution to the NME summation is smoothed. $\Delta h = 1$; Δx is arbitrary; we selected $\Delta x = 150$ kHz, for symmetric modes, and $\Delta x = 120$ kHz for antisymmetric modes.

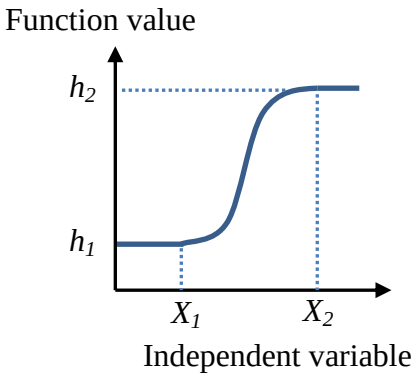

Figure 2.15. ADAMS step function.

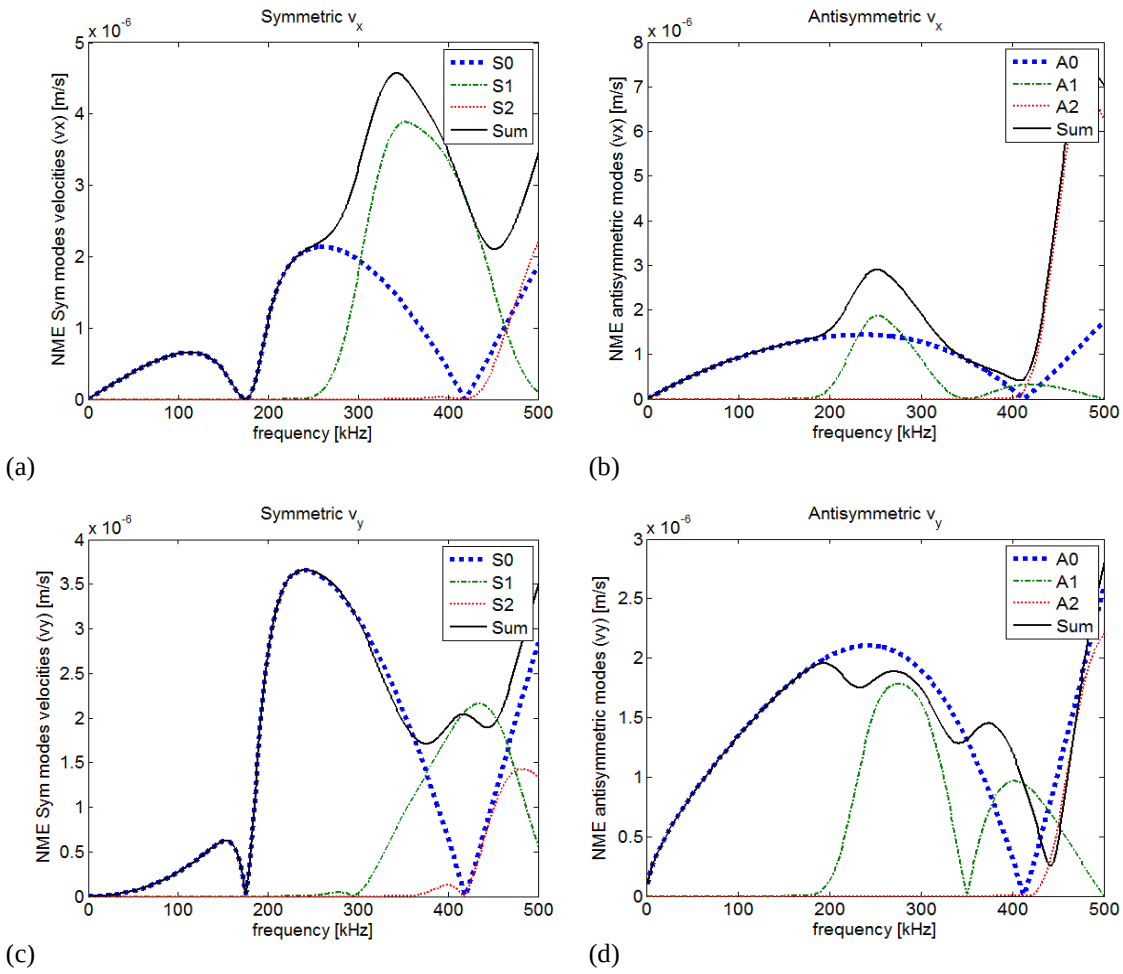

Figure 2.16. Normal mode expansion for particle velocity fields for 12.7 mm steel plate with 3 symmetric modes and 3 antisymmetric modes (smoothed). (Kamal,et al., 2013)

Normal mode expansion for velocity fields after applying smoothing are shown in **Figure 2.16**.

For the sake of clarity, it needs to be mentioned that the plots in **Figure 2.16** are the absolute values of NME velocities after applying normalized amplitudes as well as modal participation factors. Note that the summation value in some areas was less than the individual values because the individual values were plotted as absolute values, whereas the summation was done algebraically, which allows for some cancelations.

Complex values of NME velocities are due to phase differences. **Figure 2.17** shows the summary of the velocity fields; it displays the summation for the three symmetric modes as well as antisymmetric modes.

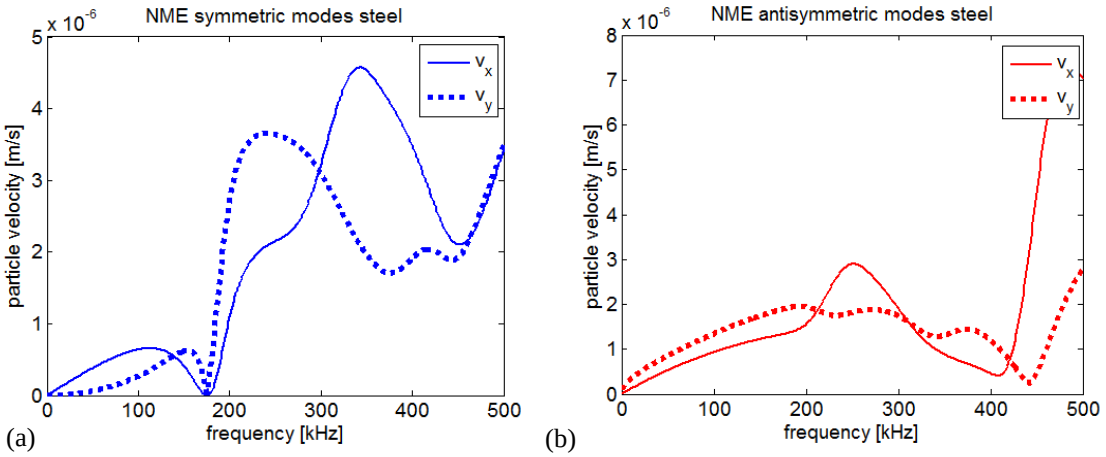

Figure 2.17. Summation of normal mode expanded velocities in x and y directions with applied modal participation factors (a) symmetric, (b) antisymmetric modes.

Figure 2.18 shows the reactive and active electrical power the PWAS utilizes to excite desired Lamb wave modes. It can be seen from **Figure 2.18**, that the reactive power was three orders of magnitude larger than the active power (active power is the power that is further converted to propagating wave power). The maximum active power attained in this simulation was ~0.9 mWatt at 500 kHz. However, if the simulation was evaluated for a larger frequency sweep, active power experiences higher maximum, but careful consideration is needed as the fourth symmetric and antisymmetric modes will come into account.

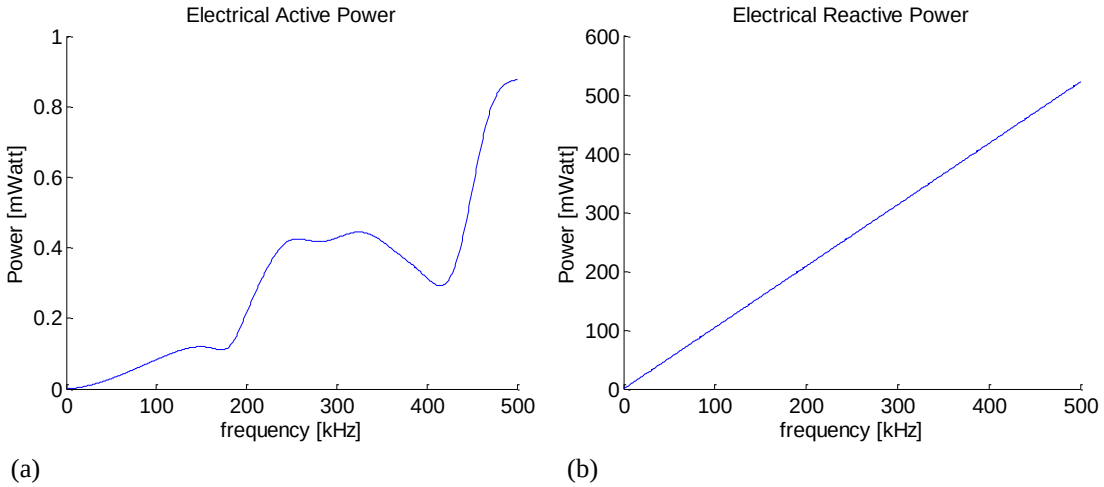

Figure 2.18. Simulation results for 12.7-mm steel plate, (a) electrical active power, (b) reactive power.

Multi-modal Lamb wave simulations for power are shown in **Figure 2.19**. It can be seen that maximum value for Lamb wave power was ~ 0.45 mWatt at 500 kHz and the plot in **Figure 2.19**a is identical to the half of active electrical power of **Figure 2.18**a.

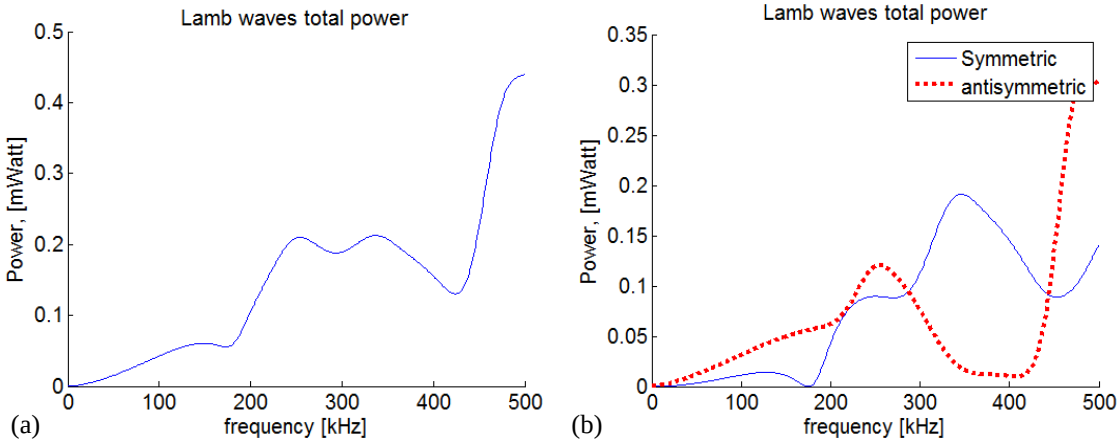

Figure 2.19. (a) Lamb wave power, (b) Lamb wave power separated as symmetric modes and antisymmetric modes.

2.4.2. Power Partitioning

The case of the ½"- thick steel beam was used to show how mode contribution factors distribute the power consumed by every mode. For this thick steel structure, with a 7-mm square PWAS attached, Lamb waves tuning were shown in **Figure 2.16**. The fundamental symmetric mode S0 mode had its rejection points ≈ 175 and 400 kHz, A0 mode had a rejection point ≈ 400 kHz. The simulated frequency range was up to 500 kHz, where there are three symmetric and three antisymmetric modes.

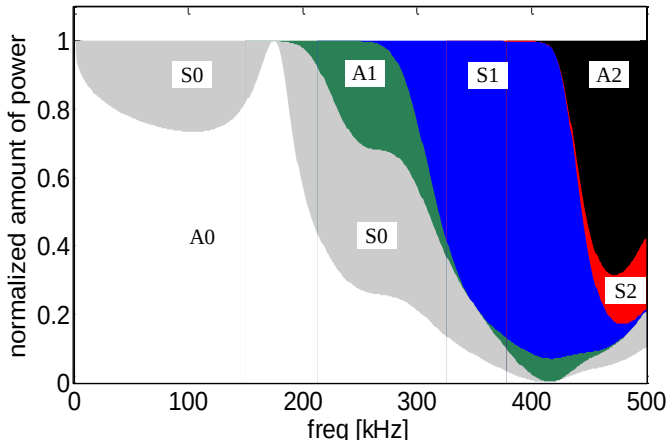

Figure 2.20. Power partitioning between modes of Lamb wave propagation in ½"-thick steel beam.

The results for power partitioning (under 10V input voltage amplitude) are shown in **Figure 2.20**, and they are representing the ratios of power between modes. At 175 kHz, S0 was rejected and A0 consumed all the power. However, at 200 kHz, A0 actually consumed more power (than at 175 kHz), but the shown amount is the ratio with S0 mode.

2.5. EXPERIMENTAL AND FEM STUDY

This section includes: (1) comparing Lamb waves tuning predicted analytically with experimental measurements using Polytec Scanning Laser Doppler Vibrometer (SLDV) system, and (2) comparing the electromechanical impedance of the bonded PWAS predicted analytically with Multiphysics FEM results as well as experimental measurements with the impedance analyzer. We started by a brief introduction of the measuring equipment, following with results and ending with concluding remarks.

The SLDV provides non-contact measurements of particle vibration on the structure surface. The laser vibrometry method is based on the Doppler effect, which is able to sense the frequency shift of back-scattered laser light from a moving surface. The main advantage of a laser vibrometer compared to other alternative methods is the fact that this technology allows the accurate measurement of vibrations without contact at frequencies up to 1.2 GHz. Scanning laser vibrometers have been used extensively in the last years for characterizing small and large amplitude ultrasonic vibrations in solid surfaces. In this study, we used the laser vibrometer system PSV-400-M2 from Polytec as shown in **Figure 2.21**.

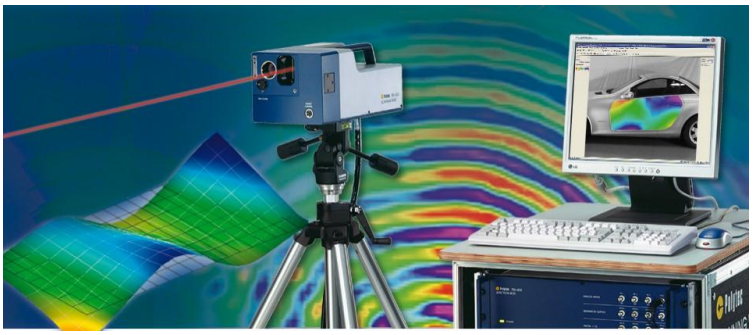

Figure 2.21. Scanning laser vibrometer PSV-400-M2, source: Polytec.com

The experimental setup included: (1) receiving A0 and S0 signals by a receiver PWAS, which is located at 160 mm from the transmitter PWAS, and capturing the received signals voltage by the oscilloscope, and (2) non-contact measurements of out-of-plane oscillation along an array of points using a laser vibrometer. A three-count tone burst voltage was used to excite the transmitter PWAS with 20V peak-to-peak and center frequency varying up to 600 kHz. The complete setup is shown in **Figure 2.22**.

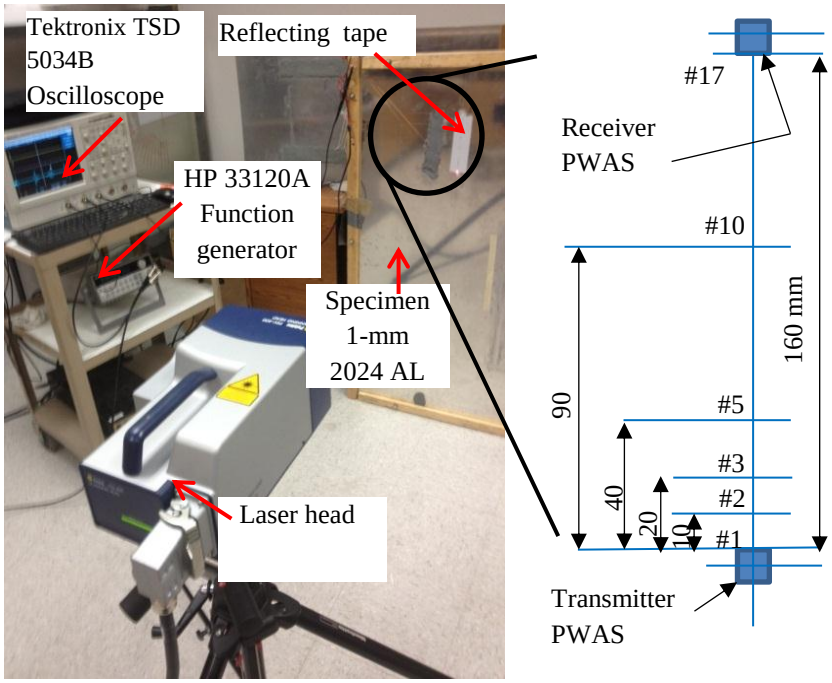

Figure 2.22. Experimental setup of function generator, laser vibrometer, and oscilloscope for measuring Lamb wave tuning.

Figure 2.23 shows a sample of received signals by receiver PWAS as well as laser measurements. As we can see, the A0 mode is dominant in laser measurements. The symmetric mode S0 could not be detected easily with a laser vibrometer, because the PSV-400-M2 laser system is a 1-D measuring system, i.e. it is capable of detecting the

out-of-plane vibration. Hence, we used it to validate the tuning of the antisymmetric A0 mode. The analytical predictions of our model were compared with received voltage by the receiver PWAS for both A0 and S0 modes. The comparison is shown by **Figure 2.24**, **Figure 2.25** and **Figure 2.25**, **Figure 2.26**.

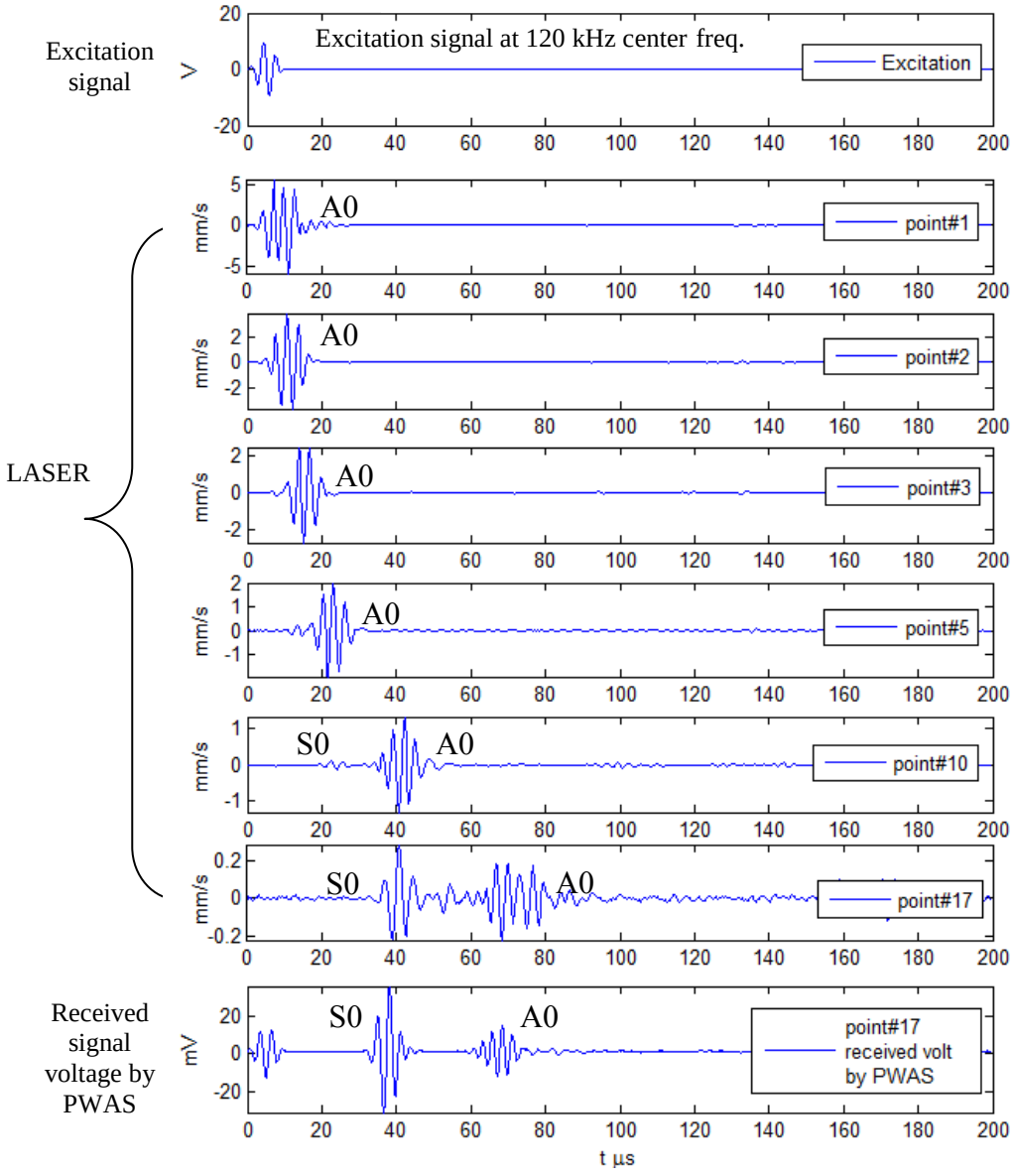

Figure 2.23. Sample of received signals by PWAS and laser measurements at 120 kHz

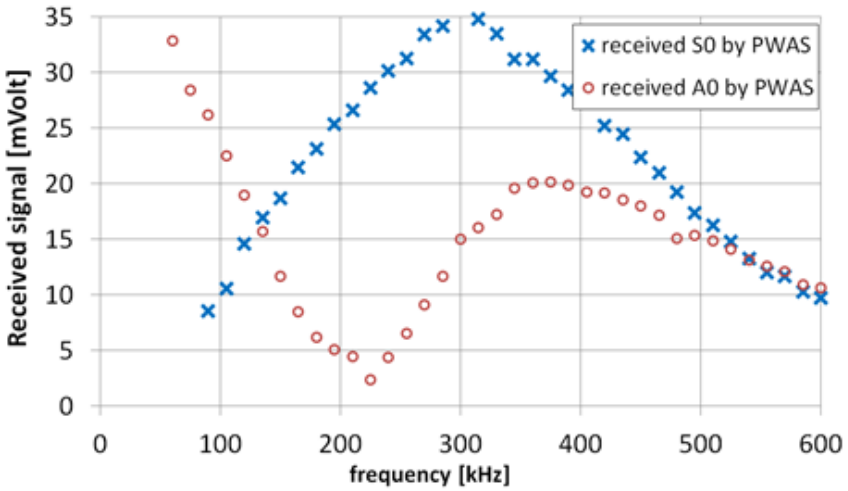

Figure 2.24. Experimental received signals by the receiver PWAS at 160 mm distance

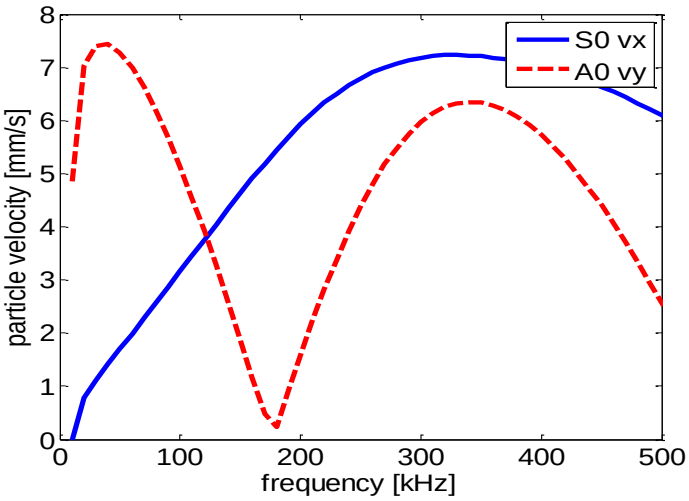

Figure 2.25. Analytical tuning curves, vx is the inplane particle velocity, vy: the out of plane.

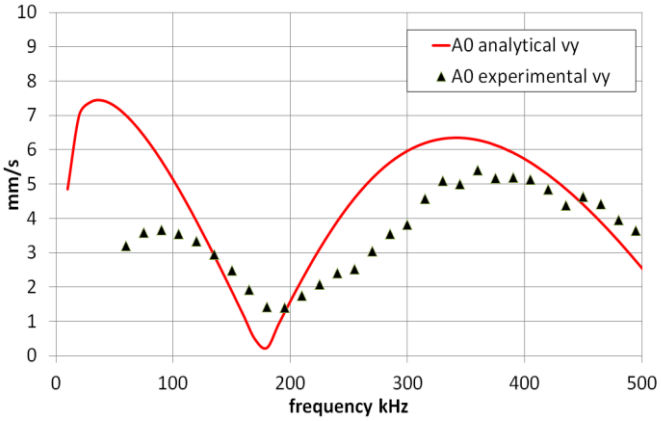

Figure 2.26. Comparison between analytical prediction and laser measurements of vy of A0

By comparing the received electric signals by receiver PWAS (**Figure 2.24**) with analytical prediction of particle motion (**Figure 2.25**), it is concluded that there was a correlation between (a) the out-of-plane structural oscillation at the receiving PWAS, and (b) the in-plane strain captured by the receiver PWAS which is associated with the received voltage through the piezoelectric effects. The comparison between the analytical prediction of out-of-plane particle velocity of A0 mode from **Figure 2.25** with the laser measurements at point #2 (**Figure 2.26**) have shown good agreement. It is important to mention that the analytical model does not account for the attenuation or damping; this implies that the results of **Figure 2.25** are the same at different points between the transmitter and the receiver.

In order to compare energy and power quantities, we needed first to compare our analytical predictions of bonded PWAS E/M impedance with experimental and finite element model results. "Impedance spectroscopy" is commonly called for the E/M impedance or the admittance of the transducer. To calculate the transmitter PWAS electrical power, we needed to calculate the PWAS admittance when attached to the structure. An HP 4194 A impedance analyzer was used for measuring the transducer E/M impedance in complex form; then the admittance was calculated. The experiments were performed on multiple beams and plates to show the constrained PWAS resonances. **Figure 2.27** shows the experimental setup for 8-mm width and 1-mm thick aluminum beam. Also, the test was performed for constrained PWAS on the square aluminum plate that was used in the laser vibrometer test (**Figure 2.22**). The frequency sweep was up to 2000 kHz.

The finite element mesh along with displacement mode shapes at resonance frequencies are shown in **Figure 2.28**. The FEM was performed using coupled field physics, where the PWAS is excited by voltage and the piezoelectric coupling introduces induced strains. Damping was defined using complex compliance and complex electric permittivity with imaginary coefficients of 0.04. Results of analytical prediction, FEM prediction, and experimental measurements are shown in **Figure 2.29**.

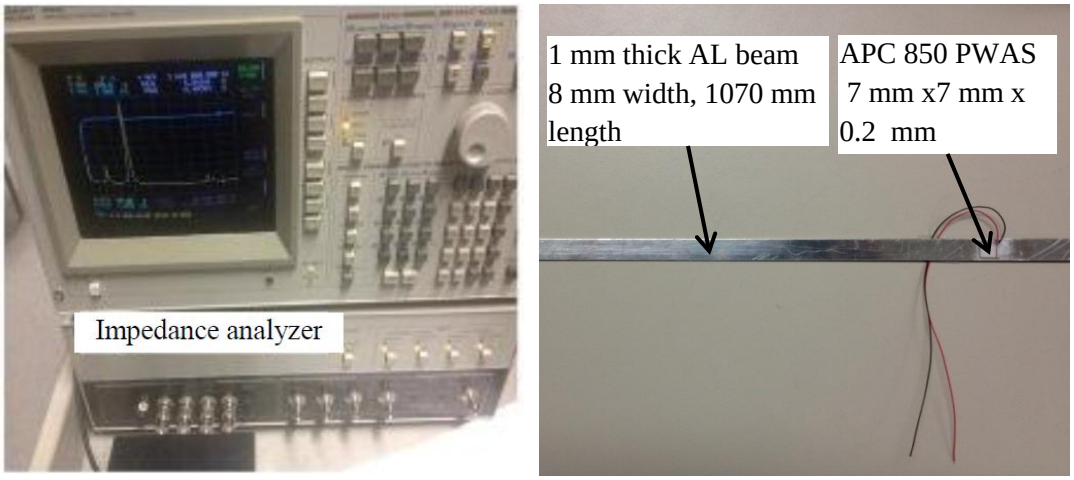

(a) (b)

Figure 2.27. Experimental setup for E/M impedance test, (a) HP4194A impedance analyzer, (b) test specimen with bonded PWAS.

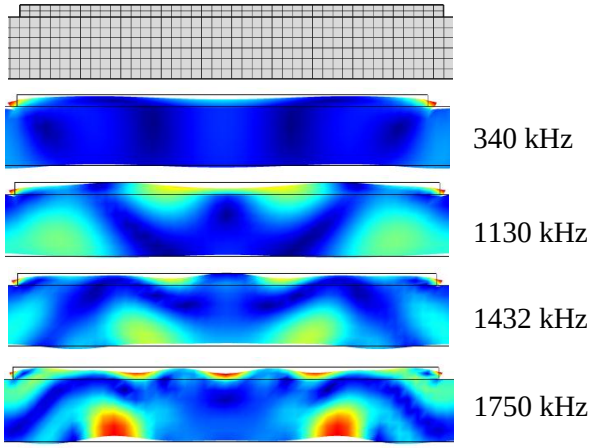

Figure 2.28. FEM mesh and mode shapes at resonances of bonded PWAS

The predicted first resonance was 340 kHz by the analytical model and FEM; which both do not account for the width dimension. The experimental result for the first resonance of the beam case was 250 kHz, while it was 400 kHz for the plate. The analytical model overestimated the admittance amplitude of the first resonance with respect to other resonances. The second resonance observed by FEM was 1130 kHz, (1200 kHz analytically and it was ≈1000-1100 kHz experimentally). The third resonance was 1432 kHz by FEM predictions and it was missed by the analytical model; experimental results were ≈ 1330-1370 kHz. The antiresonance ≈ 1500 kHz can be explained by the rejection of both S0 and A0 in tuning curves. The fourth and the last documented resonance was 1750 kHz by FEM, 1700 analytically, and ≈1625-1650 kHz experimentally (**Figure 2.29**b).

The imaginary component of the admittance is used to determine the reactive electrical power; that is the part of electrical power which is not converted to mechanical wave propagation. This study mainly focused on the real part (or the active power) that is transferable to mechanical wave power.

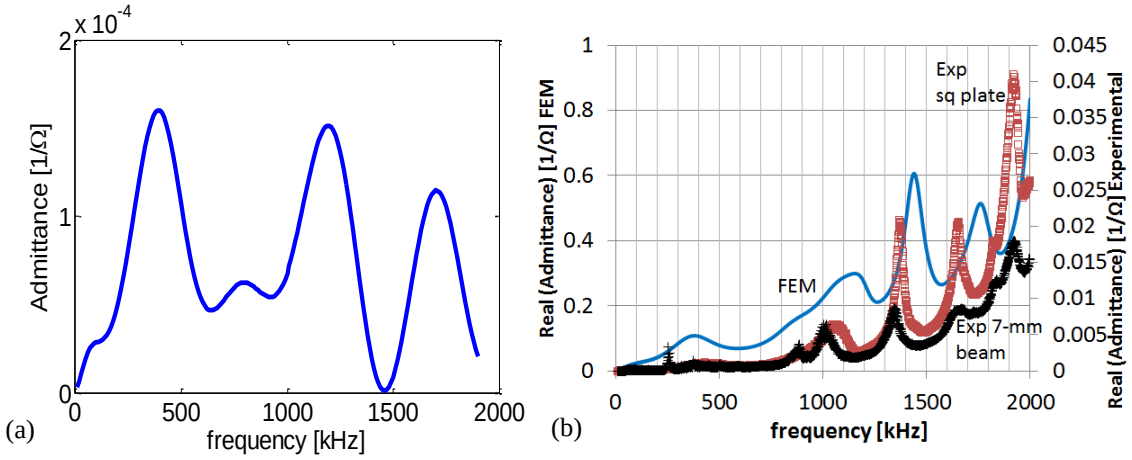

Figure 2.29. E/M admittance of a bonded PWAS on 1-mm aluminum structure: (a) analytical prediction, (b) experimental and FEM results

After determining the tuning of Lamb wave modes and the E/M admittance of the bonded PWAS, we could calculate power and energy quantities. However, due to the dispersion of wave packets (**Figure 2.30**). It was necessarily to perform the analysis in terms of wave packet total energy instead of maximum amplitude. To determine the wave packet energy, the time integral was performed for the squared signal value

$$E \propto \int_{t_0}^{t_1} |s(t)|^2 \, dt$$

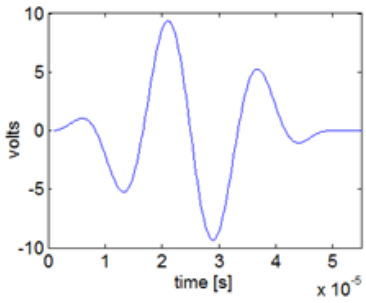

Figure 2.30. Dispersion of received wave packets

Electromechanical admittance components at every frequency were multiplied by the corresponding energy content of the received signals to get electrical power (**Figure 2.31**b). Similar analysis was done for the kinetic energy of particle velocity measured by the laser vibrometer (**Figure 2.32**b).

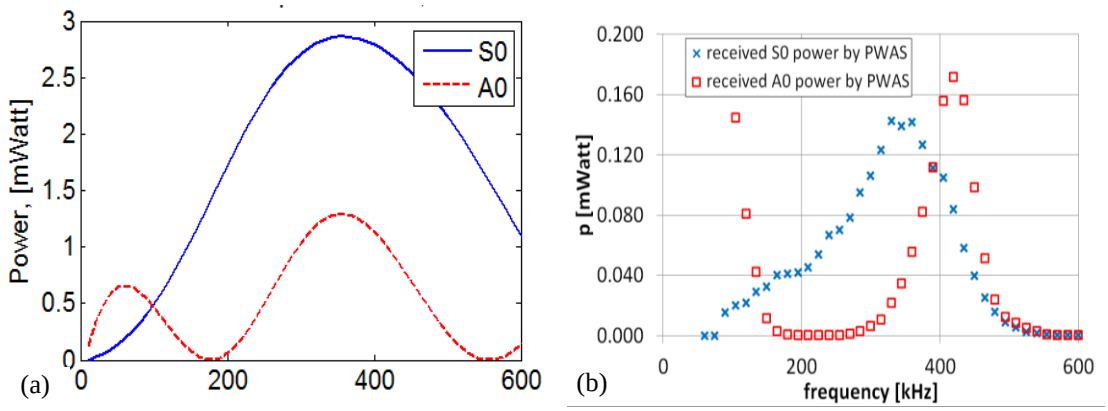

Figure 2.31. (a) Wave power predicted analytically, (b) received signals power experimentally

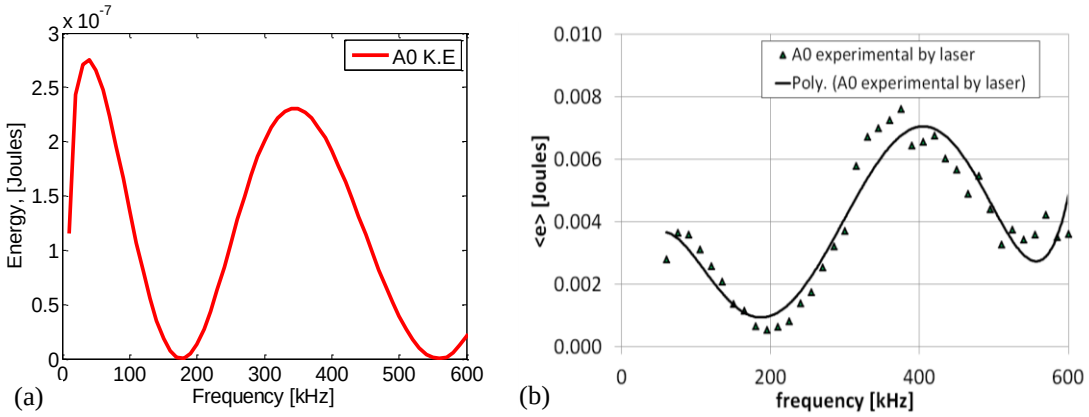

Figure 2.32. (a) A0 wave K.E predicted analytically. (b) A0 wave K.E. of point #2 on structure surface based on the laser vibrometer measurements.

It is clear from the comparison between analytical predictions and experimental measurements of power that the A0 mode had a rejection point at ≈200 kHz. S0 wave power predicted analytically had a good agreement with the received signal of the S0 mode by the oscilloscope. The difference in amplitudes may be attributed to the difference between analytically predicted and experimentally measured admittances. Besides, our analytical model is based on the harmonic wave assumption, whereas the experimental signals are based on 3-count tone burst signals. A similar conclusion is drawn for A0 kinetic energy (K.E), which is shown in **Figure 2.32**.

2.6. SUMMARY AND CONCLUSIONS

The ability to excite certain Lamb wave modes is important in structural health monitoring (SHM) because the different defects respond differently to various Lamb wave modes. Detection of through thickness cracks with the pulse-echo method is much better with the S0 mode, whereas antisymmetric modes are better for the detection of delaminations and disbonds with pitch-catch techniques. Different researchers studied the scattering of wave energy at defects e.g. cracks; hence, it became important to develop an

analytical model for the multimodal Lamb wave power and wave energy. This chapter has analyzed the power and energy transformation from electrical to mechanical by piezoelectric wafer active sensors (PWAS) bonded to host structures. The analysis was started by a literature review to show the motivation of modeling power and energy for Lamb waves for SHM applications. This was followed by a short discussions on the basics of Rayleigh-Lamb equation and the solution of the symmetric and antisymmetric Lamb wave fields, i.e. displacements, strains and velocities. The power flow analysis is based on complex reciprocity and orthogonality of Lamb waves modes; and through normalization of power flow, Lamb waves displacement amplitudes were determined. The analysis for multimodal waves was based on the Normal Modal Expansion (NME) technique; which was used to determine modal participation factors, i.e. how much each mode contributes to the final power. In order to calculate the transmitter electrical power and energy, we have calculated the input electrical power by using the input admittance of the PWAS when attached to the structure. Because of the electromechanical coupling, the impedance is strongly influenced by the dynamic behavior of the substructure and is substantially different from the free-PWAS impedance. A remarkable variation of active power with frequency was noticed. The active power (i.e., the power converted into the ultrasonic waves) is not monotonic with frequency, but manifests in peaks and valleys. As a result, the increase and decrease of active power with frequency corresponds to the PWAS tuning in and out of various ultrasonic waves traveling into the structure. For instance, for single symmetric and single antisymmetric excitation simulation example, there were certain frequencies at which there was almost no energy transfer for waves to propagate. Electrical active power was further divided and converted to forward

propagating wave power and backward wave propagating power; our simulations were performed for only the forward wave and showed that the wave power was half of electrical active power.

The developed model for Lamb waves case was compared with the axial and flexural waves, that approximate Lamb waves at relatively low frequencies and the two simulations showed good agreement. This was followed by a parametric study to optimize the transducer size with excitation frequency to guarantee maximum energy transfer between the source and the examined structure. In this study, it was shown that the maximum wave power can be achieved with different combinations of PWAS-size and excitation frequencies. Multi-modal waves simulations were presented, multi-modal waves typically exist in practical applications for most on-site thick structures at which not only S0 and A0 modes exist when excited by the PWAS. An experimental study was performed using the scanning laser vibrometer to compare the out-of-plane structural oscillation at the receiver PWAS with analytical predictions, as well as the received voltage through the piezoelectric effects. The results have shown good agreement. Afterwards, admittance of bonded PWAS was evaluated experimentally and was compared with FEM and analytical predictions. Finally, the received signals by the oscilloscope and the laser-detected out-of-plane particle velocities were used to determine the wave electric power and kinetic energy respectively.

CHAPTER 3: SHEAR HORIZONTAL COUPLED PWAS

This chapter discusses a shear horizontal coupled piezoelectric wafer active sensor (SH-PWAS). The chapter starts with a review of the state-of-the-art for the applications of SH transducers and their importance in non-destructive evaluation (NDE) and structural health monitoring (SHM). This is followed by the basic piezoelectric sensing and actuation equations with the electro- mechanical coupling coefficient d_{35}. The electro-mechanical (E/M) impedance of the SH-PWAS was studied analytically under a constant electric field assumption as well as under a constant electric displacement assumption. We also extended the analytical development to constrained SH-PWAS bonded to structures in the form of beams. The model is based on the normal mode expansion (NME) technique. The interaction between the SH-PWAS and the structure was studied. The structure frequency response functions were presented. We developed a closed-form equation of structure dynamic stiffness by coupling the mechanical response solution of the SH-PWAS to the structure elasticity solution. The analytical model was compared with experimental results and finite element analysis.

The chapter is later devoted to the discussion of shear horizontal (SH) guided-waves that can be excited with the SH-PWAS. Analytical prediction of SH wave speeds was performed. A wave propagation experimental study was conducted between different combinations of SH-PWAS and regular inplane PWAS transducers.

.

Experimental results were compared with analytical predictions for aluminum plates, and showed good agreement. 2-D wave propagation effects were studied by Multiphysics FEM. In part II of the dissertation: Applications, we apply the study on GFRP and CFRP composite structures.

The amplitudes of shear horizontal wave modes were normalized with respect to the wave power; the normal mode expansion (NME) method was used to account for superposition of multimodal SH waves. Modal participation factors were presented to show the contribution of every mode. Model assumptions included: (a) straight crested guided wave propagation; (b) ignoring evanescent waves; and (c) ideal bonding between the PWAS and structure with shear load transfer concentrated at PWAS tips. The power and energy transfer between the PWAS and structure were analyzed in order to optimize the sensor size and excitation frequency; for maximum wave energy production for a given source.

Finally, we presented simulations of our developed wave power and energy analytical models along with a MATLAB graphical user interface (GUI) for the analysis of SH-waves including dispersion phase and group velocities, mode shapes, and wave energy.

NOMENCLATURE

D_k	=	electric displacement vector [C/m^2]
d_{kj}	=	piezoelectric strain constants [m/V] or [C/N]
d_{35}	=	piezoelectric strain constant for shear mode [m/V] or [C/N]
E_i or E_k	=	electric field [V/m]

e_{35}	=	piezoelectric stress constant for shear mode [N/Vm]
g_{ij}	=	piezoelectric voltage constants [m^2/C] or [Vm/N] or [(V/m)/Pa]
g_{35}	=	piezoelectric voltage constant for shear mode [m^2/C] or [Vm/N] or [(V/m)/Pa]
S_j	=	strain tensor
s_{ij}^D	=	mechanical compliance tensor at zero electric displacement, D=0 [m^2/N]
s_{55}^D	=	mechanical shear compliance at zero electric displacement, D=0 [m^2/N]
T_i or T_j	=	stress tensor [N/m^2]
γ	=	wave number [1/m]
ε_{ik}^T	=	dielectric permittivity matrix at zero mechanical stress, T=0 [F/m]
ε_{33}^S	=	dielectric permittivity in 33 direction measured at zero mechanical strain, S=0
ε_{33}^T	=	dielectric permittivity in 33 direction measured at zero mechanical stress, T=0
K	=	electromechanical coupling factor
μ	=	shear modulus [Pa]
ω	=	angular frequency [rad/s]

Introducing some relations

$$g_{35} = \frac{d_{35}}{\varepsilon_{33}^{T}} \qquad \frac{1}{\varepsilon_{33}^{T}} = \frac{1}{\varepsilon_{33}^{S}} - \frac{g_{35}^{2}}{s_{55}^{D}} \qquad e_{35} = \frac{d_{35}}{s_{55}^{E}} \qquad \varepsilon_{33}^{T} = \varepsilon_{33}^{S} + d_{35}e_{35}$$

$$\frac{\varepsilon^{S}}{\varepsilon^{T}} = \frac{s^{D}}{s^{E}} = 1 - K^{2} \qquad \frac{e_{35}}{\varepsilon_{33}^{S}} = \frac{g_{35}}{s_{55}^{D}} \qquad K^{2} = \frac{d_{35}^{2}}{s_{55}^{E}\varepsilon_{33}^{T}} = \frac{e_{35}^{2}s_{55}^{D}}{\varepsilon_{33}^{S}}$$

3.1. LITERATURE REVIEW

A Conventional piezoelectric wafer active sensor (PWAS) is a thin rectangular or circular wafer that is poled in the thickness direction with electrodes on the top and bottom surfaces; those types of PWAS are either used in the inplane or thickness mode. In the inplane mode, applying an electric field in the thickness direction E_3 causes the transducer's lateral dimensions to increase or decrease, a longitudinal strain will occur $\varepsilon_1 = d_{13}E_3$, where d_{13} is the piezoelectric coupling coefficient measured in [m/V]. Thickness mode is a mode that occurs simultaneously with extension mode, but dominates at higher frequencies in MHz, in which strain in the thickness direction will occur $\varepsilon_3 = d_{33}E_3$, where d_{33} is the piezoelectric coupling coefficient in thickness direction. A different mode of oscillation can be achieved when the applied electric field is applied perpendicular to the poling direction; and it is referred to as shear mode. (**Figure 3.1**). The common piezoelectric coupling coefficient known for this mode is defined as d_{15} , however, this coupling coefficient is only when the electric current is applied in E_1 direction and the poling is across thickness direction. The shear coupled PWAS presented in this study is associated with the d_{35} coupling coefficient in which electric current is applied across thickness (i.e. in x_3 direction) and the poling is in x_1

direction; a few studies considered this d_{35}-mode, such as: Zhou et al. (2013); Kamal et al. (2013); Baillargeon (2003).

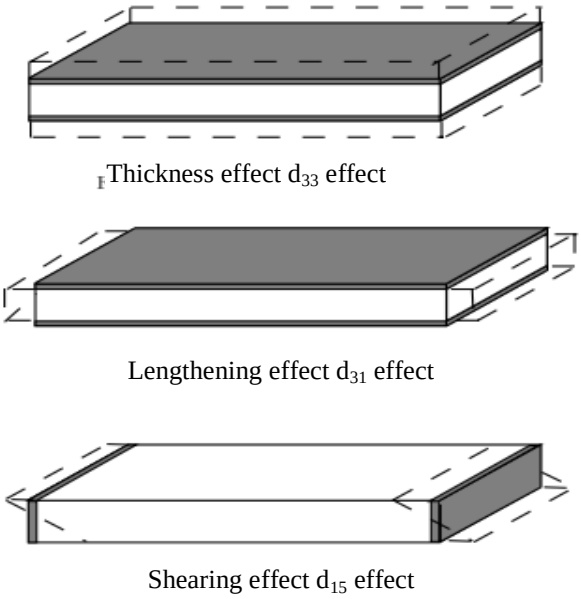

Figure 3.1. Different modes of piezoelectric actuation (Heeg, 1993)

For most piezoelectric materials, the coupling coefficients associated with shear mode have the largest value of all coefficients (Glazounov and Zhang, 1998; APC International Ltd; Ferroperm Piezoceramics). The higher values of shear coupling coefficients make SH-PWAS superior in actuation and sensing (Baillargeon, 2003). SH waves are also preferable because first symmetric mode is non-dispersive, i.e. wave speed is constant at different frequencies. On the other hand, one of the important disadvantages of SH-PWAS is that thicker transducers are needed to sustain and generate the shear actuation. Also due to the high density of piezoceramic materials (≈ 7600 kg/m^3 for APC850 piezoceramic Navy II type), using of shear mode piezoelectric elements increases the mass of the system considerably.

Shear mode piezoelectric transducers were used as an actuator element in a cantilever beam setup (Sun and Zhang, 1995). The stresses distribution across thickness and length under mechanical and electrical loading were investigated. A similar study on using shear-type piezoelectric as a shear bender was studied by Benjeddou et al. (1997).

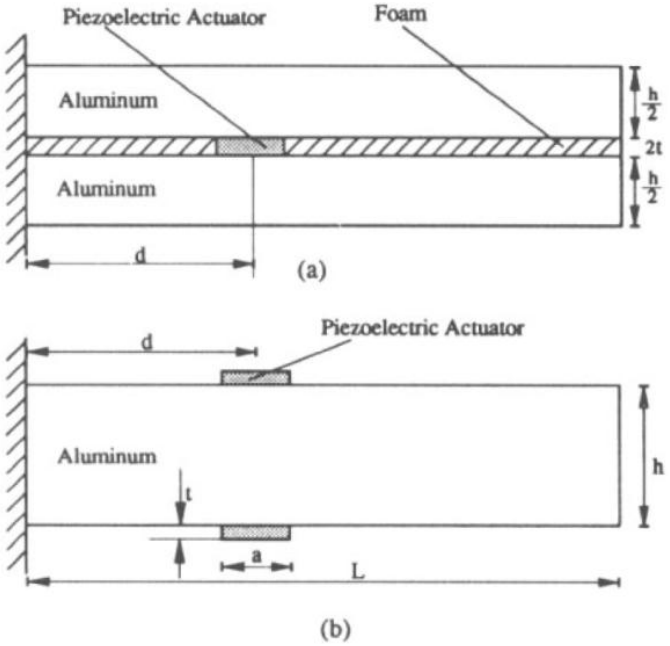

Figure 3.2. (a) Adaptive sandwich beam and (b) surface mounted actuation beam (Sun and Zhang, 1995)

A Piezoelectric device was also used for designing torsional actuators generating angular displacement (Glazounov and Zhang, 1998), as shown in **Figure 3.3**a, where the torsional element consists of different segments, the neighboring ones being of opposite poling.

The application of a torsional actuator was applied on a later study by Centolanza et al. (2002), to control rotor blade trailing edge flaps (**Figure 3.3**b).

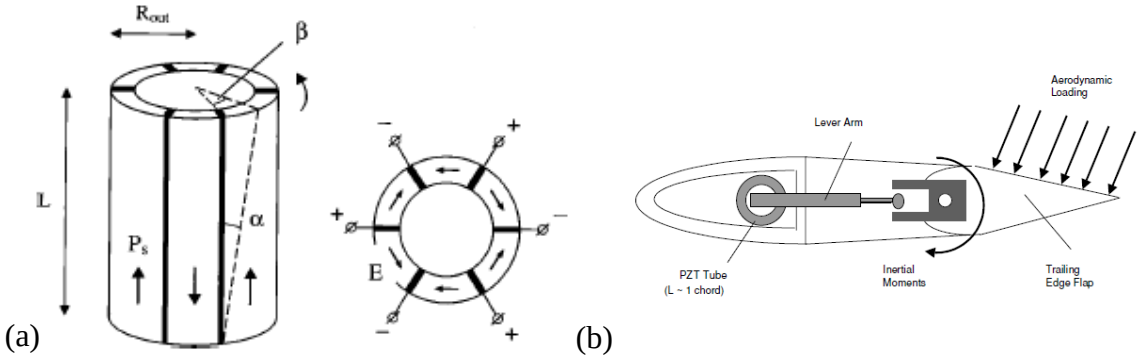

Figure 3.3. (a) Proposed torsional actuator by Glazounov and Zhang (1998), (b) proposed actuator-flap system (Centolanza et al., 2002)

For SHM and NDE applications, shear horizontal (SH) ultrasonic waves showed high potential for quantitatively detecting defects in structures (Fortunko et al., 1982; Rose et al., 2000; Su et al., 2007). Su (2007) showed that SH wave mode conversion occurred at the damage from fundamental incident S0, and it was shown that SH0 can be used to quantitatively identify delamination in composite beams. However, the type of the PZT that detected the induced SH0 waves was not provided. The experimental setup is shown in **Figure 3.4**.

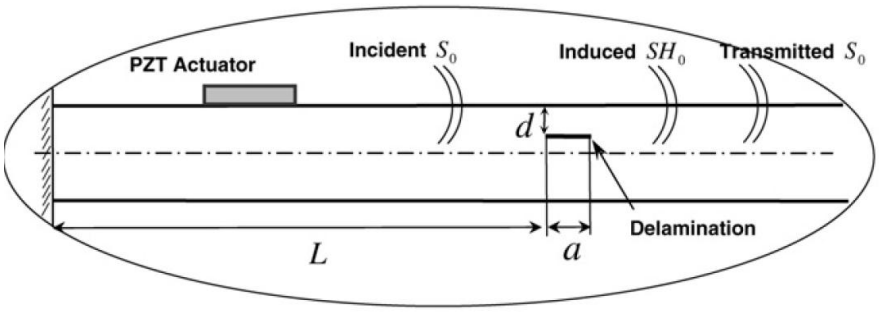

Figure 3.4. PZT actuator model for generation of Lamb mode S0 (Su et al., 2007)

In another application, SH polarized ultrasonic waves were used for evaluating the quality of bonding between the transducer and the structure (Le Crom and Castaings, 2010). SH waves are also associated with AT-cut quartz resonators. AT-cut quartz

resonators were studied, and SH modes were obtained using anisotropic elasticity equations (Zhu et al., 2013). Thickness shear vibrations of quartz crystal plates were studied using Mindlin plate equations in Du et al. (2013). Shear horizontal ultrasonic waves are usually associated also with electromagnetic acoustic transducers or EMAT (**Figure 3.5**). Lee et al. (2009) used SH waves to detect weld defects. SH waves have shown superiority over conventional shear vertical (SV) and longitudinal waves (Gao et al., 2010). Gao et al. (2010) suggested that the piezoelectric based transducers generating SH show better acoustic generation than EMAT. Also, one point to consider is that EMAT needs conductive structures, while PWAS can be used for conductive metallic structures and non-conductive composites (e.g. glass fiber reinforced polymers). SH-PWAS transducers are much more cost efficient, but in terms of effectiveness, EMAT always showed reliability for detecting damages. Recently, magnetostrictive MsS®, which was developed by Southwest Research institute (http://www.swri.org) also showed reliability in damage detection.

Recently, a study by Zhou et al. (2013) has been performed on generation, sensing and damage detection in metallic plates using a shear (d_{36} - mode) Lead Magnesium Niobium Titanate piezoelectric wafer. It was shown that SH0 waves are capable of detecting the damage along their propagation paths.

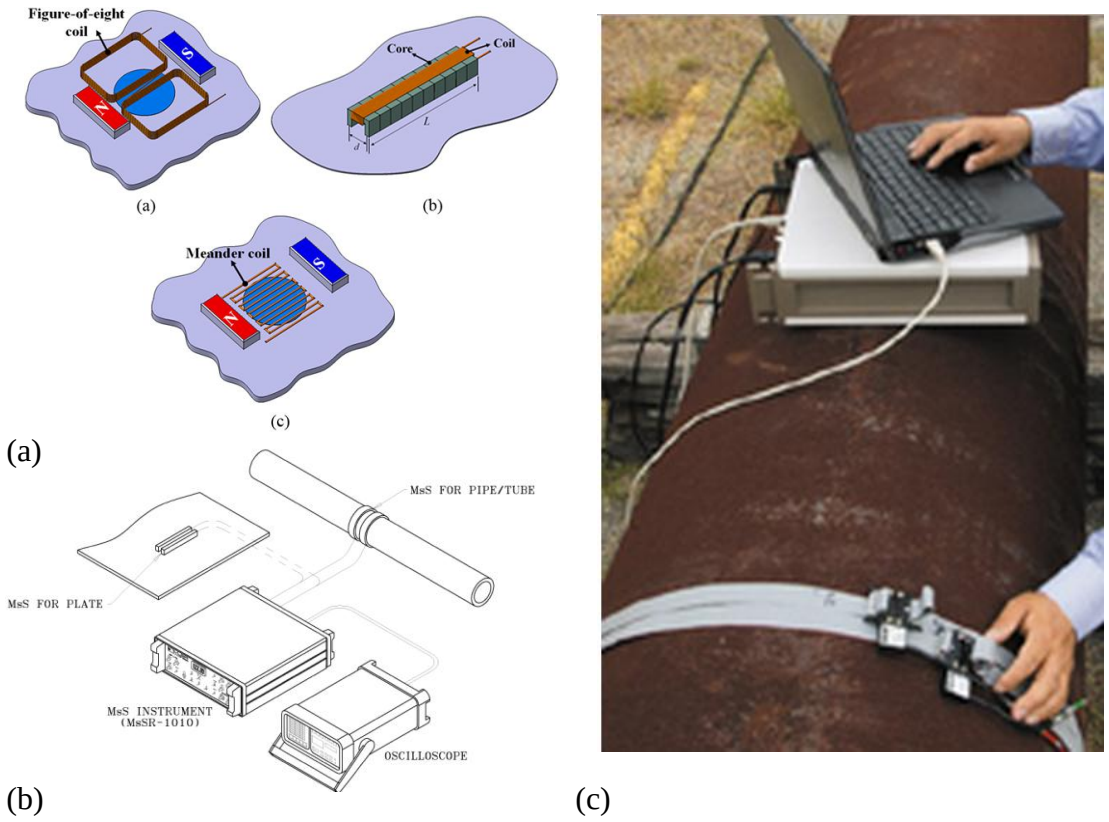

Figure 3.5. (a) Various magnetostrictive transducers used to generate SH waves (Lee et al., 2009),(b) MsS magnetostrictive sensor system, (c) MsS for pipe inspection (www.swri.org)

Nevertheless, fiber optics were also used for detecting SH waves. Li et al. (2009) used fiber optic sensors for detection of SH0 wave type generated from mode conversion from excited Lamb waves, and this was used for detecting delamination in CFRP composites.

This study focuses on piezoelectric wafer-type shear transducer, we call it SH-PWAS. The study is structured into three main parts. In the first part, an analytical model for SH-PWAS electrical admittance was developed and compared with FEM and experimental results. Analytical, FEM and experiments for the bonded SH-PWAS were covered next. The second part presents an experimental study for different possible pitch

catch configurations between SH-PWAS and regular inplane ones. Moreover, wave speeds were compared with analytical values. Finally, the power and energy of SH waves were analytically developed.

3.2. THEORETICAL MODELS OF SH-PWAS IMPEDANCE SPECTROSCOPY

Impedance spectroscopy has been used for decades to infer the health status of the structure. Shear-mode acoustic wave resonators and electromechanical (E/M) coupling were studied by Mueller and Zhang (1998); Cheng et al. (2007); Milyutin et al. (2008); Milyutin and Muralt (2011); Yanagitani (2011). The effects of electrodes were investigated in Ji and Shen (2005) and showed that the stiffness of electrodes materials affects the resonance frequency. In this section, a predictive model of impedance and admittance were developed for SH-PWAS analytically, by finite element modeling, and experimentally.

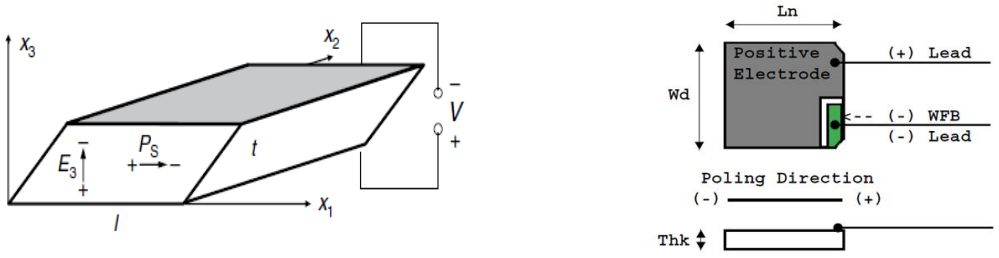

(a) (b)

Figure 3.6. (a) Schematic for SH-PWAS, shaded areas are the electrodes (Giurgiutiu, 2008), (b) transducer schematic from manufacturer, source: APC piezoceramic Int Ltd

3.2.1. SH-PWAS Sensing and Actuation Constitutive Relations

Most literature mentioned earlier deal with the shear dielectric coupling coefficient d_{15}, however, this is only applicable if the electric field (E_1) is applied in the in-plane direction and the piezoelectric poling is in thickness direction. In our model and FEM simulations we use d_{35}. The SH-PWAS transducer we used (APC International Ltd) has its electrodes on the top and bottom; hence electric field is applied along x_3 direction and the poling is applied along x_1 direction (Refer to **Figure 3.6**a). Recall the constitutive equations of piezoelectricity in contracted Voigt notations,

$$\begin{Bmatrix} S_1 \\ S_2 \\ S_3 \\ S_4 \\ S_5 \\ S_6 \end{Bmatrix} = \begin{bmatrix} s_{11}^E & s_{12}^E & s_{13}^E & & & \\ s_{21}^E & s_{22}^E & s_{23}^E & & & \\ s_{31}^E & s_{32}^E & s_{33}^E & & & \\ & & & s_{44}^E & & \\ & & & & s_{55}^E & \\ & & & & & s_{66}^E \end{bmatrix} \begin{Bmatrix} T_1 \\ T_2 \\ T_3 \\ T_4 \\ T_5 \\ T_6 \end{Bmatrix} + \begin{bmatrix} d_{11} & & \\ d_{12} & & \\ d_{13} & & \\ & & d_{35} \\ & d_{26} & \end{bmatrix} \begin{Bmatrix} E_1 \\ E_2 \\ E_3 \end{Bmatrix} \tag{3.1}$$

$$\begin{Bmatrix} D_1 \\ D_2 \\ D_3 \end{Bmatrix} = \begin{bmatrix} d_{11} & d_{12} & d_{13} & & & d_{26} \\ & & & d_{35} & & \end{bmatrix} \begin{Bmatrix} T_1 \\ T_2 \\ T_3 \\ T_4 \\ T_5 \\ T_6 \end{Bmatrix} + \begin{bmatrix} \varepsilon_{11}^T & & \\ & \varepsilon_{22}^T & \\ & & \varepsilon_{33}^T \end{bmatrix} \begin{Bmatrix} E_1 \\ E_2 \\ E_3 \end{Bmatrix} \tag{3.2}$$

where S_j are the strain components, s_{ij}^E is the compliance matrix under constant electric field condition, T_i are the stress components, d_{kj} are the piezoelectric coupling coefficients, E_k represents the electric field vector, D_k is the electric displacement vector, and ε_{ik}^T are the electric permittivity constants of the PWAS material. Equation (3.1) is considered the piezoelectric converse effect, where the applied electric field will result in

induced strain. Equation (3.2) is the direct piezoelectric effect, where applied stresses will result in electrical displacement. For the SH-PWAS transducer of **Figure 3.6**a, we have the electric field in the x_3 direction and the poling in the x_1 direction. Equations. (3.1), (3.2) reduce to

$$S_5 = u_1' = s_{55}^E T_5 + d_{35} E_3 \tag{3.3}$$

$$D_3 = d_{35} T_5 + \varepsilon_{33}^T E_3 \tag{3.4}$$

3.2.2. Free SH-PWAS Electro-mechanical Impedance and Admittance

3.2.2.1. Analytical modeling based on constant electric field E_3

As shown in **Figure 3.6**a, x_3 is the thickness direction and x_1 is the piezoelectric poling direction. When the SH-PWAS is bonded to a structure, the direction x_2 is the wave propagation direction. For a free SH-PWAS, the stress-free boundary condition is applied at $x_3 = \pm\frac{h}{2}$, which correspond to the SH-PWAS transducer's top and bottom surfaces.

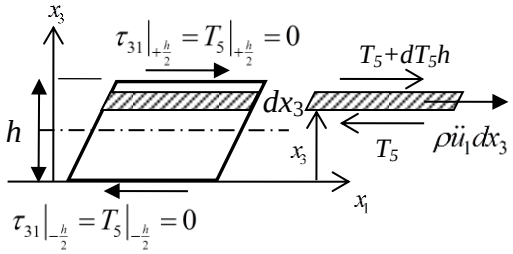

Figure 3.7. Free SH-PWAS free body diagram

Assume time-harmonic electric excitation

$$E_3 = \hat{E}_3(x) e^{i\omega t} \tag{3.5}$$

where ω is the circular frequency in rad/sec.

Considering the Newton law of motion applied to the element in **Figure 3.7**, we have

$$\cancel{T_5} + dT_5 - \cancel{T_5} = \rho \ddot{u}_1 dx_3 \tag{3.6}$$

upon simplification, Eq. (3.6) becomes,

$$T_5' = \rho \ddot{u}_1 \tag{3.7}$$

where ρ is piezoelectric material type density, $\ddot{u}_1$ is the second derivative of u_1 displacement with respect to time. Differentiating Eq. (3.3) with respect to x_3 and assuming constant electric field E_3 across thickness yields

$$S_5' = s_{55}^E T_5' \tag{3.8}$$

where $(\ )' = \dfrac{\partial(\ )}{\partial x_3}$ and T_5 is the shear stress in 13 direction. Recall strain displacement relation for shear deformation, i.e.,

$$S_5 = \frac{\partial u_1}{\partial x_3} + \frac{\cancel{\partial u_3}}{\cancel{\partial x_1}} = u_1' \tag{3.9}$$

where $\mu = 1/s_{55}^E$ is the shear modulus for piezoelectric material. Substitution of Eq. (3.9) into Eq. (3.8) yields

$$T_5 = \mu u_1' \tag{3.10}$$

Differentiation of the Eq. (3.10) with respect to x_3 and substitution into Eq. (3.7) yields,

$$\mu u_1'' = \rho \ddot{u}_1 \tag{3.11}$$

Assuming time harmonic solution $u_1 = \hat{u}_1 e^{i\omega t}$ reduces Eq. (3.11) to

$$\mu \hat{u}_1'' + \rho \omega^2 \hat{u}_1 = 0 \tag{3.12}$$

Then, the space solution of the differential Eq. (3.11) is

$$\hat{u}_1 = C_1 \sin \gamma x_3 + C_2 \cos \gamma x_3 \tag{3.13}$$

Define speed of SH-wave in the piezoelectric material as c , and the corresponding wave number as γ

$$c^2 = \frac{1}{\rho\mu} \quad , \quad c = \sqrt{\frac{\mu}{\rho}} \quad , \quad \gamma = \frac{\omega}{c} = \omega\sqrt{\frac{\rho}{\mu}} \tag{3.14}$$

Mechanical response:

Imposing stress free boundary condition $T_5\big|_{\pm\frac{h}{2}} = 0$ in Eq. (3.3) yields

$$S_5\big|_{\pm\frac{h}{2}} = d_{35}\hat{E}_3 \tag{3.15}$$

Using the strain – displacement relation Eq. (3.9) and the derivative of Eq. (3.13) into Eq. (3.15) yields

$$\begin{aligned} \hat{u}_1'\big|_{-\frac{h}{2}} &= \gamma\left(C_1 \cos \tfrac{1}{2}\gamma h + C_2 \sin \tfrac{1}{2}\gamma h\right) = d_{35}\hat{E}_3 \\ \hat{u}_1'\big|_{+\frac{h}{2}} &= \gamma\left(C_1 \cos \tfrac{1}{2}\gamma h - C_2 \sin \tfrac{1}{2}\gamma h\right) = d_{35}\hat{E}_3 \end{aligned} \tag{3.16}$$

Solving the two equations in (3.16) yields

$$C_1 = \frac{d_{35}\hat{E}_3}{\gamma \cos \tfrac{1}{2}\gamma h} \quad , \quad C_2 = 0 \tag{3.17}$$

Substitution of Eq. (3.17) into Eq. (3.13) yields the space domain solution

$$\hat{u}_1(x_3) = \frac{d_{35}\hat{E}_3}{\gamma} \; \frac{\sin \gamma x_3}{\cos \tfrac{1}{2}\gamma h} \tag{3.18}$$

Differentiation of Eq. (3.18) yields the strain

$$\hat{S}_5 = \frac{\partial \hat{u}_1}{\partial x_3} = d_{35}\hat{E}_3 \; \frac{\cos \gamma x_3}{\cos \tfrac{1}{2}\gamma h} \tag{3.19}$$

Define induced strain actuation (ISA) which is the PWAS strain in the absence of mechanical loading, i.e.,

$$(\hat{S}_5)_{ISA} = d_{35}\hat{E}_3 \tag{3.20}$$

Corresponding induced displacement is defined as

$$u_{ISA} = (\hat{S}_5)_{ISA} h = d_{35}\hat{E}_3 h \tag{3.21}$$

Equation (3.18) and Eq. (3.19) can be rearranged in the form

$$\hat{u}_1(x_3) = \frac{1}{2}\frac{u_{ISA}}{\frac{1}{2}\gamma h}\ \frac{\sin\gamma x_3}{\cos\frac{1}{2}\gamma h} \tag{3.22}$$

$$\hat{S}_5(x_3) = (\hat{S}_5)_{ISA}\ \frac{\cos\gamma x_3}{\cos\frac{1}{2}\gamma h} \tag{3.23}$$

Electrical response

Eliminating the stress T_5 between Eqs. (3.3), (3.4), and using Eq. (3.9) yields

$$D_3 = \frac{d_{35}}{s_{55}^E}\left[u_1' - d_{35}\hat{E}_3\right] + \varepsilon_{33}^T\hat{E}_3 \tag{3.24}$$

Upon rearrangement, Eq. (3.24) becomes

$$D_3 = \varepsilon_{33}^T\hat{E}_3\left[1 - K_{35}^2\left(1 - \frac{u_1'}{d_{35}\hat{E}_3}\right)\right] \tag{3.25}$$

where the electromechanical coupling factor K_{35} is defined as

$$K_{35}^2 = \frac{d_{35}^2}{s_{55}^E\varepsilon_{33}^T} \tag{3.26}$$

Integrating the electrical displacement in Eq. (3.25) over the electrodes area yields the electric charge

$$Q(x_3) = \int_A D_3(x_3)dx_1dx_2 = \int_{-\frac{l}{2}}^{+\frac{l}{2}}\int_0^b D_3(x_3)dx_1dx_2 \tag{3.27}$$

Equation (3.27) indicates that electric charge varies across the thickness. We define equivalent average charge across thickness as

$$\hat{Q}_{eq} = \frac{1}{h}\int_{-\frac{h}{2}}^{\frac{h}{2}} Q(x_3)dx_3 \tag{3.28}$$

Substituting D_3 from Eq. (3.25) into Eq. (3.28) and performing the integration yields

$$\hat{Q}_{eq} = \frac{\varepsilon_{33}\hat{E}_3 bl}{h}\left[\left(1-K_{35}^2\right)h + K_{35}^2\frac{\hat{u}_1(x_3)\Big|_{-\frac{h}{2}}^{\frac{h}{2}}}{d_{35}\hat{E}_3}\right] \tag{3.29}$$

Defining PWAS capacitance as

$$C = \varepsilon_{33}^T\frac{bl}{h} \tag{3.30}$$

Substituting $\hat{u}_1(x_3)$ from Eq. (3.22); the electric field is related to voltage by $\hat{E}_3 = \frac{\hat{V}}{h}$; and recalling u_{ISA} from Eq. (3.21); then Eq. (3.29) can be simplified to

$$\hat{Q}_{eq} = C\hat{V}\left[1-K_{35}^2\left(1-\frac{\tan\frac{1}{2}\gamma h}{\frac{1}{2}\gamma h}\right)\right] \tag{3.31}$$

The electric current *I* is defined as the time derivative of electric charge, i.e. $I = \dot{Q} = i\omega Q$, hence $\hat{I} = i\omega\hat{Q}$ and Eq. (3.31) simplifies to

$$Y = \frac{\hat{I}}{\hat{V}} = i\omega C\left[1-K_{35}^2\left(1-\frac{\tan\frac{1}{2}\gamma h}{\frac{1}{2}\gamma h}\right)\right] \tag{3.32}$$

And the free SH-PWAS electrical impedance is

$$Z = \frac{\hat{V}}{\hat{I}} = \frac{1}{i\omega C}\left[1-K_{35}^2\left(1-\frac{\tan\frac{1}{2}\gamma h}{\frac{1}{2}\gamma h}\right)\right]^{-1} \tag{3.33}$$

Result in Eq. (3.32) is slightly different from that of Milyutin et al. (2008), where the stress-charge piezoelectric equations were used and the model was for d_{15} - mode, where the transducer electrodes were on the sides not on the top and bottom surfaces like in our case.

3.2.2.2. Analytical modeling based on constant electric displacement D_3

The constant electric field assumption is usually more appropriate in piezoelectric stacks with internal electrodes, where flow of charge exists (i.e. closed circuit) and the corresponding electric displacement forms a half wave distribution at the resonator (Sherrit et al., 2013). However, in most other cases of single resonators, such as thickness shear mode, no current flows through the resonator, which makes the constant electric displacement assumption (i.e. zero current or open circuit) more realistic. Bar piezoelectric ceramic transformers were studied under constant electric displacement condition (Erhart et al., 2013), where impedance was modeled for the longitudinal mode (d_{31}). In this section, we derive analytically the E/M impedance and admittance based on constant electric displacement D_3. The predicted models are compared with experimental measurements to investigate which assumption best fits our SH-PWAS transducer.

For the electric field restricted in x_3 direction, the T_5 stress shown in **Figure 3.6**a, takes the following form in Voigt notations,

$$T_5 = \frac{1}{s_{55}^D} S_5 - \frac{g_{35}}{s_{55}^D} \hat{D}_3 \tag{3.34}$$

The electric field in the case of constant electric displacement is derived starting from Eq. (3.4)

$$D_3 = d_{35}T_5 + \varepsilon_{33}^T E_3 \tag{3.35}$$

Rearranging Eq.(3.35), and eliminating stress T_5 using Eq.(3.34) yields

$$E_3 = -\frac{d_{35}}{\varepsilon_{33}^T}T_5 + \frac{1}{\varepsilon_{33}^T}\hat{D}_3 = -g_{35}\left(\frac{1}{s_{55}^D}S_5 - \frac{g_{35}}{s_{55}^D}\hat{D}_3\right) + \frac{1}{\varepsilon_{33}^T}\hat{D}_3 \tag{3.36}$$

Upon rearrangement, Eq.(3.36) becomes

$$E_3 = \frac{-g_{35}}{s_{55}^D}S_5 + \frac{1}{\varepsilon_{33}^S}\hat{D}_3 \tag{3.37}$$

where

$$\left(\frac{g_{35}^2}{s_{55}^D} + \frac{1}{\varepsilon_{33}^T}\right) = \frac{1}{\varepsilon_{33}^S} \tag{3.38}$$

Mechanical Response

Substitute the stress free boundary condition ($T_5\big|_{x_3=\pm\frac{h}{2}} = 0$) into Eq.(3.34) to get

$$S_5\big|_{\pm\frac{h}{2}} = g_{35}\hat{D}_3 \tag{3.39}$$

Using $S_5 = u_1' = \frac{\partial u_1}{\partial x_3}$ and replacing u_1 by $\hat{u}_1$ that represents the amplitude value with

ignoring time harmonic exponential

$$\begin{aligned}\hat{u}_1'\big|_{-\frac{h}{2}} &= \gamma\left(C_1\cos\tfrac{1}{2}\gamma h + C_2\sin\tfrac{1}{2}\gamma h\right) = g_{35}\hat{D}_3\\ \hat{u}_1'\big|_{+\frac{h}{2}} &= \gamma\left(C_1\cos\tfrac{1}{2}\gamma h - C_2\sin\tfrac{1}{2}\gamma h\right) = g_{35}\hat{D}_3\end{aligned} \tag{3.40}$$

Solving the two equations in (3.40) yields

$$C_1 = \frac{g_{35}\hat{D}_3}{\gamma\cos\frac{1}{2}\gamma h} \quad , \quad C_2 = 0 \tag{3.41}$$

Substitution of Eq. (3.41) into Eq. (3.13) yields the space domain solution

$$\hat{u}_1(x_3) = \frac{g_{35}\hat{D}_3}{\gamma} \frac{\sin \gamma x_3}{\cos \frac{1}{2}\gamma h} \tag{3.42}$$

Differentiation of Eq. (3.42) yields the strain as

$$\hat{S}_5 = \frac{\partial \hat{u}_1}{\partial x_3} = g_{35}\hat{D}_3 \frac{\cos \gamma x_3}{\cos \frac{1}{2}\gamma h} \tag{3.43}$$

Electrical response

Using Eq.(3.37) and substituting strain ($\hat{S}_5$) from Eq.(3.43) yields,

$$\begin{aligned} E_3 &= \frac{-g_{35}^2 \hat{D}_3}{s_{55}^D} \frac{\cos \gamma x_3}{\cos \frac{1}{2}\gamma h} + \frac{1}{\varepsilon_{33}^S}\hat{D}_3 \\ &= \frac{\hat{D}_3}{\varepsilon_{33}^S}\left[1 - \frac{g_{35}^2 \varepsilon_{33}^S}{s_{55}^D} \frac{\cos(\gamma x_3)}{\cos \frac{1}{2}\gamma h}\right] = \frac{\hat{D}_3}{\varepsilon_{33}^S}\left[1 - K_{35}^2 \frac{\cos(\gamma x_3)}{\cos \frac{1}{2}\gamma h}\right] \end{aligned} \tag{3.44}$$

where the electromechanical coupling factor K_{35} is defined as

$$K_{35}^2 = \frac{e_{35}^2 s_{55}^D}{\varepsilon_{33}^S} = \left(\frac{g_{35}\varepsilon_{33}^S}{s_{55}^D}\right)^2 \frac{s_{55}^D}{\varepsilon_{33}^S} = \frac{g_{35}^2 \varepsilon_{33}^S}{s_{55}^D} \tag{3.45}$$

Integrating the electrical displacement over electrodes area, results in the electric charge

$$\hat{Q} = \int_A \hat{D}_3 dx_1 dx_2 = \int_{-\frac{l}{2}}^{+\frac{l}{2}} \int_0^b \hat{D}_3 dx_1 dx_2 = bl\hat{D}_3 \tag{3.46}$$

As before, the electric current *I* is calculated from the time derivative of electric charge

$$\hat{I} = \dot{\hat{Q}} = i\omega\hat{Q} = i\omega bl\hat{D}_3 \tag{3.47}$$

Electric voltage is related to electric field by

$$\hat{V} = \int_{-\frac{h}{2}}^{\frac{h}{2}} \hat{E}_3 dx_3 \tag{3.48}$$

Substitution of Eq. (3.44) into Eq. (3.48) yields

$$\begin{aligned}\hat{V} &= \frac{\hat{D}_3}{\varepsilon_{33}^S}\int_{-\frac{h}{2}}^{\frac{h}{2}}\left[1-K_{35}^2\frac{\cos\left(\gamma x_3\right)}{\cos\frac{1}{2}\gamma h}\right]dx_3 \\ &= \frac{\hat{D}_3}{\varepsilon_{33}^S}h\left[1-K_{35}^2\frac{\sin\left(\gamma x_3\right)\Big|_{-\frac{h}{2}}^{\frac{h}{2}}}{\gamma h\cos\frac{1}{2}\gamma h}\right] = \frac{\hat{D}_3}{\varepsilon_{33}^S}h\left[1-K_{35}^2\frac{2\sin\frac{1}{2}\gamma h}{\gamma h\cos\frac{1}{2}\gamma h}\right]\end{aligned} \tag{3.49}$$

As before, defining PWAS capacitance as

$$C = \varepsilon_{33}^S\frac{bl}{h} \tag{3.50}$$

The impedance is defined as $Z = \frac{\hat{V}}{\hat{I}}$ and using Eqs. (3.47), (3.49); the electromechanical impedance is

$$Z = \frac{\hat{V}}{\hat{I}} = \frac{h}{\varepsilon_{33}^S i\omega bl}\left[1-K_{35}^2\frac{1}{\frac{1}{2}\gamma h\cot\frac{1}{2}\gamma h}\right] = \frac{1}{i\omega C}\left[1-K_{35}^2\frac{1}{\frac{1}{2}\gamma h\cot\frac{1}{2}\gamma h}\right] \tag{3.51}$$

Defining $\phi = \frac{1}{2}\gamma h$, the electromechanical impedance can further be written as

$$Z = \frac{1}{i\omega C}\left[1-K_{35}^2\frac{1}{\phi\cot\phi}\right] \tag{3.52}$$

And the electromechanical admittance is

$$Y = \frac{\hat{I}}{\hat{V}} = i\omega C\left[1-K_{35}^2\frac{1}{\phi\cot\phi}\right]^{-1} \tag{3.53}$$

3.2.3. Bonded SH-PWAS Analytical Model

SH-PWAS bonded on a plate structure is shown in **Figure 3.8**. When the SH-PWAS is bonded to the structure, the direction x_2 (global *x*-direction) is the SH wave propagation direction. Depending on which plane is considered for analysis, the SH-

PWAS response can be classified into: (a) axial and flexural response, in 1-3 or z-y plane, (b) SH response, in 2-3 or x-y plane. We start with axial-flexural response in 1-3 plane (**Figure 3.9**a).

When the SH-PWAS is bonded to a structure, the displacement of the lower tip of the PWAS can be set equal to u_1^{str} which can be determined from the elasticity solution of the bonded structure of thickness *2d* and then structure dynamic stiffness associated with the transducer can be determined from the relation

$$F_{PWAS} = \tau\big|_{-\frac{h}{2}} A = k_{shear}\, U_1\big|_{-\frac{h}{2}} \tag{3.54}$$

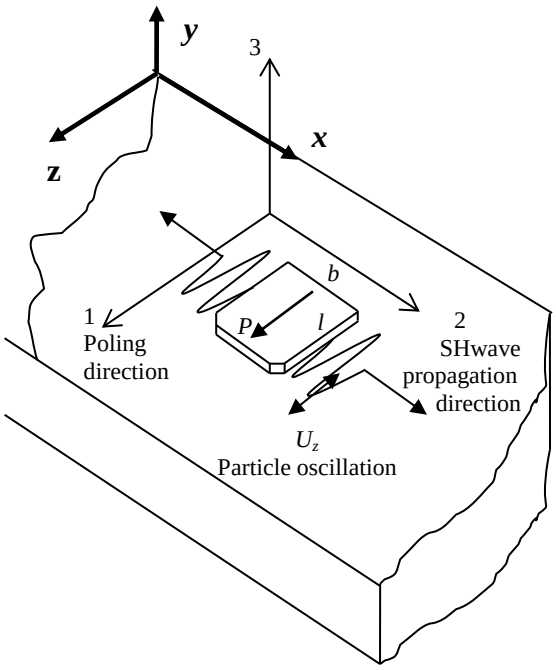

Figure 3.8. Constrained SH-PWAS model

3.2.3.1. Axial and flexural response solution

Given the boundary conditions and structural properties, the dynamic structure stiffness $k_{str}(\omega)$ can be evaluated. The applied loads are axial load

$f_e(z,t) = \hat{f}(z)e^{i\omega t} \propto F_{PWAS}$ which is acting through structure midplane in addition to the bending moment generated $m_e(z,t) = \hat{m}_e(z)e^{i\omega t} \propto F_{PWAS}d$, where d is the half plate thickness. When incorporating $k_{str}(\omega)$ into consideration, a "constrained PWAS" solution can be developed as follows: (1) The displacement of the lower tip of the SH-PWAS can be set equal to u_1^{str} , which can be determined from the elasticity solution of the structure of thickness *2d*. Then, (2) structure stiffness can be determined from Eq.(3.54).

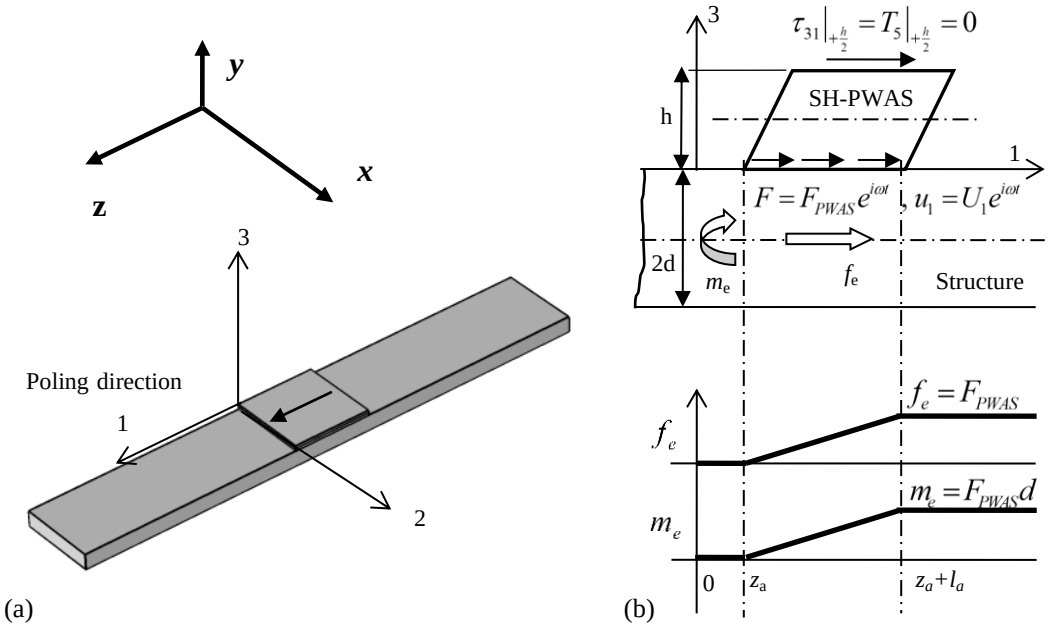

Figure 3.9. (a) Constrained SH-PWAS model for axial-flexural response, (b) Interaction between SH-PWAS with the structure, axial and flexural load transfer

The model assumptions are (i) stress free boundary condition for the top side of the SH-PWAS, (ii) perfect bonding with the structure, (iii) constant electric field $\hat{E}_3$, (iv) SH-PWAS deforms uniformly with only shear deformation (**Figure 3.9**b), and (v) axial and moment loads about centroid axis are linear ramp functions within SH-PWAS dimension (**Figure 3.9**b). The structure displacement is

$$u_z(x,z,t) = \sum_{j=1}^{\infty} C_j U_j(z) e^{-i(\gamma_x x - \omega t)} \tag{3.55}$$

Axial wave equation in *z*-direction can be written as

$$-m\omega^2 \sum_{j=1}^{\infty} C_j U_j e^{i\omega t} - EA \sum_{j=1}^{\infty} C_j U_j'' e^{i\omega t} = \hat{f}(z) e^{i\omega t} \tag{3.56}$$

$$-m\omega^2 \sum_{p=1}^{\infty} C_p U_p - EA \sum_{p=1}^{\infty} C_p U_p'' = \hat{f}(z) \tag{3.57}$$

Multiplying by mode U_q and integrate over beam length *L*

$$-\omega^2 \sum_{p=1}^{\infty} C_p \int_0^L U_p U_q dz - \sum_{p=1}^{\infty} C_p \int_0^L EAU_p'' U_q dz = \int_0^L \hat{f}(z) U_q dz, \quad \text{q} = 1,2,3 \tag{3.58}$$

Then using Orthogonality property

$$\int_0^L mU_p U_q dz = 0 \quad \text{if} \quad p \neq q \tag{3.59}$$

From wave equation $c^2 \hat{u}'' + \omega^2 \hat{u} = 0$ and using mode U_j

$$\begin{aligned} &\frac{EA}{m} U_j'' + \omega_j^2 U_j = 0 \\ &EAU_j'' + m\omega_j^2 U_j = 0 \end{aligned} \tag{3.60}$$

Multiply by mode U_q and integrating over beam length *L*

$$\begin{aligned} &\int_0^L EAU_p'' U_q dz = -\omega_p^2 \int_0^L mU_p U_q dz \\ &\int_0^L EAU_p'' U_q dz = 0 \quad \text{if} \quad p \neq q \end{aligned} \tag{3.61}$$

Defining the quantities:

$$m_j = \int_0^L mU_j^2(z) dz \quad , \quad k_j = -\int_0^L EAU_j''(z) U_j(z) dz \quad , \quad f_j = \int_0^L \hat{f}(z) U_j(z) dz \tag{3.62}$$

Substitute Eq.(3.62) in Eq.(3.58) using $p=q=j$

$$C_j(-\omega^2 m_j + k_j) = f_j \tag{3.63}$$

$$C_j(-\omega^2 + \omega_j^2) = \frac{f_j}{m_j} \qquad \text{where } \omega_j^2 = \frac{k_j}{m_j} \tag{3.64}$$

But due to orthonormality, that is orthogonality in addition to normalization to get constant C_j in $U_j = C_j \sin \gamma_j l$ substituting in orthogonality relation for $p=q$

$$m_j = \int_0^L m U_j^2(z) dz = 1 \tag{3.65}$$

Then normalization factor is $C_j = \sqrt{\frac{2}{ml}}$ and Eq.(3.64) is written as

$$C_j(-\omega^2 + \omega_j^2) = f_j \tag{3.66}$$

Define modal participation factors: $\frac{f_j}{(-\omega^2 + \omega_j^2)}$ then normal mode expansion (NME) solution can be evaluated by substituting in Eq.(3.55)

$$u_z(x,z,t) = \sum_{j=1}^{\infty} \frac{f_j}{(-\omega^2 + \omega_j^2)} U_j(z) e^{-i(\gamma_x x - \omega t)} \tag{3.67}$$

where normalization factor is included in $U_j(z)$ such that $U_j(z) = \sqrt{\frac{2}{ml}} \sin \gamma_j l$

For more realistic modeling, damping to be introduced as ζ and Eq.(3.67) is written as

$$u_z(x,z,t) = \sum_{j=1}^{\infty} \frac{f_j}{(-\omega^2 + 2i\zeta\omega\omega_j + \omega_j^2)} U_j(z) e^{-i(\gamma_x x - \omega t)} \tag{3.68}$$

For SH-PWAS bonded on structure exerting certain force pattern, NME can be further simplified. As loads exerted by SH-PWAS can be separated to axial normal force f_e and

bending moment m_e, where both are defined as linearly increasing functions from zero at one PWAS end to maxima at the other end,

$$f_e\big|_{\max} = F_{PWAS}, \quad m_e\big|_{\max} = F_{PWAS} d \tag{3.69}$$

Space wise, the axial force and bending moment can be represented by Heaviside function, $H(z-z_a)$, and linear function of *z* as shown in **Figure 3.9**b, hence

$$f_e(z,t) = F_{PWAS}\left\{\left[(z-z_a)\cdot H(z-z_a)\right]-\left[(z-(z_a+l_a))\cdot H(z-(z_a+l_a))\right]\right\}e^{i\omega t} \tag{3.70}$$

$$m_e(z,t) = F_{PWAS} d\left\{\left[(z-z_a)\cdot H(z-z_a)\right]-\left[(z-(z_a+l_a))\cdot H(z-(z_a+l_a))\right]\right\}e^{i\omega t} \tag{3.71}$$

Axial part

The forced vibration governing equation for axial responses

$$\rho A\ddot{u}(z,t) - EAu''(z,t) = f_e'(z,t) \tag{3.72}$$

Substituting axial force space distributed Heaviside function into equation of motion

$$\rho A\ddot{u}(z,t) - EAu''(z,t) = \frac{F_{PWAS}}{l}\left[H(z-z_a) - H(z-(z_a+l_a))\right]e^{i\omega t} \tag{3.73}$$

where *l* in the denominator was added to balance equation dimensions to force per unit length. Applying Eq.(3.55), and following the same procedure of free response yields,

$$C_n(-\omega^2+\omega_n^2) = \frac{f_n}{m_n} \tag{3.74}$$

$$C_n = \frac{f_n}{(-\omega^2+\omega_n^2)m_n} \tag{3.75}$$

where $f_n = \int_0^L \hat{f}(z)U_n(z)dz$ and can be calculated by multiplying by $U_n(z)$ and integrating over beam length

$$f_n = \int_0^L \frac{F_{PWAS}}{l}\left[H(z-z_a) - H(z-(z_a+l_a))\right]U_n(z)dz \tag{3.76}$$

$$f_n = \frac{F_{PWAS}}{l}\left[\int_{z_a}^{L} U_n(z)dz - \int_{z_a+l_a}^{L} U_n(z)dz\right] \tag{3.77}$$

The factor C_n can be evaluated as

$$C_n = \frac{1}{(-\omega^2+\omega_n^2)}\ \frac{F_{PWAS}}{\rho Al}\left[\int_{z_a}^{L} U_n(z)dz - \int_{z_a+l_a}^{L} U_n(z)dz\right] \tag{3.78}$$

And finally the axial displacement can be written as:

$$u_z(x,z,t) = \frac{F_{PWAS}}{\rho Al}\sum_{n=1}^{\infty}\frac{\int_{z_a}^{z_a+l_a} U_n(z)dz}{(-\omega^2+2i\zeta\omega\omega_n+\omega_n^2)}U_n(z)e^{-i(\gamma_x x-\omega t)} \tag{3.79}$$

Flexural part

Equation of motion is

$$\rho A\ddot{w}(z,t) + EIw''''(z,t) = -m_e''(z,t) \tag{3.80}$$

Using Eq.(3.71) in Eq.(3.80), considering that the second derivative of linear z function will yield a Dirac function

$$\rho A\ddot{w}(z,t) + EIw''''(z,t) = \frac{F_{PWAS}d}{l}\left[-\delta(z-z_a)+\delta(z-(z_a+l_a))\right]e^{i\omega t} \tag{3.81}$$

Applying modal expansion model:

$$w(x,z,t) = \sum_{n=1}^{\infty} C_n W_n(z)e^{-i(\gamma_x x-\omega t)} \tag{3.82}$$

With similar procedure like Eqs. (3.74) - (3.77) ,we get the C_n as

$$C_n = \frac{1}{(-\omega^2+\omega_n^2)}\ \frac{F_{PWAS}d}{\rho Al}\int_0^L [-\delta(z-z_a)+\delta(z-(z_a+l_a))]W_n(z)dz \tag{3.83}$$

Using the property of Dirac function when multiplied by a function and then integrated. This integration equals to the evaluation of the function at the shifted value of Dirac function; Eq.(3.83) reduces to

$$C_n = \frac{1}{(-\omega^2 + \omega_n^2)} \frac{F_{PWAS} d}{\rho A l} \left[-W_n(z_a) + W_n(z_a + l_a) \right] \tag{3.84}$$

Then the final normal mode expanded displacement can be evaluated

$$w(x,z,t) = \frac{F_{PWAS} d}{\rho A l} \sum_{n=1}^{\infty} \frac{\left[-W_n(z_a) + W_n(z_a + l_a) \right]}{(-\omega^2 + 2i\zeta\omega\omega_n + \omega_n^2)} W_n(z) e^{-i(\gamma_x x - \omega t)} \tag{3.85}$$

Noting that *w* displacement is the flexural displacement that is in *y*-direction in our global co-ordinates. The total axial displacement consists of the part from the axial solution as well as the effect of the slope of the flexural solution.

$$u_p = u \pm w' d \tag{3.86}$$

Ignoring the *x* and *t* terms in Eqs. (3.79) and (3.85) , and considering the effective displacement along SH-PWAS length as

$$\left(u_1^{str} \right)_{\text{effective}} = \frac{1}{l_a} \int_0^L u_1^{str}(z) dz \tag{3.87}$$

$$\hat{u}_{PWAS} = \frac{F_{PWAS}}{\rho A l^2} \left\{ \begin{array}{l} \displaystyle\sum_{n_a=1}^{\infty} \frac{\left(\displaystyle\int_{z_a}^{z_a + l_a} U_n(z) dz \right)^2}{(-\omega^2 + 2i\zeta_a \omega\omega_{n_a} + \omega_{n_a}^2)} \\ + d^2 \displaystyle\sum_{n_w=1}^{\infty} \frac{\left[W_n(z_a + l_a) - W_n(z_a) \right]^2}{(-\omega^2 + 2i\zeta_w \omega\omega_{n_w} + \omega_{n_w}^2)} \end{array} \right\} \tag{3.88}$$

And then we can define dynamic stiffness of the structure $k_{str}(\omega)$ as

$$k_{str}(\omega)=\frac{F_{PWAS}}{\hat{u}_{PWAS}}=\rho_{str}A_{str}l_{str}^{2}\left\{\begin{array}{l}\displaystyle\sum_{n_a=1}^{\infty}\frac{\left(\int_{z_a}^{z_a+l_a}U_n(z)dz\right)^{2}}{(-\omega^{2}+2i\zeta_a\omega\omega_{n_a}+\omega_{n_a}^{2})}\\ \displaystyle+d^{2}\sum_{n_w=1}^{\infty}\frac{\left[W_n(z_a+l_a)-W_n(z_a)\right]^{2}}{(-\omega^{2}+2i\zeta_w\omega\omega_{n_w}+\omega_{n_w}^{2})}\end{array}\right\}^{-1} \tag{3.89}$$

For actual evaluating the dynamic stiffness of the structure, vibration modes need to be determined, and the modes depend on boundary condition, for instance for free-free structural beam bonded with the SH-PWAS, we have (Giurgiutiu and Zagrai, 2000)

$$U_n(z)=A_{n_a}\cos(\gamma_{n_a}z),\ A_{n_a}=\sqrt{\frac{2}{ml}},\ \gamma_{n_a}=\frac{n_a\pi}{l},\ \omega_{n_a}=\gamma_{n_a}c^{str},\ c_{str}=\sqrt{\frac{E_{str}}{\rho_{str}}},n_a=1,2, \tag{3.90}$$

The speed of the SH-wave in the piezoelectric material *c* is different from the axial wave speed in the structure, hence the latter is denoted by c_{str}

For flexural modal solution,

$$W_{n_w}(z)=A_{n_w}\left[\cosh\gamma_{n_W}z+\cos\gamma_{n_w}z-\sigma_{n_w}\left(\sinh\gamma_{n_w}z+\sin\gamma_{n_w}z\right)\right] \tag{3.91}$$

$$\omega_{n_w}=\gamma_{n_w}^{2}a_{flex},\quad a_{flex}=\sqrt{\frac{EI_{str}}{\rho_{str}A_{str}}},\quad A_{nw}=1/\sqrt{\int_0^l W_{n_w}^{2}(z)dz} \tag{3.92}$$

where the numerical values for $\sigma_{n_w}, l\gamma_{n_w}$ can be found from Giurgiutiu (2008), pg. 89.

3.2.3.2. Shear horizontal response solution

Shear horizontal response can be determined with a similar procedure to the one of the axial-flexural response, but taking into consideration the plane of the analysis containing SH wave propagation direction, i.e. plane 2-3 in **Figure 3.10**a.

The corresponding interaction between SH-PWAS and the structure involving SH response is shown in **Figure 3.10**b

$$u_z(x,z,t) = \sum_{j=1}^{\infty} C_j U_j(z) e^{-i(\gamma_x x - \omega t)} \tag{3.93}$$

Equation (3.88) reduces to

$$\hat{u}_{PWAS}^{SH} = \frac{F_{PWAS}}{\rho_{str} A_{str} l_{str}^2} \left\{ \sum_{n_a=1}^{\infty} \frac{\left(\int_{z_a}^{z_a+l_a} U_n(z) dz \right)^2}{(-\omega^2 + 2i\zeta_a \omega \omega_{n_a} + \omega_{n_a}^2)} \right\} \tag{3.94}$$

where the corresponding eigenvalues will be associated with SH standing waves, i.e

$$U_n(z) = A_{n_a} \cos(\gamma_{n_a} z), A_{n_a} = \sqrt{\frac{2}{ml}}, \gamma_{n_a} = \frac{n_a \pi}{l}, \omega_{n_a} = \gamma_{n_a} c_{str}^{SH}, c_{str}^{SH} = \sqrt{\frac{G_{str}}{\rho_{str}}}, n_a = 1,2, \tag{3.95}$$

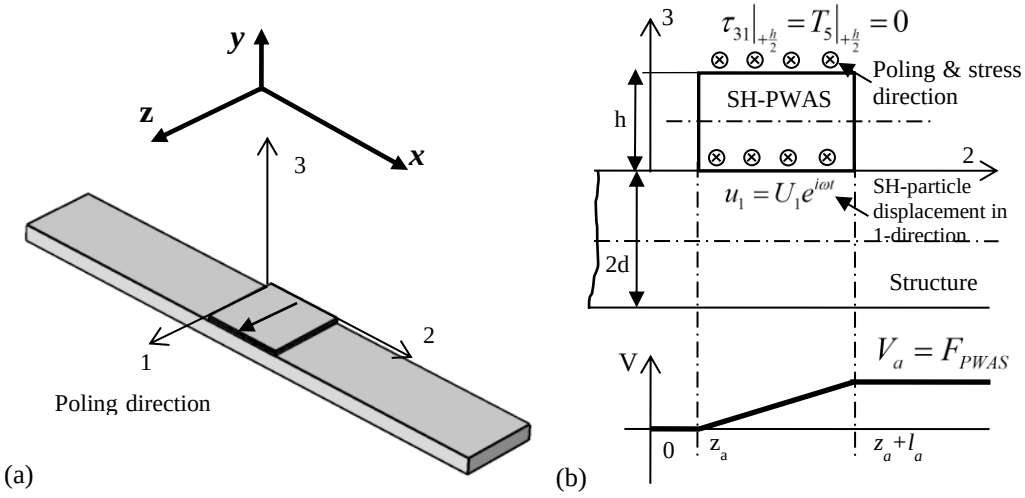

Figure 3.10 (a) Constrained SH-PWAS model for shear horizontal response, (b) Interaction between SH-PWAS and structure, SH response solution

Given the boundary conditions and structural properties, the dynamic structure stiffness $k_{shear}(\omega)$ can be found and used in the PWAS solution to model it as "constrained PWAS"

3.2.3.3. SH-PWAS tip displacement solution and connection to elasticity solution

Recall SH-PWAS equation of motion

$$\mu \frac{\partial^2 u_1}{\partial x_3^2} = \rho \frac{\partial^2 u_1}{\partial t^2} \tag{3.96}$$

$$u_1(x_3,t) = U_1(x_3)e^{i\omega t} \tag{3.97}$$

$$\mu \frac{\partial^2 U_1}{\partial x_3^2} e^{i\omega t} = -\rho\omega^2 U_1 e^{i\omega t} \tag{3.98}$$

Define the shear wave speed inside the SH-PWAS

$$c^2 = \mu / \rho \tag{3.99}$$

we get

$$c^2 \frac{\partial^2 U_1}{\partial x_3^2} + \omega^2 U_1 = 0 \tag{3.100}$$

$$U_1'' + \frac{\omega^2}{c^2} U_1 = 0 \tag{3.101}$$

Define the shear wave number

$$\gamma = \omega / c \tag{3.102}$$

we get

$$U_1 = C_1 \sin\gamma x_3 + C_2 \cos\gamma x_3 \tag{3.103}$$

$$\frac{\partial U_1}{\partial x_3} = \gamma C_1 \cos\gamma x_3 - \gamma C_2 \sin\gamma x_3 \tag{3.104}$$

$$\frac{\partial^2 U_1}{\partial x_3^2} = -\gamma^2 \left(C_1 \sin\gamma x_3 + C_2 \cos\gamma x_3\right) = -\gamma^2 U_1 \tag{3.105}$$

Defining $k_{PWAS} = \frac{G_a A}{h}$ where $A = lb$ and using the stress free boundary condition at the top electrode

$$\tau\Big|_{+\frac{h}{2}} = \mu \frac{\partial U_1}{\partial x_3}\Big|_{+\frac{h}{2}} = 0 \qquad , \qquad \tau\Big|_{-\frac{h}{2}} A = F = k_{str}\, U_1\Big|_{-\frac{h}{2}} \tag{3.106}$$

Substituting Eqs.(3.106) into SH-PWAS constitutive Eq. (3.3), yields the boundary conditions in terms of strain. The boundary condition at the top side is

$$U_1'\Big|_{\frac{h}{2}} = s_{55}^E.0 + d_{35}\hat{E}_3 \tag{3.107}$$

whereas the condition at SH-PWAS interface with the structure is

$$U_1'\Big|_{-\frac{h}{2}} = s_{55}^E.\frac{k_{str}}{A} U_1\Big|_{-\frac{h}{2}} + d_{35}\hat{E}_3 \tag{3.108}$$

$$U_1'\Big|_{-\frac{h}{2}} = \frac{1}{G_a}.\frac{k_{str}}{\frac{Ah}{h}} U_1\Big|_{-\frac{h}{2}} + d_{35}\hat{E}_3 \tag{3.109}$$

or Eq.(3.108) can be re-written in the form

$$U_1'\Big|_{-\frac{h}{2}} = \frac{r}{h} U_1\Big|_{-\frac{h}{2}} + d_{35}\hat{E}_3 \tag{3.110}$$

where

$$r = \frac{k_{str}}{k_{PWAS}} \tag{3.111}$$

is defined as the dynamic stiffness ratio

Using the displacement general solution Eq.(3.103) into Eq.(3.107) and Eq.(3.110)

$$\gamma\left(C_1 \cos\frac{\gamma h}{2} - C_2 \sin\frac{\gamma h}{2}\right) = d_{35}\hat{E}_3 \tag{3.112}$$

$$\gamma\left(C_1\cos\frac{\gamma h}{2}+C_2\sin\frac{\gamma h}{2}\right)=\frac{r}{h}\left(-C_1\sin\frac{\gamma h}{2}+C_2\cos\frac{\gamma h}{2}\right)+d_{35}\hat{E}_3 \tag{3.113}$$

solving Eq. (3.112) and Eq. (3.113),

$$C_1\left(\gamma\cos\frac{\gamma h}{2}\right)+C_2\left(-\gamma\sin\frac{\gamma h}{2}\right)=d_{35}\hat{E}_3 \tag{3.114}$$

$$C_1\left(\gamma\cos\frac{\gamma h}{2}+\frac{r}{h}\sin\frac{\gamma h}{2}\right)+C_2\left(\gamma\sin\frac{\gamma h}{2}-\frac{r}{h}\cos\frac{\gamma h}{2}\right)=d_{35}\hat{E}_3 \tag{3.115}$$

solving Eqs.(3.114), (3.115)

$$C_2\left(\gamma\cos\frac{\gamma h}{2}\left(\cot\frac{\gamma h}{2}-\frac{2\gamma h}{r}\right)-\gamma\sin\frac{\gamma h}{2}\right)=d_{35}\hat{E}_3 \quad \rightarrow$$

$$C_2=\frac{d_{35}\hat{E}_3 hr}{2\left[\phi\cos\phi(r\cot\phi-4\phi)-\phi r\sin\phi\right]} \tag{3.116}$$

Then multiplying Eq.(3.114) times $(1-r)$ and subtract Eq. (3.114) from Eq. (3.115)

$$C_1=C_2\left(\cot\frac{\gamma h}{2}-\frac{2\gamma h}{r}\right) \rightarrow C_1=\frac{d_{35}\hat{E}_3 h(r\cot\phi-4\phi)}{2\left[\phi\cos\phi(r\cot\phi-4\phi)-\phi r\sin\phi\right]} \tag{3.117}$$

The final equation of displacement using the two constants will be

$$U_1=\frac{d_{35}\hat{E}_3 h(r\cot\phi-4\phi)}{2\left[\phi\cos\phi(r\cot\phi-4\phi)-\phi r\sin\phi\right]}\sin\gamma x_3+\frac{d_{35}\hat{E}_3 hr}{2\left[\phi\cos\phi(r\cot\phi-4\phi)-\phi r\sin\phi\right]}\cos\gamma x_3 \tag{3.118}$$

when $r\to 0$ $C_2 = 0$, i.e free PWAS case; Eq. (3.118) reduced to free SH-PWAS case:

$$\begin{aligned}U_1&=\frac{d_{35}\hat{E}_3(-4\phi)}{-8\phi\cos\phi}\sin\gamma x_3\\&=\frac{1}{2}\frac{d_{35}\hat{E}_3 h}{\frac{1}{2}\gamma h}\frac{\sin\gamma x_3}{\cos\frac{\gamma h}{2}}=\frac{1}{2}\frac{u_{ISA}}{\phi}\frac{\sin\gamma x_3}{\cos\phi}\end{aligned} \tag{3.119}$$

Checking Eq.(3.119) for bottom surface ,i.e. $r \neq 0$ and $x_3 = -h/2$;

$$U_a = \frac{d_{35}\hat{E}_3 h\left[r\cos\phi - (r\cot\phi - 4\phi)\sin\phi\right]}{2\left[\phi\cos\phi(r\cot\phi - 4\phi) - \phi r\sin\phi\right]} \qquad \frac{2(1-\cos 2\phi)d_{35}\hat{E}_3 h}{2r\cos 2\phi - 4\phi\sin 2\phi} \tag{3.120}$$

For calculating the bonded SH-PWAS impedance and admittance, we substitute U_a from Eq.(3.120) with the same procedure in the electrical displacement Eq. (3.24)

$$D_3 = \frac{d_{35}}{s_{55}^E}\left[(2S_5) - d_{35}\hat{E}_3\right] + \varepsilon_{33}\hat{E}_3 \tag{3.121}$$

$$D_3 = \frac{d_{35}}{s_{55}^E}u_1' - \frac{d_{35}^2}{s_{55}^E}\hat{E}_3 + \varepsilon_{33}\hat{E}_3 \tag{3.122}$$

$$D_3 = \varepsilon_{33}\hat{E}_3\left[1 - K_{35}^2\left(1 - \frac{u_1'}{d_{35}\hat{E}_3}\right)\right] \tag{3.123}$$

Where we define the electromechanical coupling factor K_{35} as

$$K_{35} = \frac{d_{35}^2}{s_{55}^E\varepsilon_{33}} \tag{3.124}$$

Integrating the electrical displacement over electrodes area, results in the electric charge

$$Q(x_3) = \int_A D_3 dx_1 dx_2 = \int_{-\frac{l}{2}}^{+\frac{l}{2}}\int_0^b D_3 dx_1 dx_2 \tag{3.125}$$

Substituting D_3 from Eq.(3.123)

$$Q(x_3) = \varepsilon_{33}\hat{E}_3 bl\left[1 - K_{35}^2\left(1 - \frac{u_1'}{d_{35}\hat{E}_3}\right)\right] \tag{3.126}$$

Then, equivalent charge across thickness can be determined by integrating over thickness

$$\hat{Q}_{eq} = \frac{1}{h}\int_{-\frac{h}{2}}^{\frac{h}{2}} Q(x_3)dx_3 \tag{3.127}$$

Substituting Eq.(3.126) into Eq.(3.127) and integrating over the thickness, yields

$$\hat{Q}_{eq} = \frac{\varepsilon_{33}\hat{E}_3 bl}{h}\left[\left(1-K_{35}^2\right)h + K_{35}^2\frac{\hat{u}_1(x_3)\Big|_{-\frac{h}{2}}^{\frac{h}{2}}}{d_{35}\hat{E}_3}\right] \tag{3.128}$$

Substituting $\hat{u}_1(x_3)$ from Eq.(3.118) , and defining SH-PWAS capacitance $C = \varepsilon_{33}^T\frac{bl}{h}$, the electric field is related to voltage by $\hat{E}_3 = \frac{\hat{V}}{h}$ and recalling u_{ISA} from Eq.(3.21) ; then Eq.(3.128) can be simplified to

$$\hat{Q}_{eq} = C\hat{V}\left[1-K_{35}^2\left(1-\frac{(r\cot\phi-4\phi)\sin\phi}{\phi\cos\phi(r\cot\phi-4\phi)-\phi r\sin\phi}\right)\right] \tag{3.129}$$

The electric current *I* is defined as the time derivative of electric charge, i.e. $I = \dot{Q} = i\omega Q$, hence Eq.(3.129) simplifies to

$$Y = \frac{I}{V} = i\omega C\left[1-K_{35}^2\left(1-\frac{(r\cot\phi-4\phi)\sin\phi}{\phi\cos\phi(r\cot\phi-4\phi)-\phi r\sin\phi}\right)\right] \tag{3.130}$$

And the constrained SH-PWAS electrical impedance is

$$Z = \frac{V}{I} = \frac{1}{i\omega C}\left[1-K_{35}^2\left(1-\frac{(r\cot\phi-4\phi)\sin\phi}{\phi\cos\phi(r\cot\phi-4\phi)-\phi r\sin\phi}\right)\right]^{-1} \tag{3.131}$$

3.3. FINITE ELEMENT MODELING OF SH-PWAS IMPEDANCE RESPONSE

3.3.1. Free SH-PWAS Models

A multiphysics finite element model (FEM) was constructed for free SH-PWAS to compute the shear deformation modeshapes. The transducer is modeled with COMSOL multiphysics using coupled-physics finite element. The maximum element size is selected as 0.5 mm. The coordinate system is defined such that the poling of SH-PWAS is defined along the x_1 direction. Harmonic voltage is applied to the top electrode and the mechanical response is recorded. The free SH-PWAS dimensions are 15 mm x 15mm x 1 mm. The SH-PWAS material is APC850, detailed properties can be found on the APC website (APC International Ltd.). From the provided information, the transducer capacitance $C = \varepsilon_{33}^{S}(bl/h)$ is found as 3.48±20% nF. A frequency sweep from 10 kHz to 2000 kHz is performed with the frequency domain solver of the FEM software. The deformation modeshapes are captures and the electromechanical (E/M) impedance is calculated. **Figure 3.11** shows the modeshapes of vibration at (a) 200 kHz to show the shear deformation of the transducer, (b) first resonance frequency of the transducer at 900 kHz, where nonlinear effects start to appear at SH-PWAS ends.

3.3.2. Constrained SH-PWAS Models

Finite element models were constructed for bonded SH-PWAS on 1-mm thick aluminum beams as well as 3-mm thick steel beams. In both cases, three models are constructed: (i) a 2-D model for the case where poling of the SH-PWAS is along beam length, (ii) a 3-D model for the same case of having poling direction parallel to beam length (**Figure 3.9**a), and (iii) a 3-D model for the case of transducer poling

perpendicular to the beam length (**Figure 3.10**a). E/M impedance is calculated for different models for comparison with bonded SH-PWAS analytical models, and experimental results.

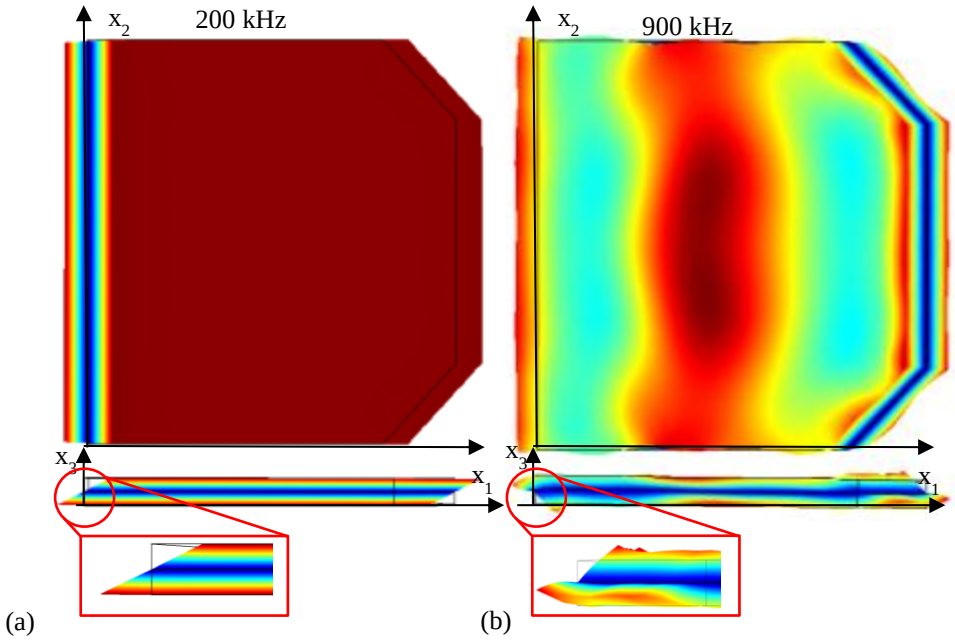

Figure 3.11. Modeshapes of vibrations for free SH-PWAS using finite element analysis, (a) mode shape at 200 kHz, (b) modeshape at resonance frequency 900 kHz

Two beams types are considered. Aluminum beam with 1-mm thickness and steel beam with 3-mm thickness. The rest of the dimensions are the same 100 mm x 10 mm. The complete listing of model dimensions and material properties are listed in Table 3.1. Steel beams configurations are used to enhance structure – to – transducer mass ratio, as will be discussed in the experimental section. **Figure 3.12** shows finite element models for the bonded SH-PWAS on the aluminum beam. SH-PWAS bonded on aluminum beams has the dimensions of 10 mm x 10 mm x 1 mm. We refer to this configuration of the SH-PWAS orientation as (PWAS orientation-1). For PWAS orientation-1, 2-D FEM (**Figure 3.12**a) and 3-D FEM (**Figure 3.12**b) were constructed. PWAS orientation-2

refers to the situation where the SH-PWAS is rotated 90° before bonding on the aluminum beam, hence, the poling direction in **Figure 3.12**b is parallel to beam width. In such a situation, our analytical model suggests the excitation of shear horizontal standing waves along the beam.

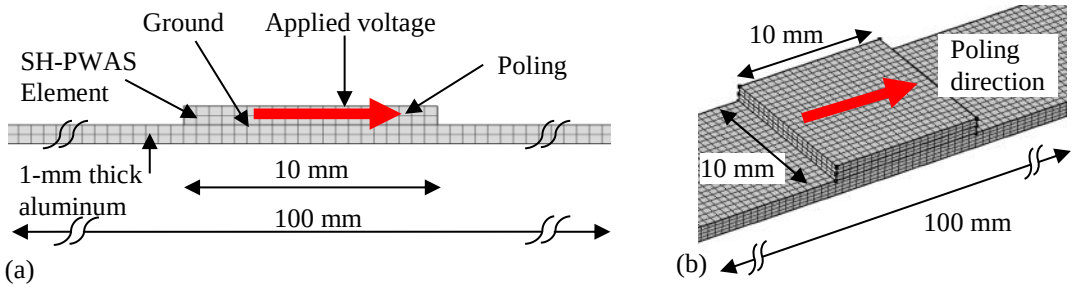

Figure 3.12. FEM for bonded SH-PWAS on 1-mm thick aluminum beams (a) 2-D model, (b) 3-D model

Table 3.1. Dimensions and material properties for FEM of SH-PWAS bonded on aluminum and steel

	Aluminum beam	steel beam	SH-PWAS
Dimensions [mm]	100 x 10 x 1	100 x 15 x 3	10 x 10 x 1 on Al 15 x 15 x 1 on steel
Density ρ [kg/m^3]	2700	7750	7600
Modulus [GPa]	E = 70	E = 200	G = 24.6
Relative dielectric constant $\varepsilon_{33}^T / \varepsilon_0$	-	-	1750
Piezoelectric coeff. d_{35} [m/V]	-	-	590E-12
Hysteresis damping ζ	0.05%	0.5%	-
Compliance damping factor η	-	-	4%
Permittivity damping δ	-	-	4%

The frequency sweep performed in the FEM is from 1kHz to 160 kHz. For 1-mm thick aluminum beams, the mesh size is 0.5 mm for the transducer element, for the 2-D model the transducer was meshed by finer mesh up to 4 elements per the 1-mm thickness.

The 3-D models are meshed with 0.5 mm element size and up to 4 elements per the 1-mm transducer thickness. The 1-mm aluminum beam domain is meshed with similar mesh like the transducer. Modeshapes are recorded and the bonded transducer E/M impedance is calculated. The same was done for 3-mm thick steel beams models.

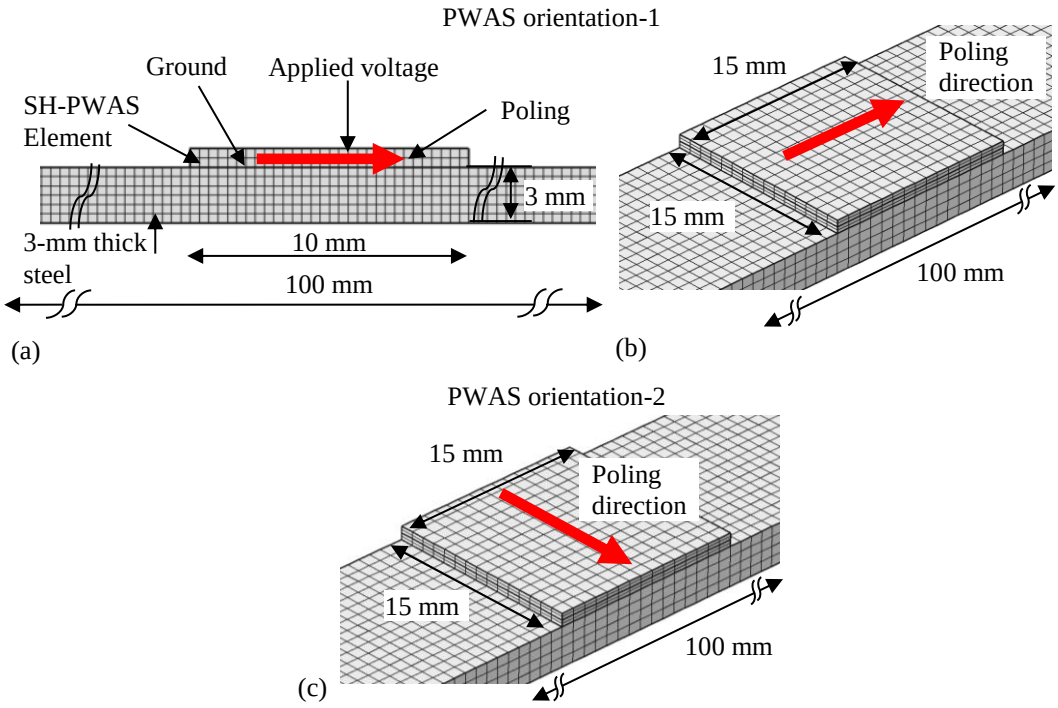

Figure 3.13. FEM for bonded SH-PWAS on 3-mm thick steel beams: SH-PWAS orientation-1: (a) 2-D model, (b) 3-D model. (c) SH-PWAS orientation-2, 3-D model

Steel beams configurations are used to enhance structure – to – transducer mass ratio, as will be discussed in experimental section. **Figure 3.13** shows the two different configurations of SH-PWAS bonded on 3-mm steel beams, 2-D and 3-D models. The frequency sweep performed is 1kHz to 160 kHz. The maximum element size used is 0.5 mm in the 2-D model. For the 3-D models, the transducer is meshed with 1-mm elements and 4-elements per the 1-mm thickness. The steel beam is meshed with 1-mm elements as well and 0.75 mm element size through thickness.

3.4. EXPERIMENTAL SETUP

The free SH-PWAS capacitance was measured experimentally and found to be 2.76±0.05 nF. SH-PWAS transducers E/M impedance is measured using an HP 4194A impedance analyzer. E/M impedance spectroscopy refers to the antiresonances of the free transducer. A sweep of frequency up to 2000 kHz was performed and the impedance spectrum is compared to FEM and analytical model predictions. SH-PWAS transducers are then bonded on multiple aluminum beams in both orientations. And the E/M impedance is measured. The E/M impedance peaks refer to beam structure antiresonances under (a) axial-flexural excitation, (b) shear horizontal excitation (**Figure 3.14**). Because the impedance spectroscopy in the bonded transducer case refers to the beam vibration modes, a frequency sweep is performed up to 160 kHz.

The mass ratio of bonded SH-PWAS to the host aluminum beams is ≈30%. This is because of the considerable higher density of PZT material compared to aluminum density (Table 3.1). This extra mass and stiffness added by the transducer is not considered in our analytical model. Another set of experiments are performed on 3-mm thick steel beams. The beam thickness and steel material was selected such that the transducer – to – beam mass ratio is 4%. The experimental setup for the steel beams case is shown in **Figure 3.15**.

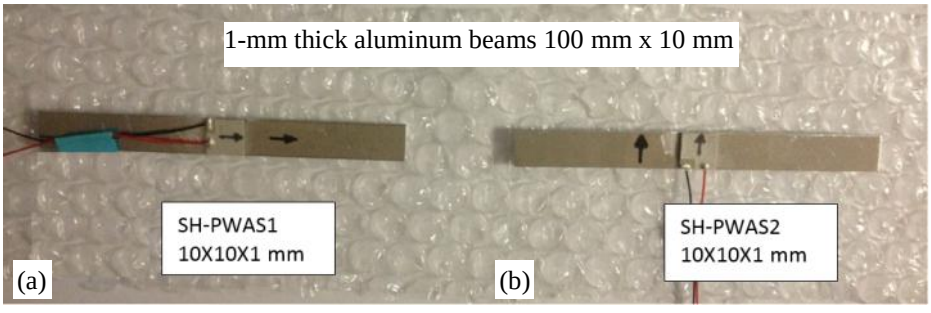

Figure 3.14. Experimental setup for SH-PWAS bonded on 1-mm aluminum beams (a) orientation-1, (b) orientation-2, (the black arrow indicates poling direction)

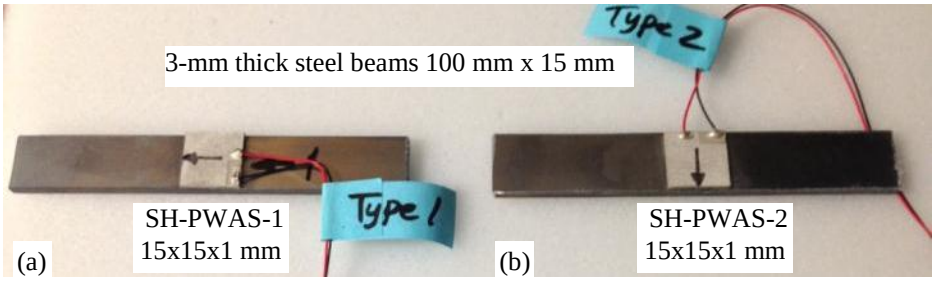

Figure 3.15. Experimental setup for SH-PWAS bonded on 3-mm steel beams (a) orientation-1, (b) orientation-2, (the black arrow indicates poling direction)

3.5. RESULTS AND DISCUSSIONS OF IMPEDANCE SPECTROSCOPY

In this section, comparisons between experimental and simulation results are reported. First, experimental results of E/M impedance for a free SH-PWAS are compared with FEM results and both analytical models (a) with constant electric field assumption, (b) constant electric displacement assumption.

3.5.1. Free SH-PWAS

Figure 3.16 shows that the first impedance peak reported experimentally = 1060 kHz ($\approx$1 MHz). From **Figure 3.16**b, it is shown that the analytical model with constant electric displacement assumption over predicts the first impedance peak (= 1330 kHz analytically). This draws the conclusion that the analytical model with constant electric displacement through the thickness (peak = 1220 kHz analytically) is more appropriate for this transducer modeling. **Figure 3.16**c shows the comparison between admittance predictions and the experimental measurements, indicating first resonance at $\approx$ 900 kHz The IQR shown in **Figure 3.16** corresponds to the interquartile range, a.k.a. the range that ignores the lower 25% and upper 25% spread of our measured data (10 transducers).

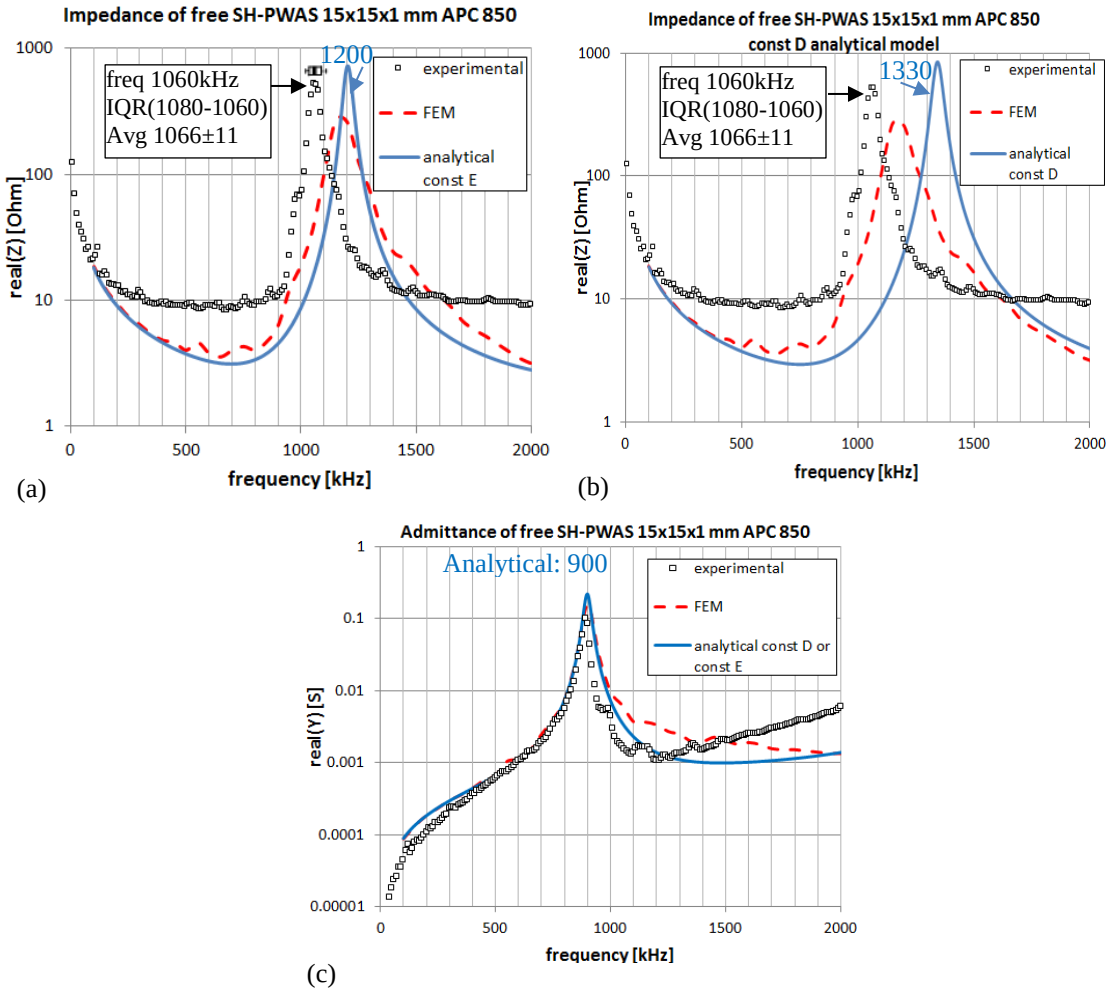

Figure 3.16. Results comparison for the free SH-PWAS (APC 850): (a) impedance, constant *E* analytical model, (b) impedance, constant *D* analytical model, (c) admittance

3.5.2. Bonded SH-PWAS on 3-mm Thick Steel Beams

For the axial-flexural response, comparison between experimental, 3-D finite element simulations, and analytical predictions showed good agreement, as shown in **Figure 3.17**. The first fundamental mode impedance peak is measured experimentally as 49.3±0.6 kHz, which agrees with 3-D and 2-D FEM. The second peak is 97±1.75 kHz, with perfect agreement with FEM, analytical prediction is 100 kHz. The third peak needs some investigation. The experimental measurement is 136±1.8 kHz, which matches with

3-D FEM. However the analytical model (152 kHz) shows more agreement with (2-D FEM $\approx$146 kHz).

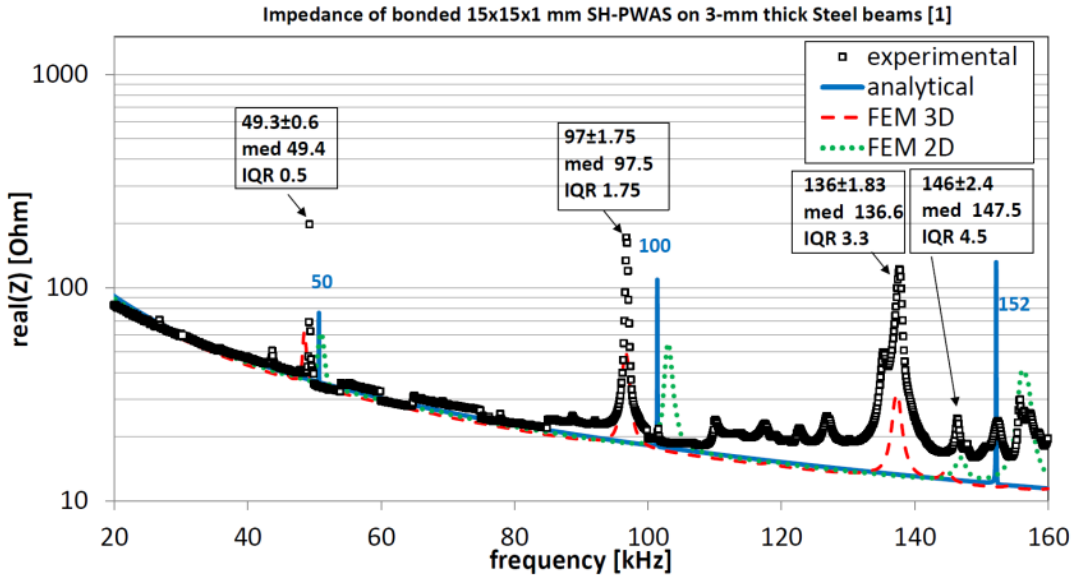

Figure 3.17. Comparison between experimental results, analytical predictions and finite element simulations for E/M impedance of SH-PWAS bonded on 3-mm thick steel beam (orientation-1)

Referring to 3-D FEM modeshapes at these frequencies (**Figure 3.18**), it is noticed that the modeshape of vibration at 137 kHz (which is captured experimentally and by 3-D FEM) involves coupled vibration in the beam length and width. This is not considered in the analytical model, which is a 1-D model (beam length and thickness). The analytical model prediction of 152 kHz is more representative of the mode shown in **Figure 3.18**c (145 kHz by 3-D FEM)

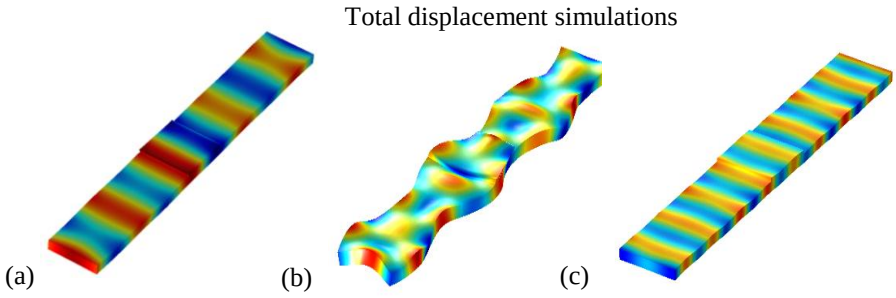

Figure 3.18 Modeshapes of vibrations of 3-mm thick steel beams with bonded SH-PWAS in orientation-1 (axial-flexural orientation), at excitation frequency: (a) 48 kHz, (b) 137 kHz, (c)145 kHz

When the SH-PWAS is installed in orientation-2 to generate SH standing waves across beam length, the predicted 3-D FEM modeshapes show the SH motion patterns (**Figure 3.19**).

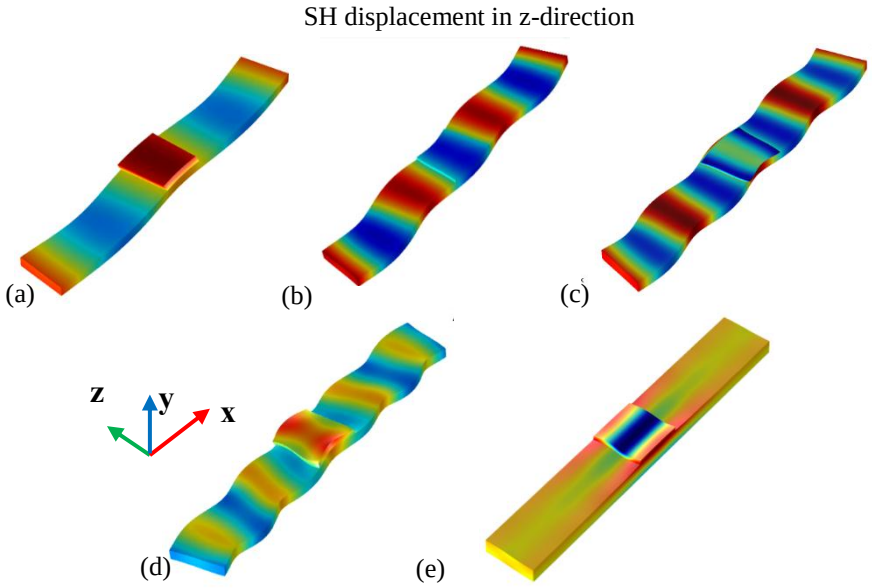

Figure 3.19. Modeshapes of vibrations of 3-mm thick steel beam with bonded SH-PWAS in orientation-2 (SH orientation) at excitation frequency: (a) 30 kHz, (b) 60 kHz, (c)90 kHz, (d)123 kHz, (e)146 kHz

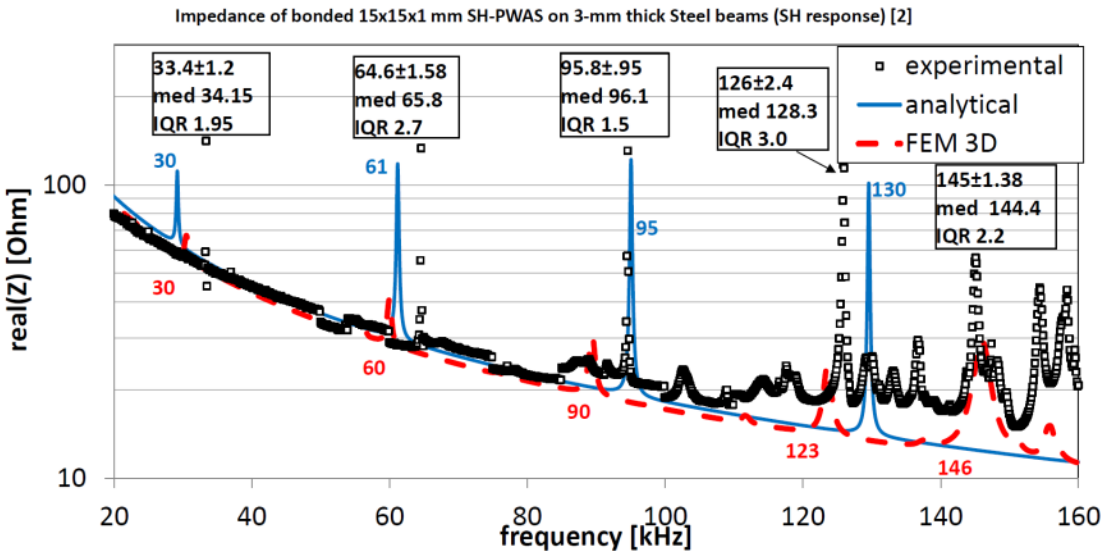

Figure 3.20. Comparison between experimental results, analytical predictions and finite element simulations for E/M impedance of SH-PWAS bonded on 3-mm thick steel beam (orientation-2)

Comparison between experimental results, analytical predictions, and finite element simulations (**Figure 3.20**) shows good agreement for SH-PWAS orientation-2 that generates SH deformation in the structure. It is noticed that the impedance peaks are multiples of ≈ 30 kHz. The third peak of 95 kHz shows the best match between experiments and simulations. Also, the experimental measurement at 145 kHz shows agreement with 3-D FEM, however this peak is not captured by the analytical prediction. Referring to modeshapes (**Figure 3.19**), it is noticed that the 5^{th} mode of vibration is a local mode and it drives the beam into some torsional vibration. The 4^{th} mode starts not to be a uniform SH deformation; it may contain coupled modes of vibration.

3.5.3. Bonded SH-PWAS on 1-mm Thick Aluminum Beams

We compare the E/M impedance measurements of bonded SH-PWAS on 1-mm aluminum beams with 2-D and 3-D finite element simulations. Analytical model predictions are reported, but are not valid, because the analytical model does not account for added mass and stiffness by the transducer.

When the SH-PWAS is bonded in orientation-1, where the excited response is an axial and flexural response, the experimental and 3-D FEM had good agreement with the first three resonant frequencies 42, 90, and 136 kHz. 2-D FEM shows a similar trend but with higher values (**Figure 3.21**). When the SH-PWAS is bonded in a 90° direction, such that the poling direction is perpendicular to the beam length, in this case the shear horizontal (SH) vibrating modes are captured at 22, 47, 77, 107, and 136 kHz (**Figure 3.22**). A good agreement is achieved between experiments and finite element simulations.

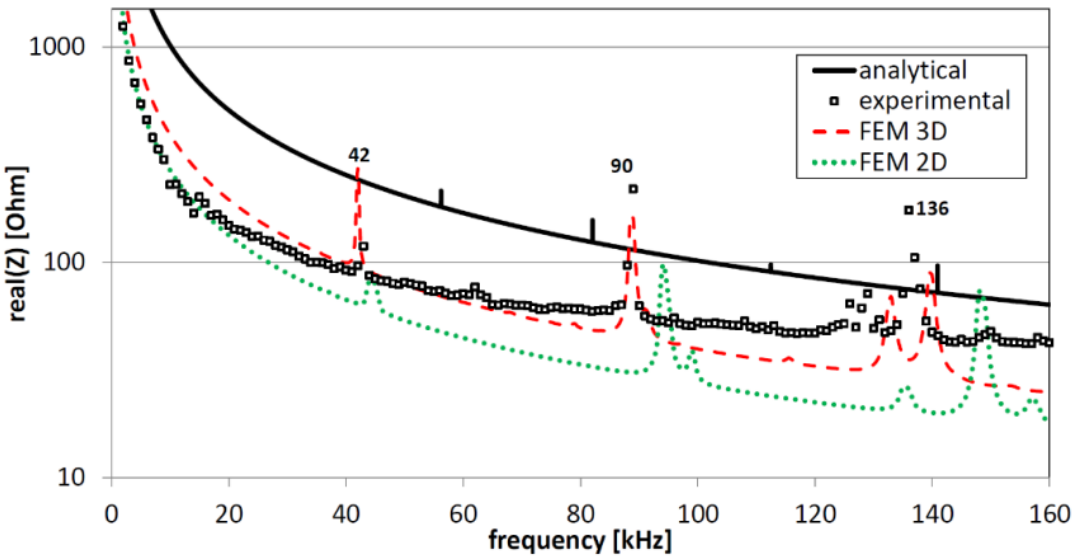

Figure 3.21 Comparison between experimental results and finite element simulations for E/M impedance of SH-PWAS bonded on 1-mm thick aluminum beam (orientation-1)

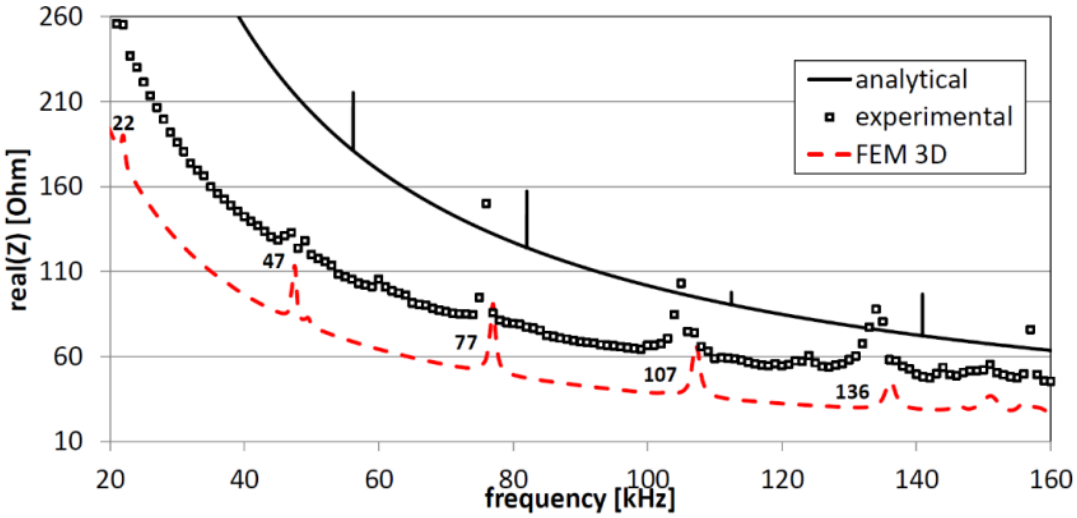

Figure 3.22 Comparison between experimental results and finite element simulations for E/M impedance of SH-PWAS bonded on 1-mm thick aluminum beam (orientation-2)

One observation for both (a) axial-flexural response, and (b) SH response, that the second, third… harmonics are almost multiples of the fundamental vibrating mode.

3.6. GUIDED WAVE EXCITATION BY SH-PWAS

3.6.1. Analytical Model

Consider SH-PWAS bonded to the structure shown in **Figure 3.8**a. The structure half thickness is *d*, and μ is the shear modulus of the structure. SH PWAS dimensions are: length *l*, width *b* and thickness *h*. Shear horizontal waves have a shear–type particle motion contained in the horizontal plane. Cartesian co-ordinates are defined such that the *x*-axis is placed along the wave propagation direction, whereas the *z*-axis is the direction of particle motion, and *y* is along plate thickness. The poling direction of the piezoelectric transducer is in the x_1 direction (coinciding with the global *z*-axis coordinate of the structure). An approximated 1-D analytical model with the z-invariant assumption is well

developed in many previous studies, such as: Auld (1990); Graff (1991); Rose (1999). The analytical model only predicts SH wave motion of particle oscillation along *z* direction and propagating in *x* direction. We use the analytical model to predict dispersion wave speeds of SH waves. The displacement is assumed to be harmonic

$$u_z(x,y,t) = U_z(y)e^{-i(\xi x-\omega t)} \tag{3.132}$$

where ξ is the wave number in *x* direction. Guided SH waves in plates (similar to guided Lamb waves) are multimodal in nature; as the frequency of excitation increases, new modes are excited in the plate. The frequencies at which new modes appear are called cut-off frequencies. The cut-off frequency can be determined by solving the characteristic equation $\sin(\eta^S d)\cos(\eta^A d) = 0$ for ηd values, and substitute in

$$f_{cut-off} = \frac{1}{2\pi}\frac{c_s}{d}(\eta d) \tag{3.133}$$

where η is defined from $\eta^2 = \omega^2/c_s^2 - \xi^2$, and c_s is the shear wave speed. We define cut-off frequency in units of Hz, or normalized frequency. The nth symmetric mode displacement is

$$u_z^n(x,y,t) = B_n \cos(\eta_n^S y)e^{-i\xi_n^S x}e^{i\omega t} \tag{3.134}$$

The nth antisymmetric mode displacement is

$$u_z^n(x,y,t) = A_n \sin(\eta_n^A y)e^{-i\xi_n^A x}e^{i\omega t} \tag{3.135}$$

The total displacement is

$$u_z(x,y,t) = \left[A_n \sin(\eta_n^A y)e^{-i\xi_n^A x} + B_n \cos(\eta_n^S y)e^{-i\xi_n^S x} \right] e^{i\omega t} \tag{3.136}$$

The amplitudes A_n, B_n are normalized with respect to power flow and found to be (Santoni, 2010)

$$B_n = \sqrt{\frac{1}{\omega\mu\xi_S^n d}} \quad , \quad A_n = \sqrt{\frac{1}{\omega\mu\xi_A^n d}} \tag{3.137}$$

Solving the characteristic equation $\sin(\eta^S d)\cos(\eta^A d) = 0$ results in finding wave speeds and group velocities.

Analytical evaluation for shear horizontal wave speeds and group velocities is presented in **Figure 3.23** for a 1-mm thick aluminum plate. Wave speeds are normalized with respect to shear (transverse) wave speed, which equals 3129 m/s for our case study aluminum 2024-T3 alloy. The predicted SH wave modes were three modes in the 4000 kHz frequency window (corresponds to $fd/c_s = 0.64$). The first SH mode is SH0, it is a symmetric mode of vibration and has a constant propagation speed at any excitation frequency. The second SH mode is SH1, it is an antisymmetric mode with cut-off frequency ≈ 0.25 $(= 1565$ kHz$)$. The third mode in our simulation results is SH3, it is symmetric like SH0, however it is dispersive, i.e. does not have a constant propagation speed. The cut-off frequency of SH3 is ≈ 0.5 $(= 3130$ kHz$)$.

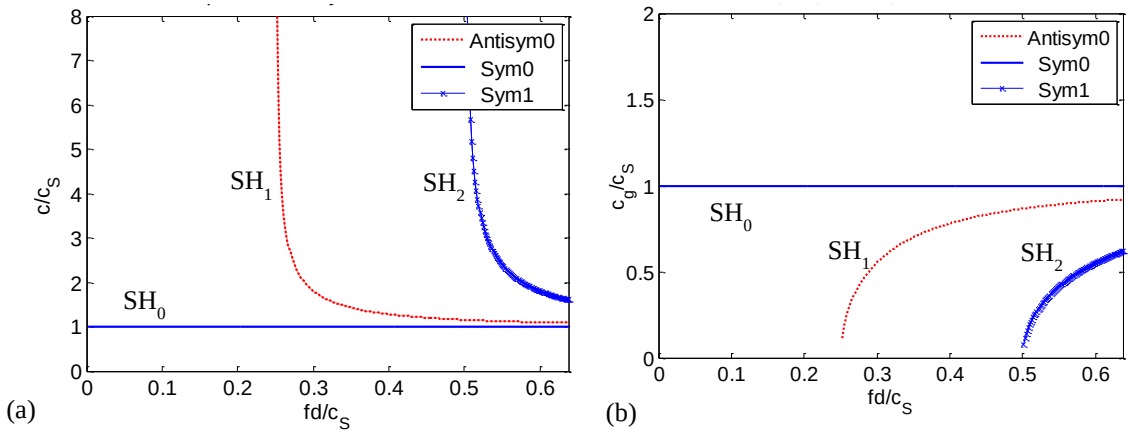

Figure 3.23. Shear horizontal wave speeds for aluminum (a) phase velocities, (b) group velocities

3.6.2. Experimental Studies

3.6.2.1. Proof of concept

Three sets of experiments are performed; the first set of experiments was a proof of concept that was performed on 3.4-mm thick aluminum 7075 T6 alloy plate (**Figure 3.24**). The SH-PWAS was 15 mm x 15 mm x 1 mm and its material was APC850. SH-PWAS poling direction was along z-direction (**Figure 3.24**c). The distance between the two SH-PWAS was 150 mm, the excitation was 3-count tone burst signal with 10 V amplitude. The excitation frequencies used were 30, 45, 60, 75, and 90 kHz as shown in the waveforms (**Figure 3.25**). It was noticed that the received signals in **Figure 3.25** were non-dispersive, (i.e. they have shown the same shape as excitation signal, ≈ 3 count tone burst), especially at frequencies 60, 75 and 90 kHz. This implies that the wave packet speed does not change with frequency and this is the intrinsic property of SH0 (the first shear horizontal guided wave in isotropic materials). In addition, it was observed that no waves propagate along (path 2) in **Figure 3.24**c. The actuation mechanism of SH-PWAS, that is shown from free transducer mode shapes (**Figure 3.11**) implies that the SH-PWAS resonates in *z*-direction and the generated waves propagate along *x*-direction. The comparison between analytical and experimental results is shown in **Figure 3.26**.

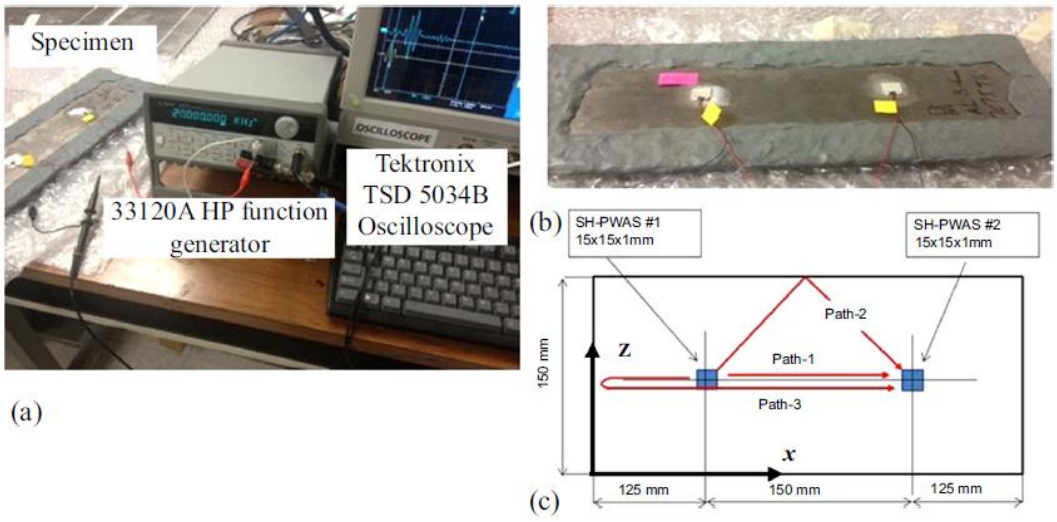

Figure 3.24 Pitch catch experiment to excite SH waves and catch it with another SH-PWAS

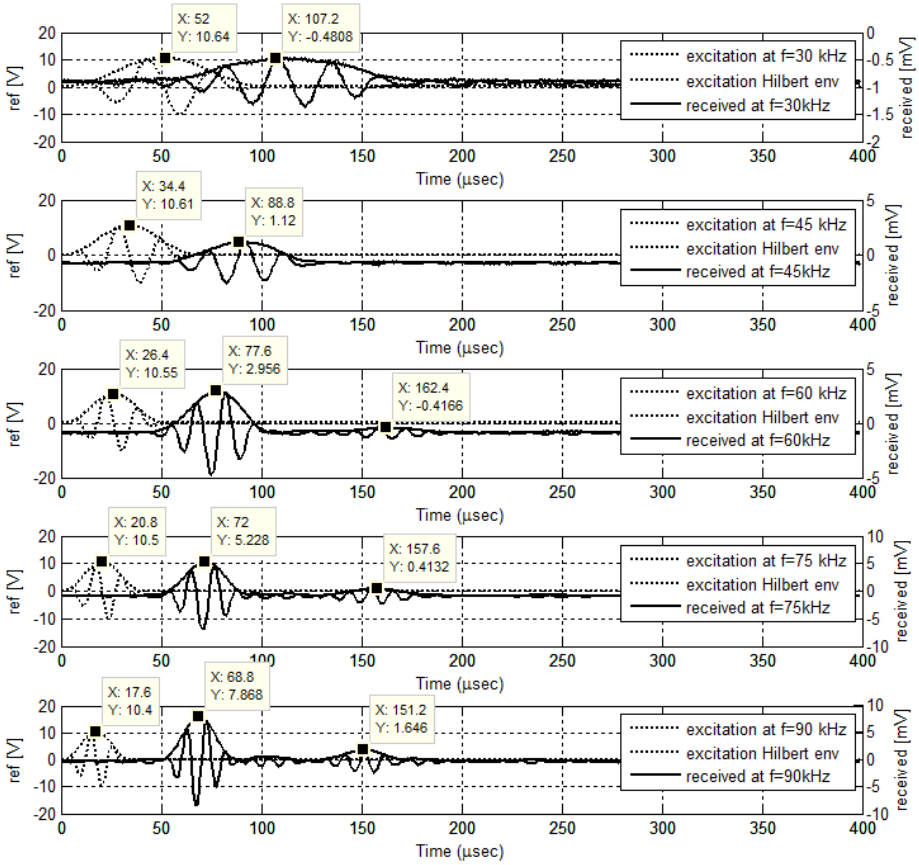

Figure 3.25. Waveforms associated with pitch catch SH waves experiment on 3.4-mm thick aluminum

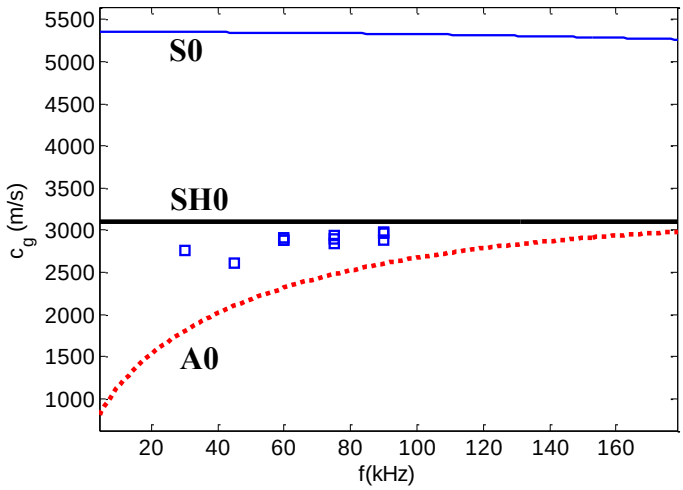

Figure 3.26. Experimental vs. analytical wave group velocity curves (SH-PWAS experiment on 3.4-mm thick aluminum plate)

3.6.2.2. Pitch catch experiments between combinations of SH-PWAS and inplane PWAS transducers

The second set of experiments were a rigorous combination of pitch catch experiments between (a) SH-PWAS transducers with different orientations (to study effect of poling direction), and (b) pitch catch experiments between SH-PWAS transducers and regular PWAS. The SH-PWAS materials was APC850 and dimensions were 15 mm x 15 mm x 1mm. The regular PWAS material was APC850 and a circular PWAS of diameter 15 mm and 0.2 mm thickness was used. A detailed set up is shown in **Figure 3.27**b. The aim behind those combinations of experiments was to have a better understanding of the following cases:

1. Does the SH-PWAS transmit only SH waves to another SH-PWAS?
2. Can regular PWAS receive SH waves transmitted by SH-PWAS?

3. How does SH-PWAS behave when excited by waves coming from regular PWAS? (The opposite situation of question-2)

4. How does SH-PWAS behave if oriented 90 degrees? Does it transmit SH waves in this case? Does it receive SH waves?

Seven experiments were performed on a 1-mm thick aluminum 2024-T3 square plate 1220x1220 mm with a frequency sweep up to 300 kHz. **Table 3.2** summarizes the experiments and captured waves in each case.

The experiment between two SH-PWAS transducers showed the generation of shear horizontal waves, providing that both transducers are installed such that their polarization vectors are parallel to each other (experiment #1), (**Figure 3.28**a).
However, for two SH-PWAS transducers installed such that their polarization directions are perpendicular to each other, the signals that SH-PWAS4 received from SH-PWAS6 had the speeds of S0 the first symmetric Lamb wave modes, (experiment #4). (**Figure 3.28**c)

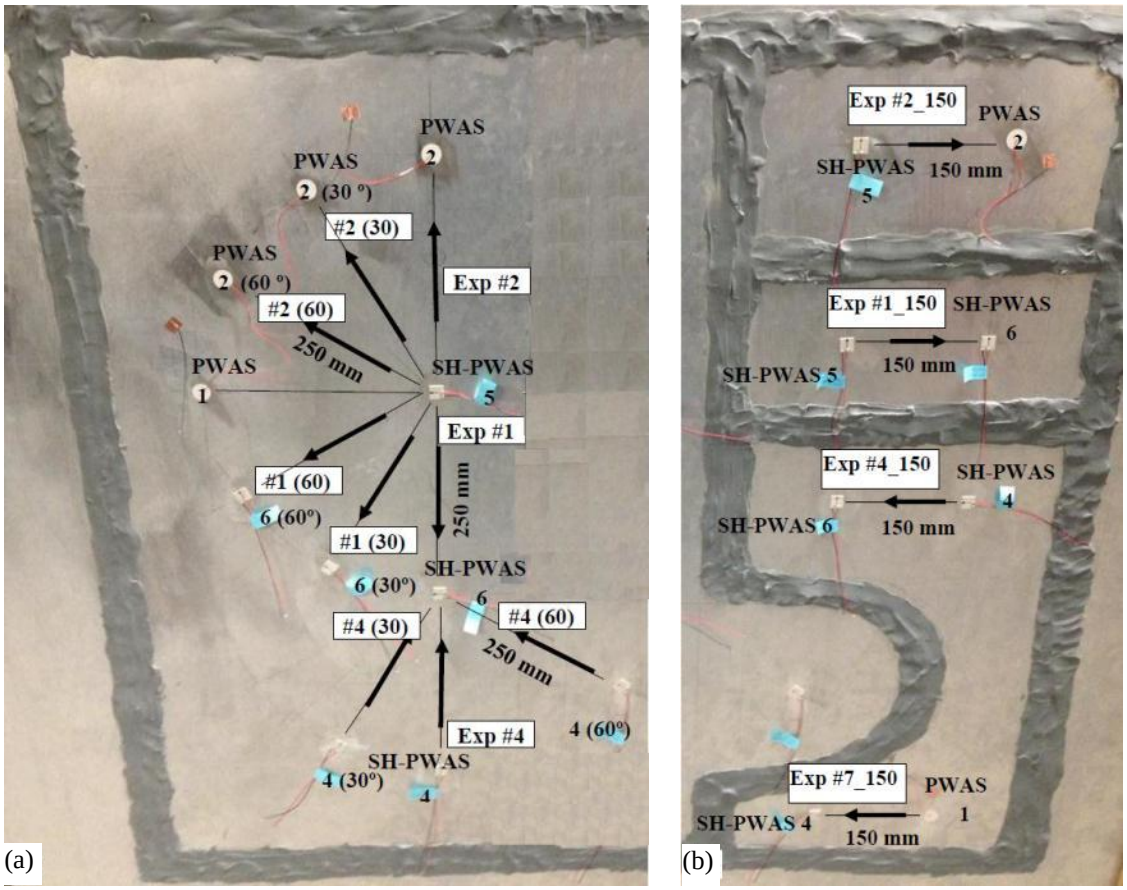

Figure 3.27. Numbering and directions of pitch catch experiments on aluminum plate, (a) directivity experiment, (b) separated experiments for combination of SH-PWAS-regular PWAS pitch catch configurations.

Table 3.2. Description of experiments showing excitation and receiver PWAS transducers for each experiment and the possible paths of wave propagation

Experiment No. and description of pitch catch configuration	Captured waves
Experiment (#1) SH5 ➔ SH6	SH0, A0
Experiment (#2) SH5 ➔PWAS2	SH0, A0
Experiment (#3) PWAS2 ➔ SH5	SH0, A0
Experiment (#4) SH4 ➔ SH6	S0
Experiment (#6) SH6 ➔ SH4	S0
Experiment (#7) PWAS1 ➔ SH4	A0, S0

Experiment #6 (the reverse situation of experiment #4), showed identical results to experiment #4. This was done to verify reciprocity and lack of nonlinear effects. The exciter SH-PWAS6 was oriented in the correct direction to send SH waves towards the receiver SH-PWAS4. SH-PWAS4 was the one oriented with 90°. In such a situation we expected that transmitter SH-PWAS6 was sending out SH waves; however, receiver SH-PWAS4 neither responded nor picked SH waves; but rather picked S0 waves (**Figure 3.28**c). This suggests that the transmitter excites an S0 wave in the measured direction. This observation is further explained in the discussion section of guided wave propagation results.

Another feature was observed, when SH-PWAS5 excites SH waves, the regular extensional mode PWAS2 picked up two types of guided waves: Lamb wave antisymmetric A0 mode, as well as SH0 wave (experiment #2) (**Figure 3.28**b). It was not expected that inplane type PWAS transducers resonate in shear mode and convert shear-mode waves to output voltage. This observation is further discussed in the discussion of guided wave propagation results section.

Finally, regular PWAS2 was excited and the signal was caught by SH-PWAS5 (experiment #3). Similarly, PWAS2 was excited and the signal was caught by SH-PWAS4 (experiment #7).

Experiment #3 was identical to experiment #2, where the SH-PWAS5 picked up SH waves (exactly like **Figure 3.28**b). In experiment #7, where PWAS2 was excited and the signal was caught by SH-PWAS4, the received waveforms were corresponding to guided Lamb waves only (**Figure 3.28**d).

3.6.2.3. Directivity of SH-PWAS

The third set of experiments involves a similar setup of set #2, but with added transducers at 30º and 60º degree angles. The complete setup is shown in **Figure 3.27**a. Experiment #1 (SH-PWAS5→SH-PWAS6) indicates the zero angle direction pitch catch, experiment #1(30) indicates the 30º pitch catch, and experiment #1(60) indicates the 60º pitch catch.

Receiver SH-PWAS6 transducers in experiment #1(30) and (60) no longer have a parallel poling direction to transmitter SH-PWAS5.

Similarly, experiments #2 and #4 are performed at different angles, 0º, 30º, and 60º. **Figure 3.29** shows the directivity patterns for received wave amplitudes at different experiments.

Figure 3.29a shows SH wave amplitudes for a pitch catch experiment between two SH-PWAS transducers. Starting from parallel poling directions (at 0º), the SH wave amplitude is the maximum (e.g. at 60 kHz). At 30º, the SH wave amplitude decreases, and then it further decreases at 60º. This is not observed with all the frequencies. On the other hand, A0 wave amplitudes received at SH-PWAS for the same experiment show an increase in amplitude as the angle increases from 0º to 30º to 60º. This agrees with the previous results of exciting axial-flexural response along the poling direction. As the angle of the pitch catch experiment changes towards 60º, a stronger A0 mode is obtained.

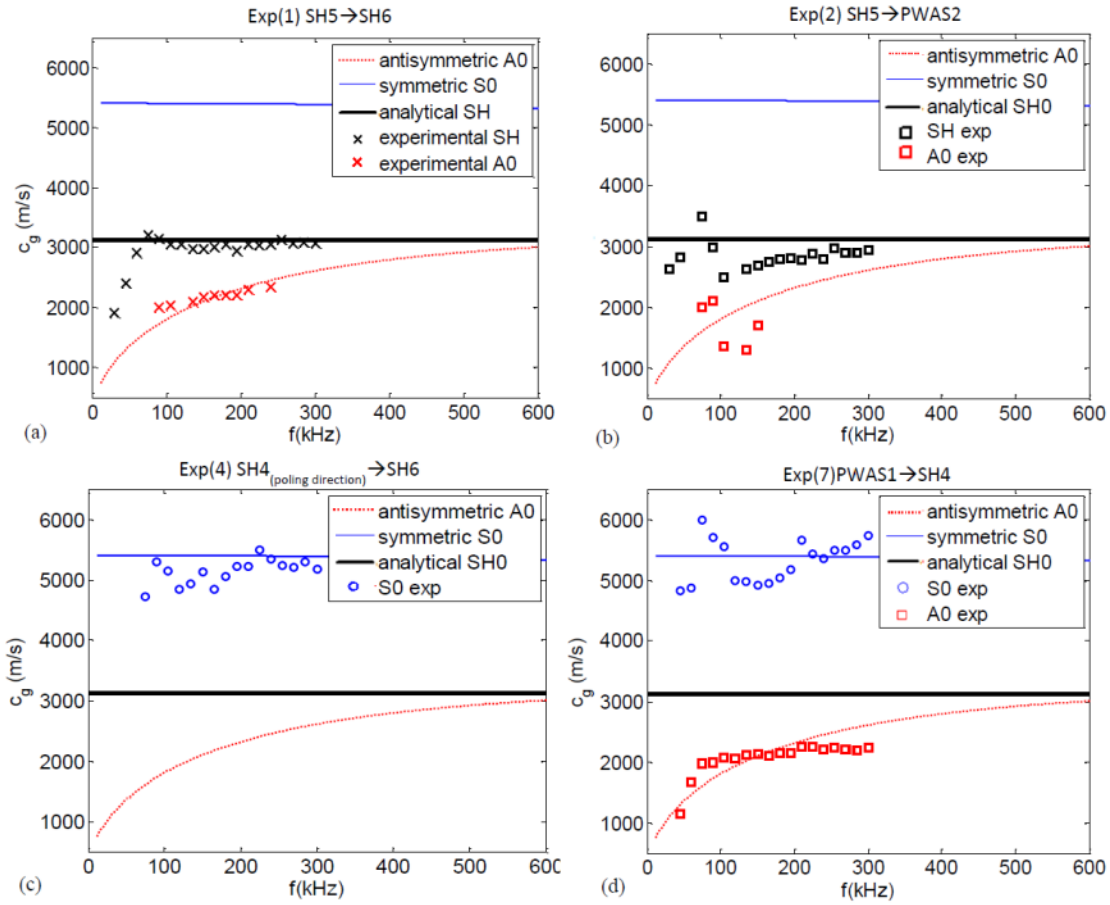

Figure 3.28. Dispersion group velocity curves for received wave signals (SH-PWAS experiment on aluminum)

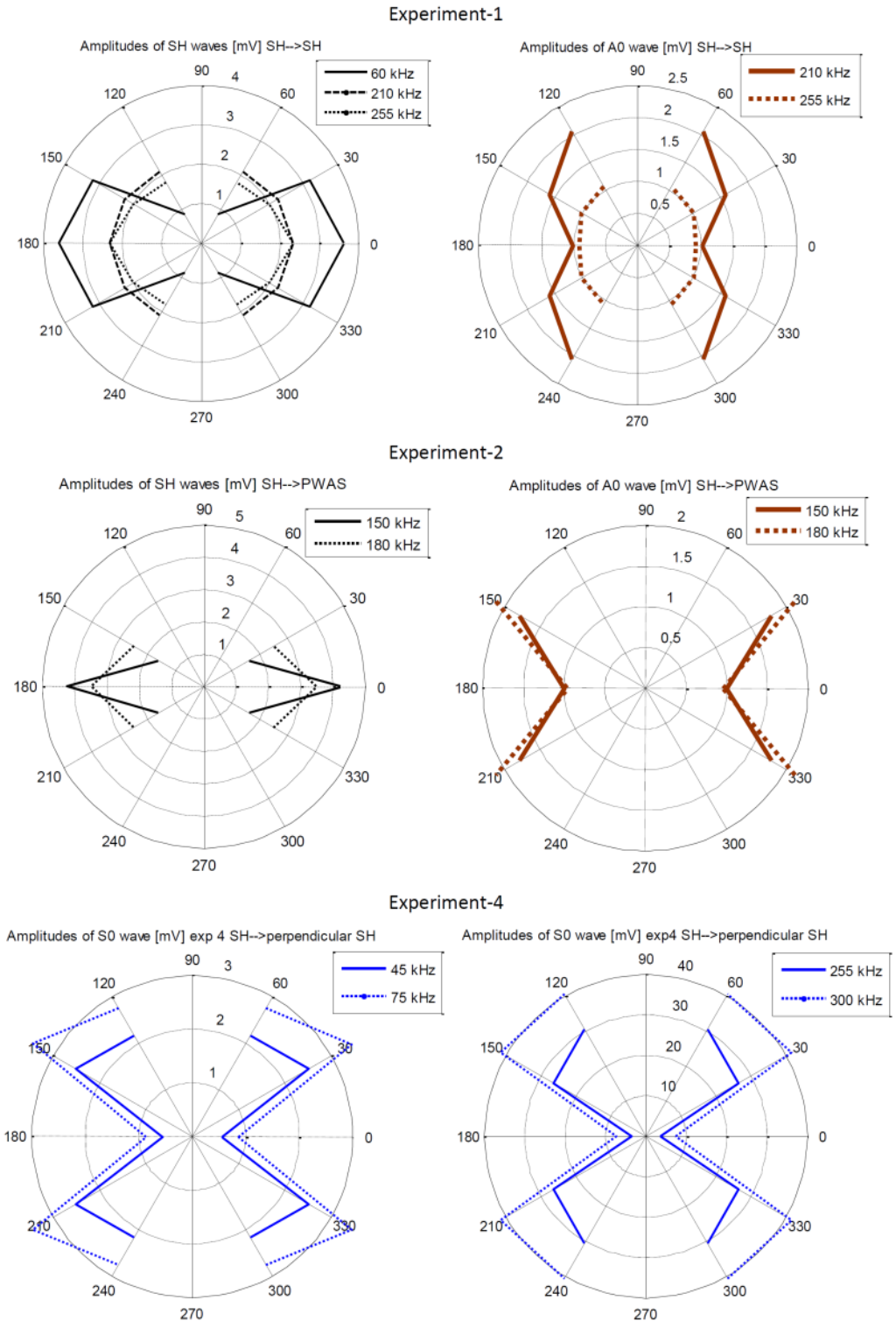

Figure 3.29 Amplitudes of different waves at different angles of pitch-catch experiments, associated with directivity experiment

Experiment #2 (SH-PWAS5→ regular PWAS2) showed similar patterns to experiment #1. However, the received signals at 60º were noisy. **Figure 3.29**c shows amplitudes of SH waves received by PWAS2 and generated by SH-PWAS5, for experiment #2, 2(30), and 2(60). **Figure 3.29**d shows amplitudes of received A0 waves. Experiments #3 are the opposites of experiments #2. Those are not performed in this study.

Experiment #4 (SH-PWAS4 →SH-PWAS6) involves the pitch catch experiments between two SH-PWAS transducers having poling directions perpendicular to each other (for 0º case). **Figure 3.29**e,f are for the same received S0 wave amplitudes, but at different frequencies. They are plotted on two polar plots, because of considerable change in amplitude values in [mV] between 45,75 kHz and 255,300 kHz. It is observed that the S0 amplitudes are much less at lower frequencies. Also, it is observed that the perpendicular poling directions – experiment #4(0) – cause the least S0 wave amplitudes. S0 wave amplitudes are much higher at 30º and 60º angles between poling directions of the two transducers.

3.6.3. Finite Element Simulations

The models in section 2.3 predict SH-PWAS effects at 0º and 90º separately. Also, it is hard to combine (axial-flexural) and (shear horizontal) separate responses of **Figure 3.9**b into 2-D analytical model. Hence 2-D multiphysics FEM simulations are constructed to better understand the possible excited waves by SH-PWAS, and to verify directivity experiments. Shear horizontal SH0, symmetric S0 and antisymmetric A0 Lamb waves were picked by FEM simulations.

Finite element model was constructed for the bonded SH-PWAS to the structure. The SH-PWAS dimensions were 15 mm x 15 mm x 1 mm while inplane PWAS dimensions were 7 mm x 7 mm x 0.2 mm. The mesh size of SH-PWAS elements was 0.5 mm, and 4 elements per the 1-mm thickness. A 1-mm aluminum 2024 alloy plate was used in our simulations. The plate was a 450 mm square plate. The structure maximum element size was set to 4 mm and 2 elements through the 1-mm thick aluminum plate. The plate was modelled with free BC and the SH-PWAS was perfectly bonded from the bottom surface and free from the upper surface.

Excitation signal was 3-count tone burst with canter frequency 60 kHz and voltage amplitude of 10V. The time step selected was 0.5 μs and simulation time was 200 μs. **Figure 3.30** shows the results of the simulations.

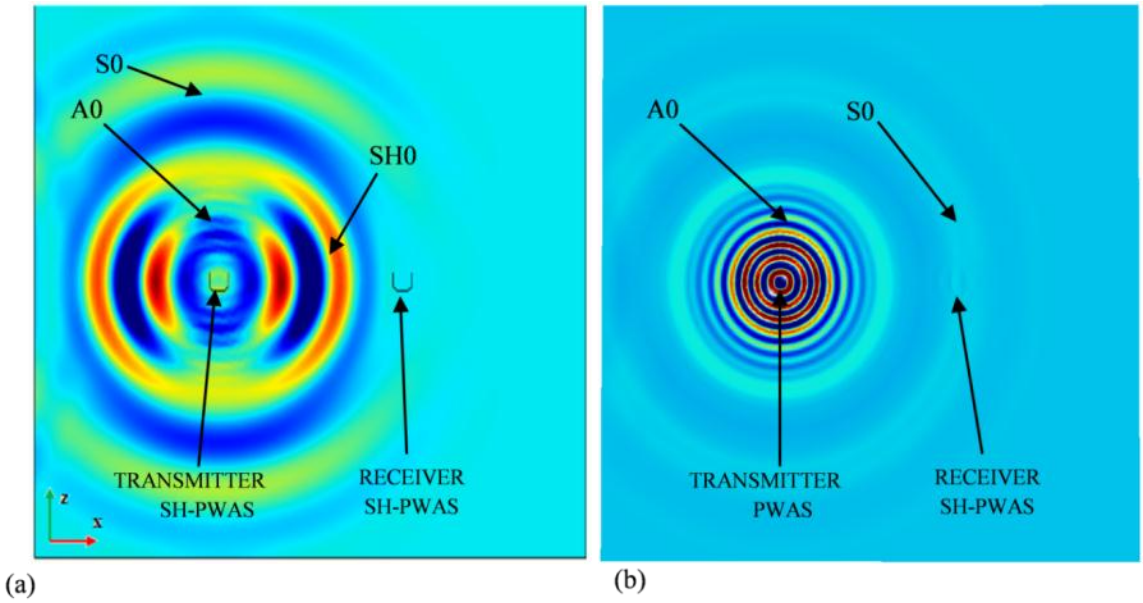

Figure 3.30. FEM simulations for waves excited at 60 kHz by (a) SH-PWAS, (b) inplane PWAS. Variable plotted in (a) is *z* displacement, variable plotted in (b) is *y* displacement

Figure 3.30a shows the displacement field in the z-direction, i.e. the direction of shear horizontal particle oscillation. SH0 waves had a strong oscillation in the *z*-direction, and propagated in the *x*-direction between the transmitter and receiver SH PWAS transducers. Antisymmetric A0 and symmetric S0 modes were observed propagating in z-direction. For comparison, the waves excited by inplane PWAS (**Figure 3.30**b) are reported, only A0 and S0 existed. The simulations in **Figure 3.30** are both captured at simulation time equals $77\,\mu s$. The displayed parameter in **Figure 3.30**b is *eZ* the out of plane strain; it was selected instead of the displacement fields to be able to show S0 and A0 modes together.

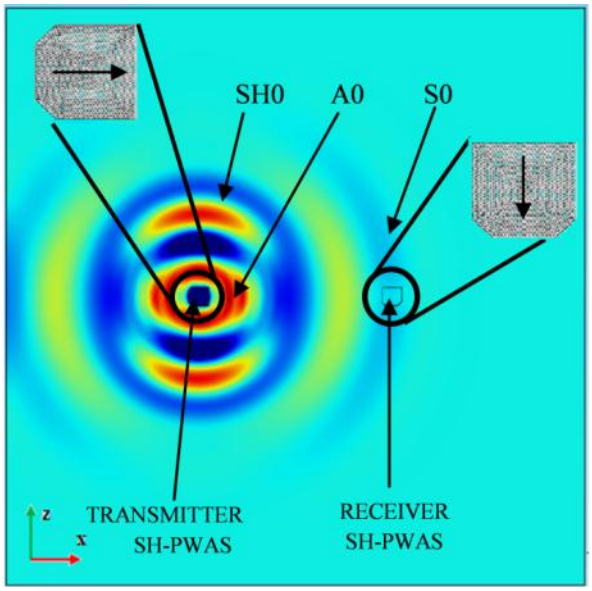

Figure 3.31. FEM simulation for the case of 90 degree orientation difference between two SH-PWAS

When FEM simulation was repeated between the two SH-PWAS transducers, but with the transmitter SH-PWAS oriented by 90 degrees (**Figure 3.31**), the waves propagated towards the receiver SH-PWAS were S0 and a noisy A0. This was in good

agreement with the observed results from experiment #4 (**Figure 3.27**b and **Figure 3.28**c).

Figure 3.31 shows the displacement fields in *x*-direction at $40\,\mu s$. Particle motion in the *x*-direction was selected; because for such configuration, SH waves had a particle oscillation in the *x*-direction and propagated in the *z*-direction. Besides, S0 Lamb wave was propagating in the *x*-direction – with dominant particle motion in the *x*-direction.

3.6.4. Discussion of Guided Wave Propagation Results

The FEM simulations of SH wave propagation between two SH-PWAS transducers (**Figure 3.30**a) validate the transducer actuation mechanism of exciting SH waves in the direction perpendicular to the poling direction. SH wave amplitude decreases as the direction of measured response changes from 0º towards 90º. This agrees with **Figure 3.29**a at excitation frequency 60 kHz. Recalling experiment #6 in the pitch catch experiments, i.e. the opposite of experiment #4 (**Figure 3.27**b). The receiving of the S0 waves seem to contradict with the results of **Figure 3.28**a, where SH0 and A0 were only captured along the direction perpendicular to the poling direction of transmitter SH-PWAS. Referring to **Figure 3.30**a, a very weak S0 mode appears along 45 degrees from the *x*-direction (almost vanishes along the *x*-direction). Hence, one can conclude that the SH-PWAS actually excites S0 waves in the same direction of exciting SH waves, and this is due to 2-D effects and the fact that structure particle vibrations at one side of the transducer definitely affect vibrating particles at the other sides. The considerably reduced S0 wave amplitudes are proven from **Figure 3.29**e,f along the 0º direction.

The feature observed in experiment #2 in section 3.6.2.2 was that the regular inplane PWAS was able to pick up SH waves. This means that it resonates in its extensional-contraction mechanism when shear wave front hits the transducer. Two dimensional effects can be the reason; that is, SH waves excited by SH-PWAS (with structure particles vibrations in the *z*-direction) arrive at regular PWAS with the *z*-direction vibrations, and due to 2-D effects, *z*-direction oscillations are actually considered extension-contraction oscillations (if viewed from another diameter of the receiver PWAS). In addition to the 2-D effects, SH waves can be mode converted at the receiver PWAS; because the transducer itself is considered an inhomogeneity in the wave field. A similar observation in Su et al. (2007) suggested that S0 wave mode converts to SH0. SH0 can be mode converted (at the time of flight of receiving SH0) to a mode that a regular PWAS interacts with.

3.7. POWER AND ENERGY TRANSDUCTION WITH SH-PWAS

The study of power and energy transduction between the PWAS and structure has been presented in chapter-2 where we studied exact guided Lamb waves power and energy. Energy transfers from electrical to mechanical in the transducer, then the mechanical energy causes the wave to propagate. This study presents an analytical model for SH waves power and energy based on the normal mode expansion (NME) technique. The solution assumes straight crested harmonic waves and no evanescent (i.e. non propagating) waves exist. Mode amplitudes are normalized with respect to power flow; and the actual amplitudes can be determined from Eq. (3.137).

Considering that only SH waves are propagating; the surviving strains are

$$S_{yz} = \frac{\partial u_z}{\partial y} \quad , \quad S_{xz} = \frac{\partial u_z}{\partial x} \tag{3.138}$$

Strains and stresses can be evaluated given the total displacement, Eq. (3.136); however, as we will show in the next page the symmetric and the antisymmetric displacements can be in separate solutions; because the orthogonality condition cancels the terms involving multiplications between cosine and sine terms from symmetric and antisymmetric modes. Hence, we can proceed with separate analysis. This can be useful to separate wave energy and power and quantify the partition of symmetric modes as well as the antisymmetric ones. Following the method presented in Santoni (2010) , modal participation factors are found to be

$$a_n^+(x) = \begin{cases} \dfrac{\tilde{v}_z^n(d)}{4P_{nn}} e^{-i\xi_n x} \displaystyle\int_{-b/2}^{b/2} e^{i\xi_n \bar{x}} t_z(\bar{x}) d\bar{x} & \text{for } \frac{b}{2} < x \\ \dfrac{\tilde{v}_z^n(d)}{4P_{nn}} e^{-i\xi_n x} \displaystyle\int_{-b/2}^{x} e^{i\xi_n \bar{x}} t_z(\bar{x}) d\bar{x} & \text{for } -\frac{b}{2} \le x \le \frac{b}{2} \\ 0 & \text{for } x < -\frac{b}{2} \end{cases} \tag{3.139}$$

Noting that this is valid for forward propagating mode only, *b* is the width of SH-PWAS and it is the transducer dimension along *x* direction in our study, *d* is half the plate thickness, P_{nn} is power flow factor $\tilde{v}_z^n(.)$ is the conjugate of velocity field in *z* direction for the mode n, t_z is the PWAS traction or shear stress. We denote $a_n^+(x)$ by a + sign to show that it is for the forward propagating mode. Modal participation factor is an extra term to be multiplied by the wave amplitudes. It is a function of the distance *x* and also accounts for the transducer dimension *b*. We define a_n^S the modal participation factor for

the n[th] symmetric mode, similarly a_n^A for the n[th] antisymmetric mode. Eqs.(3.136), (3.139) yield the strains and stresses as

$$\begin{cases} S_{yz} = \left[A_n \eta_n^A \cos \eta_n^A y e^{-i\xi_n^A x} - B_n \eta_n^S \sin \eta_n^S y e^{-i\xi_n^S x} \right] e^{i\omega t} \\ S_{xz} = -i \left[A_n \xi_n^A \sin \eta_n^A y e^{-i\xi_n^A x} + B_n \xi_n^S \cos \eta_n^S y e^{-i\xi_n^S x} \right] e^{i\omega t} \\ T_{yz} = \mu \left[A_n \eta_n^A \cos \eta_n^A y e^{-i\xi_n^A x} - B_n \eta_n^S \sin \eta_n^S y e^{-i\xi_n^S x} \right] e^{i\omega t} \\ T_{xz} = -i\mu \left[A_n \xi_n^A \sin \eta_n^A y e^{-i\xi_n^A x} + B_n \xi_n^S \cos \eta_n^S y e^{-i\xi_n^S x} \right] e^{i\omega t} \end{cases} \tag{3.140}$$

The total strain response (due to symmetric and antisymmetric waves) and the conjugate values of the strain are

$$\begin{aligned} S_{xz} &= a_n^A (-i) A_n \left(\xi_n^A \sin \eta_n^A y \right) e^{-i(\xi_n^A x - \omega t)} + a_n^S (-i) B_n \left(\xi_n^S \cos \eta_n^S y \right) e^{-i(\xi_n^S x - \omega t)} \\ \tilde{S}_{xz} &= a_n^A (i) A_n \left(\xi_n^A \sin \eta_n^A y \right) e^{i(\xi_n^A x - \omega t)} + a_n^S (i) B_n \left(\xi_n^S \cos \eta_n^S y \right) e^{i(\xi_n^S x - \omega t)} \\ S_{yz} &= a_n^A A_n \left(\eta_n^A \cos \eta_n^A y \right) e^{-i(\xi_n^A x - \omega t)} - a_n^S B_n \left(\eta_n^S \sin \eta_n^S y \right) e^{-i(\xi_n^S x - \omega t)} \\ \tilde{S}_{yz} &= a_n^A A_n \left(\eta_n^A \cos \eta_n^A y \right) e^{i(\xi_n^A x - \omega t)} - a_n^S B_n \left(\eta_n^S \sin \eta_n^S y \right) e^{i(\xi_n^S x - \omega t)} \end{aligned} \tag{3.141}$$

It needs to be mentioned that strain quantities in Eq. (3.141) are summation for one single symmetric mode and one single antisymmetric mode, taking into account the modal participation factors.

From the total displacement equation, Eq. (3.136), we obtain the velocity and the conjugate velocity as

$$\begin{aligned} v_z &= a_n^A (i\omega) A_n \left(\sin \eta_n^A y \right) e^{-i(\xi_n^A x - \omega t)} + a_n^S (i\omega) B_n \left(\cos \eta_n^S y \right) e^{-i(\xi_n^S x - \omega t)} \\ \tilde{v}_z &= a_n^A (-i\omega) A_n \left(\sin \eta_n^A y \right) e^{i(\xi_n^A x - \omega t)} + a_n^S (-i\omega) B_n \left(\cos \eta_n^S y \right) e^{i(\xi_n^S x - \omega t)} \end{aligned} \tag{3.142}$$

The time averaged power is

$$\langle p \rangle = -\frac{1}{2} \int_A \left(\bar{T}_{xz} v_z \right) dA = -\frac{b}{2} \int_{-d}^{d} \mu \left\{ \bar{S}_{xz} . v_z \right\} dy \tag{3.143}$$

Substituting Eqs. (3.141), (3.142) in Eq. (3.143) and simplifying yields the time averaged power as,

$$\langle p \rangle = -\frac{b}{2}\int_{-d}^{d} \mu \left\{ \bar{S}_{xz}.v_z \right\} dy$$

$$= -\frac{b}{2}\begin{bmatrix} [a_n^S B_n]^2(-\mu\omega\xi_n^S)\int_{-d}^{d}\left\{\cos^2 \eta_n^S y\right\}dy \\ [a_n^A A_n]^2(-\mu\omega\xi_n^A)\int_{-d}^{d}\left\{\sin^2 \eta_n^A y\right\}dy \end{bmatrix} = -\frac{b}{2}\begin{bmatrix} [a_n^S B_n]^2(-\mu\omega\xi_n^S)\left\{\left(\frac{\sin 2\eta_n^S d}{2\eta_{Sn}} + d\right)\right\} \\ [a_n^A A_n]^2(-\mu\omega\xi_n^A)\left\{\left(d - \frac{\sin 2\eta_n^A d}{2\eta_{An}}\right)\right\} \end{bmatrix}$$

(3.144)

First: terms with multiplied sine and cosine functions from the symmetric mode and the antisymmetric mode are cancelled; for the characteristic equations of the symmetric and the antisymmetric modes, either *sine* or *cosine* terms will be zero at a time. Hence, there is no dependency between symmetric and antisymmetric modes. Second: terms with $\sin(2\eta_n d)$ appearing with the analysis of single type of waves are also crossed out because $\sin(2\eta_n d) = 2\sin(\eta_n d)\cos(\eta_n d)$ and for our characteristic equations for symmetric and antisymmetric, either *sine* or *cosine* terms will be zero at a time. The final result for wave power takes the from

$$\langle p \rangle = \frac{\mu\omega}{2} bd\left[\sum_n [a_n^S B_n]^2 \xi_n^S + \sum_n [a_n^A A_n]^2 \xi_n^A\right] \tag{3.145}$$

The time-averaged power varies at different *x* values, as the *x* dependency comes from the modal participation factors. All the following numerical illustrations are shown at the top surface of the structure (*y=d*) and at the edge of the transducer, where (*x=b/2*).

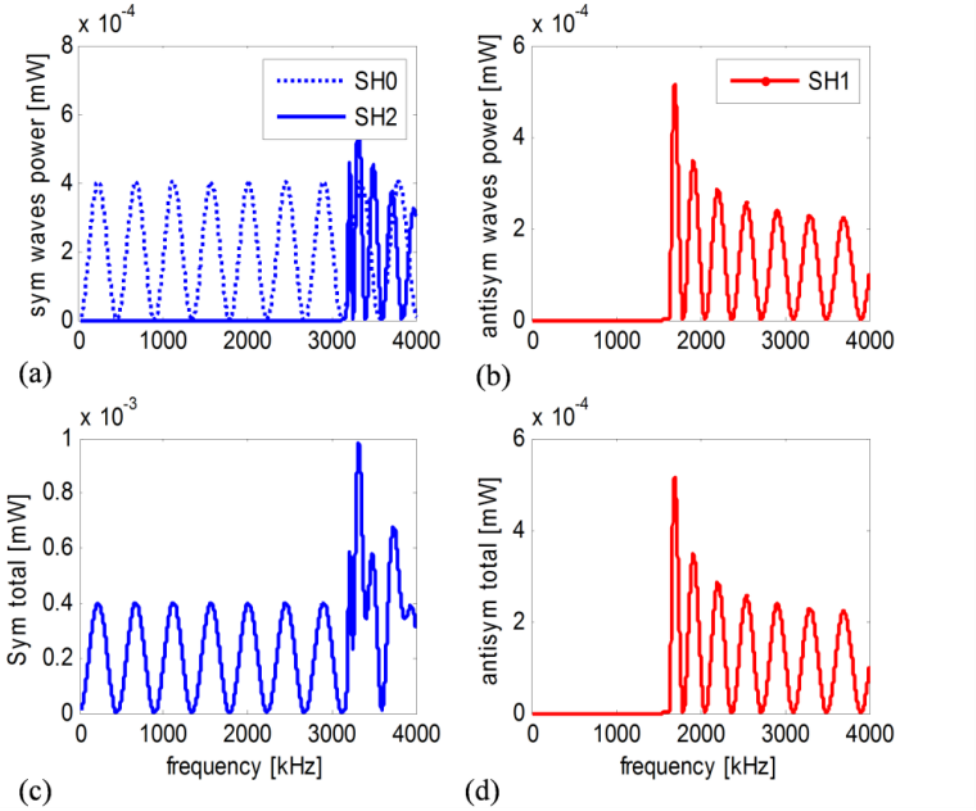

Figure 3.32. Guided SH waves power for three SH modes: two symmetric modes: SH0,SH2, and one antisymmetric mode: SH1, (a) individual wave power for SH0, SH2, (b) SH1 wave power, (c) total symmetric waves power, (d) total antisymmetric waves power.

With similar analysis, define time-averaged kinetic energy

$$\langle k_e \rangle = \frac{1}{2}\rho \int_A \frac{1}{2} v_z . \bar{v}_z dA \tag{3.146}$$

And the final analytical form will be

$$\langle k_e \rangle = \frac{b}{4}\int_{-d}^{d} \{\rho v_z . \bar{v}_z\} dy = \frac{\rho\omega^2}{4} bd \left[\sum_n [a_n^S B_n]^2 + \sum_n [a_n^A A_n]^2 \right] \tag{3.147}$$

Time averaged potential energy is defined as

$$\langle v_e \rangle = \frac{1}{4}\int_A \{(\mu) S_{xz} \bar{S}_{xz} + (\mu) S_{yz} \bar{S}_{yz}\} dA \tag{3.148}$$

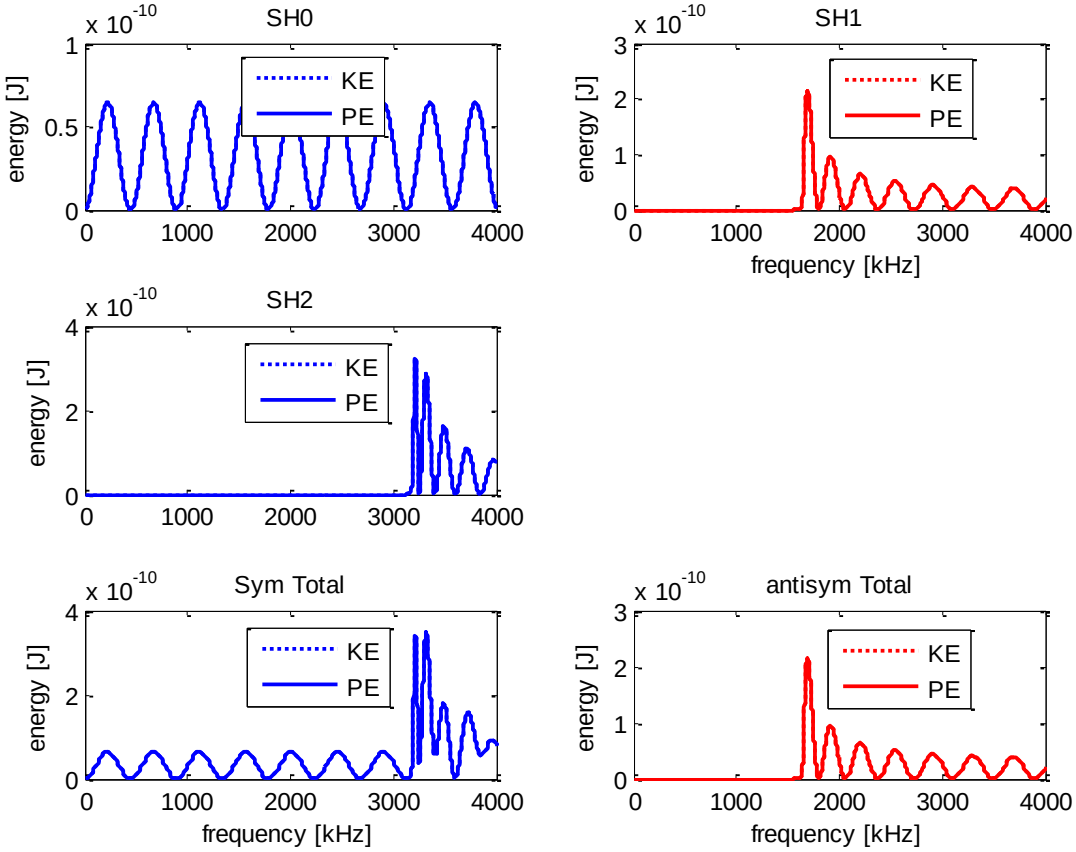

Figure 3.33. Guided SH waves energy (kinetic and potential energies) in [J]

With similar analysis like the one we followed in power and kinetic energy; then cancelling $\sin 2\eta_n d$ terms, results in

$$\begin{aligned}\langle v_e \rangle &= \frac{b}{4}\int_{-d}^{d}\left\{\begin{matrix}(\mu)S_{xz}\bar{S}_{xz}\\+(\mu)S_{yz}\bar{S}_{yz}\end{matrix}\right\}dy \\ &= \frac{b}{4}\left\{\sum_n \mu d[a_n^S B_n]^2\left[\left(\xi_n^S\right)^2+\left(\eta_n^S\right)^2\right]+\sum_n \mu d[a_n^A A_n]^2\left[\left(\xi_n^A\right)^2+\left(\eta_n^A\right)^2\right]\right\}\end{aligned} \tag{3.149}$$

Using the relation $\eta^2 = \omega^2/c_s^2 - \xi^2$, then we can prove that time-averaged potential energy equals time averaged kinetic energy

$$\begin{aligned}\langle v_e \rangle &= \frac{b}{4}\left\{\sum_n \mu d[a_n^S B_n]^2\left[\frac{\omega^2}{c_s^2}\right]+\sum_n \mu d[a_n^A A_n]^2\left[\frac{\omega^2}{c_s^2}\right]\right\} \\ &= \frac{b}{4}\left\{\sum_n \cancel{\mu} d[a_n^S B_n]^2\left[\frac{\rho\omega^2}{\cancel{\mu}}\right]+\sum_n \cancel{\mu} d[a_n^A A_n]^2\left[\frac{\rho\omega^2}{\cancel{\mu}}\right]\right\} \\ &= \frac{\rho\omega^2}{4} bd\left[\sum_n [a_n^S B_n]^2+\sum_n [a_n^A A_n]^2\right] = \langle k_e \rangle\end{aligned} \tag{3.150}$$

Numerical simulations for developed analytical models are shown in **Figure 3.32** and **Figure 3.33**. The SH0 power flow oscillates as a function of frequency with constant amplitude (because of having constant dispersion wave speed). However, the peaks and valley responses are due to the SH-PWAS finite dimension effect (what is commonly referred to as tuning of the transducer). SH1 (antisymmetric shear horizontal mode) kicked off at 1560 kHz **Figure 3.32**b,d). SH2 (symmetric mode) started at 3150 kHz (**Figure 3.32**a,c). Both SH1 and SH2 are dispersive modes with variable power consumption at different frequencies (because their wave speeds are not constant along the frequency spectrum). Similar conclusions are drawn from simulated results of wave energies (**Figure 3.33**).

3.8. SH-MATLAB GRAPHICAL USER INTERFACE

A graphical user interface has been developed to compliment the other two - Lamb wave related software developed previously in LAMSS, namely WAVESOPE, and MODESHAPE. The interface is shown in **Figure 3.34**. It can simulate SH analysis for different aluminum, steel alloys, titanium…etc. It allows changing the thickness of the plate under investigation and the maximum excited frequency. Phase and group velocities can be obtained; it allows getting the velocities in actual units, i.e. m/s or normalized velocities with respect to material shear wave speed. It can also display normalized and/ or non-normalized mode shapes.

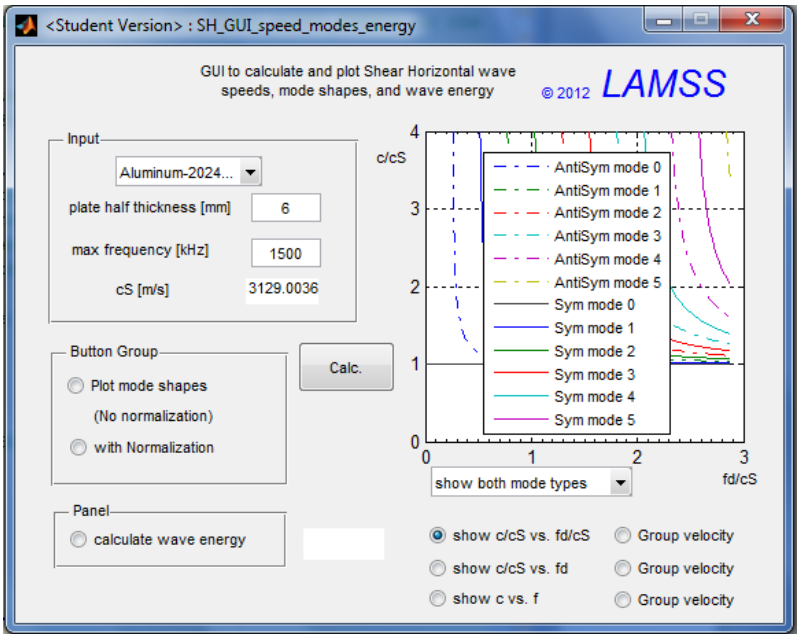

Figure 3.34. SH GUI, developed in LAMSS (www.me.sc.edu/Research/lamss/)

It can be used to plot only symmetric SH waves (e.g. SH0, SH2,…), or antisymmetric waves only, or both (**Figure 3.35**)

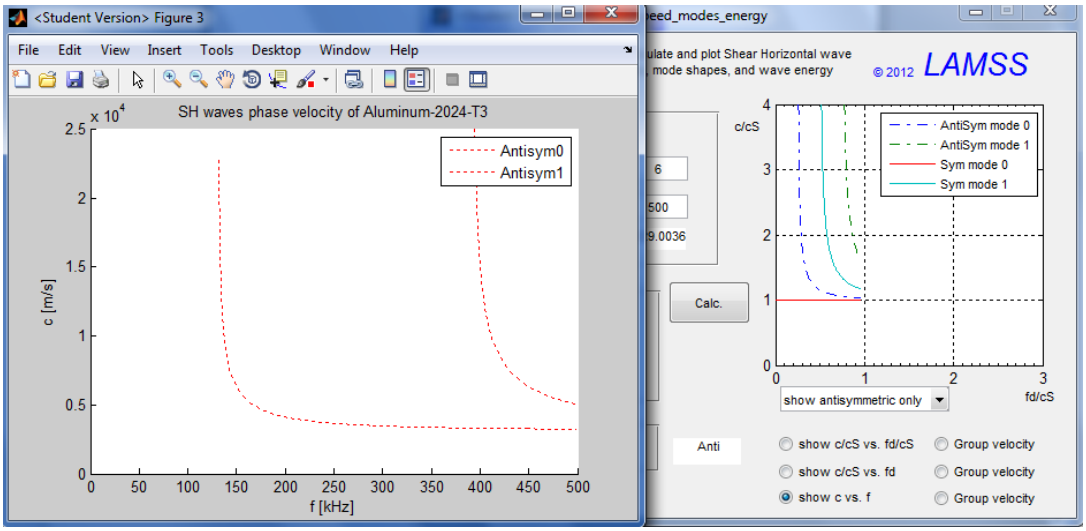

Figure 3.35. Example of plotting phase velocities of antisymmetric modes only

Figure 3.36 shows an example of plotting group velocities of both symmetric and antsymmetric modes that exist up to the specified frequency. **Figure 3.37** shows mode shapes.

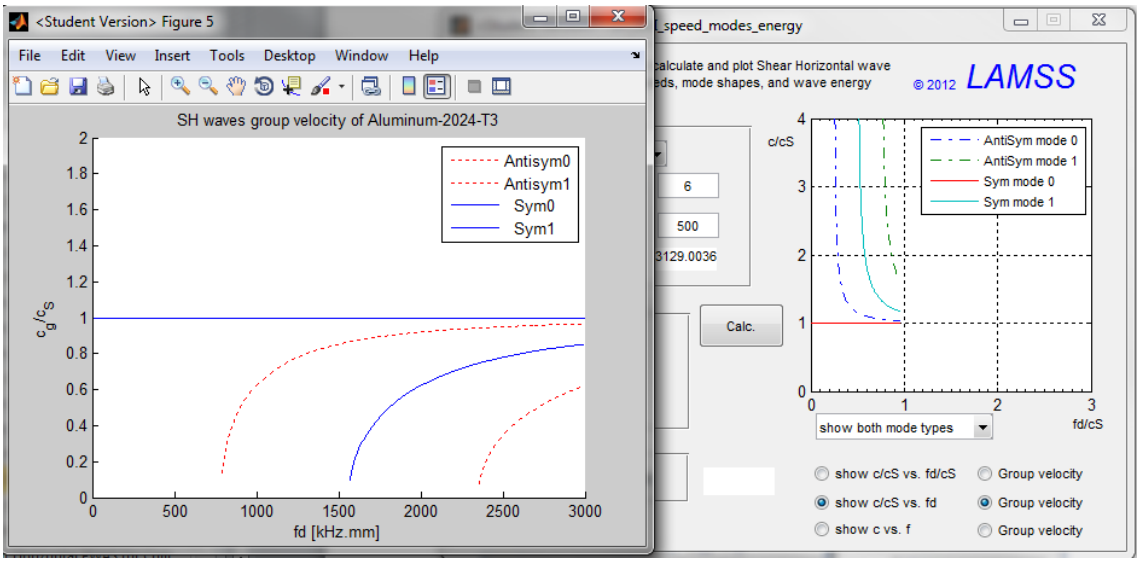

Figure 3.36. Group velocities for both symmetric and antisymmetric modes

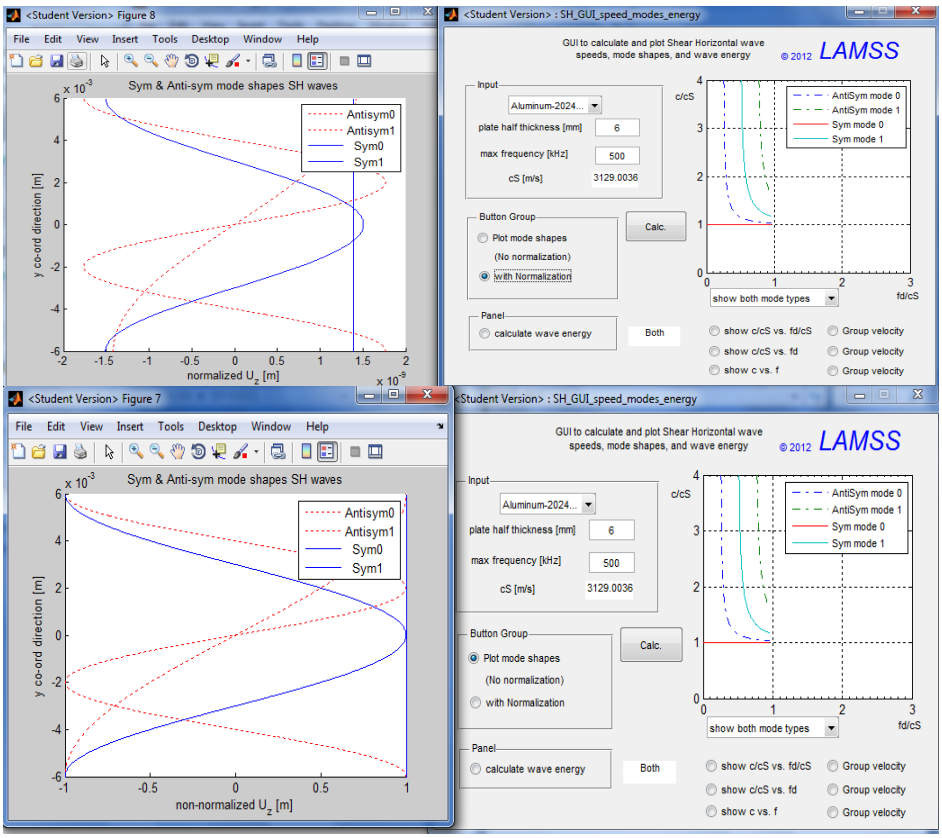

Figure 3.37. normalized and non-normalized mode shapes

3.9. SUMMARY AND CONCLUSIONS

The chapter presented predictive analytical models for electromechanical impedance of shear horizontal (SH) coupled piezoelectric wafer active sensor (PWAS) transducers. Investigation of E/M impedance of free SH-PWAS indicated that the analytical model with the constant electric field assumption is more representative of the experimental case and FEM. The first resonance frequency of the free transducer is 900 kHz. Experiments and FEM of bonded PWAS on structures showed the local resonance effects of the PWAS at frequencies greater than 100 kHz. Discrepancies exist in the analytical model of SH-PWAS bonded on a structure such that the mass ratio of the

transducer – to – beam structure is greater than 5%. This case was exemplified by SH-PWAS bonded on 1-mm aluminum beams (mass ratio was 30%). The second case studied was SH-PWAS bonded on 3-mm steel beams. In this case, the analytical model showed good agreement with FEM simulations and experimental results. It was shown that the SH-PWAS has directivity effects, where an axial-flexural response is obtained when the transducer poling direction is parallel to the beam length. When the transducer poling direction is perpendicular to the beam length, the SH response is obtained.

The study then discussed the excitation and reception of SH waves using the SH-PWAS. Excitation of SH waves was analyzed by finite element simulations and experiments. SH0 non-dispersive waves were captured in aluminum plates. Multiple experiments were performed to show the SH waves excitation and receiving capabilities of both SH-PWAS and regular inplane PWAS transducers. It was shown that positioning and orientation of SH-PWAS affects the generation of SH waves: (1) SH-PWAS excites SH waves in the direction perpendicular to its poling direction, (2) Regular inplane PWAS can sense SH waves. Additionally, (3) SH-PWAS transducers can sense A0 and S0 Lamb waves. Directivity analysis showed that excited SH wave amplitude gradually decreases as the measuring direction deviates from the maximum received amplitude direction.

A predictive model for guided SH wave's power and energy was analytically developed based on the normal mode expansion technique. The model assumed that (a) waves are of straight crested harmonic type, (b) evanescent non-propagating waves are ignored, and (c) the modes are of orthogonal functions. The amplitudes of each mode were normalized with respect to the power flow and modal participation factors were

determined. Modal participation factors are functions of transducer dimension. The wave power, kinetic energy, and potential energy were modelled and numerical results were presented. As expected, the kinetic energy equals the potential energy in total and for separate modes as well, due to the fact that modes are orthogonal. SH0 mode wave power and wave energy oscillate with frequency, but have constant amplitude due to the constant wave propagation speed of SH0 in isotropic materials. SH1 and SH2 modes are dispersive shear horizontal modes.

Investigation of SH waves excitation in composite materials, predictive finite element models for SH-PWAS electromechanical impedance for the bonded transducer on composites are covered in a following chapter.

CHAPTER 4: GUIDED WAVES PROPAGATION IN COMPOSITES

The first objective of this chapter is to review the different predictive models for evaluating dispersion curves of ultrasonic guided waves in composites. The second objective is to develop a stable robust code for predicting dispersion curves in composites, apply it to case studies, and compare the results with commercial software.

In order to fully extend power and energy models of Chapter 2 to anisotropic multilayered composite materials, dispersion wave propagation speeds needs to be determined; that is the focus of this chapter.

The algorithms which we review for the wave propagation analysis in layered composite plates are: (a) transfer matrix method (TMM), (b) global matrix method (GMM), (c) semi-analytical finite element method (SAFE), (d) local interaction simulation approach (LISA), and (e) equivalent matrix method (EMM). Description of each technique was covered. Then, the advantages and distinct features of those techniques were presented. Case studies for unidirectional, cross ply, and general quasi isotropic laminates were presented. Finally, experimental and finite element simulation studies were performed on glass fiber reinforced polymer composites (GFRP). Simulations and applications on carbon fiber reinforced polymer composites (CFRP) are presented later in Chapters 5 and 7.

NOMENCLATURE

A_k	=	transfer matrix for *k*th layer in the TM method
$A_{u\sigma}$	=	component of the TM relates displacements with stresses
A0	=	fundamental antisymmetric Lamb wave mode
B_i	=	amplitudes of partial aves in GM method
c_{ij}	=	stiffness matrix components in layer local coordinates, *i*, *j* = 1,2,…,6 Pa
c	=	stiffness in tensor notation
$\bar{c}$	=	stiffness matrix in global coordinates
$[D]$	=	the matrix relates amplitudes of partial waves to displacement and stress fields
d_{iq}	=	values relate amplitudes of partial waves to stress fields for the *q*th eigenvalue, *i* = 1,2,3
f	=	frequency, Hz
$\mathbf{f}^j$	=	element force vector
i	=	square root of (-1)
$\mathbf{K}^j$	=	layer stiffness matrix and element stiffness matrix in FEM
k	=	layer index in a composite layup
L	=	element size in FEM
$\mathbf{M}^j$	=	element mass matrix in FEM
N	=	number of nodes per wavelength in FEM
$\mathbf{N}(x_1, x_2)$	=	FEM interpolation functions
p	=	force vector in FEM

Q	=	eigenvector or mode shapes in FEM
S0	=	fundamental symmetric Lamb wave mode
SH0	=	fundamental shear horizontal guided wave mode
S	=	strains tensor
T	=	transformation matrix between local and global coordinates
T^t	=	transpose of transformation matrix
T_i	=	stress components, $i = 1, 2 \ldots 6$, Pa
t	=	time, s
t	=	traction vector
U_1, U_2, U_3	=	displacement amplitudes, m
U_{1q}	=	displacement amplitudes of the partial waves for the qth eigenvalue
$\mathbf{U}^j(x_3)$	=	nodal displacement vector of element j
u	=	displacements vector
$u^{\pm}$	=	displacements at the top (-) and bottom (+) of a layer
V_q, W_q	=	ratios of amplitudes of partial waves
v	=	velocity
w	=	displacement in LISA, m
$\ddot{w}$	=	displacement second derivative with respect to time, i.e. acceleration,
x_1, x_2, x_3	=	global coordinates, m
α	=	ratio between the wave numbers in the x_3 and x_1 directions
α_M	=	mass proportional damping coefficient, rad/s

β_K	=	stiffness proportional damping coefficient, s/rad
Γ	=	boundary
ε	=	strain tensor
θ	=	waver propagation angle with respect to fiber direction
λ	=	wave length, m
ξ	=	wave number, 1/m
ρ	=	material density, kg/m^3
σ_{ij}	=	stress components, i, j = 1,2,3, Pa
$\sigma^{\pm}$	=	stresses at the top (-) and bottom(+) of a layer
σ_{ij}*	=	normalized stress components with $i\xi$
σ	=	stress tensor
ω	=	angular frequency rad/s
:	=	double dot product of tensors

4.1. LITERATURE REVIEW

The use of composite materials is currently implemented in many structural components, including automotive parts, civil infrastructures, compensatory devices and aerospace structures. Composite materials combine the properties of two or more constituent materials, for example, carbon-fiber reinforced polymer composites (CFRP) combine the specific stiffness and strength of carbon fibers with the properties of epoxy matrix. Composite materials can be generally manufactured with metallic, polymeric, or ceramic matrix; however, in this study the focus is on polymer matrix composites for their wide application in the aerospace industry. Many parts of recent air and spacecraft are manufactured from CFRP and glass-fiber reinforced polymers (GFRP) as well.

Because of the challenge of constructing high strength structural parts with constrained light weights; polymer composites are more favorable than metallic alloys. Also, polymer composites can be manufactured into complex shaped components and their properties can be tailored by changing the stacking sequence of layup, i.e. layers or individual lamina. Detection of damages and flaws as well as structural integrity of polymer composites is receiving as much attention as the advantages and applications of these materials. Ultrasonic Lamb waves, or guided plate waves, have long been acknowledged for damage detection in composites (Rose, 1999; Su et al., 2006; Giurgiutiu and Santoni, 2011). For any study of guided wave propagation in structures, wave propagation speeds are essential for further analysis, e.g. impact source localization, reflection, transmission and mode conversion at damages. In many cases, robust predictive models of wave speeds are needed before conducting experimental studies. Therefore; in this study, our goal is comparing different methods of calculating ultrasonic guided wave speeds in composite materials.

Lamb wave theory is well documented in many references, such as: Rose (1999); Graff (1991); Viktorov (1967); Giurgiutiu (2008). For isotropic materials, the wave equation can be expressed by two potential functions, and the pressure and shear wave velocities. The shear horizontal (SH) wave propagation in this case is decoupled from symmetric and antisymmetric Lamb waves propagation. Lamb waves are symmetric and antisymmetric and they are dispersive by nature, i.e. (are having different speeds at different frequencies). The characteristic equation (Rayleigh-Lamb equation) is obtained by solving wave equation and applying stress free boundary conditions at upper and lower surfaces of the plate.

In the case of fiber reinforced polymer (FRP) composites, where the material is generally anisotropic, the three types of guided waves (P, SV, and SH) are coupled and it is not possible to find closed form solution of the dispersion curves. Several textbooks have documented guided wave propagation in composites: Nayfeh (1995); Rose (1999); Rokhlin et al. (2011). There are different methods to calculate dispersion curves in multilayered composite materials (a) transfer matrix method (TMM); (b) global matrix method (GMM); (c) semi-analytical finite element method (SAFE); (d) local interaction simulation approach (LISA); and (e) equivalent matrix method (EMM). Mathematical formulations of those techniques are presented, along with highlighting key features.

4.1.1. Transfer Matrix Method (TMM)

Transfer matrix method (Thomson, 1950; Haskell, 1953) is a technique for wave propagation analysis in layered media; its advantage is that it condenses the multi-layered system into few equations (four in the case of decoupled SH waves or six in the case of coupled SH waves) relating the boundary conditions at the first and the last interface. It eliminates all other intermediate interfaces; this saves a lot of computational time and complexity. Hence, TMM is favorable. One drawback TMM suffers is the numerical instability of the solution at large frequency-thickness product values (Lowe, 1995). We followed the formulation in Nayfeh (1995) and Santoni (2010). Considering the composite plate layer is in x_1 , x_2 plane with wave propagation along x_1 direction (**Figure 4.1**). The angle of fibers with respect to direction of wave propagation is θ.

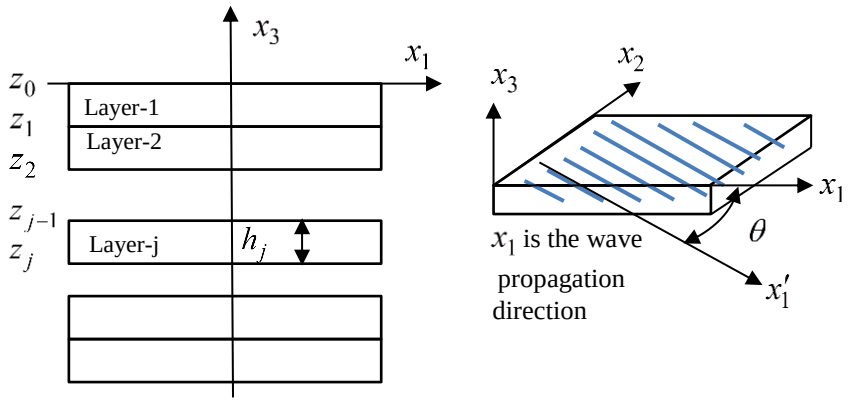

Figure 4.1. Composite layers notation and coordinates

The layer stiffness matrix in global coordinates is

$$[\bar{c}] = [T]^{-1}[c][T]^{-t} \tag{4.1}$$

where T is the transformation matrix and can be found from many composites textbooks, e.g., Jones (1999); for completeness, we include it here

$$[T] = \begin{bmatrix} m^2 & n^2 & 0 & 0 & 0 & 2mn \\ n^2 & m^2 & 0 & 0 & 0 & -2mn \\ 0 & 0 & 1 & 0 & 0 & 0 \\ 0 & 0 & 0 & m & -n & 0 \\ 0 & 0 & 0 & n & m & 0 \\ -mn & mn & 0 & 0 & 0 & m^2 - n^2 \end{bmatrix} \tag{4.2}$$

Denoting $m = \cos\theta$, $n = \sin\theta$; the conversions between local coordinates x_1' to global coordinates x_1 can be done using

$$\begin{aligned} [s] &= [T]^t[S'][T] \\ [c] &= [T]^{-1}[C'][T]^{-t} \end{aligned} \tag{4.3}$$

where capital C', S' are the layer stiffness and compliance matrices respectively in local coordinates, and c is the layer stiffness matrix in global coordinates. The maximum

anisotropy we are considering is orthotropic layer (in local coordinates); once the layer is rotated by angle θ, it becomes monoclinic anisotropy (in global coordinates).

$$C' = \begin{bmatrix} C'_{11} & C'_{12} & C'_{13} & 0 & 0 & 0 \\ C'_{12} & C'_{22} & C'_{23} & 0 & 0 & 0 \\ C'_{13} & C'_{23} & C'_{33} & 0 & 0 & 0 \\ 0 & 0 & 0 & C'_{44} & 0 & 0 \\ 0 & 0 & 0 & 0 & C'_{55} & 0 \\ 0 & 0 & 0 & 0 & 0 & C'_{66} \end{bmatrix} \qquad c = \begin{bmatrix} c_{11} & c_{12} & c_{13} & 0 & 0 & c_{16} \\ c_{12} & c_{22} & c_{23} & 0 & 0 & c_{26} \\ c_{13} & c_{23} & c_{33} & 0 & 0 & c_{36} \\ 0 & 0 & 0 & c_{44} & c_{45} & 0 \\ 0 & 0 & 0 & c_{45} & c_{55} & 0 \\ c_{16} & c_{26} & c_{36} & 0 & 0 & c_{66} \end{bmatrix} \quad (4.4)$$

Equation of motion is

$$\begin{cases} \nabla \cdot \left(\mathbf{c} : \nabla_s \mathbf{u} \right) = \rho \dfrac{\partial^2 \mathbf{u}}{\partial t^2} \\ \nabla_s \mathbf{u} = \mathbf{S} \end{cases} \quad (4.5)$$

where ρ is the density, $\mathbf{S}$ is the strains tensor, $\mathbf{u}$ is the displacements vector. The displacement vector is decomposed in the three axes components as

$$\left(u_1, u_2, u_3 \right) = \left(U_1, U_2, U_3 \right) e^{i\xi\left(x_1 + \alpha x_3 - vt \right)} \quad (4.6)$$

where ξ is the wave number in the x_1 direction, $v = \omega / \xi$ is the phase velocity, ω is the angular frequency, α is the ratio between wave number in the thickness direction x_3 and x_1 direction, and U_i is the displacement amplitude. Substituting Eq. (4.6) into equation of motion, Eq. (4.5) and cancelling the exponential terms yields

$$\begin{cases} \left(c_{11} + c_{55}\alpha^2 - \rho v^2 \right) U_1 + \left(c_{16} + c_{45}\alpha^2 \right) U_2 + \left(c_{13} + c_{55} \right) \alpha U_3 = 0 \\ \left(c_{16} + c_{45}\alpha^2 \right) U_1 + \left(c_{66} + c_{44}\alpha^2 - \rho v^2 \right) U_2 + \left(c_{45} + c_{36} \right) \alpha U_3 = 0 \\ \left(c_{13} + c_{55} \right) \alpha U_1 + \left(c_{36} + c_{45} \right) \alpha U_2 + \left(c_{55} + c_{33}\alpha^2 - \rho v^2 \right) U_3 = 0 \end{cases} \quad (4.7)$$

For a given value of v, this is an eigenvalue problem, and the determinant of Eq. (4.7) can be expressed as

$$\alpha^6 + B_1 \alpha^4 + B_2 \alpha^2 + B_3 = 0 \quad (4.8)$$

where B_i values are found in Nayfeh (1995) with slight corrections as

$$
\begin{aligned}
B_1 &= [c_{11}c_{33}c_{44} - c_{13}^2 c_{44} + 2c_{13}c_{36}c_{45} - 2c_{13}c_{44}c_{55} + 2c_{13}c_{45}^2 - 2c_{16}c_{33}c_{45} + c_{33}c_{55}c_{66} - c_{36}^2 c_{55} \\
&\quad -(c_{33}c_{44} + c_{33}c_{55} + c_{44}c_{55} - c_{45}^2)\rho v^2]/\Delta \\
B_2 &= [c_{11}c_{33}c_{66} - c_{11}c_{36}^2 - 2c_{11}c_{36}c_{45} + c_{11}c_{44}c_{55} - c_{11}c_{45}^2 - c_{13}^2 c_{66} + 2c_{13}c_{16}c_{36} + 2c_{13}c_{16}c_{45} - 2c_{13}c_{55}c_{66} \\
&\quad -c_{16}^2 c_{33} + 2c_{16}c_{36}c_{55} \\
&\quad -(c_{11}c_{33} + c_{11}c_{44} - c_{13}^2 - 2c_{13}c_{55} - 2c_{16}c_{45} + c_{33}c_{66} - c_{36}^2 - 2c_{36}c_{45} + c_{44}c_{55} - c_{45}^2 + c_{55}c_{66})\rho v^2 \\
&\quad +(c_{33} + c_{44} + c_{55})\rho^2 v^4]/\Delta \\
B_3 &= [c_{11}c_{55}c_{66} - c_{16}^2 c_{55} - (c_{11}c_{55} + c_{11}c_{66} - c_{16}^2 + c_{55}c_{66})\rho v^2 + (c_{11} + c_{55} + c_{66})\rho^2 v^4 - \rho^3 v^6]/\Delta \\
\Delta &= c_{33}c_{44}c_{55} - c_{33}c_{45}^2
\end{aligned}
\tag{4.9}
$$

By solving Eq. (4.8) symbolically, it can be shown that the eigenvalues α_i are found in pairs, i.e.

$$\alpha_2 = -\alpha_1 \ , \ \alpha_4 = -\alpha_3 \ , \ \alpha_6 = -\alpha_5 \tag{4.10}$$

Each pair of eigenvalues represents a pair of similar partial waves propagating in opposite x_3 directions, one downward, and the other upward. Using any two equations in Eq. (4.7), we find the displacements ratios (i.e. eigenvectors). However, careful selection of the two equations is important. If this algorithm is used for isotropic metallic layer or a composite layer that is almost isotropic, the displacements ratio $W_q = U_{3q}/U_{1q}$ suffers a singularity situation. Therefore, the ratios documented in Nayfeh (1995) and Santoni (2010) were exchanged by (Rokhlin et al., 2011)

$$
\begin{cases}
V_q = \dfrac{U_{2q}}{U_{1q}} = \dfrac{\left(c_{11} + c_{55}\alpha_q^2 - \rho v^2\right)\left(c_{45} + c_{36}\right)\alpha_q - \left(c_{16} + c_{45}\alpha_q^2\right)\left(c_{13} + c_{55}\right)\alpha_q}{\left(c_{13} + c_{55}\right)\alpha_q\left(c_{66} + c_{44}\alpha_q^2 - \rho v^2\right) - \left(c_{16} + c_{45}\alpha_q^2\right)\left(c_{45} + c_{36}\right)\alpha_q} \\
W_q = \dfrac{U_{3q}}{U_{1q}} = \dfrac{\left(c_{11} + c_{55}\alpha_q^2 - \rho v^2\right)\left(c_{66} + c_{44}\alpha_q^2 - \rho v^2\right) - \left(c_{16} + c_{45}\alpha_q^2\right)^2}{\left(c_{16} + c_{45}\alpha_q^2\right)\left(c_{45} + c_{36}\right)\alpha_q - \left(c_{13} + c_{55}\right)\alpha_q\left(c_{66} + c_{44}\alpha_q^2 - \rho v^2\right)}
\end{cases}
\tag{4.11}
$$

where $q = 1,\ldots 6$ represents the partial wave number. By doing this, a more general robust algorithm is attained. The displacements in Eq. (4.6) can be written as

$$\left(u_1, u_2, u_3\right) = \sum_{q=1}^{6} \left(1, V_q, W_q\right) U_{1q} e^{i\xi\left(x_1 + \alpha_q x_3 - vt\right)} \tag{4.12}$$

The stresses are

$$\begin{Bmatrix} T_1 \\ T_2 \\ T_3 \\ T_4 \\ T_5 \\ T_6 \end{Bmatrix} = i\xi \sum_q \begin{Bmatrix} c_{11} + \alpha_q c_{13} W_q + c_{16} V_q \\ c_{12} + \alpha_q c_{23} W_q + c_{26} V_q \\ c_{13} + \alpha_q c_{33} W_q + c_{36} V_q \\ \alpha_q c_{44} V_q + c_{45}\left(\alpha_q + W_q\right) \\ \alpha_q c_{45} V_q + c_{55}\left(\alpha_q + W_q\right) \\ c_{16} + \alpha_q c_{36} W_q + c_{66} V_q \end{Bmatrix} U_{1q} e^{i\xi\left(x_1 + \alpha_q x_3 - vt\right)} \tag{4.13}$$

The stresses that are of interest are $\sigma_{33}, \sigma_{13}, \sigma_{23}$. Stress free boundary condition is applied on them; we define

$$\left(\sigma_{33}^*, \sigma_{13}^*, \sigma_{23}^*\right) = \left(T_3^*, T_5^*, T_4^*\right) = \sum_{q=1}^{6} \left(d_{1q}, d_{2q}, d_{3q}\right) U_{1q} e^{i\xi\left(x_1 + \alpha_q x_3 - vt\right)} \tag{4.14}$$

where $\sigma^* = \sigma / i\xi$, and d_{1q}, d_{2q}, d_{3q} are terms extracted from Eq. (4.13)

$$\begin{bmatrix} d_{1q} \\ d_{2q} \\ d_{3q} \end{bmatrix} = \begin{bmatrix} c_{13} + \alpha_q c_{33} W_q + c_{36} V_q \\ \alpha_q c_{45} V_q + c_{55}\left(\alpha_q + W_q\right) \\ \alpha_q c_{44} V_q + c_{45}\left(\alpha_q + W_q\right) \end{bmatrix} \tag{4.15}$$

Combining the displacement and stress relations yields the state vector in a layer

$$\begin{Bmatrix} \{u\} \\ \{\sigma\} \end{Bmatrix} = \begin{bmatrix} u_1 \\ u_2 \\ u_3 \\ \sigma_{33}^* \\ \sigma_{13}^* \\ \sigma_{23}^* \end{bmatrix} = \begin{bmatrix} 1 & 1 & 1 & 1 & 1 & 1 \\ V_1 & V_1 & V_3 & V_3 & V_5 & V_5 \\ W_1 & -W_1 & W_3 & -W_3 & W_5 & -W_5 \\ d_{11} & d_{11} & d_{13} & d_{13} & d_{15} & d_{15} \\ d_{21} & -d_{21} & d_{23} & -d_{23} & d_{25} & -d_{25} \\ d_{31} & -d_{31} & d_{31} & -d_{31} & d_{35} & -d_{35} \end{bmatrix} \begin{bmatrix} U_{11} e^{i\xi\alpha_1 x_3} \\ U_{12} e^{-i\xi\alpha_1 x_3} \\ U_{13} e^{i\xi\alpha_3 x_3} \\ U_{14} e^{-i\xi\alpha_3 x_3} \\ U_{15} e^{i\xi\alpha_5 x_3} \\ U_{16} e^{-i\xi\alpha_5 x_3} \end{bmatrix} e^{i\xi\left(x_1 - vt\right)} \tag{4.16}$$

The idea of the TMM is relating the layer properties and the boundary conditions at the top and bottom surfaces with those of the other layers. This is done by applying continuity of displacements and equilibrium of stresses. The layer transfer matrix A_k relates the displacements and stresses of the top of the layer to those of the bottom of the layer

$$\begin{Bmatrix} \{u^+\} \\ \{\sigma^+\} \end{Bmatrix} = \begin{bmatrix} [A_{uu}] & [A_{u\sigma}] \\ [A_{u\sigma}] & [A_{\sigma\sigma}] \end{bmatrix} \begin{Bmatrix} \{u^-\} \\ \{\sigma^-\} \end{Bmatrix} \tag{4.17}$$

Call A_k the 4 x 4 hyper matrix of Eq. (4.17), X the 6 x 6 matrix of Eq. (4.16), U the vector of U_{1i} elements, and H the diagonal matrix of elements $e^{i\xi\alpha_i x_3}$; hence,

$$A_k = X_k H_k X_k^{-1} \tag{4.18}$$

The total TM is calculated by multiplying the transfer matrix of individual layers consecutively. And to satisfy stress free boundary condition for the whole laminate; σ^+ and σ^- in Eq. (4.17) are set to zero, hence the characteristic equation to find dispersion phase velocities versus wavenumbers is

$$\left|A_{u\sigma}\right| = 0 \tag{4.19}$$

Usually Eq. (4.19) is solved numerically to find dispersion phase velocities versus wavenumbers or frequencies.

4.1.2. Instability of Transfer Matrix Method

Rokhlin et al. (2011) showed that, due to refraction within one or more layers of the laminate, some of the plane waves can be internally reflected, meaning that their

partial waves will be evanescent within the layer, i.e. the propagating constant will be imaginary in the exponential $e^{\pm i\xi x_3}$ resulting in real exponential $e^{\xi x_3}$. Depending on the layer thickness and the frequency, the real term $e^{\xi x_3}$ can be very large or very small. The TM formulation in itself has no deficiency. But numerical computation of this real exponential that rises and falls quickly suffers frequent instabilities. As shown in **Figure 4.2**a,b, the instability for a 1-mm aluminum plate starts around wavenumber-thickness product equals 40 and frequency of 20 MHz. Whereas, for a layer of unidirectional CFRP, the instability starts at a considerably lower frequency and wavenumber-thickness value. As shown from **Figure 4.2**c,d, the instability starts at wavenumber-thickness ≈ 3 and over all the frequency range.

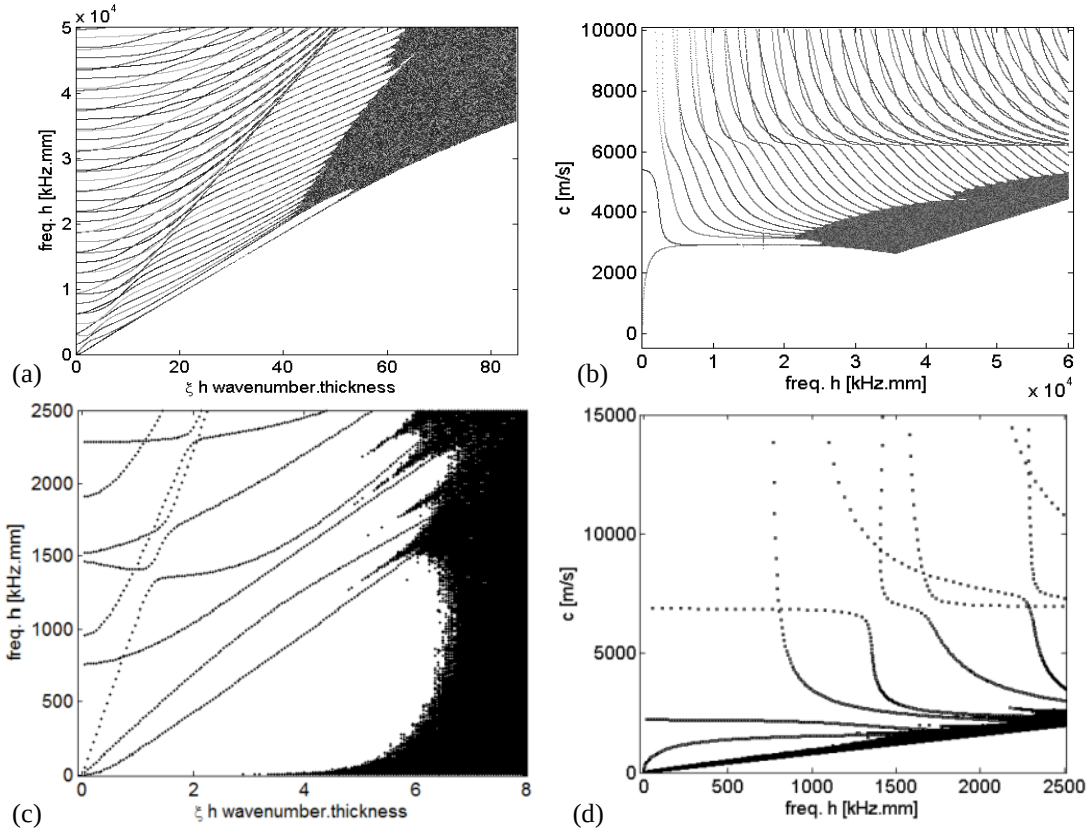

Figure 4.2. Instability of TMM at high frequency-thickness products, (a),(b) 1-mm aluminum layer, (c),(d) 1-mm unidirectional CFRP lamina with 45 fibers

4.1.3. Global Matrix Method (GMM)

Global matrix method (GMM) was first developed by Knopoff (1964). It combines stresses and displacements at the boundaries of each layer with the overall boundary conditions and assembles them in one single matrix. Compared to Thomson-Haskell TMM, the GMM has the advantage that it remains stable at high frequency-thickness products. The disadvantage is that the global matrix end to be a large matrix for laminates with large numbers of layers. Following is a brief description of the method (Pavlakovic and Lowe, 2003).

In the GMM, one matrix represents the overall system, and the general size of the matrix is $6(n-1)$ equations, where *n* is the number of layers including the two semi-infinite media, as illustrated in **Figure 4.3** for a three-layer composite. The corresponding GM is also shown in **Figure 4.3**. If the waves are decoupled, then the number of equations reduces to $4(n-1)$. The assembled equations are

$$\begin{bmatrix} [D_{1b}^{-}] & [-D_{2t}] & & & \\ & [D_{2b}] & [-D_{3t}] & & \\ & & [D_{3b}] & [-D_{4t}] & \\ & & & [D_{4b}] & [D_{5b}^{+}] \end{bmatrix} \begin{bmatrix} [B_1] \\ [B_2] \\ [B_3] \\ [B_4] \\ [B_5] \end{bmatrix} = 0 \qquad (4.20)$$

where $[D]$ is a 4x4 matrix that relates the amplitudes of the partial waves to the displacement and stress fields in a layer; $[B_i]$ is a vector containing the amplitudes of the partial waves in layer *i*; *t* ,*b* refer to top and bottom of each layer; $+, -$ refer to the waves going downwards or upwards (**Figure 4.3**).

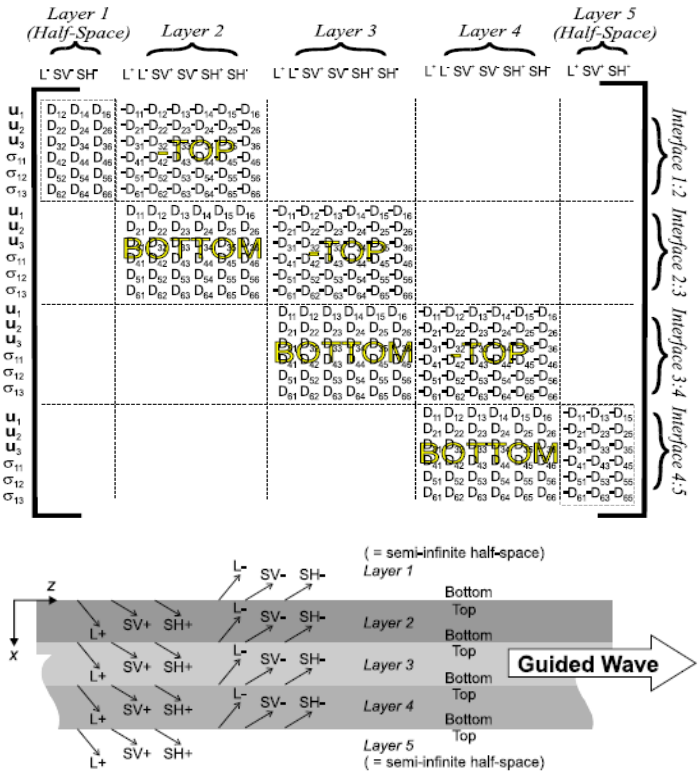

Figure 4.3. GMM formulation (Pavlakovic and Lowe, 2003).

4.1.4. Semi Analytical Finite Element Method (SAFE)

SAFE is becoming popular for analyzing guided wave propagation in composites (Bartoli et al., 2006). SAFE is basically a finite element method discretizing the structure cross section allowing different cross sections to be analyzed. In the same time it solves analytically in the direction of wave propagation. This makes it more efficient in terms of computational time and memory than a complete FEM (Gavric, 1995; Sorohan et al., 2011). The advantage of discretizing the cross section is that it allows the modeling of any arbitrary cross sections, e.g. track rails (Hayashi et al., 2003; Bartoli et al., 2006). The material is defined in FEM by stiffness matrix; this makes SAFE method very straight forward for application of anisotropic materials. SAFE solutions are obtained in a

stable manner through an algebraic eigenvalue problem, and thus do not require the root-searching algorithms used in the TMM and GMM approaches. A brief description of the SAFE method is presented following Hayashi et al. (2003). The virtual work principle states,

$$\int_{\Gamma} \delta \mathbf{u}^T \mathbf{t} d\Gamma = \int_{V} \delta \mathbf{u}^T (\rho \ddot{\mathbf{u}}) dV + \int_{V} \delta \boldsymbol{\varepsilon}^T \boldsymbol{\sigma} \, dV \tag{4.21}$$

where ^{T} is the transpose; ρ is the density; $\int_{\Gamma}(.)d\Gamma$ and $\int_{V}(.)dV$ are the surface and the volume integrations of the element, respectively. $\int_{\Gamma} \delta \mathbf{u}^T \mathbf{t} d\Gamma$ denotes the work done by the external traction $\mathbf{t}$. The two terms on the right hand side of Eq. (4.21) are the kinetic energy and the potential energy. The wave solution along the wave propagation direction is represented by exponential orthogonal functions $\exp(i\xi_i x_3)$. The next step is similar to FEM discretization, where we define the displacement vector at an arbitrary point

$$\mathbf{u} = \mathbf{N}(x_1, x_2)\mathbf{U}^j(x_3)\exp(-i\omega t) \tag{4.22}$$

where $\mathbf{N}(x, y)$ is the interpolation function, and $\mathbf{U}^j(z)$ is the nodal displacement vector of the element j. Strains are determined from the displacements and the derivatives of the interpolation functions with respect to x_1, x_2. Similar formulation is used for the traction vector $\mathbf{t}$ in terms of the nodal external traction vector. The stress vector is $\boldsymbol{\sigma} = \mathbf{c}\boldsymbol{\varepsilon}$ in which material stiffness matrix $\mathbf{c}$ is incorporated. Substituting displacements, tractions, strains, and stresses in Eq. (4.21) yields

$$\mathbf{f}^j = \left(\mathbf{K}_1^j + i\xi\mathbf{K}_2^j + \xi^2\mathbf{K}_3^j\right)\bar{\mathbf{U}}^j - \omega^2\mathbf{M}^j\bar{\mathbf{U}}^j \tag{4.23}$$

where $\mathbf{f}^j$ is the element force vector; $\mathbf{K}_i^j$, i = 1,2,3, and $\mathbf{M}^j$ are the integrals determined by numerical integration techniques and they are functions of geometry; ξ is the wave

number; ω is the angular frequency. $\bar{\mathbf{U}}^j$ is the element nodal displacement vector. Results at common nodes are overlapped and the total system's governing equations are determined. It is easy to introduce damping by considering complex form of the K matrices. The final governing equation (Hayashi et al., 2003; Bartoli et al., 2006),

$$\left(\mathbf{A}-\xi\mathbf{B}\right)\mathbf{Q}=\mathbf{p}$$

$$\mathbf{A}=\begin{bmatrix} 0 & \mathbf{K}_1-\omega^2\mathbf{M} \\ \mathbf{K}_1-\omega^2\mathbf{M} & i\mathbf{K}_2 \end{bmatrix} \quad , \quad \mathbf{B}=\begin{bmatrix} \mathbf{K}_1-\omega^2\mathbf{M} & 0 \\ 0 & -\mathbf{K}_3 \end{bmatrix} \quad , \quad \mathbf{Q}=\begin{bmatrix} \bar{\mathbf{U}} \\ \xi\bar{\mathbf{U}} \end{bmatrix} \quad , \quad \mathbf{p}=\begin{bmatrix} 0 \\ \mathbf{f} \end{bmatrix} \tag{4.24}$$

When the force vector $\mathbf{p}$ equals to zero, the eigenvalues ξ_m of the system can be determined and the phase velocity is given by $c_m=\omega/\xi_m$. Consequently; nodal solutions and the mode shapes can be determined.

4.1.5. Local Interaction Simulation Approach (LISA)

LISA discretizes the system into a lattice like in the finite difference method and its formulation is based on elastodynamic equations. The advantage of LISA appears when discontinuities or changes needed to be applied to the material properties; those changes are treated by modifying the properties of the lattice at the corresponding locations. LISA was studied by Delsanto et al. (1997) for 3-D case, starting from the elastodynamic wave equation

$$\partial_l(S_{klmn}w_{m,n})=\rho\ddot{w}_k \quad (k,l,m,n=1,3) \tag{4.25}$$

where *S* is the stiffness tensor, ρ is the material density, *w* is the displacement. Time is discretized; the propagation medium is discretized into a lattice with special steps (Ruzzene et al., 2005). Finite difference (FD) formulation is used in recursive equations

to represent the second order space derivatives of the neighboring points of a generic point O in the lattice.

The finite difference formalism is used with the elastodynamic equation of motion to generate three iterative equations which allow computation of displacements u_p at time $t+1$ as a linear combination of displacement components at time t and $t-1$. A well-organized formulation was reported in Nadella and Cesnik (2012) with experimental validations of LISA for both isotropic and anisotropic media. Another study (Ruzzene et al., 2005) compared LISA approach with experimental results using laser vibrometer measurements on elastic plates.

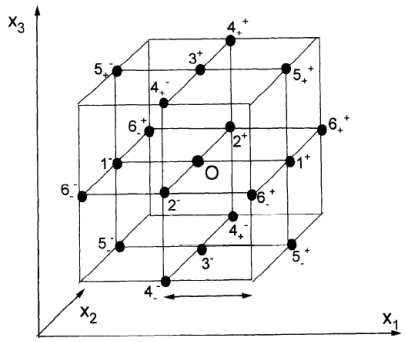

Figure 4.4. Generic point O and its 18 neighboring points in the lattice (Delsanto et al., 1997)

4.1.6. Equivalent Matrix Method (EMM)

Equivalent matrix method (EMM) is a quick and robust approach to analyze cross ply laminates. It uses the fact that the transformation matrix between 0 and 90 degrees is straight forward and can be done manually. EMM can be applied for generally orientated layers as well. This method was used in Monnier (2006). The code developed in this study was only for cross ply laminates. The procedure is as follows

$$[s_{uni}] = [c_{uni}]^{-1}$$
$$[s_w] = [T]^t [s_{fill}][T] \tag{4.26}$$

where *s* is the compliance matrix, and *c* is the stiffness matrix, *T* is the transformation matrix. *Fill* direction is the unidirectional fiber orientation, and *warp* is the perpendicular direction. The corresponding *warp* stiffness is calculated and the average is determined as

$$[c_w] = [s_w]^{-1}$$
$$[c_{eq}] = (c_{uni} + c_w)/2 \tag{4.27}$$

The example used in this study is T300/914 CFRP and the corresponding unidirectional lamina's stiffness coefficients and the EM are

$$c_{uni} = \begin{pmatrix} 143.8 & 6.2 & 6.2 & 0 & 0 & 0 \\ 6.2 & 13.3 & 6.5 & 0 & 0 & 0 \\ 6.2 & 6.5 & 13.3 & 0 & 0 & 0 \\ 0 & 0 & 0 & 3.6 & 0 & 0 \\ 0 & 0 & 0 & 0 & 5.7 & 0 \\ 0 & 0 & 0 & 0 & 0 & 5.7 \end{pmatrix} \text{GPa}, c_{eq} = \begin{pmatrix} 78.5 & 6.2 & 6.35 & 0 & 0 & 0 \\ 6.2 & 78.5 & 6.5 & 0 & 0 & 0 \\ 6.35 & 6.5 & 13.3 & 0 & 0 & 0 \\ 0 & 0 & 0 & 4.65 & 0 & 0 \\ 0 & 0 & 0 & 0 & 4.65 & 0 \\ 0 & 0 & 0 & 0 & 0 & 5.7 \end{pmatrix} \tag{4.28}$$

4.2. DETAILS OF TMM AND STIFFNESS MATRIX DERIVATIONS

Numerous commercial software have been developed in the past few years for calculating of dispersion curves of wave propagation speeds in composites, e.g. DISPERSE (Pavlakovic and Lowe, 2003) based on GMM; and GUIGUW (Bocchini et al., 2011) based on SAFE method. However, we did not find a commercial code based on TMM. Hence, we programmed our own code continuing the effort started by Santoni (2010). Our TMM code has been used to calculate guided waves dispersion curves. As mentioned earlier, TMM has the advantage of speed, but suffers from numerical instability at high frequency-thickness values especially in multilayered composites. In

this section, we present the framework that has been followed by many researchers, e.g., Schmidt and Jensen (1985); Wang and Rokhlin (2001); Glushkov et al. (2011) to overcome this instability problem using the stiffness matrix method (SMM). Detailed formulation of the approach is presented for the following cases: isotropic; orthotropic unidirectional fibers along wave propagation direction or perpendicular to it; and generally anisotropic layers. In the next section, we integrate SMM and TMM into an integrated approach called the stiffness transfer matrix method (STMM) and we study the following cases: isotropic layer, anisotropic layer, and anisotropic multilayer composite.

4.2.1. Transfer Matrix Method Details

In this part we added extra steps for the analytical development that was covered in Nayfeh (1995) and Santoni (2010), we highlighted some typos that were identified in the original text and which are relevant for coding these equations in a computer program to obtain the dispersion curves. This is followed by detailed derivation of the roots of Eq. (4.8) for two cases: (a) an isotropic layer, and (b) orthotropic composite layer with fibers along 0 or 90 directions. In both cases, guided waves are decoupled into (1) symmetric and antisymmetric Lamb waves, (2) shear horizontal (SH) waves.

Starting from the equation of motion, Eq. (4.5)

$$\begin{cases} \nabla \cdot \left(\mathbf{c} : \nabla_s \mathbf{u} \right) = \rho \dfrac{\partial^2 \mathbf{u}}{\partial t^2} \\ \nabla_s \mathbf{u} = \mathbf{S} \end{cases} \tag{4.29}$$

we expand the double dot product between stiffness tensor **c** and the gradient operator ∇,

where ∇ is order one vector (rank = 1) and is multiplied by ($\mathbf{c}:\nabla_s\mathbf{u}$), which is a 4th rank tensor of stiffness multiplied by inner product with ($\nabla_s\mathbf{u}$ = second order). The result of $\mathbf{c}:\nabla_s\mathbf{u}$ is second order. Hence (∇ order one) inner product with (second order) yields an order one quantity that is the acceleration $\frac{\partial^2\mathbf{u}}{\partial t^2}$ vector. Details as follows,

$$\begin{bmatrix} c_{11} & c_{12} & c_{13} & 0 & 0 & c_{16} \\ c_{12} & c_{22} & c_{23} & 0 & 0 & c_{26} \\ c_{13} & c_{23} & c_{33} & 0 & 0 & c_{36} \\ 0 & 0 & 0 & c_{44} & c_{45} & 0 \\ 0 & 0 & 0 & c_{45} & c_{55} & 0 \\ c_{16} & c_{26} & c_{36} & 0 & 0 & c_{66} \end{bmatrix} : \begin{Bmatrix} S_{11} \\ S_{22} \\ S_{33} \\ S_{23} \\ S_{13} \\ S_{12} \end{Bmatrix} = \begin{bmatrix} c_{11} & c_{12} & c_{13} & 0 & 0 & c_{16} \\ c_{12} & c_{22} & c_{23} & 0 & 0 & c_{26} \\ c_{13} & c_{23} & c_{33} & 0 & 0 & c_{36} \\ 0 & 0 & 0 & c_{44} & c_{45} & 0 \\ 0 & 0 & 0 & c_{45} & c_{55} & 0 \\ c_{16} & c_{26} & c_{36} & 0 & 0 & c_{66} \end{bmatrix} : \begin{Bmatrix} S_1 \\ S_2 \\ S_3 \\ S_4 \\ S_5 \\ S_6 \end{Bmatrix} = \begin{Bmatrix} T_{11} \\ T_{22} \\ T_{33} \\ T_{23} \\ T_{13} \\ T_{12} \end{Bmatrix}$$

(4.30)

$$\underbrace{\begin{bmatrix} c_{11} & c_{12} & c_{13} & 0 & 0 & c_{16} \\ c_{12} & c_{22} & c_{23} & 0 & 0 & c_{26} \\ c_{13} & c_{23} & c_{33} & 0 & 0 & c_{36} \\ 0 & 0 & 0 & c_{44} & c_{45} & 0 \\ 0 & 0 & 0 & c_{45} & c_{55} & 0 \\ c_{16} & c_{26} & c_{36} & 0 & 0 & c_{66} \end{bmatrix}}_{\text{This is Voigt notation, but for 'correct' double dot product this must be in 4-rank tensor form}} : \begin{Bmatrix} \frac{\partial u_1}{\partial x_1} \\ \frac{\partial u_2}{\partial x_2} \\ \frac{\partial u_3}{\partial x_3} \\ \left(\frac{\partial u_2}{\partial x_3}+\frac{\partial u_3}{\partial x_2}\right) \\ \left(\frac{\partial u_1}{\partial x_3}+\frac{\partial u_3}{\partial x_1}\right) \\ \left(\frac{\partial u_1}{\partial x_2}+\frac{\partial u_2}{\partial x_1}\right) \end{Bmatrix} or \begin{bmatrix} \frac{\partial u_1}{\partial x_1} & 0 & 0 \\ 0 & \frac{\partial u_2}{\partial x_2} & 0 \\ 0 & 0 & \frac{\partial u_3}{\partial x_3} \\ 0 & \frac{\partial u_2}{\partial x_3} & \frac{\partial u_3}{\partial x_2} \\ \frac{\partial u_1}{\partial x_3} & 0 & \frac{\partial u_3}{\partial x_1} \\ \frac{\partial u_1}{\partial x_2} & \frac{\partial u_2}{\partial x_1} & 0 \end{bmatrix} = \begin{Bmatrix} T_{11} \\ T_{22} \\ T_{33} \\ T_{23} \\ T_{13} \\ T_{12} \end{Bmatrix} = \begin{Bmatrix} T_1 \\ T_2 \\ T_3 \\ T_4 \\ T_5 \\ T_6 \end{Bmatrix} = \begin{bmatrix} T_1 & T_6 & T_5 \\ T_6 & T_2 & T_4 \\ T_5 & T_4 & T_3 \end{bmatrix}$$

(4.31)

The result is 6 x 1 array ($T_1\ T_2 \ldots T_6$) that is equivalent to 3 x 3 tensor ($T_{11}\ T_{12}\ T_{13} \ldots\ T_{33}$). This 3 x 3 tensor is to be multiplied by $\nabla = \left\{\frac{\partial}{\partial x} \quad \frac{\partial}{\partial y} \quad \frac{\partial}{\partial z}\right\}$ as inner product as in the following rule

$$\{a \quad b \quad c\}.\begin{bmatrix}(11) & (12) & (13)\\ (21) & (22) & (23)\\ (31) & (32) & (33)\end{bmatrix}=\begin{Bmatrix}a(11)+b(12)+c(13)\\ a(21)+b(22)+c(23)\\ a(31)+b(32)+c(33)\end{Bmatrix} \tag{4.32}$$

The stress tensor in Eq. (4.31) becomes

$$\left\{\frac{\partial}{\partial x} \quad \frac{\partial}{\partial y} \quad \frac{\partial}{\partial z}\right\}.\begin{bmatrix} c_{11}\frac{\partial u_1}{\partial x_1}+c_{16}\frac{\partial u_1}{\partial x_2}+c_{16}\frac{\partial u_2}{\partial x_1} & c_{66}\frac{\partial u_1}{\partial x_2}+c_{16}\frac{\partial u_1}{\partial x_1}+c_{26}\frac{\partial u_2}{\partial x_2} & c_{55}\frac{\partial u_1}{\partial x_3}+c_{45}\frac{\partial u_2}{\partial x_3}+c_{55}\frac{\partial u_3}{\partial x_1} \\ c_{12}\frac{\partial u_2}{\partial x_2}+c_{13}\frac{\partial u_3}{\partial x_3} & +c_{66}\frac{\partial u_2}{\partial x_1}+c_{36}\frac{\partial u_3}{\partial x_3} & +c_{45}\frac{\partial u_3}{\partial x_2} \\ c_{16}\frac{\partial u_1}{\partial x_1}+c_{66}\frac{\partial u_2}{\partial x_1}+c_{66}\frac{\partial u_1}{\partial x_2} & c_{26}\frac{\partial u_1}{\partial x_2}+c_{22}\frac{\partial u_2}{\partial x_2}+c_{12}\frac{\partial u_1}{\partial x_1} & c_{45}\frac{\partial u_1}{\partial x_3}+c_{44}\frac{\partial u_2}{\partial x_3}+c_{44}\frac{\partial u_3}{\partial x_2} \\ +c_{26}\frac{\partial u_2}{\partial x_2}+c_{36}\frac{\partial u_3}{\partial x_3} & +c_{26}\frac{\partial u_2}{\partial x_1}+c_{23}\frac{\partial u_3}{\partial x_3} & +c_{45}\frac{\partial u_3}{\partial x_1} \\ c_{55}\frac{\partial u_1}{\partial x_3}+c_{45}\frac{\partial u_2}{\partial x_3}+c_{55}\frac{\partial u_3}{\partial x_1} & c_{45}\frac{\partial u_1}{\partial x_3}+c_{44}\frac{\partial u_2}{\partial x_3}+c_{44}\frac{\partial u_3}{\partial x_2} & c_{13}\frac{\partial u_1}{\partial x_1}+c_{23}\frac{\partial u_2}{\partial x_2}+c_{33}\frac{\partial u_3}{\partial x_3} \\ +c_{45}\frac{\partial u_3}{\partial x_2} & +c_{45}\frac{\partial u_3}{\partial x_1} & +c_{36}\frac{\partial u_1}{\partial x_2}+c_{36}\frac{\partial u_2}{\partial x_1} \end{bmatrix}=\rho\frac{\partial^2\mathbf{u}}{\partial t^2} \tag{4.33}$$

That was the preceding step before equations (10.9), (10.18), and (10.19) in Santoni (2010) pp. 300.

Applying inner product results in the complete monoclinic equations of motion, i.e. relations between stiffness coefficients, and second derivatives of displacements and accelerations, we get

$$\begin{Bmatrix}\frac{\partial}{\partial x}(11)+\frac{\partial}{\partial y}(12)+\frac{\partial}{\partial z}(13)\\ \frac{\partial}{\partial x}(21)+\frac{\partial}{\partial y}(22)+\frac{\partial}{\partial z}(23)\\ \frac{\partial}{\partial x}(31)+\frac{\partial}{\partial y}(32)+\frac{\partial}{\partial z}(33)\end{Bmatrix}=\begin{Bmatrix}\rho\frac{\partial^2 u_1}{\partial t^2}\\ \rho\frac{\partial^2 u_2}{\partial t^2}\\ \rho\frac{\partial^2 u_3}{\partial t^2}\end{Bmatrix} \tag{4.34}$$

This yields

$$
\begin{cases}
c_{11}\dfrac{\partial^2 u_1}{\partial x_1^2}+c_{66}\dfrac{\partial^2 u_1}{\partial x_2^2}+c_{55}\dfrac{\partial^2 u_1}{\partial x_3^2}+2c_{16}\dfrac{\partial^2 u_1}{\partial x_1\partial x_2}+c_{16}\dfrac{\partial^2 u_2}{\partial x_1^2}+\left(c_{12}+c_{66}\right)\dfrac{\partial^2 u_2}{\partial x_1\partial x_2}+c_{26}\dfrac{\partial^2 u_2}{\partial x_2^2} \\
+c_{45}\dfrac{\partial^2 u_2}{\partial x_3^2}+\left(c_{13}+c_{55}\right)\dfrac{\partial^2 u_3}{\partial x_1\partial x_3}+\left(c_{45}+c_{36}\right)\dfrac{\partial^2 u_3}{\partial x_2\partial x_3}=\rho\dfrac{\partial^2 u_1}{\partial t^2} \\
c_{16}\dfrac{\partial^2 u_1}{\partial x_1^2}+\left(c_{12}+c_{66}\right)\dfrac{\partial^2 u_1}{\partial x_1\partial x_2}+c_{26}\dfrac{\partial^2 u_1}{\partial x_2^2}+c_{45}\dfrac{\partial^2 u_1}{\partial x_3^2}+c_{66}\dfrac{\partial^2 u_2}{\partial x_1^2}+c_{22}\dfrac{\partial^2 u_2}{\partial x_2^2}+c_{44}\dfrac{\partial^2 u_2}{\partial x_3^2} \\
+2c_{26}\dfrac{\partial^2 u_2}{\partial x_1\partial x_2}+\left(c_{23}+c_{44}\right)\dfrac{\partial^2 u_3}{\partial x_2\partial x_3}+\left(c_{45}+c_{36}\right)\dfrac{\partial^2 u_3}{\partial x_1\partial x_3}=\rho\dfrac{\partial^2 u_2}{\partial t^2} \\
\left(c_{13}+c_{55}\right)\dfrac{\partial^2 u_1}{\partial x_1\partial x_3}+\left(c_{36}+c_{45}\right)\dfrac{\partial^2 u_1}{\partial x_2\partial x_3}+\left(c_{36}+c_{45}\right)\dfrac{\partial^2 u_2}{\partial x_1\partial x_3}+\left(c_{23}+c_{44}\right)\dfrac{\partial^2 u_2}{\partial x_2\partial x_3}+c_{55}\dfrac{\partial^2 u_3}{\partial x_1^2} \\
+c_{44}\dfrac{\partial^2 u_3}{\partial x_2^2}+c_{33}\dfrac{\partial^2 u_3}{\partial x_3^2}+2c_{45}\dfrac{\partial^2 u_3}{\partial x_1\partial x_2}=\rho\dfrac{\partial^2 u_3}{\partial t^2}
\end{cases}
\tag{4.35}
$$

Equation (4.35) proves equation (10.9) of Santoni (2010) pp. 298.

Substituting the wave displacements solution, Eq. (4.6), in Eq. (4.35) and cancelling the exponential terms after derivations yields

$$
\begin{aligned}
&c_{11}(-\xi^2 U_1)+c_{55}(-\xi^2\alpha^2 U_1)+c_{16}(-\xi^2 U_2)+c_{45}(-\xi^2\alpha^2 U_2)+\left(c_{13}+c_{55}\right)(-\xi^2\alpha U_3)=\rho(-\xi^2 v^2 U_1) \\
&c_{16}(-\xi^2 U_1)+c_{45}(-\xi^2\alpha^2 U_1)+c_{66}(-\xi^2 U_2)+c_{44}(-\xi^2\alpha^2 U_2)+\left(c_{45}+c_{36}\right)(-\xi^2\alpha U_3)=\rho(-\xi^2 v^2 U_2) \\
&\left(c_{13}+c_{55}\right)(-\xi^2\alpha U_1)+\left(c_{36}+c_{45}\right)(-\xi^2\alpha U_2)+c_{55}(-\xi^2 U_3)+c_{33}(-\xi^2\alpha^2 U_3)=\rho(-\xi^2 v^2 U_3)
\end{aligned}
\tag{4.36}
$$

After re-arranging

$$
\begin{cases}
\left(c_{11}+c_{55}\alpha^2-\rho v^2\right)U_1+\left(c_{16}+c_{45}\alpha^2\right)U_2+\left(c_{13}+c_{55}\right)\alpha U_3=0 \\
\left(c_{16}+c_{45}\alpha^2\right)U_1+\left(c_{66}+c_{44}\alpha^2-\rho v^2\right)U_2+\left(c_{45}+c_{36}\right)\alpha U_3=0 \\
\left(c_{13}+c_{55}\right)\alpha U_1+\left(c_{36}+c_{45}\right)\alpha U_2+\left(c_{55}+c_{33}\alpha^2-\rho v^2\right)U_3=0
\end{cases}
\tag{4.37}
$$

If the material coordinate and the global coordinate systems coincide (0º orientation), the stiffness coefficients $c_{16}, c_{26}, c_{36}, c_{45}$ are equal to zero. However, we keep this equation as is, since those coefficients are used for oriented layers at angles other than 0º, So even for

orthotropic lamina at e.g. 30º, the transformation will be monoclinic and $c_{16}, c_{26}, c_{36}, c_{45}$ will appear in the analysis.

4.2.1.1. Isotropic layers and decoupled case of orthotropic layers (0/90 fiber orientations)

For the case of isotropic material, and for orthotropic layer with fiber orientation along or perpendicular to wave propagation direction, equations (4.37) reduce to

$$\begin{cases} \left(c_{11}+c_{55}\alpha^2-\rho v^2\right)U_1+\left(c_{13}+c_{55}\right)\alpha U_3=0 \\ \left(c_{66}+c_{44}\alpha^2-\rho v^2\right)U_2=0 \\ \left(c_{13}+c_{55}\right)\alpha U_1+\left(c_{55}+c_{33}\alpha^2-\rho v^2\right)U_3=0 \end{cases} \tag{4.38}$$

The first and the third equations of Eq. (4.38) give Lamb waves with displacements U_1, U_3. The eigenvalues are found by using the characteristic equation

$$\det\begin{bmatrix} \left(c_{11}+c_{55}\alpha^2-\rho v^2\right) & \left(c_{13}+c_{55}\right)\alpha \\ \left(c_{13}+c_{55}\right)\alpha & \left(c_{55}+c_{33}\alpha^2-\rho v^2\right) \end{bmatrix}=0 \tag{4.39}$$

Detailed steps of solving Eq. (4.39)are as follows,

$$\left[\left(c_{11}-\rho v^2\right)+c_{55}\alpha^2\right]\left[\left(c_{55}-\rho v^2\right)+c_{33}\alpha^2\right]-\left(c_{13}+c_{55}\right)^2\alpha^2=0 \tag{4.40}$$

$$\left(c_{11}-\rho v^2\right)\left(c_{55}-\rho v^2\right)+\left[c_{33}\left(c_{11}-\rho v^2\right)+c_{55}\left(c_{55}-\rho v^2\right)-\left(c_{13}+c_{55}\right)^2\right]\alpha^2+c_{55}c_{33}\alpha^4=0 \tag{4.41}$$

$$A\alpha^4+B\alpha^2+C=0 \tag{4.42}$$

where

$$\begin{aligned} A&=c_{55}c_{33} \\ B&=\left[c_{33}\left(c_{11}-\rho v^2\right)+c_{55}\left(c_{55}-\rho v^2\right)-\left(c_{13}+c_{55}\right)^2\right] \\ &=\left[\left(c_{11}-\rho v^2\right)c_{33}+\left(c_{55}-\rho v^2\right)c_{55}-\left(c_{13}+c_{55}\right)^2\right] \\ C&=\left(c_{11}-\rho v^2\right)\left(c_{55}-\rho v^2\right) \end{aligned} \tag{4.43}$$

This is the corrected version of Nayfeh (1995) equation (5.30) page 79. Now we prove the solution that was claimed to be:

$$\alpha_{3,4} = \pm\sqrt{\frac{v^2}{c_p^2} - 1} \quad , \quad \alpha_{5,6} = \pm\sqrt{\frac{v^2}{c_s^2} - 1} \tag{4.44}$$

The roots of Eq. (4.42) are

$$\alpha^2 = \frac{-B \pm \sqrt{B^2 - 4AC}}{2A} \tag{4.45}$$

Upon substitution from Eq. (4.43), we get

$$\alpha^2 = \frac{\left(c_{13}+c_{55}\right)^2 - \left[c_{11}\left(c_{11}-\rho v^2\right) + c_{55}\left(c_{55}-\rho v^2\right)\right] \pm \sqrt{\begin{array}{l}\left(c_{13}+c_{55}\right)^4 + \left[c_{11}\left(c_{11}-\rho v^2\right) + c_{55}\left(c_{55}-\rho v^2\right)\right]^2 \\ -2\left(c_{13}+c_{55}\right)^2\left[c_{11}\left(c_{11}-\rho v^2\right) + c_{55}\left(c_{55}-\rho v^2\right)\right] \\ -4c_{55}c_{11}\left(c_{11}-\rho v^2\right)\left(c_{55}-\rho v^2\right)\end{array}}}{2c_{55}c_{11}} \tag{4.46}$$

Note: $c_{11} = c_{33}$ so we kept all terms as function of c_{11} (only for isotropic materials). Other useful relations include

$$\begin{gathered} c_{66} = c_{55} = \mu, \quad c_{11} = \lambda + 2\mu, \quad c_{13} = \lambda, \quad c_{13} + c_{55} = \lambda + \mu \\ c_s^2 = \frac{\mu}{\rho}, \quad c_p^2 = \frac{\lambda + 2\mu}{\rho} \end{gathered} \tag{4.47}$$

Upon substitution in Eq. (4.46), we get

$$\alpha^2 = \left\{ \begin{array}{l} \dfrac{(\lambda+\mu)^2}{2(\lambda+2\mu)\mu} - \dfrac{(\lambda+2\mu)(\lambda+2\mu-\rho v^2) + \mu(\mu-\rho v^2)}{2(\lambda+2\mu)\mu} \\ \pm \dfrac{\sqrt{\begin{array}{l}(\lambda+\mu)^4 + \left[(\lambda+2\mu)(\lambda+2\mu-\rho v^2) + \mu(\mu-\rho v^2)\right]^2 \\ -2(\lambda+\mu)^2\left[(\lambda+2\mu)(\lambda+2\mu-\rho v^2) + \mu(\mu-\rho v^2)\right] - 4\left(\lambda+2\mu-\rho v^2\right)\left(\mu-\rho v^2\right)(\lambda+2\mu)\mu\end{array}}}{2(\lambda+2\mu)\mu} \end{array} \right\} \tag{4.48}$$

$$\alpha^2 = \left\{ \begin{array}{l} \dfrac{\lambda^2+2\lambda\mu+\mu^2-((\overbrace{\lambda^2+2\lambda\mu+2\lambda\mu+4\mu^2+\mu^2}^{\lambda^2+4\lambda\mu+5\mu^2})-\rho v^2(\overbrace{\lambda+2\mu+\mu}^{\lambda+3\mu}))}{2(\lambda+2\mu)\mu} \\ \pm \dfrac{\sqrt{\begin{array}{l}\left(\lambda^4+4\lambda^3\mu+6\lambda^2\mu^2+4\lambda\mu^3+\mu^4\right)+\overbrace{(\lambda^2+4\lambda\mu+5\mu^2)^2}^{\begin{array}{l}\lambda^4+4\lambda^3\mu+5\lambda^2\mu^2\\+4\lambda^3\mu+16\lambda^2\mu^2+20\lambda\mu^3\\+5\lambda^2\mu^2+20\lambda\mu^3+25\mu^4\end{array}}+\rho^2v^4\left(\lambda+3\mu\right)^2-2\rho v^2(\lambda+3\mu)(\lambda^2+4\lambda\mu+5\mu^2)\\ -2\underbrace{\left(\lambda^2+2\lambda\mu+\mu^2\right)[\lambda^2+4\lambda\mu+5\mu^2}_{\begin{array}{l}\lambda^4+4\lambda^3\mu+5\lambda^2\mu^2\\+2\lambda^3\mu+8\lambda^2\mu^2+10\lambda\mu^3\\+\lambda^2\mu^2+4\lambda\mu^3+5\mu^4\end{array}}-\rho v^2\left(\lambda+3\mu\right)]-4\mu\left(\mu-\rho v^2\right)\left[\lambda^2+4\lambda\mu+4\mu^2-\rho v^2(\lambda+2\mu)\right]\end{array}}}{2(\lambda+2\mu)\mu} \end{array} \right\} \tag{4.49}$$

Upon simplification, we get,

$$\alpha^2 = \frac{(-2\lambda\mu-4\mu^2)+\rho v^2(\lambda+3\mu)}{2(\lambda+2\mu)\mu} \pm \frac{\sqrt{\text{Under sqrt = UnSq}}}{2(\lambda+2\mu)\mu} \tag{4.50}$$

where

$$\begin{aligned} \text{UnSq} = & \left[\begin{array}{l}\left(\lambda^4+4\lambda^3\mu+6\lambda^2\mu^2+4\lambda\mu^3+\mu^4\right)+\left(\lambda^4+8\lambda^3\mu+26\lambda^2\mu^2+40\lambda\mu^3+25\mu^4\right)\\ -2\left(\lambda^4+6\lambda^3\mu+14\lambda^2\mu^2+14\lambda\mu^3+5\mu^4\right)-4\mu^2\left(\lambda^2+4\lambda\mu+4\mu^2\right)\end{array}\right] \text{all cancel} \\ & +\left[\begin{array}{l}-2(\lambda+3\mu)(\lambda^2+4\lambda\mu+5\mu^2)\\ 2\left(\lambda^2+2\lambda\mu+\mu^2\right)\left(\lambda+3\mu\right)+4\mu(\lambda^2+4\lambda\mu+4\mu^2)+4\mu^2(\lambda+2\mu)\end{array}\right]\rho v^2 \\ & +\left[\left(\lambda+3\mu\right)^2-4\mu(\lambda+2\mu)\right]\rho^2v^4 \end{aligned} \tag{4.51}$$

$$\text{UnSq} = \left\{ \begin{array}{l} \left[\begin{array}{l}\overbrace{-2\lambda^3-8\lambda^2\mu-10\lambda\mu^2-6\lambda^2\mu-24\lambda\mu^2-30\mu^3}^{\begin{array}{l}-2+2\quad -8-6+4+6+4\quad -10-24+2+12+16+4\quad -30+6+16+8\end{array}}\\ \left(+2\lambda^3+4\lambda^2\mu+2\lambda\mu^2+6\lambda^2\mu+12\lambda\mu^2+6\mu^3\right)\\ +4\lambda^2\mu+16\lambda\mu^2+16\mu^3+4\lambda\mu^2+8\mu^3\end{array}\right]\rho v^2 \quad \text{all cancel} \\ +\underbrace{\left[\left(\lambda+3\mu\right)^2-4\mu(\lambda+2\mu)\right]}_{\lambda^2+2\lambda\mu+\mu^2}\rho^2v^4 \end{array} \right\} \tag{4.52}$$

Finally, the roots reduce to

$$\alpha^2 = \frac{-2\mu(\lambda+2\mu)+\rho v^2(\lambda+3\mu)}{2(\lambda+2\mu)\mu} \pm \frac{\sqrt{(\lambda+\mu)^2\rho^2v^4}}{2(\lambda+2\mu)\mu} \tag{4.53}$$

$$\alpha_{\text{first}}^2 = \frac{-2\mu(\lambda+2\mu)+\rho v^2(\lambda+3\mu)-(\lambda+\mu)\rho v^2}{2(\lambda+2\mu)\mu}$$

$$\alpha_{3,4} = \pm\sqrt{\frac{2\mu[\rho v^2-(\lambda+2\mu)]}{2\mu(\lambda+2\mu)}} \tag{4.54}$$

$$= \pm\sqrt{\frac{\rho v^2 - c_{11}}{c_{11}}} = \pm\sqrt{\frac{\rho v^2}{c_{11}}-1} = \pm\sqrt{\frac{v^2}{c_p^2}-1}$$

and

$$\alpha_{\text{second}}^2 = \frac{-2\mu(\lambda+2\mu)+\rho v^2(\lambda+3\mu)+(\lambda+\mu)\rho v^2}{2(\lambda+2\mu)\mu}$$

$$\alpha_{5,6} = \pm\sqrt{\frac{2(\lambda+2\mu)[\rho v^2-\mu]}{2\mu(\lambda+2\mu)}} = \pm\sqrt{\frac{\rho v^2-\mu}{\mu}} \tag{4.55}$$

$$= \pm\sqrt{\frac{\rho v^2 - c_{55}}{c_{55}}} = \pm\sqrt{\frac{\rho v^2}{c_{55}}-1} = \pm\sqrt{\frac{v^2}{c_s^2}-1}$$

Also we had proved earlier in Eq. (4.10) that the eigenvalues α_i exist in pairs. So for Lamb-type waves we have 4 roots, i.e., 4 values for α_i. The mode shapes associated with Lamb waves can be determined from the first and third equations of Eq. (4.38), i.e.,

$$W_q = \frac{U_{3q}}{U_{1q}} \text{ (for Lamb waves)}, \quad V_q = \frac{U_{2q}}{U_{1q}} \text{ (forSH:not defined in this case)} \tag{4.56}$$

q = 1,2,3, …6, but as discussed before, the roots exist in pairs, hence for Lamb wave solution, we have subscripts q=3 and 5. The subscript q=1 is for SH solution, which is not considered here. Expanding W_q for the cases of q = 3, and q = 5 yields

$$W_3 = \frac{U_{33}}{U_{13}} = -\frac{c_{11}+c_{55}\alpha^2-\rho v^2}{(c_{13}+c_{55})\alpha_3} \qquad \underbrace{\alpha_3^2 = \frac{\rho v^2 - c_{11}}{c_{11}}}_{\rho v^2 = c_{11}+c_{11}\alpha_3^2}$$

$$= \frac{\rho v^2 - c_{11} - c_{55}\alpha_3^2}{(c_{13}+c_{55})\alpha_3} = \frac{c_{11}+c_{11}\alpha_3^2 - c_{11} - c_{55}\alpha_3^2}{(c_{13}+c_{55})\alpha_3} \tag{4.57}$$

$$= \left(\frac{c_{11}-c_{55}}{c_{13}+c_{55}}\right)\alpha_3 = \left(\frac{\lambda+2\mu-\mu}{\lambda+\mu}\right)\alpha_3 = \alpha_3$$

and

$$W_5 = \frac{U_{35}}{U_{15}} = -\frac{c_{11} + c_{55}\alpha^2 - \rho v^2}{(c_{13} + c_{55})\alpha_5} \qquad \alpha_5^2 = \frac{\rho v^2 - \mu}{\mu}$$
$$= \frac{\rho v^2 - c_{11} - c_{55}\alpha_5^2}{(c_{13} + c_{55})\alpha_5} = \frac{\mu + \mu\alpha_5^2 - c_{11} - \mu\alpha_5^2}{(c_{13} + c_{55})\alpha_3} \tag{4.58}$$
$$= \left(\frac{\mu - c_{11}}{(c_{13} + c_{55})\alpha_5} \right) = \left(\frac{\mu - \lambda - 2\mu}{\lambda + \mu} \right) \frac{1}{\alpha_5} = \frac{-1}{\alpha_5}$$

Recall the values d_{1q}, d_{2q}, d_{3q} extracted from Eq. (4.13), i.e.

$$\begin{aligned} d_{1q} &= c_{13} + \alpha_q c_{33} W_q + c_{36} V_q \\ d_{2q} &= \alpha_q c_{45} V_q + c_{55}\left(\alpha_q + W_q\right) \\ d_{3q} &= \alpha_q c_{44} V_q + c_{45}\left(\alpha_q + W_q\right) \end{aligned} \tag{4.59}$$

Recall that $c_{36} = 0$, $c_{45} = 0$; hence, the quantities in Eq. (4.59) associated with Lamb-type waves are

$$\begin{aligned} d_{13} &= c_{13} + \alpha_3 c_{33} W_3 = \lambda + \alpha_3^2(\lambda + 2\mu) \\ &= \lambda + \frac{\rho v^2 - c_{11}}{c_{11}} \cancel{(\lambda + 2\mu)} = \lambda + \rho v^2 - (\lambda + 2\mu) \\ &= \rho v^2 - 2\mu = \mu\left(\frac{\rho v^2 - \mu}{\mu} - 1 \right) = \mu\left(\alpha_5{}^2 - 1\right) \end{aligned} \tag{4.60}$$

$$\begin{aligned} d_{15} &= c_{13} + \alpha_5 c_{33} W_5 = (\lambda) + \alpha_5(\lambda + 2\mu)\left(\frac{-1}{\alpha_5} \right) = -2\mu \\ d_{23} &= c_{55}\left(\alpha_3 + W_3\right) = 2\mu\alpha_3 \\ d_{25} &= c_{55}\left(\alpha_5 + W_5\right) = \mu\frac{\alpha_5{}^2 - 1}{\alpha_5} \end{aligned} \tag{4.61}$$

Recalling Eq. (4.16), and cancelling SH-related terms yields

$$\begin{bmatrix} u_1 \\ \cancel{u_2} \\ u_3 \\ \sigma_{33}^* \\ \sigma_{13}^* \\ \cancel{\sigma_{23}^*} \end{bmatrix} = \begin{bmatrix} 1 & 1 & 1 & 1 & 1 & 1 \\ V_1 & V_1 & V_3 & V_3 & V_5 & V_5 \\ W_1 & -W_1 & W_3 & -W_3 & W_5 & -W_5 \\ d_{11} & d_{11} & d_{13} & d_{13} & d_{15} & d_{15} \\ d_{21} & -d_{21} & d_{23} & -d_{23} & d_{25} & -d_{25} \\ d_{31} & -d_{31} & d_{33} & -d_{33} & d_{35} & -d_{35} \end{bmatrix} \begin{bmatrix} \cancel{U_{11}e^{i\xi\alpha_1 x_3}} \\ \cancel{U_{12}e^{-i\xi\alpha_1 x_3}} \\ U_{13}e^{i\xi\alpha_3 x_3} \\ U_{14}e^{-i\xi\alpha_3 x_3} \\ U_{15}e^{i\xi\alpha_5 x_3} \\ U_{16}e^{-i\xi\alpha_5 x_3} \end{bmatrix} e^{i\xi(x_1 - vt)} \tag{4.62}$$

Upon simplification, the displacements and the stresses for Lamb-type wave solution are given by

$$\begin{bmatrix} u_1 \\ u_3 \\ \sigma_{33}^* \\ \sigma_{13}^* \end{bmatrix} = \begin{bmatrix} 1 & 1 & 1 & 1 \\ W_3 & -W_3 & W_5 & -W_5 \\ d_{13} & d_{13} & d_{15} & d_{15} \\ d_{23} & -d_{23} & d_{25} & -d_{25} \end{bmatrix} \begin{bmatrix} U_{13}e^{i\xi\alpha_3 x_3} \\ U_{14}e^{-i\xi\alpha_3 x_3} \\ U_{15}e^{i\xi\alpha_5 x_3} \\ U_{16}e^{-i\xi\alpha_5 x_3} \end{bmatrix} e^{i\xi(x_1 - vt)} \tag{4.63}$$

We define our layer thickness as *h*, and take $x_3 = 0$ at the top "j-1", $x_3 = -h$ at the bottom "j". To follow Rokhlin et al. (2011), we call the displacements and stress vector in the left hand side of Eq. (4.63) P_k , and we call the 4x4 matrix *X*. The right hand side vector can be decomposed into a diagonal matrix H_k multiplied by the amplitudes vector U_k

$$\begin{bmatrix} u_1 \\ u_3 \\ \sigma_{33}^* \\ \sigma_{13}^* \end{bmatrix} = \begin{bmatrix} 1 & 1 & 1 & 1 \\ W_3 & -W_3 & W_5 & -W_5 \\ d_{13} & d_{13} & d_{15} & d_{15} \\ d_{23} & -d_{23} & d_{25} & -d_{25} \end{bmatrix} \begin{bmatrix} e^{i\xi\alpha_3 x_3} & 0 & 0 & 0 \\ 0 & e^{-i\xi\alpha_3 x_3} & 0 & 0 \\ 0 & 0 & e^{i\xi\alpha_5 x_3} & 0 \\ 0 & 0 & 0 & e^{-i\xi\alpha_5 x_3} \end{bmatrix} \begin{bmatrix} U_{13} \\ U_{14} \\ U_{15} \\ U_{16} \end{bmatrix} e^{i\xi(x_1 - vt)} \tag{4.64}$$

Equation (4.64) is written with *H* functions as

$$\begin{bmatrix} u_1 \\ u_3 \\ \sigma_{33}^* \\ \sigma_{13}^* \end{bmatrix} = \begin{bmatrix} 1 & 1 & 1 & 1 \\ W_3 & -W_3 & W_5 & -W_5 \\ d_{13} & d_{13} & d_{15} & d_{15} \\ d_{23} & -d_{23} & d_{25} & -d_{25} \end{bmatrix} \begin{bmatrix} H_1(x_3) & 0 & 0 & 0 \\ 0 & H_2(x_3) & 0 & 0 \\ 0 & 0 & H_3(x_3) & 0 \\ 0 & 0 & 0 & H_4(x_3) \end{bmatrix} \begin{bmatrix} U_{13} \\ U_{14} \\ U_{15} \\ U_{16} \end{bmatrix} \tag{4.65}$$

i.e. in compact notations and ignoring $e^{i\xi(x_1 - vt)}$,

$$P(x_3) = X\ H(x_3)\ U \tag{4.66}$$

At the top surface "j-1", where $x_3 = 0$, the H diagonal matrix becomes unit matrix, $H(0) = \mathrm{I}$, and Eq. (4.65) becomes

$$\begin{bmatrix} u_1^{j-1} \\ u_3^{j-1} \\ \sigma_{33}^{j-1} \\ \sigma_{13}^{j-1} \end{bmatrix} = \begin{bmatrix} 1 & 1 & 1 & 1 \\ W_3 & -W_3 & W_5 & -W_5 \\ d_{13} & d_{13} & d_{15} & d_{15} \\ d_{23} & -d_{23} & d_{25} & -d_{25} \end{bmatrix} \begin{bmatrix} U_{13} \\ U_{14} \\ U_{15} \\ U_{16} \end{bmatrix} \tag{4.67}$$

At the bottom surface "j", where $x_3 = -h$, we substitute in $e^{i\alpha_3 \xi x_3}$ by $\xi x_3 = -\xi h$, and we call the quantities H_1,..H_4

$$\begin{bmatrix} u_1^{j} \\ u_3^{j} \\ \sigma_{33}^{j} \\ \sigma_{13}^{j} \end{bmatrix} = \begin{bmatrix} H_1 & H_2 & H_3 & H_4 \\ W_3 H_1 & -W_3 H_2 & W_5 H_3 & -W_5 H_4 \\ d_{13} H_1 & d_{13} H_2 & d_{15} H_3 & d_{15} H_4 \\ d_{23} H_1 & -d_{23} H_2 & d_{25} H_3 & -d_{25} H_4 \end{bmatrix} \begin{bmatrix} U_{13} \\ U_{14} \\ U_{15} \\ U_{16} \end{bmatrix} \tag{4.68}$$

Equations (4.67), (4.68) can be written as

$$\begin{aligned} P^{(Top)\,j-1} &= X_k H_k^{j-1} U_k = X_k U_k \quad , \quad H_k^{j-1} = \mathrm{I} \\ P^{(Bottom)\,j} &= X_k H_k^{j} U_k \end{aligned} \tag{4.69}$$

P_k for the top and the bottom of a layer can be combined together as

$$P_k^{(Bot)\,j} = A_k P_k^{(Top)\,j-1} \tag{4.70}$$

where the transfer matrix (TM) is defined as

$$A_k = X_k H_k X_k^{-1} \quad \text{or} \quad A_k = X_k H_k x_k \tag{4.71}$$

where $x_k = X_k^{-1}$. The TM can be multiplied by each other for multilayers

$$A = A_n A_{n-1} \cdots A_1 \tag{4.72}$$

MATLAB consumes considerable time and computation for calculating inverse of matrices. We found that providing MATLAB with the matrix's inverse as elements will

allow us to input them as array of values. This is considered for the efforts to increase the speed of our code. We report here the explicit form for both matrix 'X' and matrix 'x'

$$X = \begin{bmatrix} 1 & 1 & 1 & 1 \\ W_3 & -W_3 & W_5 & -W_5 \\ d_{13} & d_{13} & d_{15} & d_{15} \\ d_{23} & -d_{23} & d_{25} & -d_{25} \end{bmatrix} = \begin{bmatrix} 1 & 1 & 1 & 1 \\ \alpha_3 & -\alpha_3 & \frac{-1}{\alpha_5} & \frac{1}{\alpha_5} \\ d_{13} & d_{13} & d_{15} & d_{15} \\ d_{23} & -d_{23} & d_{25} & -d_{25} \end{bmatrix} \tag{4.73}$$

$$x = \begin{bmatrix} \frac{-d_{15}}{a} & \frac{d_{25}}{b} & \frac{1}{a} & \frac{-W_5}{b} \\ \frac{-d_{15}}{a} & \frac{-d_{25}}{b} & \frac{1}{a} & \frac{W_5}{b} \\ \frac{d_{13}}{a} & \frac{-d_{23}}{b} & \frac{-1}{a} & \frac{W_3}{b} \\ \frac{d_{13}}{a} & \frac{d_{23}}{b} & \frac{-1}{a} & \frac{-W_3}{b} \end{bmatrix} = \begin{bmatrix} \frac{-d_{15}}{a} & \frac{d_{25}}{b} & \frac{1}{a} & \frac{1/\alpha_5}{b} \\ \frac{-d_{15}}{a} & \frac{-d_{25}}{b} & \frac{1}{a} & \frac{-1/\alpha_5}{b} \\ \frac{d_{13}}{a} & \frac{-d_{23}}{b} & \frac{-1}{a} & \frac{\alpha_3}{b} \\ \frac{d_{13}}{a} & \frac{d_{23}}{b} & \frac{-1}{a} & \frac{-\alpha_3}{b} \end{bmatrix} \tag{4.74}$$

$$a = 2(d_{13} - d_{15}) \quad , b = 2\left(W_3 d_{25} - W_5 d_{23}\right) = 2\left(\alpha_3 d_{25} - \left(\frac{-1}{\alpha_5}\right) d_{23}\right)$$

The idea of calculating the matrix inverse before programming is applied also for SH 2x2 matrix; coupled 6x6 matrix; and stiffness matrix method. For a single-layer problem, the procedure can be further simplified. The amplitudes vector U is evaluated from Eq. (4.66)

$$U = \left\{X \; H(0)\right\}^{-1} P^{Top} = \left\{H(0)\right\}^{-1} X^{-1} P^{Top} \tag{4.75}$$

The state vector P for the bottom surface is

$$P^{Bottom} = X \; H(-h) \left\{H(0)\right\}^{-1} X^{-1} P^{Top} \tag{4.76}$$

The transfer matrix for a single layer is defined as

$$A = X \; H(-h) \left\{H(0)\right\}^{-1} X^{-1} \tag{4.77}$$

The TM can be expanded as before in Eq. (4.17) as

$$\begin{Bmatrix} \{\mathbf{u}^{Bottom}\} \\ \{\boldsymbol{\sigma}^{Bottom}\} \end{Bmatrix} = \begin{bmatrix} [\mathbf{A}_{uu}] & [\mathbf{A}_{u\sigma}] \\ [\mathbf{A}_{u\sigma}] & [\mathbf{A}_{\sigma\sigma}] \end{bmatrix} \begin{Bmatrix} \{\mathbf{u}^{Top}\} \\ \{\boldsymbol{\sigma}^{Top}\} \end{Bmatrix} \tag{4.78}$$

Imposing stress free boundary conditions on Eq. (4.78) yields

$$\begin{Bmatrix} \{\mathbf{u}^{Bottom}\} \\ 0 \end{Bmatrix} = \begin{bmatrix} [\mathbf{A}_{uu}] & [\mathbf{A}_{u\sigma}] \\ [\mathbf{A}_{u\sigma}] & [\mathbf{A}_{\sigma\sigma}] \end{bmatrix} \begin{Bmatrix} \{\mathbf{u}^{Top}\} \\ 0 \end{Bmatrix} \tag{4.79}$$

Equation (4.79) can be expanded as

$$\mathbf{u}^{Bottom} = \mathbf{A}_{uu}\mathbf{u}^{Top} \tag{4.80}$$

$$\mathbf{A}_{u\sigma}\mathbf{u}^{Top} = 0 \tag{4.81}$$

Equation (4.81) is an eigenvalue problem that yields to eigenvalues $(\xi h)_j$, *j=1,2,…*using a search of the root of the determinant $|A_{u\sigma}| = 0$. For each eigenvalue ξh we can find the associate eigenvector u_j^{Top}. For each u^{Top}, we use Eq. (4.66) to find P^{Top}, i.e.

$$P^{Top} = \begin{bmatrix} u^{Top} \\ 0 \end{bmatrix} \tag{4.82}$$

Equation (4.82) is substituted into Eq. (4.75) to obtain *U*, i.e.

$$U = \{H(0)\}^{-1} X^{-1} P^{Top} \tag{4.83}$$

The partial amplitudes vector *U* is now used in Eq. (4.66) to get the state vector at each location within the thickness. As a final check, *P* is to evaluated at $x_3 = 0$ to find P^{Bottom} as

$$P^{Bottom} = \begin{bmatrix} u^{Bottom} \\ \sigma^{Bottom} = 0 \end{bmatrix} = X\ H(-h)\ U \tag{4.84}$$

This value of P^{Bottom} should be the same as the value obtained from Eq. (4.80).

Repeating the same steps for SH-solution, i.e., roots of α_i where *q*=1 and 2; the equation to be solved is the middle equation of the system (4.38), i.e.

$$\left(c_{66}+c_{44}\alpha^2-\rho v^2\right)=0 \tag{4.85}$$

for the orthotropic case, the roots of α^2 are

$$\alpha_{1,2}=\pm\sqrt{\frac{\rho v^2-c_{66}}{c_{44}}} \tag{4.86}$$

For the isotropic case, Eq. (4.86) further simplifies as follows

$$\begin{aligned} c_{66}&=\mu \quad , \quad c_{11}=\lambda+2\mu \\ c_s^2&=\frac{\mu}{\rho} \quad , \quad c_p^2=\frac{\lambda+2\mu}{\rho} \end{aligned} \tag{4.87}$$

$$\mu+\mu\alpha^2=\rho v^2 \tag{4.88}$$

$$\alpha_{1,2}=\pm\sqrt{\frac{\rho v^2-\mu}{\mu}}=\pm\sqrt{\frac{\rho v^2}{\rho c_s^2}-1}=\pm\sqrt{\frac{v^2}{c_s^2}-1}=\alpha_{5,6} \tag{4.89}$$

Equation (4.62) reduces to

$$\begin{bmatrix} u_2 \\ \sigma_{23}^* \end{bmatrix}=\begin{bmatrix} V_1 & V_1 \\ d_{31} & -d_{31} \end{bmatrix}\begin{bmatrix} U_{11}e^{i\xi\alpha_1 x_3} \\ U_{12}e^{-i\xi\alpha_1 x_3} \end{bmatrix}e^{i\xi(x_1-vt)} \tag{4.90}$$

The mode shape ratio V_q cannot be determined from the relation $V_q=\frac{U_{2q}}{U_{1q}}$; hence V_1 =1,

and Eq. (4.59) gives

$$d_{31}=\alpha_1 c_{44} \tag{4.91}$$

The layer transfer matrix can be formulated as

$$\begin{bmatrix} u_2^j \\ \sigma_{23}^j \end{bmatrix}=\begin{bmatrix} 1 & 1 \\ d_{31} & -d_{31} \end{bmatrix}\begin{bmatrix} H_1 & 0 \\ 0 & H_2 \end{bmatrix}\begin{bmatrix} 1 & 1 \\ d_{31} & -d_{31} \end{bmatrix}^{-1}\begin{bmatrix} u_2^{j-1} \\ \sigma_{23}^{j-1} \end{bmatrix} \tag{4.92}$$

Matrix X and matrix 'x' can be defined as

$$X=\begin{bmatrix} 1 & 1 \\ d_{31} & -d_{31} \end{bmatrix}, \qquad x=\begin{bmatrix} 1/2 & 1/(2d_{31}) \\ 1/2 & -1/(2d_{31}) \end{bmatrix} \tag{4.93}$$

4.2.1.2. General orthotropic case (arbitrary fiber orientation angle) (monotonic)

Starting from Eq. (4.62), we can expand the exponentials in a diagonal matrix

$$\begin{bmatrix} u_1 \\ u_2 \\ u_3 \\ \sigma^*_{33} \\ \sigma^*_{13} \\ \sigma^*_{23} \end{bmatrix} = \begin{bmatrix} 1 & 1 & 1 & 1 & 1 & 1 \\ V_1 & V_1 & V_3 & V_3 & V_5 & V_5 \\ W_1 & -W_1 & W_3 & -W_3 & W_5 & -W_5 \\ d_{11} & d_{11} & d_{13} & d_{13} & d_{15} & d_{15} \\ d_{21} & -d_{21} & d_{23} & -d_{23} & d_{25} & -d_{25} \\ d_{31} & -d_{31} & d_{33} & -d_{33} & d_{35} & -d_{35} \end{bmatrix} \begin{bmatrix} e^{i\xi\alpha_1 x_3} & & & & & \\ & e^{-i\xi\alpha_1 x_3} & & & & \\ & & e^{i\xi\alpha_3 x_3} & & & \\ & & & e^{-i\xi\alpha_3 x_3} & & \\ & & & & e^{i\xi\alpha_5 x_3} & \\ & & & & & e^{-i\xi\alpha_5 x_3} \end{bmatrix} \begin{bmatrix} U_{11} \\ U_{12} \\ U_{13} \\ U_{14} \\ U_{15} \\ U_{16} \end{bmatrix} e^{i\xi(x_1 - vt)} \tag{4.94}$$

For top surface "j-1" where $x_3 = 0$, the H diagonal matrix becomes unit matrix $H(0) = \mathrm{I}$

$$\begin{bmatrix} u_1^{j-1} \\ u_2^{j-1} \\ u_3^{j-1} \\ \sigma_{33}^{*j-1} \\ \sigma_{13}^{*j-1} \\ \sigma_{23}^{*j-1} \end{bmatrix} = \begin{bmatrix} 1 & 1 & 1 & 1 & 1 & 1 \\ V_1 & V_1 & V_3 & V_3 & V_5 & V_5 \\ W_1 & -W_1 & W_3 & -W_3 & W_5 & -W_5 \\ d_{11} & d_{11} & d_{13} & d_{13} & d_{15} & d_{15} \\ d_{21} & -d_{21} & d_{23} & -d_{23} & d_{25} & -d_{25} \\ d_{31} & -d_{31} & d_{33} & -d_{33} & d_{35} & -d_{35} \end{bmatrix} \begin{bmatrix} U_{11} \\ U_{12} \\ U_{13} \\ U_{14} \\ U_{15} \\ U_{16} \end{bmatrix} \tag{4.95}$$

For the bottom "j" we substitute $x_3 = -h$ in $e^{i\alpha\ \xi x_3}$ to get $\xi x_3 = -\xi h$

$$\begin{bmatrix} u_1^{j} \\ u_2^{j} \\ u_3^{j} \\ \sigma_{33}^{*j} \\ \sigma_{13}^{*j} \\ \sigma_{23}^{*j} \end{bmatrix} = \begin{bmatrix} H_1 & H_2 & H_3 & H_4 & H_5 & H_6 \\ V_1H_1 & V_1H_2 & V_3H_3 & V_3H_4 & V_5H_5 & V_5H_6 \\ W_1H_1 & -W_1H_2 & W_3H_3 & -W_3H_4 & W_5H_5 & -W_5H_6 \\ d_{11}H_1 & d_{11}H_2 & d_{13}H_3 & d_{13}H_4 & d_{15}H_5 & d_{15}H_6 \\ d_{21}H_1 & -d_{21}H_2 & d_{23}H_3 & -d_{23}H_4 & d_{25}H_5 & -d_{25}H_6 \\ d_{31}H_1 & -d_{31}H_2 & d_{33}H_3 & -d_{33}H_4 & d_{35}H_5 & -d_{35}H_6 \end{bmatrix} \begin{bmatrix} U_{11} \\ U_{12} \\ U_{13} \\ U_{14} \\ U_{15} \\ U_{16} \end{bmatrix} \tag{4.96}$$

Although we usually separate the terms $H_1 \ldots H_6$ in the diagonal matrix, but we include them with X matrix as one matrix, because this form will be needed to derive the stiffness matrices.

X matrix is the 6x6 matrix in Eq. (4.95), while the inverse $x_k = X_k^{-1}$ is

$$x = \begin{bmatrix} \frac{d_{15}V_3 - d_{13}V_5}{2a} & \frac{d_{13} - d_{15}}{2a} & \frac{d_{35}d_{23} - d_{33}d_{25}}{2b} & \frac{V_5 - V_3}{2a} & \frac{d_{33}W_5 - d_{35}W_3}{2b} & \frac{d_{25}W_3 - d_{23}W_5}{2b} \\ \frac{d_{15}V_3 - d_{13}V_5}{2a} & \frac{d_{13} - d_{15}}{2a} & -\frac{d_{35}d_{23} - d_{33}d_{25}}{2b} & \frac{V_5 - V_3}{2a} & -\frac{d_{33}W_5 - d_{35}W_3}{2b} & -\frac{d_{25}W_3 - d_{23}W_5}{2b} \\ -\frac{d_{15}V_1 - d_{11}V_5}{2a} & -\frac{d_{11} - d_{15}}{2a} & -\frac{d_{35}d_{21} - d_{31}d_{25}}{2b} & -\frac{V_5 - V_1}{2a} & -\frac{d_{31}W_5 - d_{35}W_1}{2b} & -\frac{d_{25}W_1 - d_{21}W_5}{2b} \\ -\frac{d_{15}V_1 - d_{11}V_5}{2a} & -\frac{d_{11} - d_{15}}{2a} & \frac{d_{35}d_{21} - d_{31}d_{25}}{2b} & -\frac{V_5 - V_1}{2a} & \frac{d_{31}W_5 - d_{35}W_1}{2b} & \frac{d_{25}W_1 - d_{21}W_5}{2b} \\ -\frac{d_{11}V_3 - d_{13}V_1}{2a} & -\frac{d_{13} - d_{11}}{2a} & -\frac{d_{31}d_{23} - d_{33}d_{21}}{2b} & -\frac{V_1 - V_3}{2a} & -\frac{d_{33}W_1 - d_{31}W_3}{2b} & -\frac{d_{21}W_3 - d_{23}W_1}{2b} \\ -\frac{d_{11}V_3 - d_{13}V_1}{2a} & -\frac{d_{13} - d_{11}}{2a} & \frac{d_{31}d_{23} - d_{33}d_{21}}{2b} & -\frac{V_1 - V_3}{2a} & \frac{d_{33}W_1 - d_{31}W_3}{2b} & \frac{d_{21}W_3 - d_{23}W_1}{2b} \end{bmatrix}$$

$$a = (d_{13} - d_{15})V_1 + (d_{15} - d_{11})V_3 + (d_{11} - d_{13})V_5 \quad ,$$
$$b = (d_{35}d_{23} - d_{33}d_{25})W_1 + (d_{31}d_{25} - d_{35}d_{21})W_3 + (d_{33}d_{21} - d_{31}d_{23})W_5 \tag{4.97}$$

4.2.2. Stiffness Matrix Method and the Recursive Algorithm for Multi-Layer Composite

We follow the method of Rokhlin et al. (2011) for constructing the stiffness matrix (SM) instead of TM; this is done by re-arranging terms of the TM such that the displacements at both the top and the bottom of the *j* layer are in a single column matrix. Similarly, the tractions at both the top and the bottom of the *j* layer are combined in one single column matrix. The transfer function between them will be the stiffness matrix $\mathbf{K}^{\mathbf{j}}$

$$\begin{bmatrix} \sigma_{j-1} \\ \sigma_j \end{bmatrix} = \mathbf{K}^{\mathbf{j}} \begin{bmatrix} u_{j-1} \\ u_j \end{bmatrix} \tag{4.98}$$

This is in contrast to the transfer matrix in which the displacements and tractions for each boundary are combined in the one single column vector, Eq. (4.78). The recursive approach to find the "total" stiffness matrix of all layers is documented in Rokhlin et al. (2011). That approach is not as straight forward as the one applied for finding the total

TM. For the total TM, we simply multiply transfer matrix of all individual layers. But the combined SM for two layers A and B as shown by Rokhlin et al. (2011) is

$$\begin{bmatrix}\sigma_0\\ \sigma_2\end{bmatrix}=\begin{bmatrix}K_{11}^{A}+K_{12}^{A}\left(K_{11}^{B}-K_{22}^{A}\right)^{-1}K_{21}^{A} & -K_{12}^{A}\left(K_{11}^{B}-K_{22}^{A}\right)^{-1}K_{12}^{B}\\ K_{21}^{B}\left(K_{11}^{B}-K_{22}^{A}\right)^{-1}K_{21}^{A} & K_{22}^{B}-K_{21}^{B}\left(K_{11}^{B}-K_{22}^{A}\right)^{-1}K_{12}^{B}\end{bmatrix}\begin{bmatrix}u_0\\ u_2\end{bmatrix} \tag{4.99}$$

where σ_0 is the stress vector at the top surface and σ_2 is the stress vector at the bottom surface. For complete understanding of the SMM and the recursive approach, we show how to implement SMM in Nayfeh formulation (Nayfeh, 1995). Recall the *X* matrix of Eq.(4.63), where for simplicity, we consider the case of Lamb waves only (SH waves are decoupled); the *X* matrix is reduced to 4 x 4. Recalling Eqs. (4.67) and (4.68), i.e. the displacements and stress equations at the top and the bottom of a layer. The stiffness matrix is then constructed by combining all stresses terms in one vector and displacement terms in another,

$$\begin{bmatrix}\sigma_{33}^{j-1}\\ \sigma_{13}^{j-1}\\ \sigma_{33}^{j}\\ \sigma_{13}^{j}\end{bmatrix}=\begin{bmatrix}d_{13} & d_{13} & d_{15} & d_{15}\\ d_{23} & -d_{23} & d_{25} & -d_{25}\\ d_{13}H_1 & d_{13}H_2 & d_{15}H_3 & d_{15}H_4\\ d_{23}H_1 & -d_{23}H_2 & d_{25}H_3 & -d_{25}H_4\end{bmatrix}\begin{bmatrix}U_{13}\\ U_{14}\\ U_{15}\\ U_{16}\end{bmatrix} \tag{4.100}$$

$$\begin{bmatrix}u_1^{j-1}\\ u_3^{j-1}\\ u_1^{j}\\ u_3^{j}\end{bmatrix}=\begin{bmatrix}1 & 1 & 1 & 1\\ W_3 & -W_3 & W_5 & -W_5\\ H_1 & H_2 & H_3 & H_4\\ W_3H_1 & -W_3H_2 & W_5H_3 & -W_5H_4\end{bmatrix}\begin{bmatrix}U_{13}\\ U_{14}\\ U_{15}\\ U_{16}\end{bmatrix} \tag{4.101}$$

Define the 4x4 matrix in Eq. (4.100) as **Y**, and the 4x4 matrix of Eq. (4.101) as $\mathbf{Y_2}$; The layer SM is determined from

$$\begin{pmatrix}\boldsymbol{\sigma}_{x_3=0}\\ \boldsymbol{\sigma}_{x_3=h_j}\end{pmatrix}=\mathbf{Y}\ \mathbf{Y}_2^{-1}\begin{pmatrix}\mathbf{u}_{x_3=0}\\ \mathbf{u}_{x_3=h_j}\end{pmatrix} \tag{4.102}$$

where $\mathbf{SM = Y\ Y_2^{-1}}$. Then, the total SM as reported in Rokhlin et al. (2011) and Eq. (4.99) is achieved by the recursive algorithm. For the sake of implementation into Nayfeh (1995) formulation, we constructed a flow chart of Rokhlin algorithm in (**Figure 4.5**) that can be used along with Eqs. (4.100) and (4.101) as a recursive algorithm in the coding of SM in a computer program.

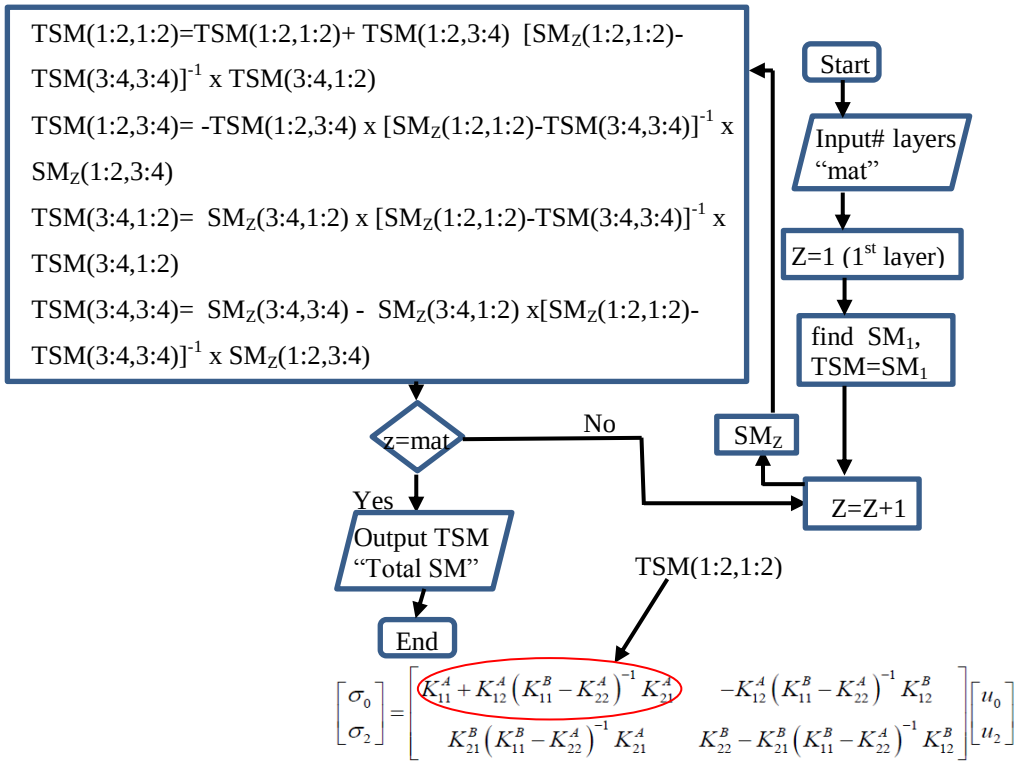

Figure 4.5. Flow chart of total SM recursive algorithm.

We include the intermediate steps of the proof of Eq. (4.99), as it was not reported in Rokhlin et al. (2011). The stiffness matrices for individual layers A and B are defined as

$$\begin{bmatrix}\sigma_0\\ \sigma_1\end{bmatrix}=\begin{bmatrix}K_{11}^A & K_{12}^A\\ K_{21}^A & K_{22}^A\end{bmatrix}\begin{bmatrix}u_0\\ u_1\end{bmatrix}\quad,\quad\begin{bmatrix}\sigma_1\\ \sigma_2\end{bmatrix}=\begin{bmatrix}K_{11}^B & K_{12}^B\\ K_{21}^B & K_{22}^B\end{bmatrix}\begin{bmatrix}u_1\\ u_2\end{bmatrix}\qquad(4.103)$$

The notation of displacements and stresses are shown in **Figure 4.6**; expanding system of equations in (4.103), yields

$$\sigma_0 = K_{11}^A u_0 + K_{12}^A u_1 \tag{4.104}$$

$$\sigma_1 = K_{21}^A u_0 + K_{22}^A u_1 \tag{4.105}$$

$$\sigma_1 = K_{11}^B u_1 + K_{12}^B u_2 \tag{4.106}$$

$$\sigma_2 = K_{21}^B u_1 + K_{22}^B u_2 \tag{4.107}$$

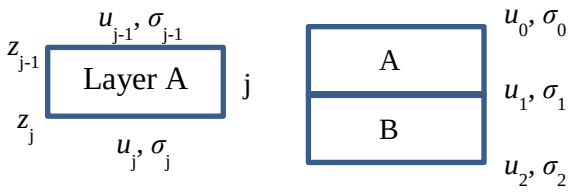

Figure 4.6. Notation of subscripts for displacements and stresses at top and bottom of each layer.

Rearranging Eq. (4.106) and substituting σ_1 from Eq. (4.105) yields

$$K_{11}^B u_1 = \sigma_1 - K_{12}^B u_2 = K_{21}^A u_0 + K_{22}^A u_1 - K_{12}^B u_2 \tag{4.108}$$

$$\left(K_{11}^B - K_{22}^A\right) u_1 = K_{21}^A u_0 - K_{12}^B u_2 \tag{4.109}$$

$$u_1 = \left(K_{11}^B - K_{22}^A\right)^{-1} K_{21}^A u_0 - \left(K_{11}^B - K_{22}^A\right)^{-1} K_{12}^B u_2 \tag{4.110}$$

Substituting the displacement u_1 from Eq. (4.110) into Eq. (4.104), we get

$$\sigma_0 = K_{11}^A u_0 + K_{12}^A \left(K_{11}^B - K_{22}^A\right)^{-1} K_{21}^A u_0 - K_{12}^A \left(K_{11}^B - K_{22}^A\right)^{-1} K_{12}^B u_2 \tag{4.111}$$

$$\sigma_0 = \left[K_{11}^A + K_{12}^A \left(K_{11}^B - K_{22}^A\right)^{-1} K_{21}^A\right] u_0 - \left[K_{12}^A \left(K_{11}^B - K_{22}^A\right)^{-1} K_{12}^B\right] u_2 \tag{4.112}$$

We get the stress at the bottom σ_2 by substituting Eq. (4.110) into Eq. (4.107) as

$$\sigma_2 = \left[K_{21}^B \left(K_{11}^B - K_{22}^A\right)^{-1} K_{21}^A\right] u_0 + \left[K_{22}^B - K_{21}^B \left(K_{11}^B - K_{22}^A\right)^{-1} K_{12}^B\right] u_2 \tag{4.113}$$

Combining Eqs. (4.112) ,(4.113) will result in the form reported by Rokhlin et al. (2011)

$$\begin{bmatrix}\sigma_0\\ \sigma_2\end{bmatrix}=\begin{bmatrix}K_{11}^{A}+K_{12}^{A}\left(K_{11}^{B}-K_{22}^{A}\right)^{-1}K_{21}^{A} & -K_{12}^{A}\left(K_{11}^{B}-K_{22}^{A}\right)^{-1}K_{12}^{B}\\ K_{21}^{B}\left(K_{11}^{B}-K_{22}^{A}\right)^{-1}K_{21}^{A} & K_{22}^{B}-K_{21}^{B}\left(K_{11}^{B}-K_{22}^{A}\right)^{-1}K_{12}^{B}\end{bmatrix}\begin{bmatrix}u_0\\ u_2\end{bmatrix} \tag{4.114}$$

For getting the guided waves roots for dispersion curves, we impose stress-free boundary conditions at the top and the bottom of the overall system, i.e.

$$\begin{bmatrix}\sigma_0\\ \sigma_N\end{bmatrix}=\begin{bmatrix}0\\ 0\end{bmatrix} \tag{4.115}$$

The problem can be solved either by setting $|\mathrm{SM}|=0$, or by solving the homogeneous system of equations. For the 6x6 matrices form (where SH waves are coupled with Lamb-type waves), the following flow chart can be used for coding the algorithm to determine the total SM for multi-layer case.

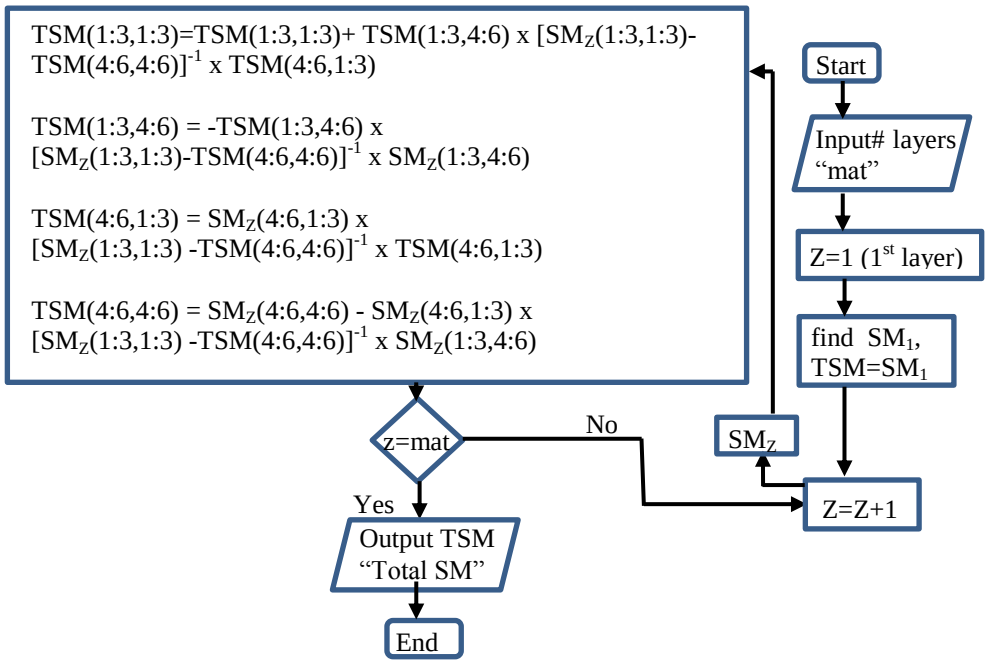

Figure. 4.5(2). Flow chart of total SM recursive algorithm for 6x6 matrix case with three types of waves Symmetric, antisymmetric Lamb waves and shear horizontal waves

4.3. STIFFNESS MATRIX METHOD (SMM) AND STABLE FORMULATION

The Transfer matrices developed earlier had the issue of having exponentials (the exponents' function of the coordinate x_3) either on one column or the diagonal, recalling the abstract form by Rokhlin et al. (2011)

$$\begin{bmatrix} u_j \\ \sigma_j \end{bmatrix} = \begin{bmatrix} P^- H^- & P^+ \\ D^- H^- & D^+ \end{bmatrix}_j \begin{bmatrix} P^- H^- & P^+ \\ D^- H^- & D^+ \end{bmatrix}_j^{-1} \begin{bmatrix} u_{j-1} \\ \sigma_{j-1} \end{bmatrix} \tag{4.116}$$

where P represent the coefficients associated with displacements, i.e. 1 values and W_3, W_5 of Eq. (4.63), while D are the d_{13},d_{15}…d_{25} associated with stresses.

The way the equations are rearranged in the SM needs to consider removing H sub matrices from these critical locations (at one column or the diagonal)

$$\begin{bmatrix} \sigma_{j-1} \\ \sigma_j \end{bmatrix} = \begin{bmatrix} D^- & D^+ H^+ \\ D^- H^- & D^+ \end{bmatrix}_j \begin{bmatrix} P^- & P^+ H^+ \\ P^- H^- & P^+ \end{bmatrix}_j^{-1} \begin{bmatrix} u_{j-1} \\ u_j \end{bmatrix} \tag{4.117}$$

Our objective here is to formulate the equations in the form of 4x4 matrix and in the next section as 6x6 matrix in the form which Rokhlin recommended; so it is easy to be coded, instead of writing the matrices in compact forms. In the following pages, we make the analytical development needed to get the 4x4 SM form and show that H matrices are no longer on diagonal or single column.

The way this is done is by factoring out other exponentials that are going to be merged with the displacement amplitudes of the partial waves, i.e.U_{1q}. By doing that, we eliminate the growing nature of the exponentials as the number of layers increase, or as the wavenumber-thickness increases.

4.3.1. Stable STMM Algorithm for cases of Decoupled Lamb /SH waves in Single, Multi Isotropic Layers and Orthotropic Layers (0/90 fiber orientations)

The deficiency in the numerical evaluation of the TMM (Rokhlin et al., 2011) can be eliminated if the *H* matrices are removed from both diagonal and at single column. We expand the system of Eq. (4.64) as

$$\begin{aligned}
u_1 &= U_{13}e^{i\xi\alpha_3 x_3} + U_{14}e^{-i\xi\alpha_3 x_3} + U_{15}e^{i\xi\alpha_5 x_3} + U_{16}e^{-i\xi\alpha_5 x_3} \\
u_3 &= W_3U_{13}e^{i\xi\alpha_3 x_3} - W_3U_{14}e^{-i\xi\alpha_3 x_3} + W_5U_{15}e^{i\xi\alpha_5 x_3} - W_5U_{16}e^{-i\xi\alpha_5 x_3} \\
\sigma_{33}^{*} &= d_{13}U_{13}e^{i\xi\alpha_3 x_3} + d_{13}U_{14}e^{-i\xi\alpha_3 x_3} + d_{15}U_{15}e^{i\xi\alpha_5 x_3} + d_{15}U_{16}e^{-i\xi\alpha_5 x_3} \\
\sigma_{13}^{*} &= d_{23}U_{13}e^{i\xi\alpha_3 x_3} - d_{23}U_{14}e^{-i\xi\alpha_3 x_3} + d_{25}U_{15}e^{i\xi\alpha_5 x_3} - d_{25}U_{16}e^{-i\xi\alpha_5 x_3}
\end{aligned} \tag{4.118}$$

Re-arranging yields,

$$\begin{aligned}
u_1 &= \left(U_{13}e^{i\xi\alpha_3 z_{j-1}}\right)e^{i\xi\alpha_3\left(x_3 - z_{j-1}\right)} + \left(U_{14}e^{-i\xi\alpha_3 z_j}\right)e^{-i\xi\alpha_3\left(x_3 - z_j\right)} + \\
&\quad \left(U_{15}e^{i\xi\alpha_5 z_{j-1}}\right)e^{i\xi\alpha_5\left(x_3 - z_{j-1}\right)} + \left(U_{16}e^{-i\xi\alpha_5 z_j}\right)e^{-i\xi\alpha_5\left(x_3 - z_j\right)} \\
u_3 &= \left(U_{13}e^{i\xi\alpha_3 z_{j-1}}\right)W_3e^{i\xi\alpha_3\left(x_3 - z_{j-1}\right)} - \left(U_{14}e^{-i\xi\alpha_3 z_j}\right)W_3e^{-i\xi\alpha_3\left(x_3 - z_j\right)} + \\
&\quad \left(U_{15}e^{i\xi\alpha_5 z_{j-1}}\right)W_5e^{i\xi\alpha_5\left(x_3 - z_{j-1}\right)} - \left(U_{16}e^{-i\xi\alpha_5 z_j}\right)W_5e^{-i\xi\alpha_5\left(x_3 - z_j\right)} \\
\sigma_{33}^{*} &= \left(U_{13}e^{i\xi\alpha_3 z_{j-1}}\right)d_{13}e^{i\xi\alpha_3\left(x_3 - z_{j-1}\right)} + \left(U_{14}e^{-i\xi\alpha_3 z_j}\right)d_{13}e^{-i\xi\alpha_3\left(x_3 - z_j\right)} + \\
&\quad \left(U_{15}e^{i\xi\alpha_5 z_{j-1}}\right)d_{15}e^{i\xi\alpha_5\left(x_3 - z_{j-1}\right)} + \left(U_{16}e^{-i\xi\alpha_5 z_j}\right)d_{15}e^{-i\xi\alpha_5\left(x_3 - z_j\right)} \\
\sigma_{13}^{*} &= \left(U_{13}e^{i\xi\alpha_3 z_{j-1}}\right)d_{23}e^{i\xi\alpha_3\left(x_3 - z_{j-1}\right)} - \left(U_{14}e^{-i\xi\alpha_3 z_j}\right)d_{23}e^{-i\xi\alpha_3\left(x_3 - z_j\right)} + \\
&\quad \left(U_{15}e^{i\xi\alpha_5 z_{j-1}}\right)d_{25}e^{i\xi\alpha_5\left(x_3 - z_{j-1}\right)} - \left(U_{16}e^{-i\xi\alpha_5 z_j}\right)d_{25}e^{-i\xi\alpha_5\left(x_3 - z_j\right)}
\end{aligned} \tag{4.119}$$

Now we rearrange the displacements and stresses of Eq. (4.119) in a matrix form. Note that $z_{j-1} - z_j = h_j$. For the top surface "j-1" of the layer, i.e. $x_3 = z_{j-1}$ (**Figure 4.1**)

$$\begin{bmatrix} u_1^{j-1} \\ u_3^{j-1} \\ \sigma_{33}^{j-1} \\ \sigma_{13}^{j-1} \end{bmatrix} = \begin{bmatrix} 1 & e^{i\xi\alpha_3 h_j} & 1 & e^{i\xi\alpha_5 h_j} \\ W_3 & -W_3e^{i\xi\alpha_3 h_j} & W_5 & -W_5e^{i\xi\alpha_5 h_j} \\ d_{13} & d_{13}e^{i\xi\alpha_3 h_j} & d_{15} & d_{15}e^{i\xi\alpha_5 h_j} \\ d_{23} & -d_{23}e^{i\xi\alpha_3 h_j} & d_{25} & -d_{25}e^{i\xi\alpha_5 h_j} \end{bmatrix} \begin{bmatrix} U_{13}e^{i\xi\alpha_3 z_{j-1}} \\ U_{14}e^{-i\xi\alpha_3 z_j} \\ U_{15}e^{i\xi\alpha_5 z_{j-1}} \\ U_{16}e^{-i\xi\alpha_5 z_j} \end{bmatrix} \tag{4.120}$$

For the bottom surface "j", i.e. $x_3 = z_j$

$$\begin{bmatrix} u_1^j \\ u_3^j \\ \sigma_{33}^j \\ \sigma_{13}^j \end{bmatrix} = \begin{bmatrix} e^{i\xi\alpha_3 h_j} & 1 & e^{i\xi\alpha_5 h_j} & 1 \\ W_3 e^{i\xi\alpha_3 h_j} & -W_3 & W_5 e^{i\xi\alpha_5 h_j} & -W_5 \\ d_{13} e^{i\xi\alpha_3 h_j} & d_{13} & d_{15} e^{i\xi\alpha_5 h_j} & d_{15} \\ d_{23} e^{i\xi\alpha_3 h_j} & -d_{23} & d_{25} e^{i\xi\alpha_5 h_j} & -d_{25} \end{bmatrix} \begin{bmatrix} U_{13} e^{i\xi\alpha_3 z_{j-1}} \\ U_{14} e^{-i\xi\alpha_3 z_j} \\ U_{15} e^{i\xi\alpha_5 z_{j-1}} \\ U_{16} e^{-i\xi\alpha_5 z_j} \end{bmatrix} \tag{4.121}$$

The right hand side array of the partial wave amplitudes is always the same and will be eliminated later. Equations (4.120) and (4.121) are rearranged such that we keep exponentials containing the layer thickness at one side of the matrix. This is done by rearranging the elements of the partial wave amplitudes array, without changing the rows sequence of left hand side arrays, Eq. (4.120) will be rearranged as

$$\begin{bmatrix} u_1^{j-1} \\ u_3^{j-1} \\ \sigma_{33}^{j-1} \\ \sigma_{13}^{j-1} \end{bmatrix} = \begin{bmatrix} 1 & 1 & e^{i\xi\alpha_3 h_j} & e^{i\xi\alpha_5 h_j} \\ W_3 & W_5 & -W_3 e^{i\xi\alpha_3 h_j} & -W_5 e^{i\xi\alpha_5 h_j} \\ d_{13} & d_{15} & d_{13} e^{i\xi\alpha_3 h_j} & d_{15} e^{i\xi\alpha_5 h_j} \\ d_{23} & d_{25} & -d_{23} e^{i\xi\alpha_3 h_j} & -d_{25} e^{i\xi\alpha_5 h_j} \end{bmatrix} \begin{bmatrix} U_{13} e^{i\xi\alpha_3 z_{j-1}} \\ U_{15} e^{i\xi\alpha_5 z_{j-1}} \\ U_{14} e^{-i\xi\alpha_3 z_j} \\ U_{16} e^{-i\xi\alpha_5 z_j} \end{bmatrix} \tag{4.122}$$

Call the modified array of the partial wave amplitudes $\{\mathbf{U}\}$. We kept the elements of $\{\mathbf{U}\}$ array to show how they are rearranged. Equation (4.121) will be rearranged in the same way as follows

$$\begin{bmatrix} u_1^j \\ u_3^j \\ \sigma_{33}^j \\ \sigma_{13}^j \end{bmatrix} = \begin{bmatrix} e^{i\xi\alpha_3 h_j} & e^{i\xi\alpha_5 h_j} & 1 & 1 \\ W_3 e^{i\xi\alpha_3 h_j} & W_5 e^{i\xi\alpha_5 h_j} & -W_3 & -W_5 \\ d_{13} e^{i\xi\alpha_3 h_j} & d_{15} e^{i\xi\alpha_5 h_j} & d_{13} & d_{15} \\ d_{23} e^{i\xi\alpha_3 h_j} & d_{25} e^{i\xi\alpha_5 h_j} & -d_{23} & -d_{25} \end{bmatrix} \{\mathbf{U}\} \tag{4.123}$$

So far, the instability sources still exist by having H sub matrices, i.e., elements with exponentials containing layer thickness h_j in complete columns; however, when we

formulate the SM by collecting all the stresses in one array and all the displacements in another array, we get

$$\begin{bmatrix} \sigma_{33}^{j-1} \\ \sigma_{13}^{j-1} \\ \sigma_{33}^{j} \\ \sigma_{13}^{j} \end{bmatrix} = \begin{bmatrix} d_{13} & d_{15} & d_{13}e^{i\xi\alpha_3 h_j} & d_{15}e^{i\xi\alpha_5 h_j} \\ d_{23} & d_{25} & -d_{23}e^{i\xi\alpha_3 h_j} & -d_{25}e^{i\xi\alpha_5 h_j} \\ d_{13}e^{i\xi\alpha_3 h_j} & d_{15}e^{i\xi\alpha_5 h_j} & d_{13} & d_{15} \\ d_{23}e^{i\xi\alpha_3 h_j} & d_{25}e^{i\xi\alpha_5 h_j} & -d_{23} & -d_{25} \end{bmatrix} \cdot \begin{bmatrix} 1 & 1 & e^{i\xi\alpha_3 h_j} & e^{i\xi\alpha_5 h_j} \\ W_3 & W_5 & -W_3 e^{i\xi\alpha_3 h_j} & -W_5 e^{i\xi\alpha_5 h_j} \\ e^{i\xi\alpha_3 h_j} & e^{i\xi\alpha_5 h_j} & 1 & 1 \\ W_3 e^{i\xi\alpha_3 h_j} & W_5 e^{i\xi\alpha_5 h_j} & -W_3 & -W_5 \end{bmatrix}^{-1} \begin{bmatrix} u_1^{j-1} \\ u_3^{j-1} \\ u_1^{j} \\ u_3^{j} \end{bmatrix} \tag{4.124}$$

The product of the two 4x4 matrices is the SM, and to compare the system with Rokhlin et al. (2011) formulation, we condense the system as

$$\begin{bmatrix} \sigma_{j-1} \\ \sigma_j \end{bmatrix} = \begin{bmatrix} D^- & D^+H^+ \\ D^-H^- & D^+ \end{bmatrix}_j \begin{bmatrix} P^- & P^+H^+ \\ P^-H^- & P^+ \end{bmatrix}_j^{-1} \begin{bmatrix} u_{j-1} \\ u_j \end{bmatrix} \tag{4.125}$$

The key point is that H matrices are no longer in the main diagonal nor in a single column. This prevents getting singularity cases when diagonally-placed exponentials containing h_j approach very small numbers, so neither the left 4x4 matrix will be singular nor the right inverse of 4x4 matrix will be undefined.

The above formulation was coded and applied to an isotropic layer of aluminum; this case solved with TMM was shown before in **Figure 4.2**a,b with instability starting at 20 MHz. The new results obtained with SMM and STMM are shown in **Figure 4.7**. The SMM solely is robust and stable at high frequency-thickness values; but it does not find the roots "accurately" in low frequency range. Hence, applying the combined TMM and SMM, (or stable combined STMM), is the best way to get the desired results.

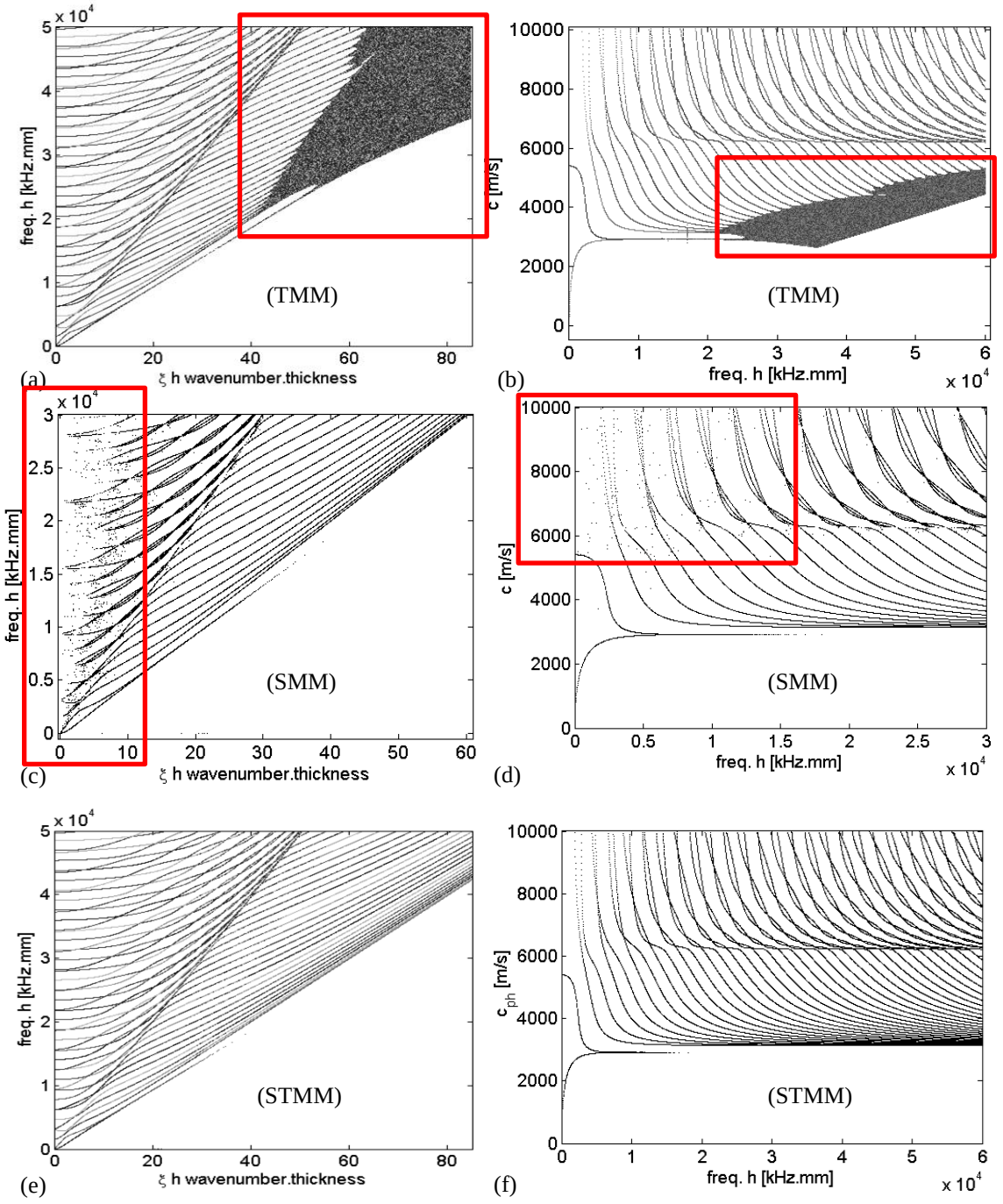

Figure 4.7. Stable STMM for aluminum layer: (a) unstable TMM results in wavenumber-frequency domain; (b) unstable TMM results in frequency-speed domain; (c) stable SMM results in ξh-freq domain; (d) stable SMM results in freq-c domain; (e) stable robust STMM in ξh-freq domain; (f) stable robust STMM in freq-c domain. The frames indicate the regions of numerical instability.

The decoupled SH waves solution is

$$\begin{bmatrix} u_2 \\ \sigma_{23}^* \end{bmatrix} = \begin{bmatrix} V_1 & V_1 \\ d_{31} & -d_{31} \end{bmatrix} \begin{bmatrix} U_{11} e^{i\xi\alpha_1 x_3} \\ U_{12} e^{-i\xi\alpha_1 x_3} \end{bmatrix} \tag{4.126}$$

By following the same procedure, expanding the equations of the system (4.126),

$$\begin{aligned} u_2 &= U_{11} e^{i\xi\alpha_1 x_3} + U_{12} e^{-i\xi\alpha_1 x_3} \\ \sigma_{23}^* &= d_{31} U_{11} e^{i\xi\alpha_1 x_3} - d_{31} U_{12} e^{-i\xi\alpha_1 x_3} \end{aligned} \tag{4.127}$$

$$\begin{aligned} u_2 &= \left(U_{11} e^{i\xi\alpha_1 z_{j-1}} \right) e^{i\xi\alpha_1 \left(x_3 - z_{j-1} \right)} + \left(U_{12} e^{-i\xi\alpha_1 z_j} \right) e^{-i\xi\alpha_1 \left(x_3 - z_j \right)} \\ \sigma_{23}^* &= \left(U_{11} e^{i\xi\alpha_1 z_{j-1}} \right) d_{31} e^{i\xi\alpha_1 \left(x_3 - z_{j-1} \right)} - \left(U_{12} e^{-i\xi\alpha_1 z_j} \right) d_{31} e^{-i\xi\alpha_1 \left(x_3 - z_j \right)} \end{aligned} \tag{4.128}$$

Now we rearrange displacement and stress in matrix form for the upper surface "j-1" of the layer, i.e. $x_3 = z_{j-1}$ and for the bottom surface "j", where $x_3 = z_j$

$$\begin{aligned} \begin{bmatrix} u_2^{j-1} \\ \sigma_{23}^{j-1} \end{bmatrix} &= \begin{bmatrix} 1 & e^{i\xi\alpha_1 h_j} \\ d_{31} & -d_{31} e^{i\xi\alpha_1 h_j} \end{bmatrix} \begin{bmatrix} U_{11} e^{i\xi\alpha_1 z_{j-1}} \\ U_{12} e^{-i\xi\alpha_1 z_j} \end{bmatrix} \\ \begin{bmatrix} u_2^{j} \\ \sigma_{23}^{j} \end{bmatrix} &= \begin{bmatrix} e^{i\xi\alpha_1 h_j} & 1 \\ d_{31} e^{i\xi\alpha_1 h_j} & -d_{31} \end{bmatrix} \begin{bmatrix} U_{11} e^{i\xi\alpha_1 z_{j-1}} \\ U_{12} e^{-i\xi\alpha_1 z_j} \end{bmatrix} \end{aligned} \tag{4.129}$$

For these simple matrices, we can just develop the SM as

$$\begin{bmatrix} \sigma_{23}^{j-1} \\ \sigma_{23}^{j} \end{bmatrix} = \begin{bmatrix} d_{31} & -d_{31} e^{i\xi\alpha_1 h_j} \\ d_{31} e^{i\xi\alpha_1 h_j} & -d_{31} \end{bmatrix} \cdot \begin{bmatrix} 1 & e^{i\xi\alpha_1 h_j} \\ e^{i\xi\alpha_1 h_j} & 1 \end{bmatrix}^{-1} \begin{bmatrix} u_2^{j-1} \\ u_2^{j} \end{bmatrix} \tag{4.130}$$

The product of the two 2x2 matrices is the SM, and it is matching the system of Rokhlin et al. (2011) formulation, the *H* matrices are no longer on the main diagonal nor in a single column. This prevents getting singularity cases when the exponentials containing $\xi\alpha_1 h_j$ approach very small numbers, or big ones; so neither the left 2x2 matrix will be singular nor the inverse of 2x2 matrix will be undefined.

4.3.2. Coupled Guided Waves Case for Orthotropic Layer with Arbitrary Fiber Orientation Angles (Monoclinic)

Expanding the system of equations in (4.94), we can write

$$
\begin{aligned}
u_1 &= U_{11}e^{i\xi\alpha_1 x_3} + U_{12}e^{-i\xi\alpha_1 x_3} + U_{13}e^{i\xi\alpha_3 x_3} + U_{14}e^{-i\xi\alpha_3 x_3} + U_{15}e^{i\xi\alpha_5 x_3} + U_{16}e^{-i\xi\alpha_5 x_3} \\
u_2 &= U_{11}V_1e^{i\xi\alpha_1 x_3} + U_{12}V_1e^{-i\xi\alpha_1 x_3} + U_{13}V_3e^{i\xi\alpha_3 x_3} + U_{14}V_3e^{-i\xi\alpha_3 x_3} + U_{15}V_5e^{i\xi\alpha_5 x_3} + U_{16}V_5e^{-i\xi\alpha_5 x_3} \\
u_3 &= U_{11}W_1e^{i\xi\alpha_1 x_3} - U_{12}W_1e^{-i\xi\alpha_1 x_3} + U_{13}W_3e^{i\xi\alpha_3 x_3} - U_{14}W_3e^{-i\xi\alpha_3 x_3} + U_{15}W_5e^{i\xi\alpha_5 x_3} - U_{16}W_5e^{-i\xi\alpha_5 x_3} \\
\sigma_{33}^{*} &= U_{11}d_{11}e^{i\xi\alpha_1 x_3} + U_{12}d_{11}e^{-i\xi\alpha_1 x_3} + U_{13}d_{13}e^{i\xi\alpha_3 x_3} + U_{14}d_{13}e^{-i\xi\alpha_3 x_3} + U_{15}d_{15}e^{i\xi\alpha_5 x_3} + U_{16}d_{15}e^{-i\xi\alpha_5 x_3} \\
\sigma_{13}^{*} &= U_{11}d_{21}e^{i\xi\alpha_1 x_3} - U_{12}d_{21}e^{-i\xi\alpha_1 x_3} + U_{13}d_{23}e^{i\xi\alpha_3 x_3} - U_{14}d_{23}e^{-i\xi\alpha_3 x_3} + U_{15}d_{25}e^{i\xi\alpha_5 x_3} - U_{16}d_{25}e^{-i\xi\alpha_5 x_3} \\
\sigma_{23}^{*} &= U_{11}d_{31}e^{i\xi\alpha_1 x_3} - U_{12}d_{31}e^{-i\xi\alpha_1 x_3} + U_{13}d_{33}e^{i\xi\alpha_3 x_3} - U_{14}d_{33}e^{-i\xi\alpha_3 x_3} + U_{15}d_{35}e^{i\xi\alpha_5 x_3} - U_{16}d_{35}e^{-i\xi\alpha_5 x_3}
\end{aligned}
\tag{4.131}
$$

Rearranging yields,

$$
\begin{aligned}
u_1 &= \left(U_{11}e^{i\xi\alpha_1 z_{j-1}}\right)e^{i\xi\alpha_1\left(x_3-z_{j-1}\right)} + \left(U_{12}e^{-i\xi\alpha_1 z_j}\right)e^{-i\xi\alpha_1\left(x_3-z_j\right)} + \left(U_{13}e^{i\xi\alpha_3 z_{j-1}}\right)e^{i\xi\alpha_3\left(x_3-z_{j-1}\right)} \\
&\quad + \left(U_{14}e^{-i\xi\alpha_3 z_j}\right)e^{-i\xi\alpha_3\left(x_3-z_j\right)} + \left(U_{15}e^{i\xi\alpha_5 z_{j-1}}\right)e^{i\xi\alpha_5\left(x_3-z_{j-1}\right)} + \left(U_{16}e^{-i\xi\alpha_5 z_j}\right)e^{-i\xi\alpha_5\left(x_3-z_j\right)} \\
u_2 &= \left(U_{11}e^{i\xi\alpha_1 z_{j-1}}\right)V_1e^{i\xi\alpha_1\left(x_3-z_{j-1}\right)} + \left(U_{12}e^{-i\xi\alpha_1 z_j}\right)V_1e^{-i\xi\alpha_1\left(x_3-z_j\right)} + \left(U_{13}e^{i\xi\alpha_3 z_{j-1}}\right)V_3e^{i\xi\alpha_3\left(x_3-z_{j-1}\right)} \\
&\quad + \left(U_{14}e^{-i\xi\alpha_3 z_j}\right)V_3e^{-i\xi\alpha_3\left(x_3-z_j\right)} + \left(U_{15}e^{i\xi\alpha_5 z_{j-1}}\right)V_5e^{i\xi\alpha_5\left(x_3-z_{j-1}\right)} + \left(U_{16}e^{-i\xi\alpha_5 z_j}\right)V_5e^{-i\xi\alpha_5\left(x_3-z_j\right)} \\
u_3 &= \left(U_{11}e^{i\xi\alpha_1 z_{j-1}}\right)W_1e^{i\xi\alpha_1\left(x_3-z_{j-1}\right)} - \left(U_{12}e^{-i\xi\alpha_1 z_j}\right)W_1e^{-i\xi\alpha_1\left(x_3-z_j\right)} + \left(U_{13}e^{i\xi\alpha_3 z_{j-1}}\right)W_3e^{i\xi\alpha_3\left(x_3-z_{j-1}\right)} \\
&\quad - \left(U_{14}e^{-i\xi\alpha_3 z_j}\right)W_3e^{-i\xi\alpha_3\left(x_3-z_j\right)} + \left(U_{15}e^{i\xi\alpha_5 z_{j-1}}\right)W_5e^{i\xi\alpha_5\left(x_3-z_{j-1}\right)} - \left(U_{16}e^{-i\xi\alpha_5 z_j}\right)W_5e^{-i\xi\alpha_5\left(x_3-z_j\right)} \\
\sigma_{33}^{*} &= \left(U_{11}e^{i\xi\alpha_1 z_{j-1}}\right)d_{11}e^{i\xi\alpha_1\left(x_3-z_{j-1}\right)} + \left(U_{12}e^{-i\xi\alpha_1 z_j}\right)d_{11}e^{-i\xi\alpha_1\left(x_3-z_j\right)} + \left(U_{13}e^{i\xi\alpha_3 z_{j-1}}\right)d_{13}e^{i\xi\alpha_3\left(x_3-z_{j-1}\right)} \\
&\quad + \left(U_{14}e^{-i\xi\alpha_3 z_j}\right)d_{13}e^{-i\xi\alpha_3\left(x_3-z_j\right)} + \left(U_{15}e^{i\xi\alpha_5 z_{j-1}}\right)d_{15}e^{i\xi\alpha_5\left(x_3-z_{j-1}\right)} + \left(U_{16}e^{-i\xi\alpha_5 z_j}\right)d_{15}e^{-i\xi\alpha_5\left(x_3-z_j\right)} \\
\sigma_{13}^{*} &= \left(U_{11}e^{i\xi\alpha_1 z_{j-1}}\right)d_{21}e^{i\xi\alpha_1\left(x_3-z_{j-1}\right)} - \left(U_{12}e^{-i\xi\alpha_1 z_j}\right)d_{21}e^{-i\xi\alpha_1\left(x_3-z_j\right)} + \left(U_{13}e^{i\xi\alpha_3 z_{j-1}}\right)d_{23}e^{i\xi\alpha_3\left(x_3-z_{j-1}\right)} \\
&\quad - \left(U_{14}e^{-i\xi\alpha_3 z_j}\right)d_{23}e^{-i\xi\alpha_3\left(x_3-z_j\right)} + \left(U_{15}e^{i\xi\alpha_5 z_{j-1}}\right)d_{25}e^{i\xi\alpha_5\left(x_3-z_{j-1}\right)} - \left(U_{16}e^{-i\xi\alpha_5 z_j}\right)d_{25}e^{-i\xi\alpha_5\left(x_3-z_j\right)} \\
\sigma_{23}^{*} &= \left(U_{11}e^{i\xi\alpha_1 z_{j-1}}\right)d_{31}e^{i\xi\alpha_1\left(x_3-z_{j-1}\right)} - \left(U_{12}e^{-i\xi\alpha_1 z_j}\right)d_{31}e^{-i\xi\alpha_1\left(x_3-z_j\right)} + \left(U_{13}e^{i\xi\alpha_3 z_{j-1}}\right)d_{33}e^{i\xi\alpha_3\left(x_3-z_{j-1}\right)} \\
&\quad - \left(U_{14}e^{-i\xi\alpha_3 z_j}\right)d_{33}e^{-i\xi\alpha_3\left(x_3-z_j\right)} + \left(U_{15}e^{i\xi\alpha_5 z_{j-1}}\right)d_{35}e^{i\xi\alpha_5\left(x_3-z_{j-1}\right)} - \left(U_{16}e^{-i\xi\alpha_5 z_j}\right)d_{35}e^{-i\xi\alpha_5\left(x_3-z_j\right)}
\end{aligned}
\tag{4.132}
$$

Rearranging the displacements and stresses of Eq. (4.132) in a matrix form, we obtain:

For the top surface "j-1" of the layer, i.e., $x_3 = z_{j-1}$,

$$\begin{bmatrix} u_1^{j-1} \\ u_2^{j-1} \\ u_3^{j-1} \\ \sigma_{33}^{*j-1} \\ \sigma_{13}^{*j-1} \\ \sigma_{23}^{*j-1} \end{bmatrix} = \begin{bmatrix} 1 & e^{i\xi\alpha_1 h_j} & 1 & e^{i\xi\alpha_3 h_j} & 1 & e^{i\xi\alpha_5 h_j} \\ V_1 & V_1 e^{i\xi\alpha_1 h_j} & V_3 & V_3 e^{i\xi\alpha_3 h_j} & V_5 & V_5 e^{i\xi\alpha_5 h_j} \\ W_1 & -W_1 e^{i\xi\alpha_1 h_j} & W_3 & -W_3 e^{i\xi\alpha_3 h_j} & W_5 & -W_5 e^{i\xi\alpha_5 h_j} \\ d_{11} & d_{11} e^{i\xi\alpha_1 h_j} & d_{13} & d_{13} e^{i\xi\alpha_3 h_j} & d_{15} & d_{15} e^{i\xi\alpha_5 h_j} \\ d_{21} & -d_{21} e^{i\xi\alpha_1 h_j} & d_{23} & -d_{23} e^{i\xi\alpha_3 h_j} & d_{25} & -d_{25} e^{i\xi\alpha_5 h_j} \\ d_{31} & -d_{31} e^{i\xi\alpha_1 h_j} & d_{33} & -d_{33} e^{i\xi\alpha_3 h_j} & d_{35} & -d_{35} e^{i\xi\alpha_5 h_j} \end{bmatrix} \begin{bmatrix} U_{11} e^{i\xi\alpha_1 z_{j-1}} \\ U_{12} e^{-i\xi\alpha_1 z_j} \\ U_{13} e^{i\xi\alpha_3 z_{j-1}} \\ U_{14} e^{-i\xi\alpha_3 z_j} \\ U_{15} e^{i\xi\alpha_5 z_{j-1}} \\ U_{16} e^{-i\xi\alpha_5 z_j} \end{bmatrix}$$

(4.133)

For the bottom surface "j", i.e., $x_3 = z_j$,

$$\begin{bmatrix} u_1^{j} \\ u_2^{j} \\ u_3^{j} \\ \sigma_{33}^{*j} \\ \sigma_{13}^{*j} \\ \sigma_{23}^{*j} \end{bmatrix} = \begin{bmatrix} e^{i\xi\alpha_1 h_j} & 1 & e^{i\xi\alpha_3 h_j} & 1 & e^{i\xi\alpha_5 h_j} & 1 \\ V_1 e^{i\xi\alpha_1 h_j} & V_1 & V_3 e^{i\xi\alpha_3 h_j} & V_3 & V_5 e^{i\xi\alpha_5 h_j} & V_5 \\ W_1 e^{i\xi\alpha_1 h_j} & -W_1 & W_3 e^{i\xi\alpha_3 h_j} & -W_3 & W_5 e^{i\xi\alpha_5 h_j} & -W_5 \\ d_{11} e^{i\xi\alpha_1 h_j} & d_{11} & d_{13} e^{i\xi\alpha_3 h_j} & d_{13} & d_{15} e^{i\xi\alpha_5 h_j} & d_{15} \\ d_{21} e^{i\xi\alpha_1 h_j} & -d_{21} & d_{23} e^{i\xi\alpha_3 h_j} & -d_{23} & d_{25} e^{i\xi\alpha_5 h_j} & -d_{25} \\ d_{31} e^{i\xi\alpha_1 h_j} & -d_{31} & d_{33} e^{i\xi\alpha_3 h_j} & -d_{33} & d_{35} e^{i\xi\alpha_5 h_j} & -d_{35} \end{bmatrix} \begin{bmatrix} U_{11} e^{i\xi\alpha_1 z_{j-1}} \\ U_{12} e^{-i\xi\alpha_1 z_j} \\ U_{13} e^{i\xi\alpha_3 z_{j-1}} \\ U_{14} e^{-i\xi\alpha_3 z_j} \\ U_{15} e^{i\xi\alpha_5 z_{j-1}} \\ U_{16} e^{-i\xi\alpha_5 z_j} \end{bmatrix}$$

(4.134)

The right hand side array of the partial wave amplitudes is always the same and will be eliminated later. Equations (4.133), (4.134) are rearranged such that we keep exponentials containing the layer thickness at one side of the matrix. This is done by rearranging the elements of the partial wave amplitudes array without changing the rows sequence of left hand side arrays, Eq. (4.133) will be rearranged as

$$\begin{bmatrix} u_1^{j-1} \\ u_2^{j-1} \\ u_3^{j-1} \\ \sigma_{33}^{*j-1} \\ \sigma_{13}^{*j-1} \\ \sigma_{23}^{*j-1} \end{bmatrix} = \begin{bmatrix} 1 & 1 & 1 & e^{i\xi\alpha_1 h_j} & e^{i\xi\alpha_3 h_j} & e^{i\xi\alpha_5 h_j} \\ V_1 & V_3 & V_5 & V_1 e^{i\xi\alpha_1 h_j} & V_3 e^{i\xi\alpha_3 h_j} & V_5 e^{i\xi\alpha_5 h_j} \\ W_1 & W_3 & W_5 & -W_1 e^{i\xi\alpha_1 h_j} & -W_3 e^{i\xi\alpha_3 h_j} & -W_5 e^{i\xi\alpha_5 h_j} \\ d_{11} & d_{13} & d_{15} & d_{11} e^{i\xi\alpha_1 h_j} & d_{13} e^{i\xi\alpha_3 h_j} & d_{15} e^{i\xi\alpha_5 h_j} \\ d_{21} & d_{23} & d_{25} & -d_{21} e^{i\xi\alpha_1 h_j} & -d_{23} e^{i\xi\alpha_3 h_j} & -d_{25} e^{i\xi\alpha_5 h_j} \\ d_{31} & d_{33} & d_{35} & -d_{31} e^{i\xi\alpha_1 h_j} & -d_{33} e^{i\xi\alpha_3 h_j} & -d_{35} e^{i\xi\alpha_5 h_j} \end{bmatrix} \begin{bmatrix} U_{11} e^{i\xi\alpha_1 z_{j-1}} \\ U_{13} e^{i\xi\alpha_3 z_{j-1}} \\ U_{15} e^{i\xi\alpha_5 z_{j-1}} \\ U_{12} e^{-i\xi\alpha_1 z_j} \\ U_{14} e^{-i\xi\alpha_3 z_j} \\ U_{16} e^{-i\xi\alpha_5 z_j} \end{bmatrix}$$

(4.135)

Call the modified array of partial wave amplitudes $\{\mathbf{U}\}$. We kept the elements of $\{\mathbf{U}\}$ array to show how they are rearranged. Equation (4.134) will be rearranged in the same was as follows

$$\begin{bmatrix} u_1^{j} \\ u_2^{j} \\ u_3^{j} \\ \sigma_{33}^{*j} \\ \sigma_{13}^{*j} \\ \sigma_{23}^{*j} \end{bmatrix} = \begin{bmatrix} e^{i\xi\alpha_1 h_j} & e^{i\xi\alpha_3 h_j} & e^{i\xi\alpha_5 h_j} & 1 & 1 & 1 \\ V_1 e^{i\xi\alpha_1 h_j} & V_3 e^{i\xi\alpha_3 h_j} & V_5 e^{i\xi\alpha_5 h_j} & V_1 & V_3 & V_5 \\ W_1 e^{i\xi\alpha_1 h_j} & W_3 e^{i\xi\alpha_3 h_j} & W_5 e^{i\xi\alpha_5 h_j} & -W_1 & -W_3 & -W_5 \\ d_{11} e^{i\xi\alpha_1 h_j} & d_{13} e^{i\xi\alpha_3 h_j} & d_{15} e^{i\xi\alpha_5 h_j} & d_{11} & d_{13} & d_{15} \\ d_{21} e^{i\xi\alpha_1 h_j} & d_{23} e^{i\xi\alpha_3 h_j} & d_{25} e^{i\xi\alpha_5 h_j} & -d_{21} & -d_{23} & -d_{25} \\ d_{31} e^{i\xi\alpha_1 h_j} & d_{33} e^{i\xi\alpha_3 h_j} & d_{35} e^{i\xi\alpha_5 h_j} & -d_{31} & -d_{33} & -d_{35} \end{bmatrix} \{\mathrm{U}\} \quad (4.136)$$

So far, the instability sources still exist by having H sub matrices, i.e., elements with exponentials containing layer thickness h_j in complete columns; however, when we formulate the SM by collecting all the stresses in one array and all the displacements in another array, we get

$$\begin{bmatrix} \sigma_{33}^{*j-1} \\ \sigma_{13}^{*j-1} \\ \sigma_{23}^{*j-1} \\ \sigma_{33}^{*j} \\ \sigma_{13}^{*j} \\ \sigma_{23}^{*j} \end{bmatrix} = \begin{bmatrix} d_{11} & d_{13} & d_{15} & d_{11}e^{i\xi\alpha_1 h_j} & d_{13}e^{i\xi\alpha_3 h_j} & d_{15}e^{i\xi\alpha_5 h_j} \\ d_{21} & d_{23} & d_{25} & -d_{21}e^{i\xi\alpha_1 h_j} & -d_{23}e^{i\xi\alpha_3 h_j} & -d_{25}e^{i\xi\alpha_5 h_j} \\ d_{31} & d_{33} & d_{35} & -d_{31}e^{i\xi\alpha_1 h_j} & -d_{33}e^{i\xi\alpha_3 h_j} & -d_{35}e^{i\xi\alpha_5 h_j} \\ d_{11}e^{i\xi\alpha_1 h_j} & d_{13}e^{i\xi\alpha_3 h_j} & d_{15}e^{i\xi\alpha_5 h_j} & d_{11} & d_{13} & d_{15} \\ d_{21}e^{i\xi\alpha_1 h_j} & d_{23}e^{i\xi\alpha_3 h_j} & d_{25}e^{i\xi\alpha_5 h_j} & -d_{21} & -d_{23} & -d_{25} \\ d_{31}e^{i\xi\alpha_1 h_j} & d_{33}e^{i\xi\alpha_3 h_j} & d_{35}e^{i\xi\alpha_5 h_j} & -d_{31} & -d_{33} & -d_{35} \end{bmatrix} \cdot$$
$$\begin{bmatrix} 1 & 1 & 1 & e^{i\xi\alpha_1 h_j} & e^{i\xi\alpha_3 h_j} & e^{i\xi\alpha_5 h_j} \\ V_1 & V_3 & V_5 & V_1 e^{i\xi\alpha_1 h_j} & V_3 e^{i\xi\alpha_3 h_j} & V_5 e^{i\xi\alpha_5 h_j} \\ W_1 & W_3 & W_5 & -W_1 e^{i\xi\alpha_1 h_j} & -W_3 e^{i\xi\alpha_3 h_j} & -W_5 e^{i\xi\alpha_5 h_j} \\ e^{i\xi\alpha_1 h_j} & e^{i\xi\alpha_3 h_j} & e^{i\xi\alpha_5 h_j} & 1 & 1 & 1 \\ V_1 e^{i\xi\alpha_1 h_j} & V_3 e^{i\xi\alpha_3 h_j} & V_5 e^{i\xi\alpha_5 h_j} & V_1 & V_3 & V_5 \\ W_1 e^{i\xi\alpha_1 h_j} & W_3 e^{i\xi\alpha_3 h_j} & W_5 e^{i\xi\alpha_5 h_j} & -W_1 & -W_3 & -W_5 \end{bmatrix}^{-1} \begin{bmatrix} u_1^{j-1} \\ u_2^{j-1} \\ u_3^{j-1} \\ u_1^{j} \\ u_2^{j} \\ u_3^{j} \end{bmatrix} \quad (4.137)$$

The product of the two 6x6 matrices is the SM. Comparing the system with Rokhlin et al. (2011) formulation, the system condenses to

$$\begin{bmatrix} \sigma_{j-1} \\ \sigma_j \end{bmatrix} = \begin{bmatrix} D^- & D^+H^+ \\ D^-H^- & D^+ \end{bmatrix}_j \begin{bmatrix} P^- & P^+H^+ \\ P^-H^- & P^+ \end{bmatrix}_j^{-1} \begin{bmatrix} u_{j-1} \\ u_j \end{bmatrix} \quad (4.138)$$

4.4. FRAMEWORK OF STMM AND SEPARATING MODES BY MODE TRACING

Root solving methods are mostly numerical and iterative; it was reported in Lowe (1995); Pavlakovic and Lowe (2003) that roots can be determined in a robust way by varying the phase velocity at fixed frequency or vice versa. An initial guess is needed and root tracing is achieved by linear extrapolation of two roots. Afterwards, when sufficient number of roots is determined, a quadratic extrapolation is used. We used this approach on our roots to get initial separation for individual modes; later on, mode shapes can be used to identify similar wave types, e.g. symmetric Lamb waves, antisymmetric Lamb

waves, and SH waves, which in turn are symmetric and antisymmetric. We show in **Figure 4.8** how to separate modes based on their modeshapes solution, once the roots of dispersion wavenumber-frequency are obtained; the displacement fields (e.g., u_x) for the top surface and the bottom surface can be evaluated. The displacements U_T, U_B represent the x-displacements of the top and the bottom respectively.

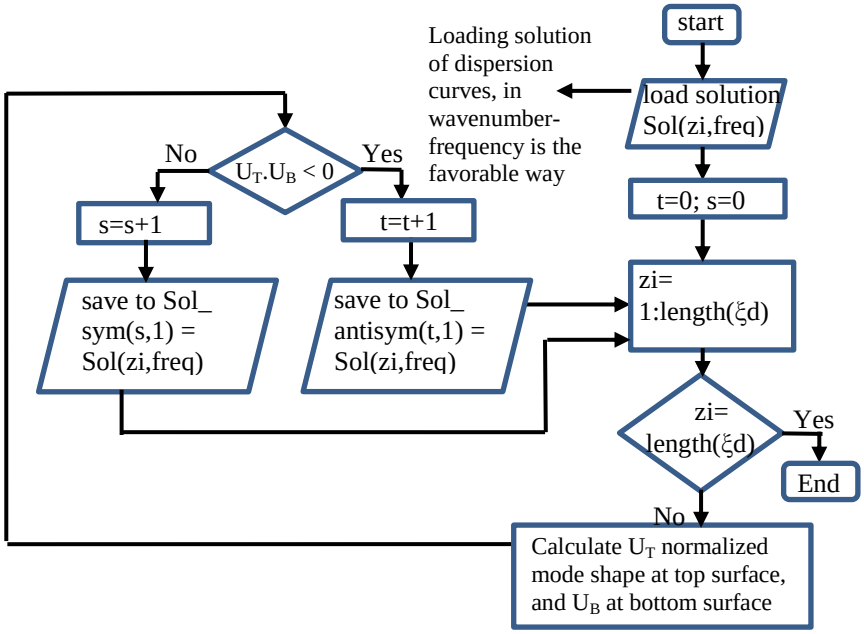

Figure 4.8. The technique for separating modes based on mode shapes

We exemplify the procedure of separating modes by the cubic splines extrapolation for a unidirectional T300/914 CFRP layer with the material properties in Eq. (4.28). We used just one single unidirectional layer and obtained the plots in **Figure 4.9**a for $\xi h < 7$. Because the fibers are orthotropic with fiber orientation angle zero with respect to wave propagation direction; the SH-wave solution is decoupled from Lamb-type waves (**Figure 4.9**). The instability of TMM solution for high ξh values is shown in **Figure 4.11**a. However, the TMM gives a good and accurate solution in the region with ξh less than ≈ 7. An exponential function was used to separate the frequency-

wavenumber domain into two regions. The separation function used was $y = 6.2(e^{1.1x} - 1)$, where y is the frequency axis, and x is the wavenumber axis. The SMM solution alone showed a stable solution in the region $\xi h > 7$. However, it did not give a correct solution pattern at the low wavenumber region (**Figure 4.10**). Hence, a combined solution by TMM and SMM is used to obtain a stable and correct solution over the entire solving domain. We call this combined method the stiffness transfer matrix method (STMM). **Figure 4.11**b shows the complete frequency - wavenumber solution using STMM. **Figure 4.11**c,d show phase velocity and group velocity solutions, respectively.

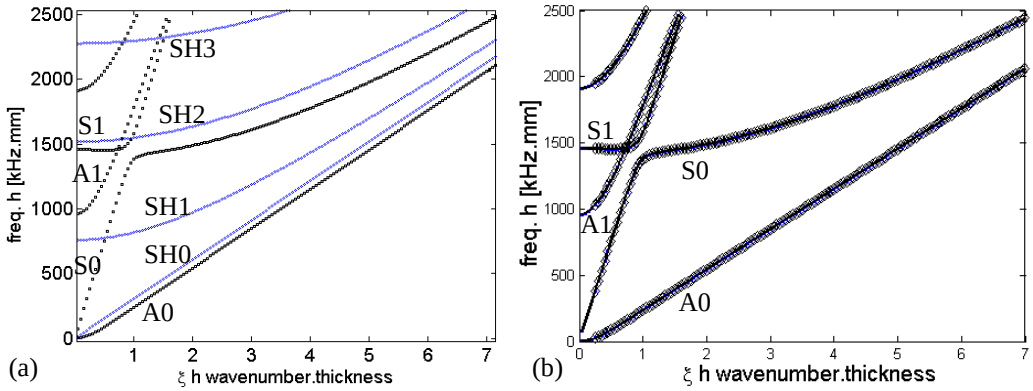

Figure 4.9. The TMM wavenumber-frequency dispersion plots for a unidirectional CFRP layer: (a) the raw data or roots; (b) separation of modes based on cubic extrapolation

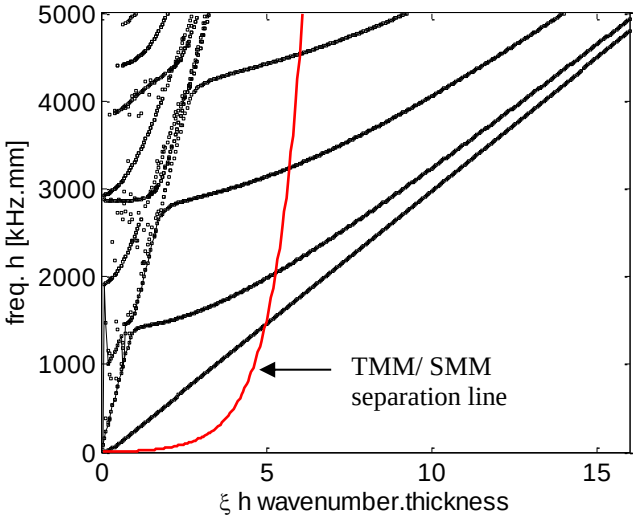

Figure 4.10. SMM solution over the whole domain for a unidirectional CFRP layer.

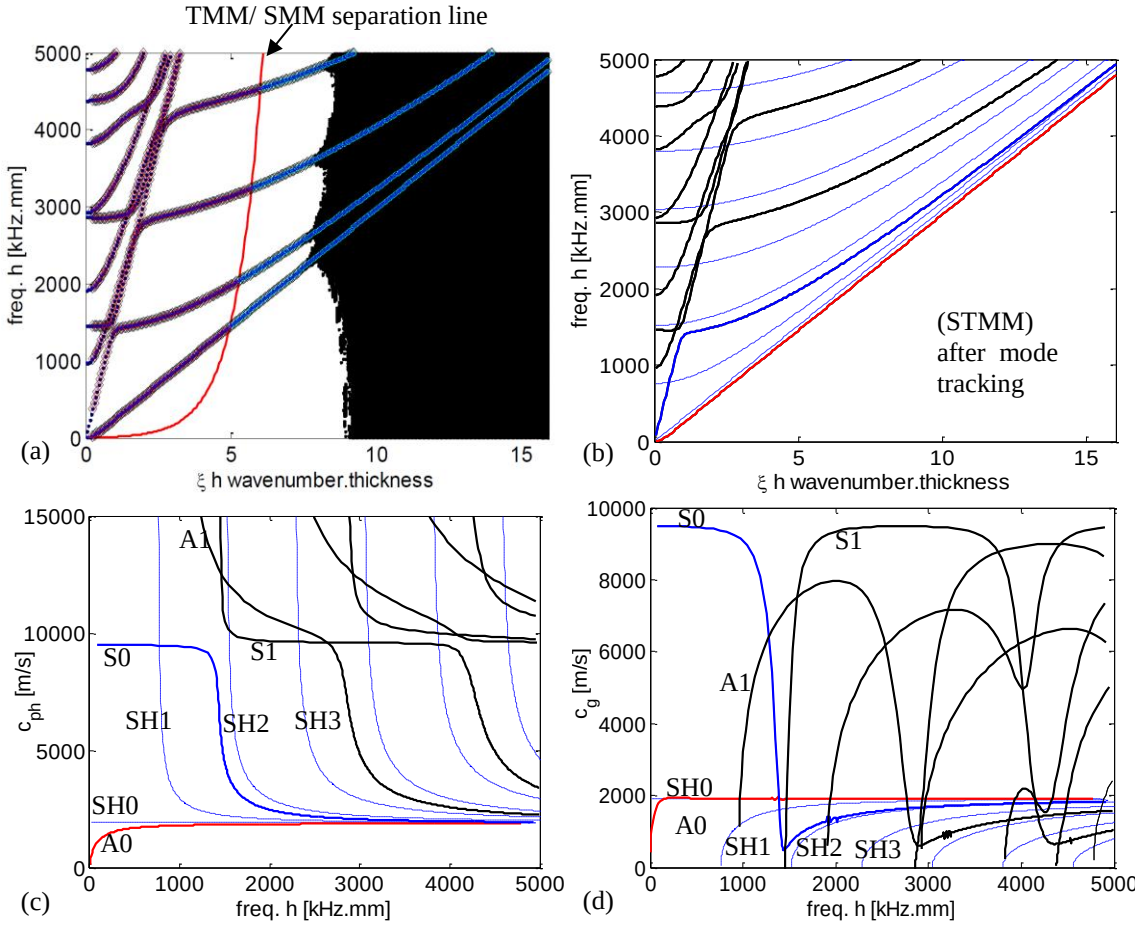

Figure 4.11. Dispersion plots of a unidirectional CFRP layer: (a) instability of TMM and mode tracking between TMM solution, then SMM solution; (b) complete solution using STMM; (c) complete phase velocity solution using STMM; (d) complete group velocity solution using STMM. —— Lamb wave solution, - - - Shear horizontal wave solution

Similar analysis was performed for unidirectional CFRP lamina with fibers at 45º angle from wave propagation direction. **Figure 4.12**a shows the instability of TMM and the STMM combined solution using TMM to the left of the separation line and SMM to the right of the separation line. **Figure 4.12**b shows the complete STMM frequency - wavenumber solution. **Figure 4.12**c,d show the phase velocity solution of TMM and the STMM, respectively. **Figure 4.12**e,f show the group velocity solution of TMM and STMM, respectively.

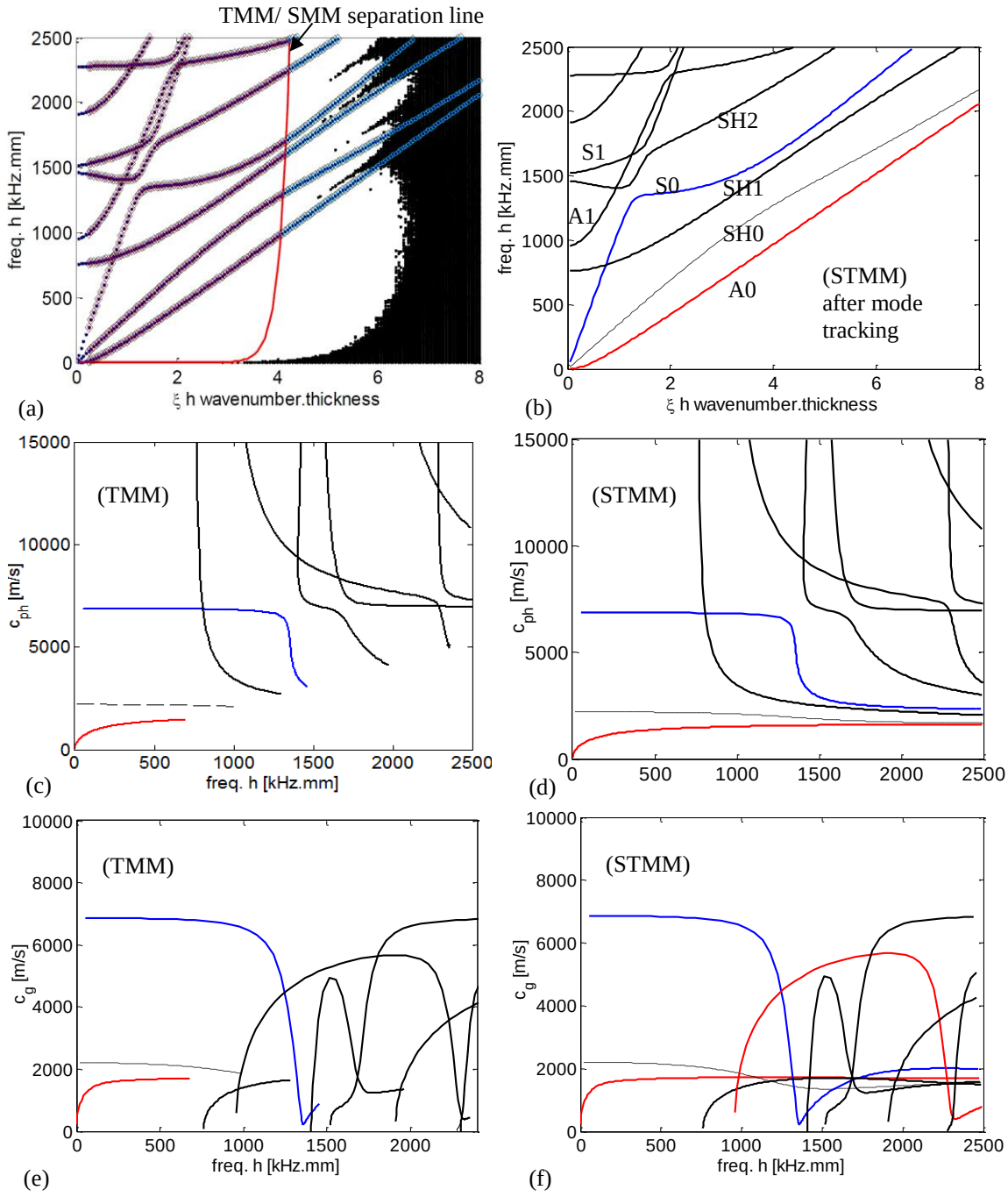

Figure 4.12. Dispersion plots of a unidirectional CFRP layer with 45º fibers: (a) instability of TMM and mode tracking between TMM solution, then SMM solution; (b) complete solution using STMM; (c) phase velocity using only the stable region of the TMM solution (d) complete phase velocity solution using STMM; (e) group velocity using only the stable region of the TMM solution; (f) complete group velocity solution using STMM. —— Lamb wave solution, - - - Shear horizontal wave solution

The last case study is applying STMM to anisotropic multilayer composite laminate.

We used cross-ply CFRP composite laminate [0/90] to show the STMM solution in the $\xi h - \text{freq}$ domain. The phase and group velocities are shown in the comparative study section. The layer of 0º fibers has the same stiffness coefficients of previous unidirectional CFRP. The layer of the 90º fibers has stiffness coefficients that can be calculated by transformation matrix. **Figure 4.13**a shows the $\xi h - \text{freq}$ roots of the final solution. **Figure 4.13**b shows the separated modes in the $\xi h - \text{freq}$ domain.

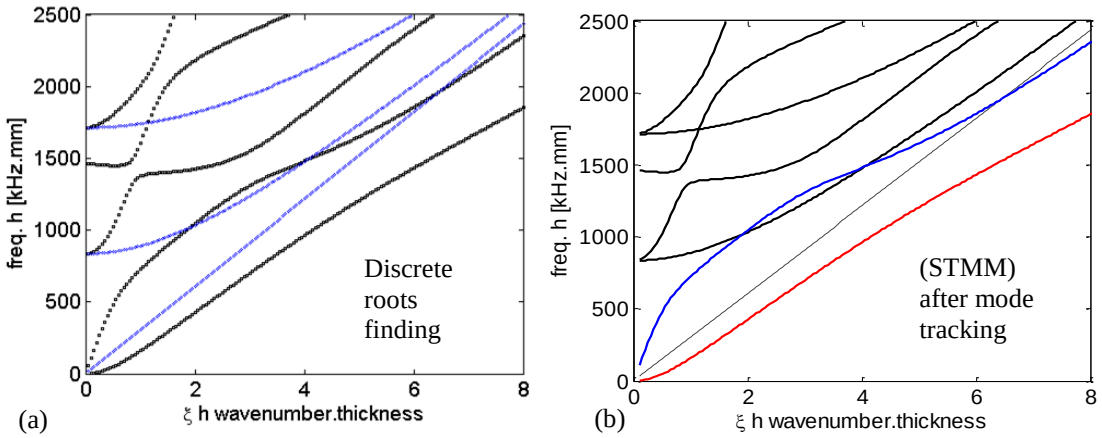

Figure 4.13. Dispersion plots of cross ply fiber composite laminate [0/90]: (a) root finding; (b) complete wavenumber-frequency solution using STMM. —— Lamb wave solution, - - - Shear horizontal wave solution

4.5. STMM MATLAB GRAPHICAL USER INTERFACE

A MATLAB graphical user interface (GUI) has been developed and the STMM procedure was coded for quicker and easier analysis (**Figure 4.14**). First, the unstable TMM solution can be loaded either in wavenumber-frequency domain or frequency-phase velocity domain. The software aims at providing displacement and stress mode shapes at any given root of dispersion plots. STMM button is used to provide the complete stable dispersion curves in frequency-phase velocity domain, as shown in **Figure 4.15**. Finally, after selecting a point on the dispersion curves, Calc. button is used

to display displacements and stresses modeshapes. It is noticed that stresses $\sigma_{32}, \sigma_{13}, \sigma_{33}$ vanish at the plate surfaces. This agrees with stress-free boundary condition.

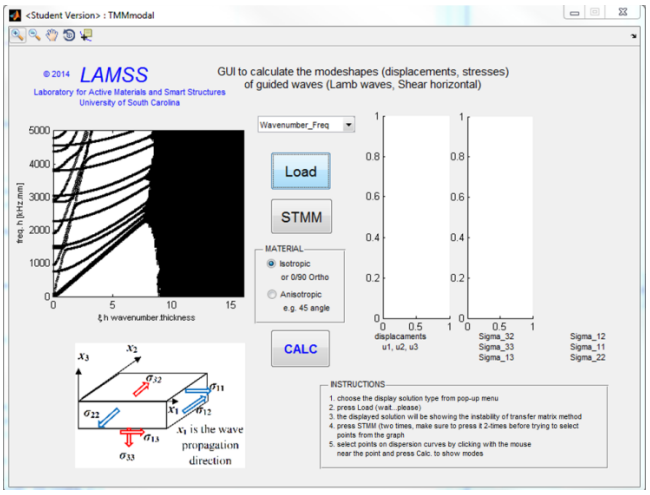

Figure 4.14. LAMSS STMM graphical user interface for dispersion curves analysis in composites

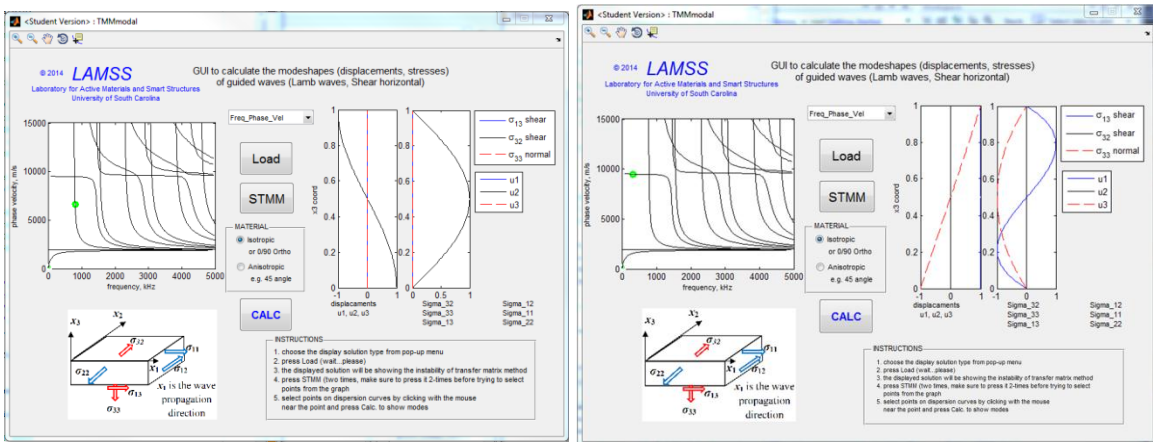

Figure 4.15. Modeshapes for unidirectional CFRP layer with 0º fibers: (a) SH1 mode, (b) S0 mode.

4.6. COMPARATIVE STUDY BETWEEN SEVERAL METHODS FOR CALCULATING ULTRASONIC GUIDED WAVES IN COMPOSITES

In this section, results are shown for dispersion curves (phase velocities, and group velocity curves). The material used as a case study is T300/914 CFRP used in

DISPERSE software manual (Pavlakovic and Lowe, 2003) and other studies (Bartoli et al., 2006; Santoni, 2010). The unidirectional layer stiffness matrix values are the values of C_{uni} in Eq.(4.28), the density is $\rho = 1560$ kg/m^3. These material properties are used for unidirectional case studies as well as cross ply cases. DISPERSE software is used for GMM (with both phase and group velocity curves). GUIGUW computer package, which was used in (Bartoli, et al., 2006) and is available online, was used for SAFE method; the core GUIGUW code was used with help from the developers instead of the online interface. Both TMM and STMM are developed in our group. Finally results reported for LISA are reported from literature (Nadella & Cesnik, 2012) as we did not find yet a turn key code based on LISA.

4.6.1. Unidirectional Fiber Laminated Composites along Different Angles

This section presents predicted dispersion curves of a one layer unidirectional CFRP composite with fiber angle cases of 0º, 30º, 45º, 60º, and 90º with respect to wave propagation direction. SAFE and GMM dispersion curves of Table 4.1 are exactly reported in Pavlakovic and Lowe (2003) pp155 and Bartoli et al. (2006) pp698. Both GMM and SAFE are matching very well. Our developed TMM and STMM matched exactly with GMM and SAFE. S0 mode has the initial speed around 9500 m/s. SH0 mode has the speed of 2000 m/s. DISPERSE automatic tracing misses SH0. As the angle between wave propagation direction and the fiber increases; e.g. $\theta = 30$ in Table 4.2; the material becomes more compliant. We can see the phase velocity of S0 mode (at near zero frequency) drops from 9000m/s to 8000 m/s; also group velocity drops from $\approx$9500 m/s to $\approx$8200 m/s.

Table 4.1. T300/914 unidirectional fiber laminate with fiber along wave propagation direction U0 ($\theta = 0^{\circ}$)

Phase velocity	Group velocity
GMM (DISPERSE) 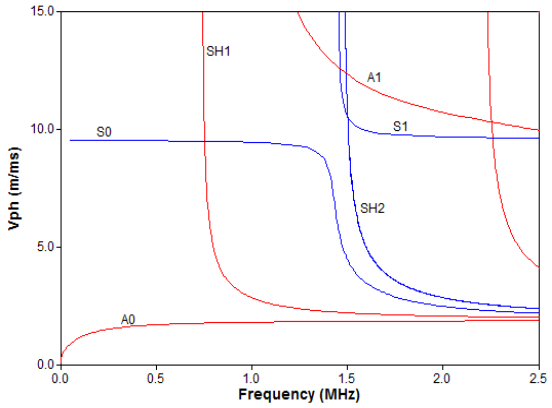	GMM (DISPERSE) 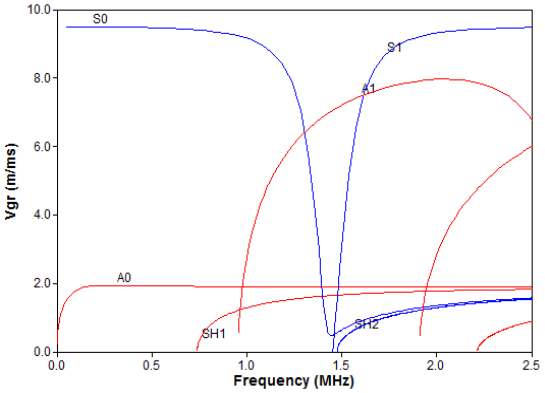
SAFE (GUIGUW) 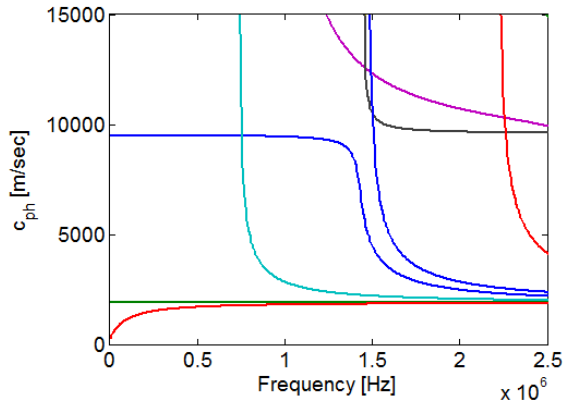	SAFE (GUIGUW) 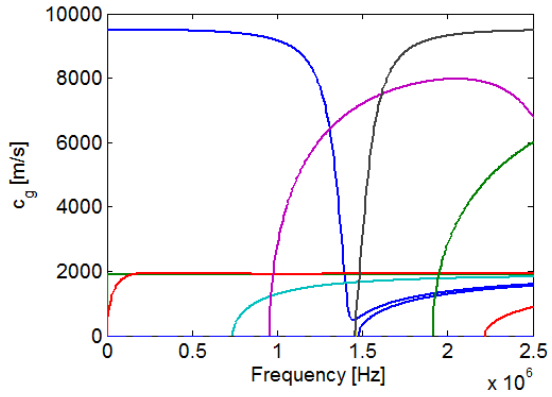
STMM (LAMSS) 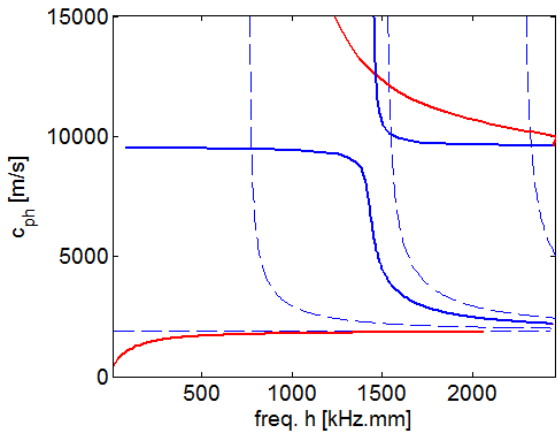	STMM (LAMSS) 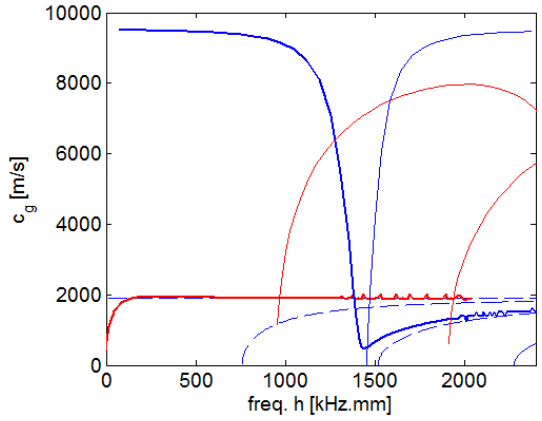

Table 4.2. T300/914 unidirectional fiber laminate U30 ($\theta = 30^{\circ}$)

Phase velocity	Group velocity
GMM (DISPERSE) 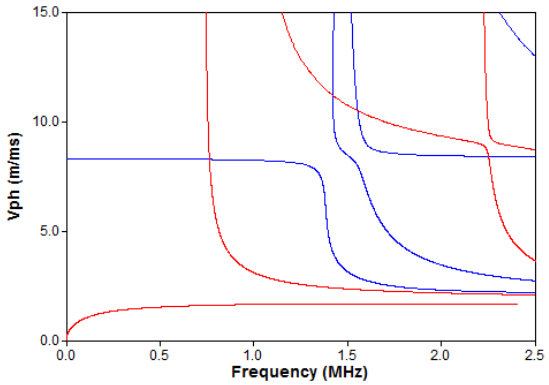	GMM (DISPERSE) 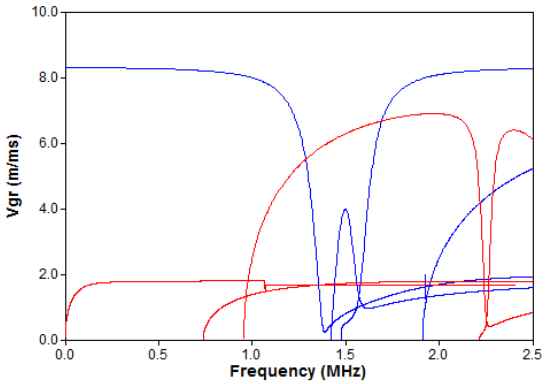
SAFE (GUIGUW) 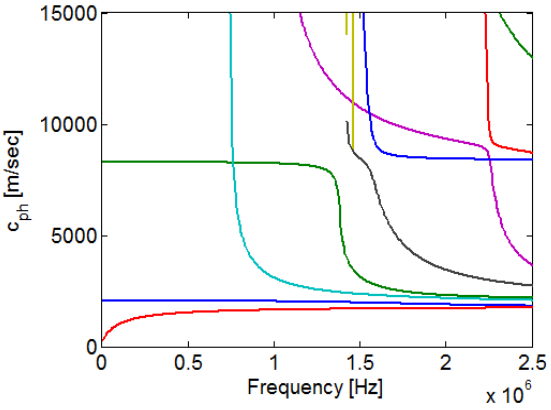	SAFE (GUIGUW) 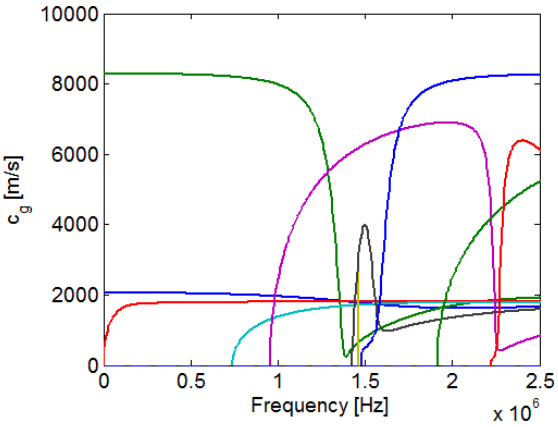
STMM (LAMSS) 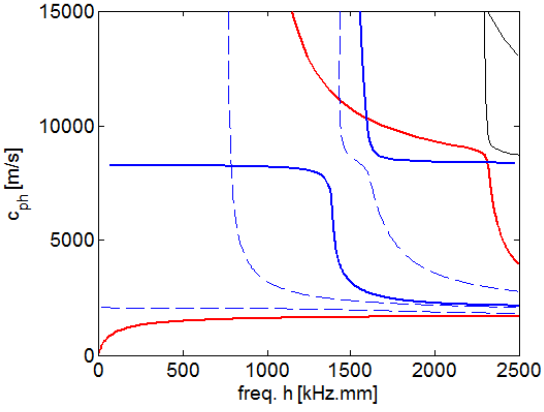	STMM (LAMSS) 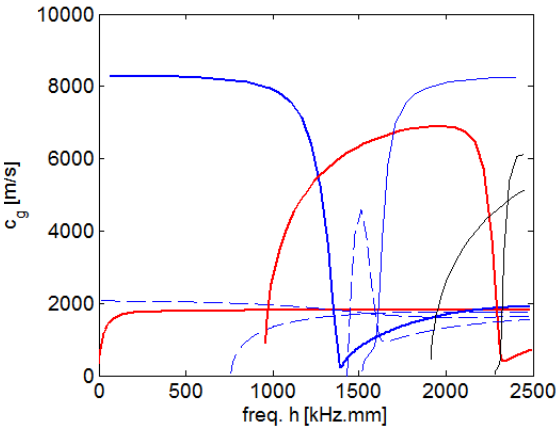

Table 4.3. T300/914 unidirectional fiber laminate U45 ($\theta = 45^{\circ}$)

Phase velocity	Group velocity
GMM (DISPERSE) 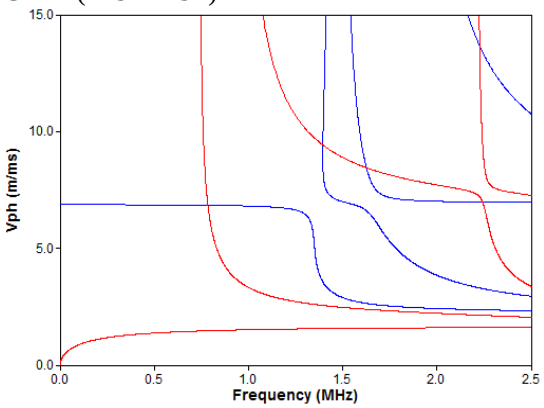	GMM (DISPERSE) 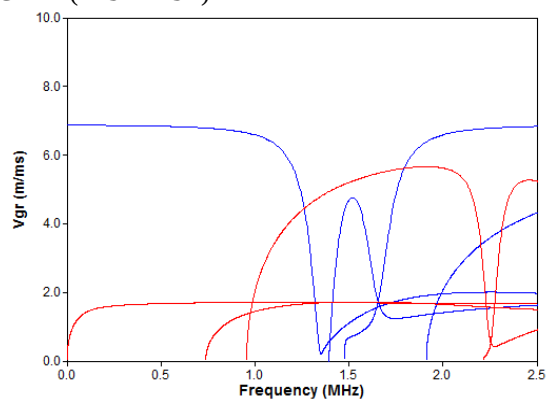
SAFE (GUIGUW) 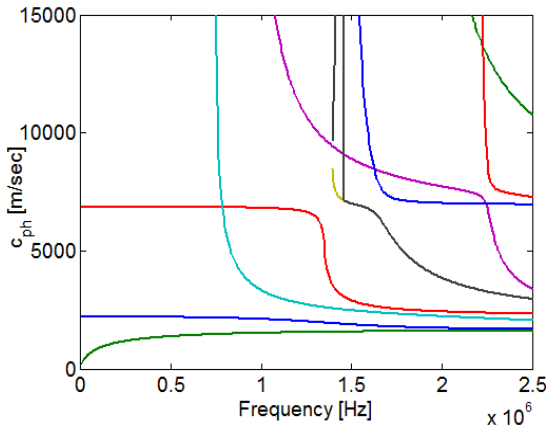	SAFE (GUIGUW) 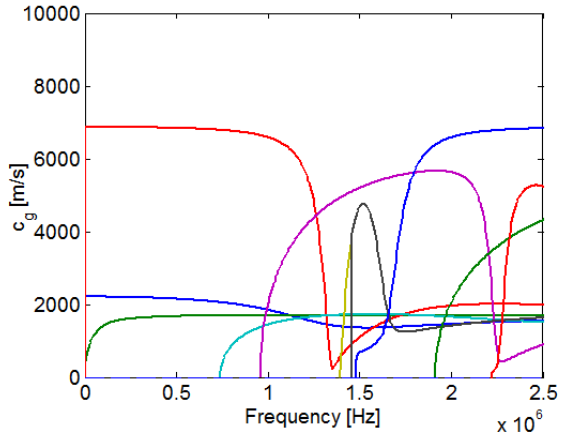
STMM (LAMSS) 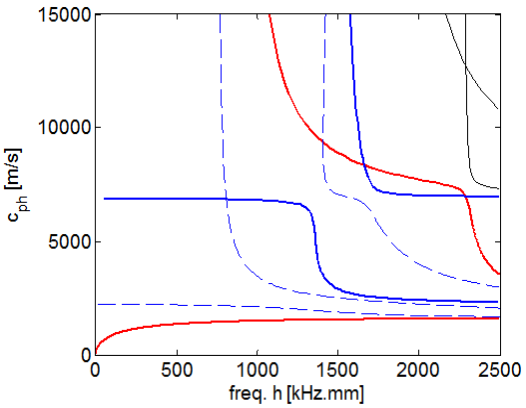	STMM (LAMSS) 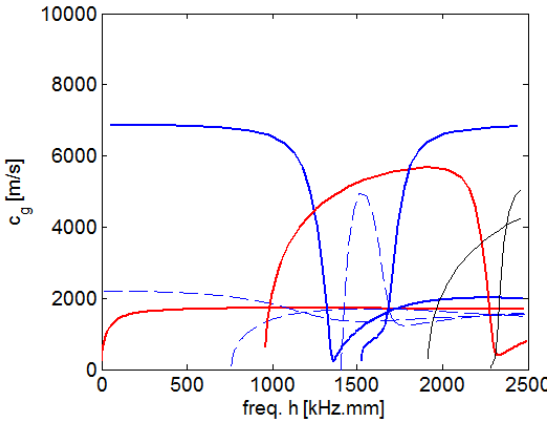

As fiber angle increases to 45º, the phase and group velocities further reduce to ≈7000 m/s. SH0 tends to be more dispersive and not having the constant speed with frequency.

Table 4.4. T300/914 unidirectional fiber laminate U60 ($\theta = 60^{\circ}$)

Phase velocity	Group velocity
GMM (DISPERSE) 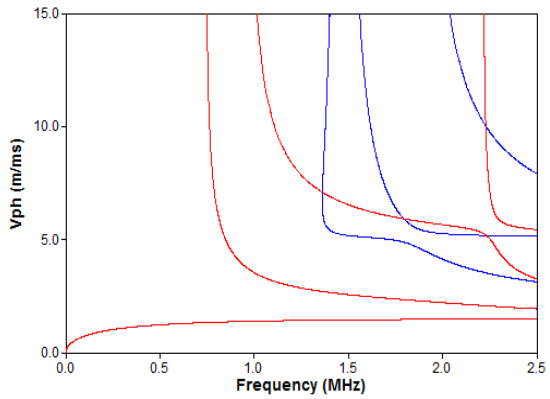	GMM (DISPERSE) 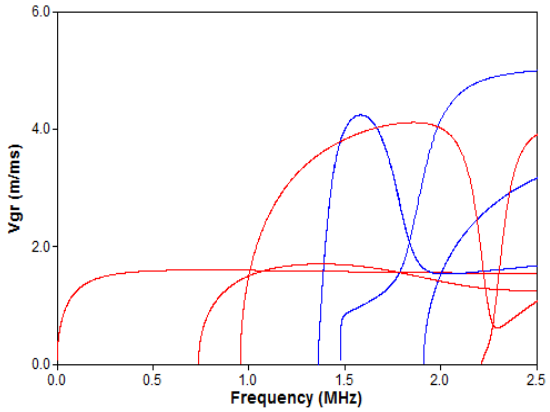
SAFE (GUIGUW) 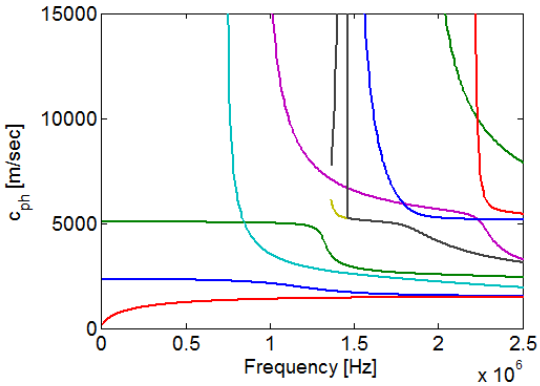	SAFE (GUIGUW) 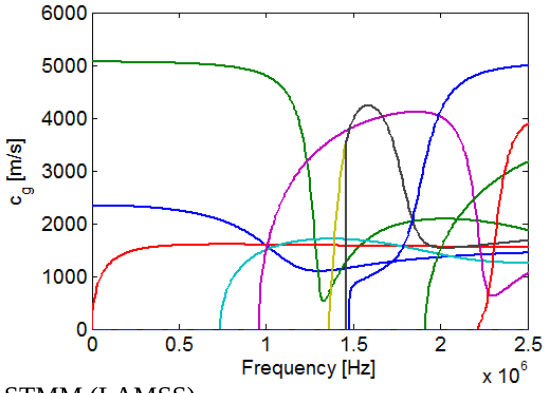
STMM (LAMSS) 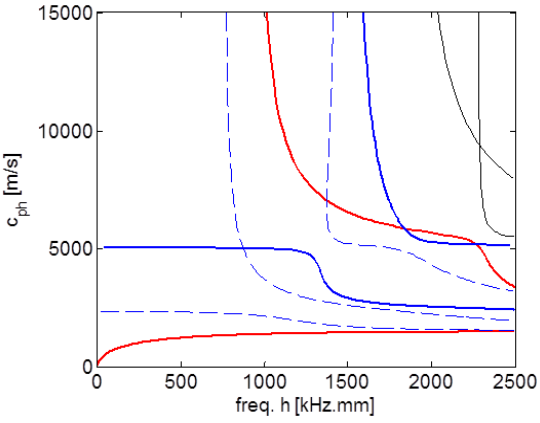	STMM (LAMSS) 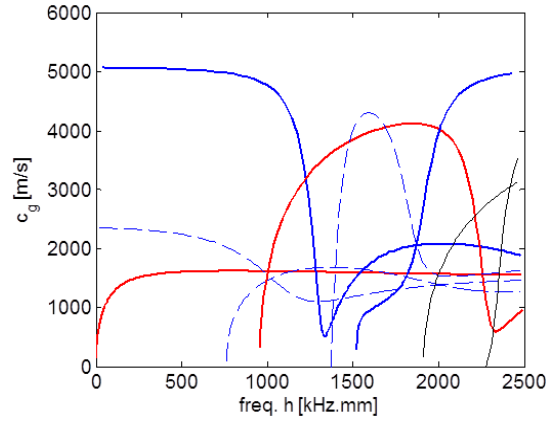

SH0 at fiber orientation 60º degrees is also tends to be more and more dispersive, the phase and group velocities of S0 at near zero frequency further reduce to 5000 m/s. DISPERSE misses S0.

Table 4.5.T300/914 unidirectional fiber laminate U90 ($\theta = 90^{\circ}$)

Phase velocity	Group velocity
GMM (DISPERSE) 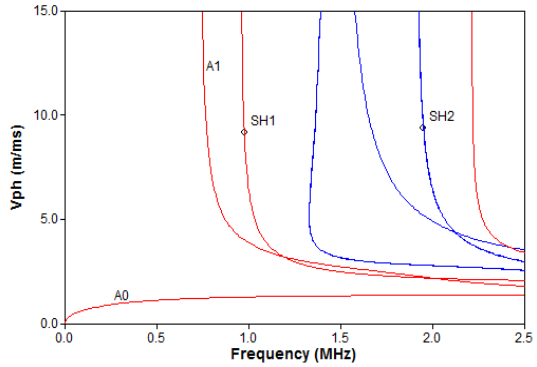	GMM (DISPERSE) 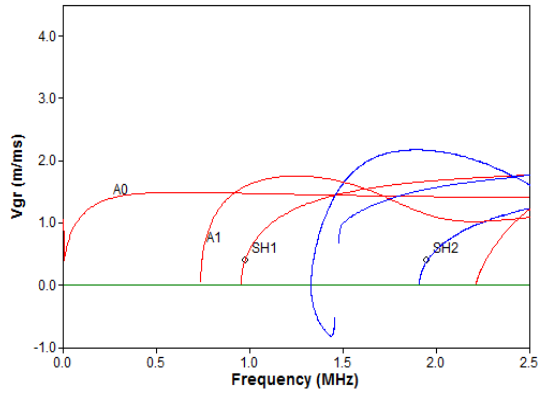
SAFE (GUIGUW) 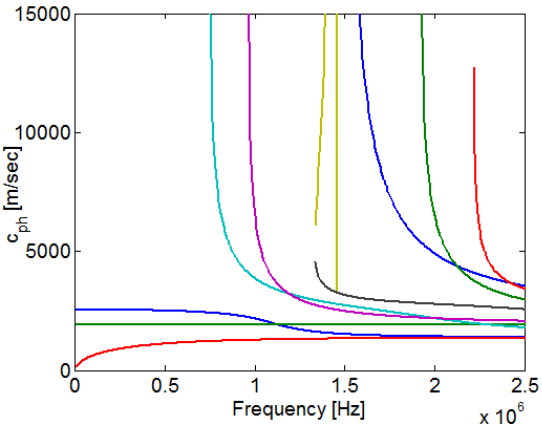	SAFE (GUIGUW) 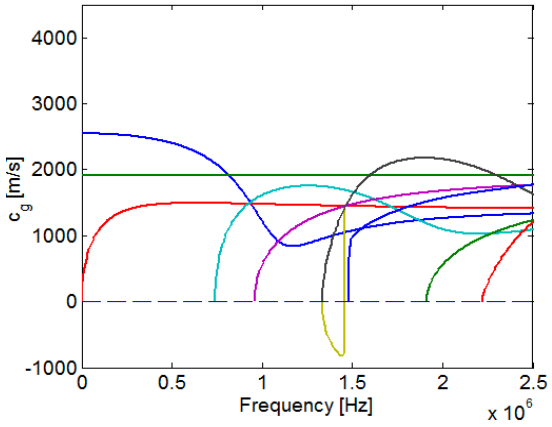
STMM (LAMSS) 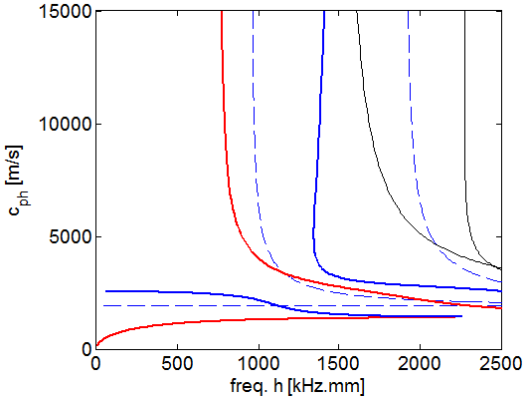	STMM (LAMSS) 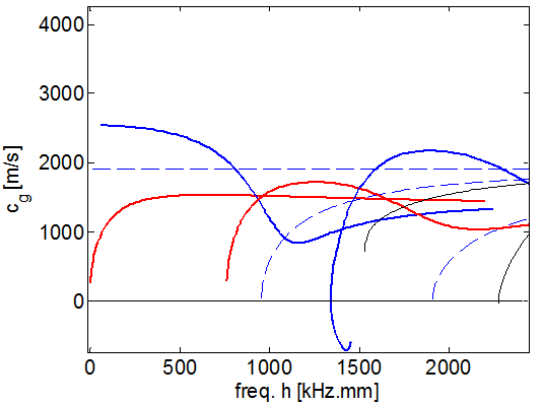

As the fiber orientation becomes exactly perpendicular to wave propagation direction; SH0 returns to non-dispersive nature, i.e., SH waves are decoupled from the other guided waves in the solution.

DISPERSE misses S0 mode in the $\theta = 90$ case. In this case, the speeds are the smallest compared to other angles, because for the fibers along 90 degrees the material is in the most compliant situation along wave propagation direction.

A comparison between LISA method, and DISPERSE (i.e., GMM) is reported in Nadella and Cesnik (2012). The material used is unidirectional IM7 Cycom 977-3 multilayer unidirectional laminate with 1.5 mm thick. The authors compared A_0 mode using group velocity dispersion curves (**Figure 4.16**).

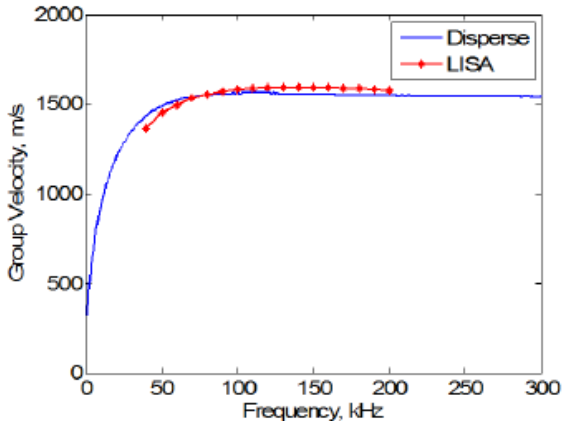

Figure 4.16.LISA vs. GMM for 1.5-mm thick unidirectional IM7 Cycom 977-3 composite (Nadella and Cesnik, 2012)

4.6.2. Cross Ply Laminated Composites

In this subsection, we study two cases: 2-layer [0/90] laminate with each layer 0.5-mm thick and 4-layer $[0/90]_s$ with each layer 0.25-mm thick. The material is again T300/914. Beside GMM and SAFE, The equivalent matrix method (EMM) was also used for comparison.

Table 4.6. Two layer 1-mm T300/914 cross ply fiber laminate [0/90]

Phase velocity	Group velocity
GMM (DISPERSE) 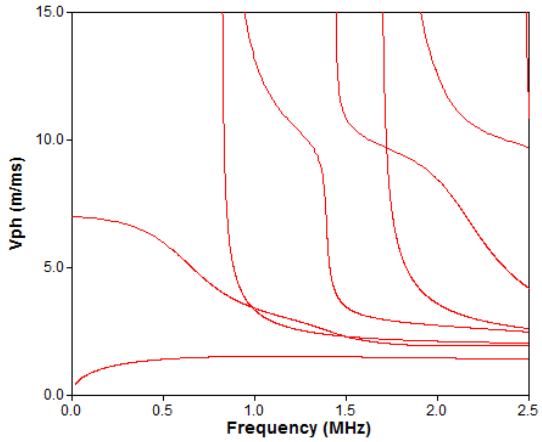	GMM (DISPERSE) 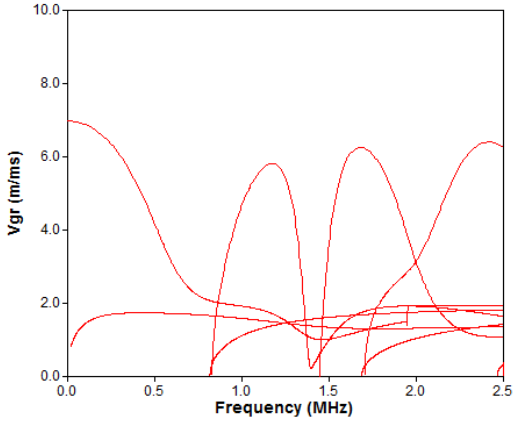
SAFE (GUIGUW) 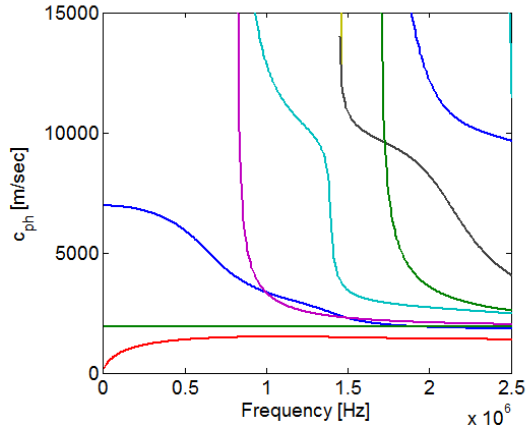	SAFE (GUIGUW) 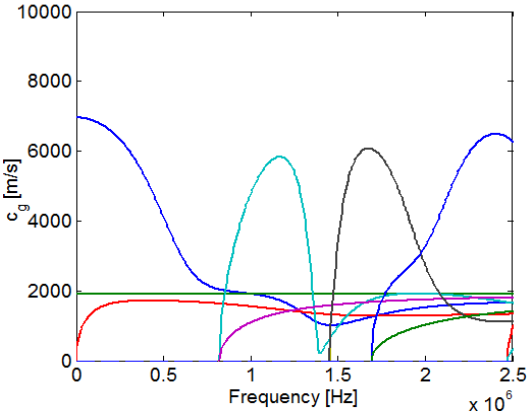
STMM (LAMSS) 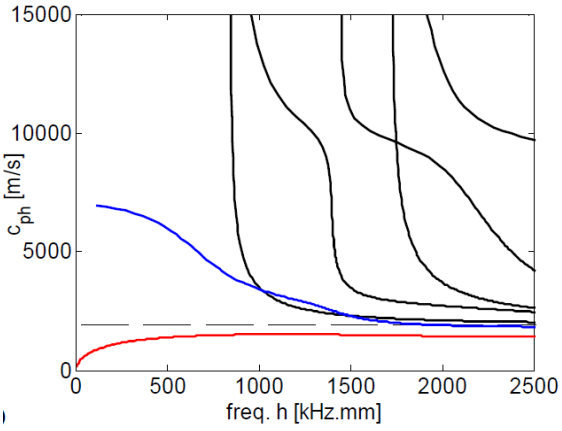	STMM (LAMSS) 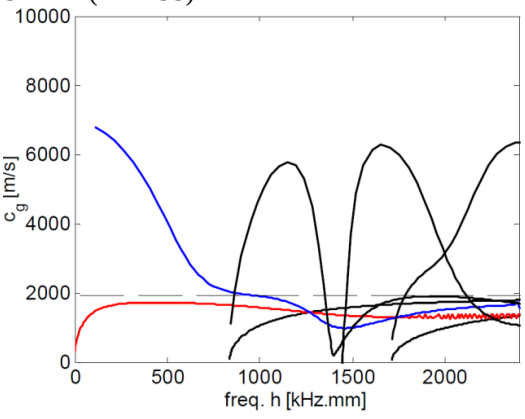

Table 4.7. Four-layer 1-mm T300/914 cross ply fiber laminate $[0/90]_s$

Phase velocity	Group velocity
GMM (DISPERSE)	GMM (DISPERSE)
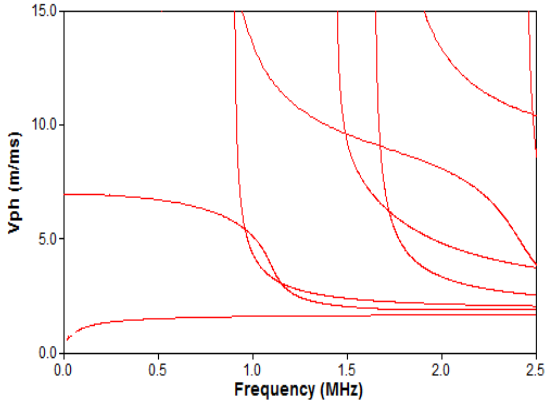	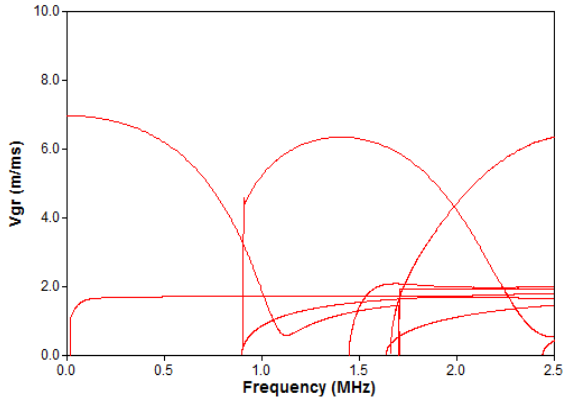
SAFE (GUIGUW)	SAFE (GUIGUW)
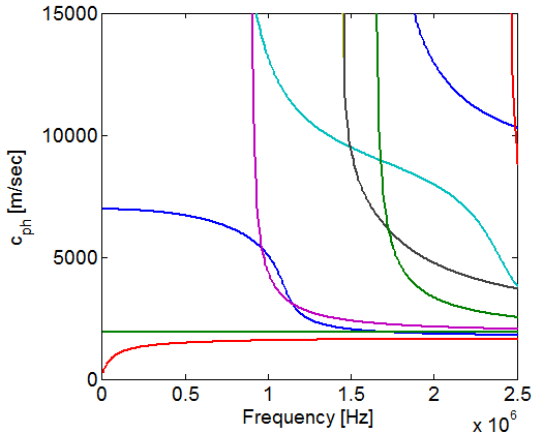	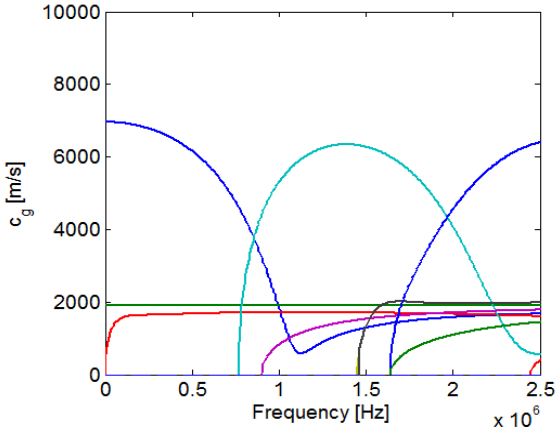
STMM (LAMSS)	STMM (LAMSS)
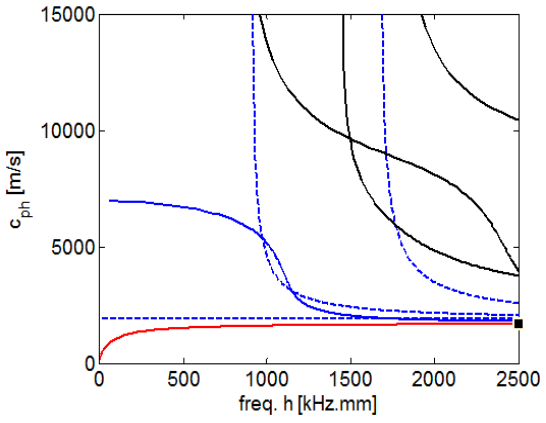	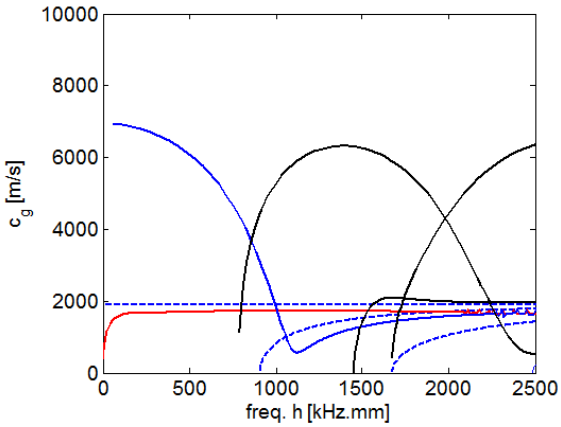

The case of cross ply of $[0/90]_s$, i.e. 0/90/90/0 (Table 4.7) shows slight different results than the simple 0/90 case (Table 4.6). On the other hand, the EMM predicts the exact same result for both cases (Figure 4.17) because it just averages the properties of the 0-

direction fibers and 90-direction fibers; the EMM does not account the difference between the 2-layer 0/90 and the 4-layer [0/90]s cases. **Figure 4.17** shows EMM result for [0/90] CFRP. Although EMM predicts the starting points of S0 and SH0 fairly close, it is obviously different from the actual predictions of a system of 2-layers reported in Table 4.6.

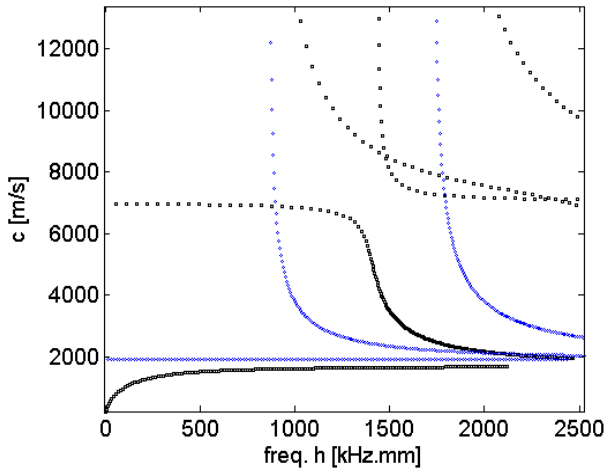

Figure 4.17. Equivalent Matrix method for [0/90] T300/914 CFRP laminate

4.6.3. Quasi Isotropic Composite Laminate

The material used for this case study is T800/924 CFRP following the example in Pavlakovic and Lowe (2003) pp. 158. The laminate stack orientation is defined as $[+45/-45/0/90]_s$. The layer material properties are

$$E_{11} = 161 \text{ GPa}, E_{33} = 9.25 \text{ GPa}, G_{13} = 6 \text{ GPa}, \nu_{13} = 0.34, \nu_{23} = 0.41, \rho = 1500 \text{ kg/m}^3$$

The corresponding stiffness coefficients are

$$C_{11} = 164.7 \text{ GPa}, \quad C_{12} = C_{13} = 5.45 \text{ GPa}, \quad C_{22} = C_{33} = 11.3 \text{ GPa}$$
$$C_{23} = 4.7 \text{ GPa}, \quad C_{44} = 3.3 \text{ GPa}, \quad C_{55} = C_{66} = 6 \text{ GPa}$$

The results are presented in Table 4.8. DISPERSE and SAFE results match well. It is noticed also that SH0 is dispersive for such complicated structure.

Table 4.8. T800/924 Quasi isotropic composite laminate $[+45/-45/0/90]_S$

Phase velocity	Group velocity
GMM (DISPERSE) 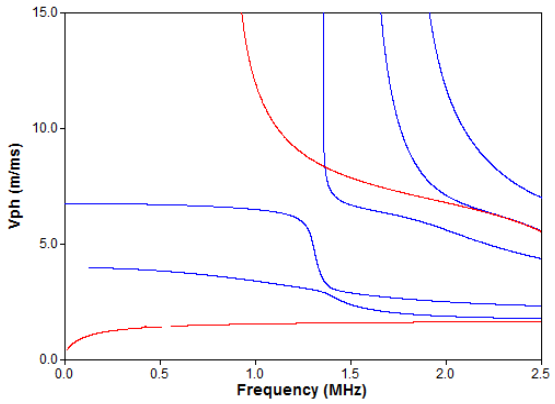	GMM (DISPERSE) 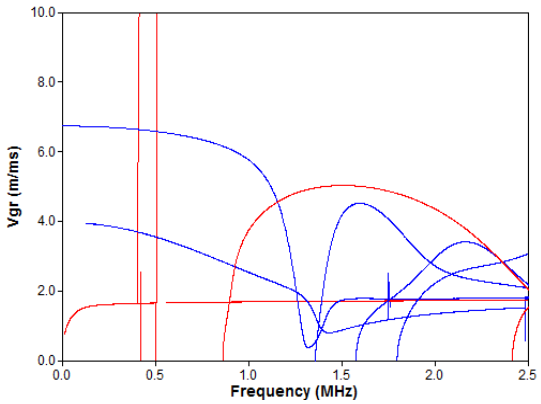
SAFE (GUIGUW) 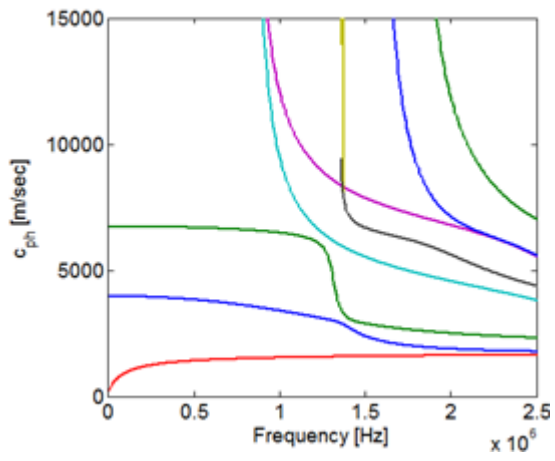	SAFE (GUIGUW) 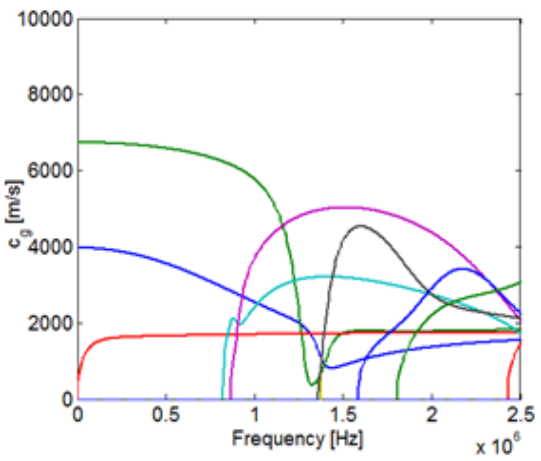

4.7. EXPERIMENTAL VS. PREDICTIVE FINITE ELEMENT CASE STUDY

The objective of this part is to measure the experimental group velocities of guided waves propagating in a composite laminate and compare them with results from predictive tools, (DISPERSE, STMM, and FEM) with the aim of simulating guided waves and the propagating scheme for non-isotropic materials.

4.7.1. Experimental Study

The structure investigated is a woven GFRP plate in an epoxy resin. The plate dimensions were 910 x 620 mm and 1-mm thickness. It has 6 plies of glass fiber woven fabric. The material density is 1960 kg/m^3. The layer stiffness matrix [C] provided (Pollock et al., 2012) is

$$C = \begin{bmatrix} 28.7 & 5.7 & 3 & 0 & 0 & 0 \\ 5.7 & 28.7 & 3 & 0 & 0 & 0 \\ 3 & 3 & 12.6 & 0 & 0 & 0 \\ 0 & 0 & 0 & 4.9 & 0 & 0 \\ 0 & 0 & 0 & 0 & 4.9 & 0 \\ 0 & 0 & 0 & 0 & 0 & 4.1 \end{bmatrix} \text{GPa} \qquad (4.139)$$

The stiffness matrix is for the woven system directly, i.e. the stiffness coefficients are already considering the fibers in 0 and 90 directions. As we can see C_{11}=C_{22}=28.7 GPa. Because of that, we don't need to use EMM to find equivalent system of the 0/90 system, instead, we can input stiffness matrix directly in a unidirectional code with ($\theta = 0$).

Two PWAS transducers were bonded on the structure; we used 7 mm x 7mm x0.2 mm PWAS as the transmitting transducer. The receiver was 15 mm x 15 mm x 1 mm SH-PWAS poled in thickness shear direction (for more details, please see Chapter 3: SH-

Coupled PWAS). We used SH-PWAS to be able to detect the SH waves that may be generated through mode conversion in the composite material. The experimental setup is shown in **Figure 4.18**.

As an application for predictive tools of guided wave propagation in composites, we show in **Figure 4.19** the comparison between DISPERSE and our STMM for calculating group velocities up to 2000 kHz. However, our experimental work was done up to 300 kHz, where we could distinguish the three fundamental modes, S0, A0 and SH0. The transmitter PWAS was excited using 3-count tone burst signals with center frequency from 1 kHz to 300 kHz.

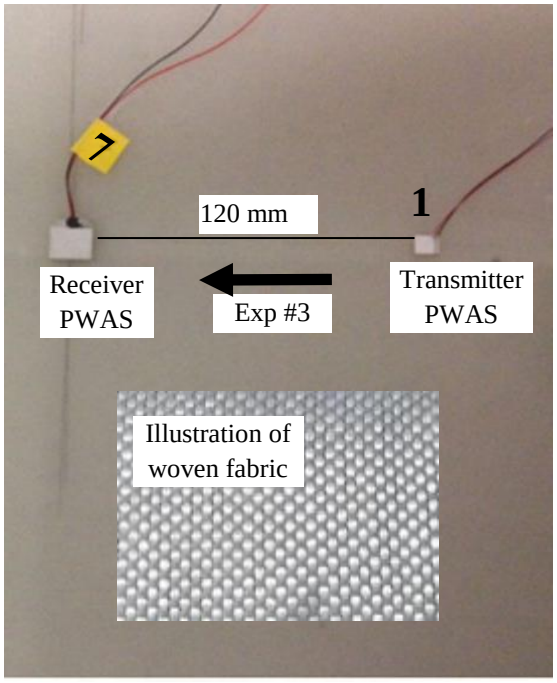

Figure 4.18. Experimental setup for guided wave propagation between in-plane PWAS and SH-PWAS in 1-mm thick GFRP plate

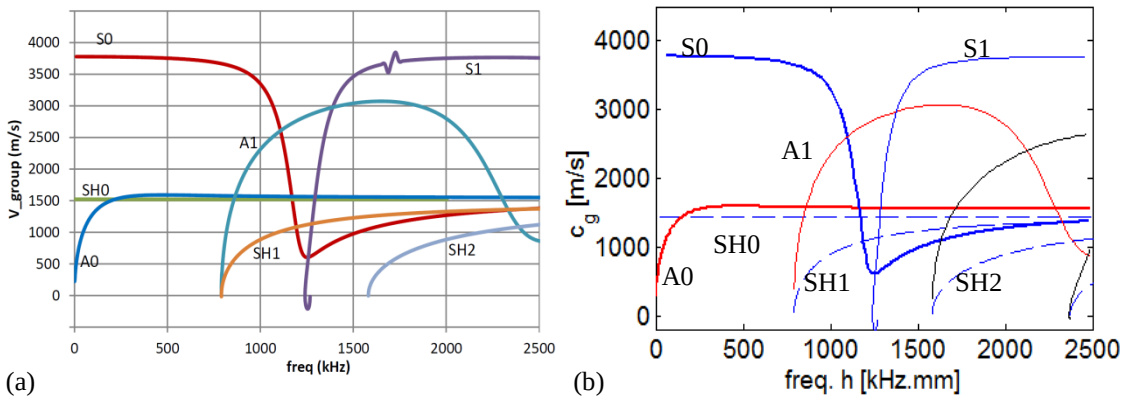

Figure 4.19. Group velocities in 1-mm woven GFRP plate, (a) DISPERSE, (b) LAMSS STMM

The distance between the two PWAS transducers is 120 mm, and the experimental group velocity was calculated by dividing the distance by the time of flight measured between the excitation signal and the received signals. The results are shown in **Figure 4.20**. This study was done for only one direction (along 0 direction). To see the wave propagation pattern, we constructed an FEM model.

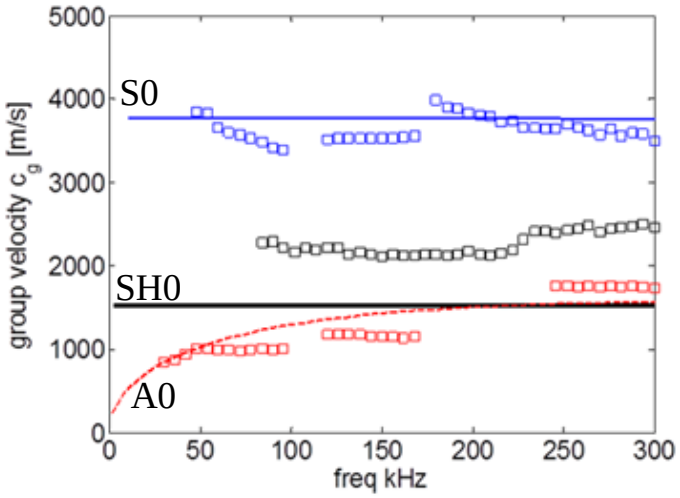

Figure 4.20. Experimental group velocities of guided waves in 1-mm thick woven GFRP plate, analytical predictions ___, experimental □□□

4.7.2. Finite Element Model for Guided Wave Propagation in GFRP

The finite element model plate dimensions were 450 mm x 450 mm x 1-mm. The material was GFRP. Two PWAS transducers were bonded in the middle as shown in **Figure 4.21**. We used COMSOL Multiphysics coupled-field element for piezoelectric transducers; this allowed us to apply excitation voltage as the input excitation and receive the signal at the SH-receiver PWAS as voltage (rather than input a mechanical wave excitation or force excitation). The excitation signal was 3-count tone burst with 10 V signal amplitude and center frequency of 48 kHz. The reason for selecting this relatively low frequency is to satisfy convergence and accuracy requirements with the available computational resources. The model was run for 200 μs with 0.5 μs time step. The structure domain was divided into 9 domains as shown in **Figure 4.21** such that the meshing of the domain in the middle was done by free mesh and then extruded by two elements through the thickness (i.e. 0.5-mm mesh size through thickness). The meshing of the other external domains was done by structural mesh and was extruded as two elements through thickness. The mesh size that was used in this study was 3-mm for GFRP material. Coupled field elements for the PWAS transducers were meshed by 1-mm mesh size and 4 elements through the thickness of each PWAS (i.e. 0.25-mm mesh size through the thickness of 1-mm thick SH-PWAS, and 0.05-mm mesh size through the thickness of the 0.2-mm PWAS1.)

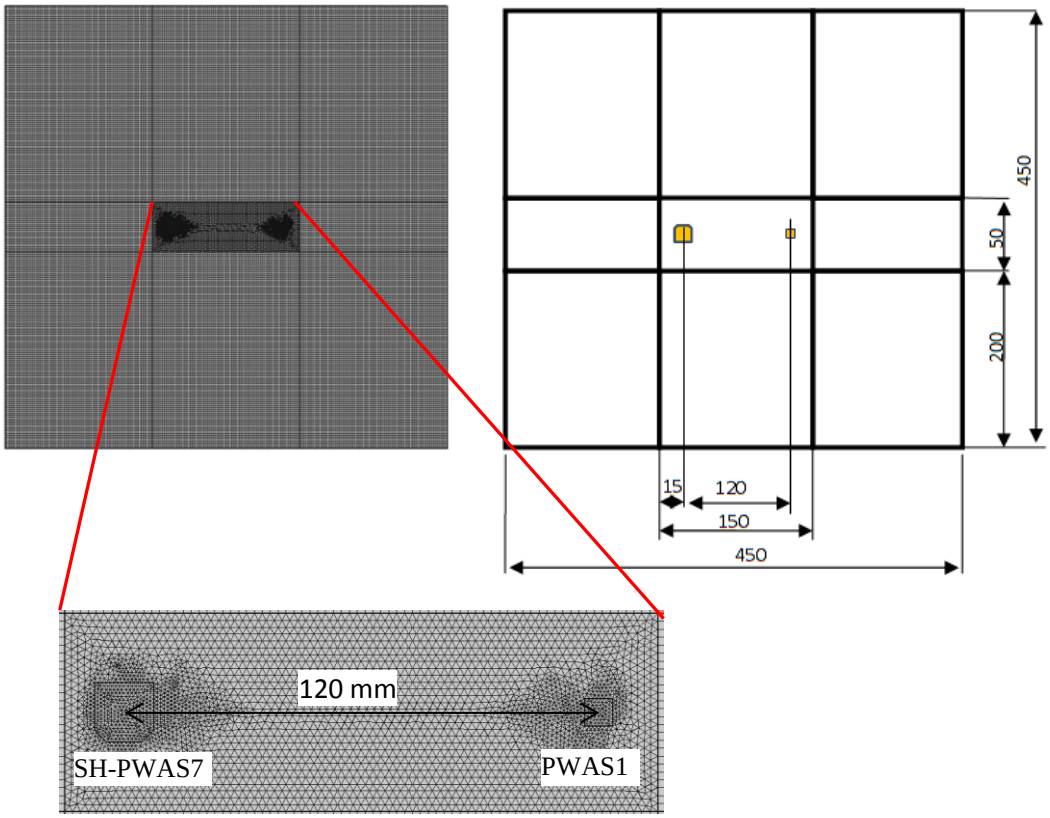

Figure 4.21. FEM for guided wave propagation between PWAS1 and SH-PWAS7 on GFRP

For getting accurate results, it is required that for each mode, the number of elements per wavelength is ≥ 10. recalling **Figure 4.20**, and for 48 kHz excitation, the speeds for S0, SH0, and A0 are ≈ 3800m/s, 1500m/s, and 1000 m/s respectively; this correspond to wavelengths ≈ 80, 31, and 21 mm respectively. The critical mode is A0, which enforces the 2-mm mesh size requirement. But we used 3-mm mesh size because of the available computational resources. We would expect that the results for 2-D solution for A0 mode would not look very smooth, as shown in **Figure 4.22**. For convergence, the required time step should be $\leq (1/30 f_c)$ which in our 48 kHz case should be $0.7\,\mu s$; we used 0.5 μs time step and 200 μs total simulation time. The

simulation was done on dual 2.8 GHz XEON 2ML2 processor, and used up to 96 GB of RAM; the simulation took 9 hours.

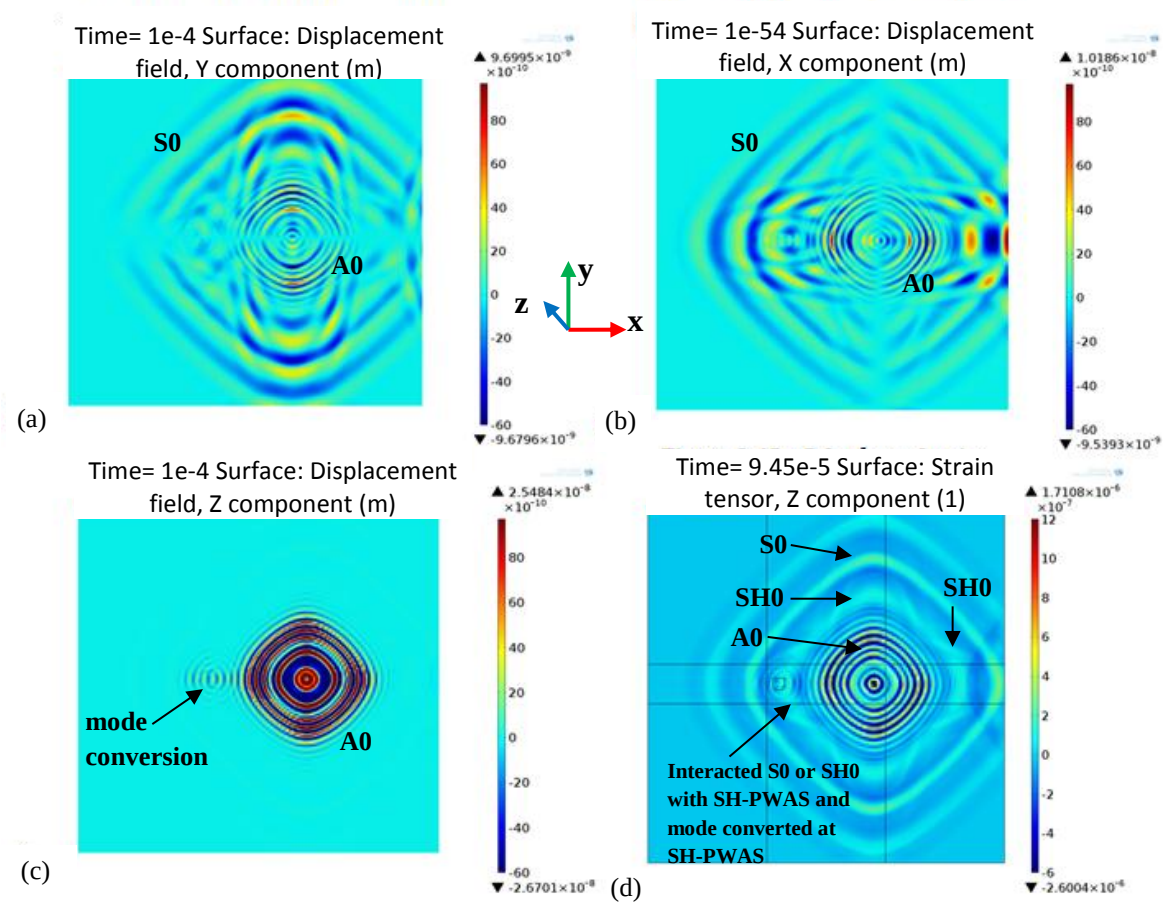

Figure 4.22. 2-D simulation results for wave propagation in1-mm thick woven GFRP plate at, (a) particle displacement inplane Y direction, (b) inplane X direction, (c) out of plane Z direction, (d) out of plane strain tensor

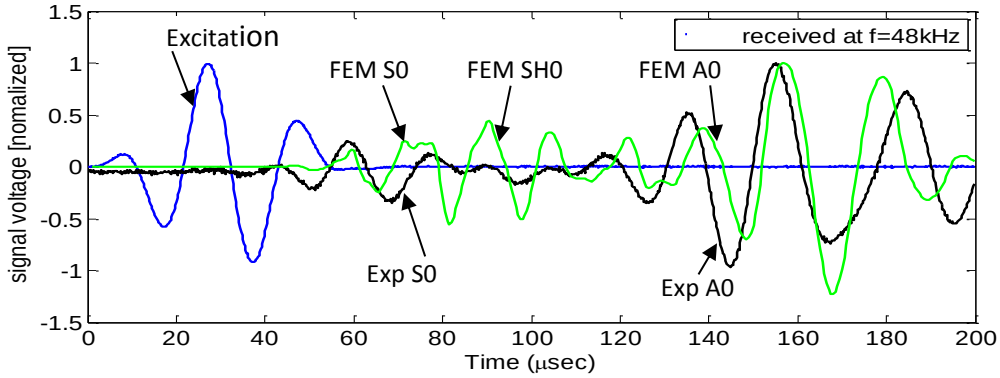

Figure 4.23. FEM vs. experimental results for guided wave propagation in 1-mm thick woven GFRP

The 2-D simulations allowed us to see the wave propagation patterns. **Figure 4.22**a,b show the symmetric S0 and antisymmetric A0 modes very clearly. A0 mode is the mode with the smaller wavelength because of its lower wave speed. The fact that both S0 and A0 have inplane components of particle motion allowed the simulation to capture both S0 and A0 for inplane displacement plots. Whereas the out of plane (the Z component) of the symmetric S0 mode is very weak, as we can see from **Figure 4.22**c in which S0 mode almost did not exist.

Figure 4.22c shows the A0 mode out of plane displacement very clearly at 100 μs. A small excitation can be seen around the receiver SH-PWAS, while it is just a receiver PWAS and was not used as excitation source; this can be explained by the active/passive behavior of the PWAS transducer. While A0 mode excited by PWAS1 did not yet arrive at SH-PWAS, the other faster modes (e.g. S0 and SH0) had already arrived and interacted with the transducer, mode converted as A0, and the SH-PWAS appeared as if it was exciting A0 mode towards PWAS1.

Figure 4.22d shows the out of plane component of the strain tensor; we selected this variable as it was found to be the best one showing most of the interesting modes and mode conversion phenomenon. Finally, the fact that the GFRP plate was woven showed that the propagating waves were not propagating in circles, but rather in diamond-shaped pattern. This is because the material stiffness properties are identical in 0^o and 90^o directions, but the material is less stiff in the 45 directions.

Figure 4.23 shows the experimental and FEM-predicted signals. The S0, SH0 and A0 modes were identified in the signal. The A0 mode had good agreement with

experimental results; the S0 mode predicted by FEM and measured experimentally were fairly close; but the SH0 at this particular frequency was not very clear experimentally.

A final observation can be concluded from Santoni (2010). **Figure 4.24** shows that all the guided wave beyond 500 kHz are extremely damped out in such woven GFRP composite; this indicates the practical range that we can use for predicting wave propagation speeds and SHM applications.

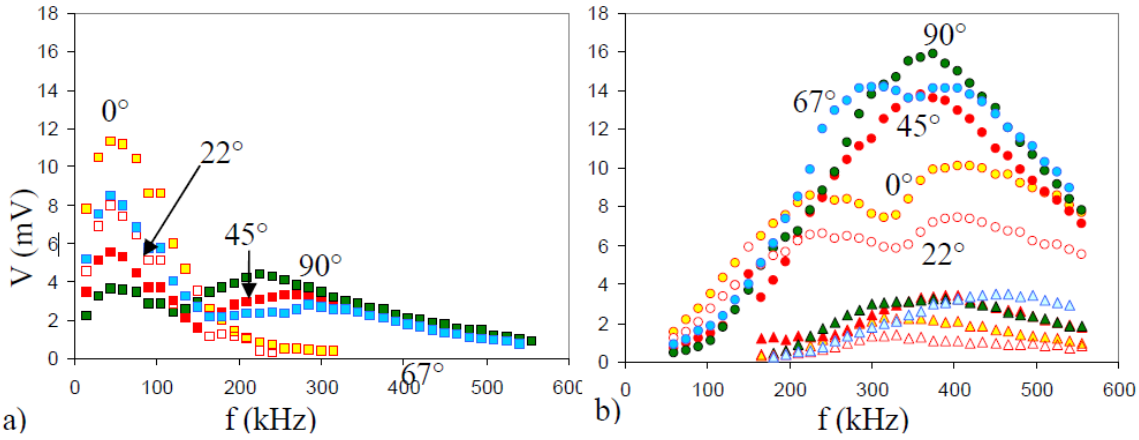

Figure 4.24. Tuning experimental data for wave propagation in GFRP composite, □□□ A0 mode, ooo S0 mode; Δ Δ Δ SH0 mode (Santoni, 2010).

4.8. SUMMARY AND CONCLUSIONS

Different algorithms can be used for calculating dispersion wave speeds in composites. This study has briefly covered the mathematical formulation of each method. This work focused on the transfer matrix method (TMM) and the efforts for generating a stable robust algorithm. TMM is a convenient technique for wave propagation analysis in layered media; its advantage is that it condenses the multi-layered system into four equations (for the case of decoupled SH waves) or six equations relating the boundary

conditions at the first and the last interfaces. It eliminates all other intermediate interfaces; this saves a lot in terms of computation and complexity. One drawback TMM suffers is the numerical instability of the solution at large frequency-thickness product values. There have been many publications proposing reformulation of TM equations to avoid this problem. One method is based on using stiffness matrix (SM) instead of TM; this is done by rearranging terms of the TM such that displacements at both the top and the bottom of the layer are in a single column matrix, and similarly the stresses.

Global matrix method (GMM) combines stresses and displacements at the boundaries of each layer with the overall system boundary conditions and assembles them in one single matrix. GMM has the advantage that it remains stable at high frequency-thickness products. The disadvantage is that the GM turns out to be a large matrix for laminates with large numbers of layers. Semi Analytical Finite Element (SAFE) discretizes the structure cross section allowing different cross sections to be analyzed because of the finite element discretizing in cross section. In the same time it solves analytically in the wave propagation direction; this makes SAFE more efficient in terms of computational time and memory than a complete FEM. In general, the material is defined in FEM by stiffness matrix; this makes SAFE method a very straight forward for application for anisotropic materials. SAFE is becoming popular for analyzing guided wave propagation in composites. Local Interaction Simulation Approach (LISA) discretizes the system into a lattice like the finite difference method; its formulation is based on the elastodynamic equations. The advantage of LISA appears when discontinuities or changes need to be applied to the material properties; those changes are treated by modifying the properties of the lattice at the corresponding locations.

Equivalent matrix method (EMM) is a quick approach for analyzing cross ply laminates due to the fact that transformation matrix between 0 and 90 degrees is straight forward and can be done manually. However it does not catch the differences between different layup sequences of 0 and 90 fiber layers, such as 0/90/0/90 and 0/90/90/0.

The instability of TMM was discussed in details, and the mathematical formulation of stiffness matrix method (SMM) was presented. It was shown that SMM gives a stable solution at the high frequency- thickness products. But SMM does not give correct roots pattern at low wavenumber and low frequency domain. Hence, a combined stiffness transfer matrix method (STMM) was proposed and used to obtain correct and stable results over the entire domain of interest.

The study presented case studies for unidirectional composites with wave propagation along different angles. GMM and SAFE methods had very good agreement with our STMM in terms of cut off frequencies and speeds values (both phase and group velocities). Next, we presented case studies on cross-ply laminates; in this case, results were compared with EMM method as well. EMM predicted both [0/90] and [0/90/90/0] in the same way, although their dispersion curves are actually different. This highlights one drawback of EMM: it gives generally a good approximation but not accurate predictions. The chapter also presented comparisons on quasi-isotropic laminates and it showed good agreement between GMM and SAFE methods.

Finally, experimental and finite element studies on a GFRP woven composite specimen were discussed. PWAS transducers were used for pitch catch experiments using tone burst excitation signals. Experimental dispersion group velocities showed good agreement with the theory. COMSOL Multiphysics finite element model was constructed

using coupled-field elements for the PWAS; this allowed simulation of the input excitation and output response in voltage directly. FEM showed the propagation pattern of guided waves in composites. For the specific case of a woven GFRP composite, the wave propagation along 0 and 90 degrees was similar, but was different along 45 degrees, which resulted in diamond pattern instead of the conventional propagation in circles obtained for isotropic materials. New methods need to be designed for even complex sandwich composites with complex filling structures (e.g. honeycomb).

PART II APPLICATIONS

CHAPTER 5: SHEAR HORIZONTAL PWAS FOR COMPOSITES SHM

In this chapter, we apply the material studied in Chapter 3 (SH waves and SH-PWAS) and Chapter 4 (guided wave propagation in composites) on two case studies: (a) a woven GFRP plate with installed SH-PWAS network; (b) quasi-isotropic $[0/45/45/0]_s$ CFRP with each layer as woven ply. The goal of this study is to establish the experimental and predictive modeling procedures for testing and modeling the SH-PWAS impedance spectroscopy and guided wave propagation in composites. The ultimate goal is to discuss the challenges and applicability of using the SH-PWAS for SHM of polymer composite materials in structural components. Both electromechanical impedance spectroscopy (EMIS) technique and guided wave propagation methods are good candidates for SHM systems. The first part of this study is the modeling of EMIS with finite element analysis tools; then comparing FEM results with experimental measurements. The second part covers SH wave propagation between different transducers: SH-coupled PWAS and regular extensional-mode PWAS transducers, followed by FEM case studies to show 2-D wave propagation. A similar FEM studies were performed on aluminum (Zhou et al., 2013) and SH piezoelectric transducers were used for excitation.

5.1. MATERIALS

The first material under investigation is 1-mm thick woven GFRP plate with dimensions 910 mm x 620 mm. It has 6 plies of woven fabric. The material density is

$\rho = 1960$ kg/m^3.The provided stiffness matrix [C] (Pollock et al., 2012) is

$$C = \begin{bmatrix} 28.7 & 5.7 & 3 & 0 & 0 & 0 \\ 5.7 & 28.7 & 3 & 0 & 0 & 0 \\ 3 & 3 & 12.6 & 0 & 0 & 0 \\ 0 & 0 & 0 & 4.9 & 0 & 0 \\ 0 & 0 & 0 & 0 & 4.9 & 0 \\ 0 & 0 & 0 & 0 & 0 & 4.1 \end{bmatrix} \text{GPa}$$

For modeling purpose, we use Rayleigh damping with the mass proportional coefficient α_M is 0.2 rad/s and the stiffness proportional coefficient β_K is 10^{-8} s/rad.

The 2-mm thick CFRP plate consists of woven prepreg carbon fabrics in epoxy resin. There are 8 layers with orientation $[0/45/45/0]_s$. The material density is $\rho = 1605$ kg/m^3. The material properties for the 0-direction ply was provided by Hexcel manufacturer as

E_{11}	E_{22}	E_{33}	n_{12}	n_{13}	n_{23}	G_{12}	G_{13}	G_{23}
65 GP$_a$	67 GP$_a$	8.6 GPa	0.09	0.09	0.3	5 GPa	5 GPa	5 GPa

The corresponding stiffness [C] is

$$C = \begin{bmatrix} 65.6 & 5.5 & 1 & 0 & 0 & 0 \\ 5.5 & 58.2 & 2.7 & 0 & 0 & 0 \\ 1 & 2.7 & 8.7 & 0 & 0 & 0 \\ 0 & 0 & 0 & 5 & 0 & 0 \\ 0 & 0 & 0 & 0 & 5 & 0 \\ 0 & 0 & 0 & 0 & 0 & 5 \end{bmatrix} \text{GPa}$$

However a previous study by Gresil and Giurgiutiu (2013) showed that the manufacturer properties may be overestimated and the updated material properties are

$$C = \begin{bmatrix} 37.57 & 4.36 & 1.35 & 0 & 0 & 0 \\ 4.36 & 40.43 & 3.23 & 0 & 0 & 0 \\ 1.35 & 3.23 & 10.28 & 0 & 0 & 0 \\ 0 & 0 & 0 & 5 & 0 & 0 \\ 0 & 0 & 0 & 0 & 5 & 0 \\ 0 & 0 & 0 & 0 & 0 & 5 \end{bmatrix} \text{GPa}$$

Rayleigh damping for CFRP was considered $\alpha_M = 0$ rad/s, $\beta_K = 10^{-8}$ s/rad. The PWAS transducers used in this study are (a) regular in-plane extensional-mode PWAS transducers with dimensions 7 mm x7 mm x 0.2 mm from STEMiNC (www.steminc.com) and (b) SH-PWAS with dimensions 15 mm x15 mm x1 mm and manufactured by APC International Ltd. (www.americanpiezo.com). For standardized modeling, we use the same piezoelectric material properties for both as APC850 Navy II-type piezo with density $\rho = 7600\,\text{kg/m}^2$ and material properties

$$C = \begin{bmatrix} 97 & 49 & 49 & & & & \\ & 97 & 44 & & & & \\ & & 84 & & & & \\ & & & 24 & & & \\ & & & & 22 & & \\ & & & & & 22 & \end{bmatrix} \text{GPa}, \quad \text{complex damping coeff. =4\%}$$

$$[\varepsilon_r] = \begin{bmatrix} 947 & & \\ & 605 & \\ & & 947 \end{bmatrix}, \quad [e] = \begin{bmatrix} -8.02 & -8.02 & 18.31 & & & \\ & & & & & 12.84 \\ & & & & 12.84 & \end{bmatrix} \text{C/m}^2$$

When modeling PWAS in FEM using COMSOL Multiphysics, the poling direction is defined. By default, the poling is in x_3 direction which is the thickness direction. For modeling SH-PWAS, we define an auxiliary coordinate system with x_3' in the direction of inplane poling direction. So the two PWAS transducers were defined with the same

material properties; the SH-PWAS is only different by rotating the material properties such that the local x_3' coincides with the global y direction (**Figure 5.1**).

5.2. ELECTROMECHANICAL IMPEDANCE SPECTROSCOPY AND ADMITTANCE

Electromechanical (E/M) impedance of the SH-PWAS was measured using HP 4194A impedance analyzer. Recalling the free SH-PWAS from Chapter3, i.e., not bonded to any structure, the impedance first peak was shown experimentally to be ≈ 1.060 MHz.

5.2.1. EMIS for woven GFRP Plate

The experimental measurements were performed as a sweep up to 5 MHz. The real and the imaginary components of E/M impedance *(Z)* were recorded. Experimental results are shown in **Figure 5.2**. We display the measured real*(Z)* and the corresponding real(*Y*), where *Y* is the E/M admittance. The admittance is more representing parameter for the resonance of the structure, where the structure vibrates more when the admittance reaches a peak value; while the impedance is the resistance or the anti-resonance situation.

Beside the experimental study, a FEM was constructed in COMSOL Multiphysics software using the coupled field element for the piezoelectric material. The plate model had the dimensions 150 mm x150 mm x1 mm. The excitation signal amplitude was 10 V and the solver was the frequency domain analysis solver, where a frequency sweep is performed and the output response is calculated.

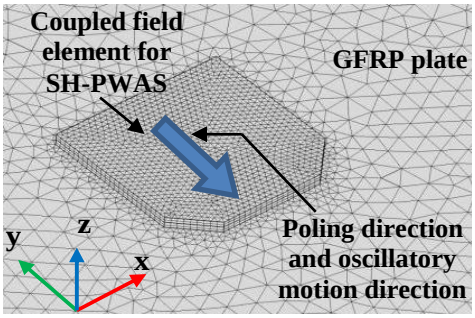

Figure 5.1. FEM mesh of the SH-PWAS bonded to GFRP plate

PWAS in-plane mesh size was 0.5 mm whereas 4 elements were used per the 1-mm thickness; the plate was meshed with 2-mm mesh size whereas 2 elements were used per the 1-mm thickness. The meshing of composite materials is one of the challenges for modeling multilayered composites by finite element analysis tools. For this woven GFRP plate consisting of 6 identical layers of woven fabric, we could mesh the whole thickness by one element, or the number of elements required in accordance with minimum simulated wavelength. However, if the layers are of different properties, like the second case study of CFRP with 8 layers, we have to mesh the thickness by 8 elements at least. For our case of having the second peak of interest around 3.2 MHz (experimentally) and the shear wave speed of SH0 =1500 m/s (**Figure 4.20**), the corresponding wavelength is 0.5 mm. This required the mesh size to be within 1/10 of 0.5 mm (one tenth of 0.5 mm, or 0.05 mm). However, the PWAS mesh we used was 0.5 mm and the plate mesh was 2 mm. This is one of the limitations of our model, i.e., the maximum frequency at which we can trust the FEM results is 75 kHz. If we did not consider the 1/10 rule, the maximum trusted frequency would be 750 kHz. The simulation time was 25 hours on 3.4 GHz intel i7 processor with 8-core 16 GB RAM PC. Comparing the FEM results with experimental results in **Figure 5.2**, we still can see that the FEM and the experimental

results had good agreement with only little frequency shifts being observed, e.g. the free PWAS experimental antiresonance of 1090 kHz is matching well with FEM predictions. However, there are two extra experimental peaks associated with bonded PWAS on the structure, 300 kHz and 800 kHz. In addition, we notice that the FEM over predicted the 300 kHz as 430 kHz, and missed the 800 kHz.

Admittance results had better agreement, especially, at 420 kHz and 870 kHz. Having such agreement without satisfying the wavelength minimum mesh size rules can be explained by getting the desired convergence without the need of such small mesh.

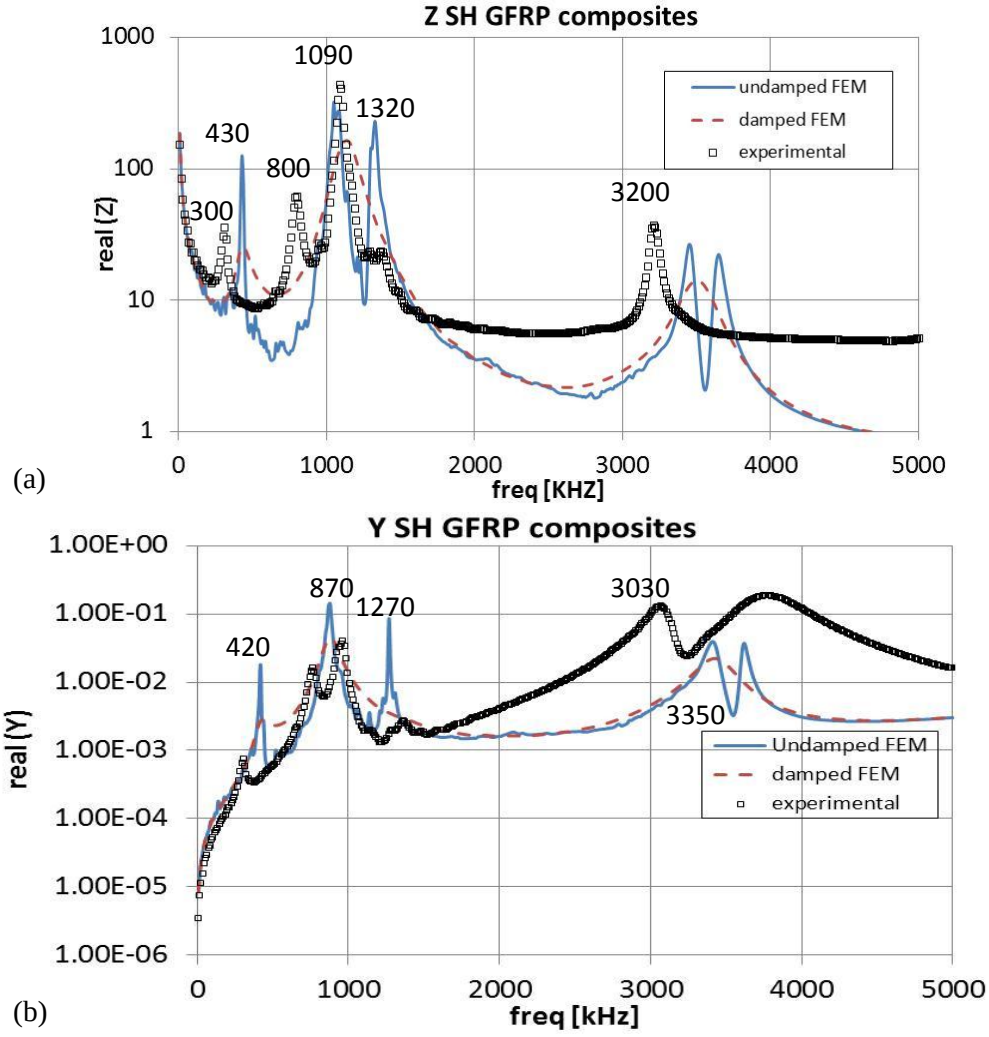

Figure 5.2. E/M response of SH-PWAS bonded on woven GFRP: (a) impedance, (b) admittance

The EMIS method is a good candidate for SHM systems to detect small damages in the vicinity of the transducer. This statement can be reasoned by looking to the simulated response at an arbitrary frequency of 400 kHz. **Figure 5.3** shows that the effects on the plate associated with exciting the SH-PWAS at 400 kHz are local effects. Hence the PWAS can capture the changes if they are within this localized area. By contrast, exciting the PWAS at relatively smaller frequencies would resonate the whole structure, and simulations results at 20 kHz and 50 kHz are shown in **Figure 5.4**.

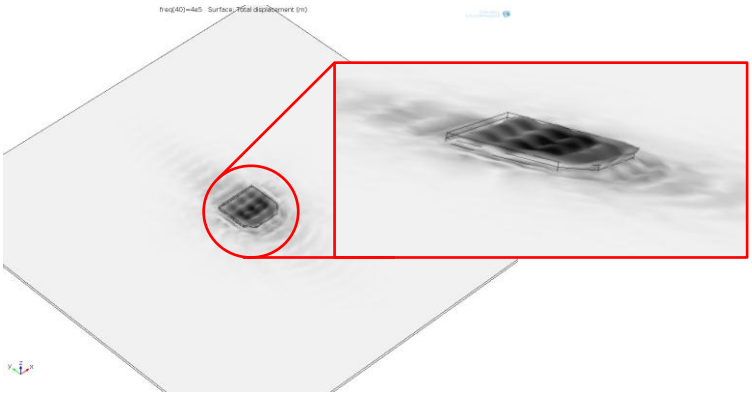

Figure 5.3. COMSOL simulation of 400 kHz response of the SH-PWAS bonded to GFRP plate

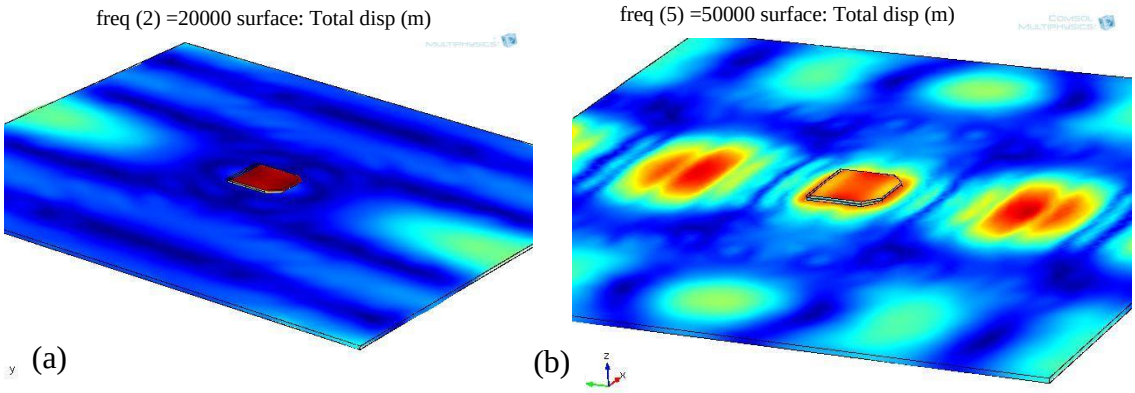

Figure 5.4. COMSOL simulation of GFRP plate resonance modes under excitation of SH-PWAS: (a) at 20 kHz, (b) at 50 kHz.

5.2.2. EMIS of quasi-isotropic CFRP plate

Similar experimental EMIS measurements were performed on the 2-mm thick CFRP plate; the frequency sweep was done up to 4 MHz. For the FEM, the CFRP plate consists of 8 layers each of thickness 0.25 mm (total plate thickness is 2 mm). The material properties of the plies #2, 3, 6, 7 are transformed by a 45-degree rotation from the original material properties. The mesh size used here was a rough one, the plate mesh size was 5-mm with 8 elements per thickness (i.e. 1 element per layer). The PWAS mesh size was 0.5 mm as before and 4 elements per the 1-mm thickness. The solution time was ≈9 days on the same 3.4 GHz i7 intel processor with 8-core PC and 16 GB RAM.

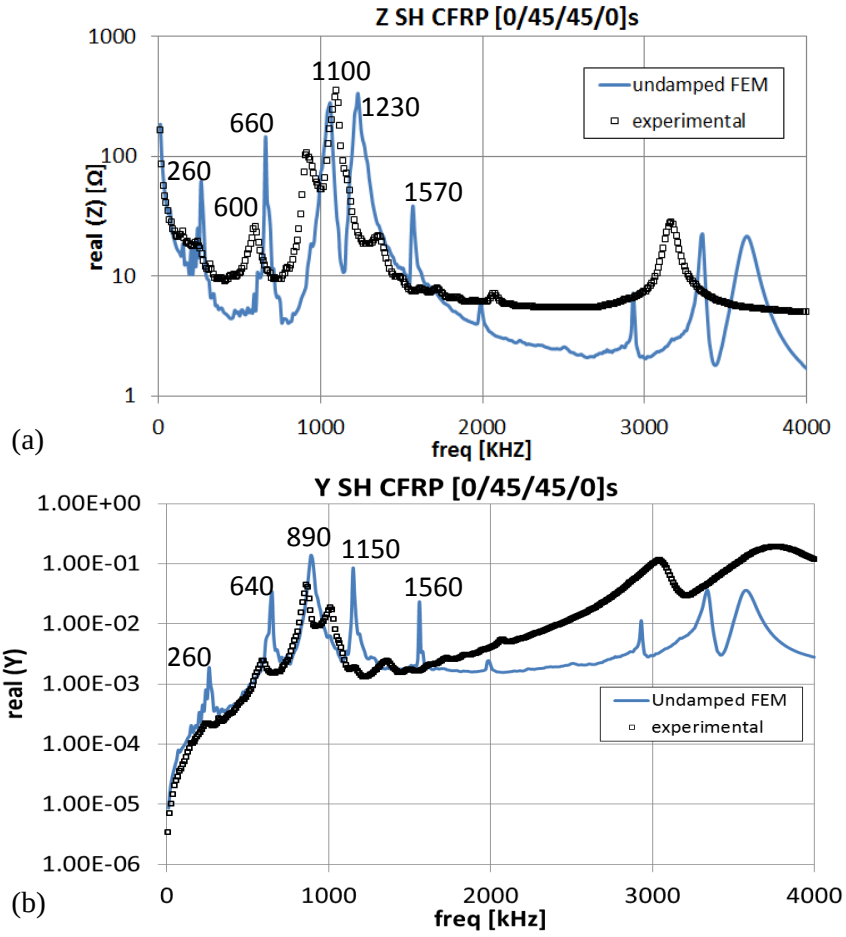

Figure 5.5. E/M response of SH-PWAS bonded on [0/45/45/0]s CFRP: (a) impedance, (b) admittance.

The comparison between experimental and FEM results is shown in **Figure 5.5**. For the mesh size 5 mm and SH wave propagation speed in the laminate $\approx$2200m/s (the next section discusses the SH wave propagation speed), the maximum frequency that we can trust in the FEM model results is 44 kHz. However running the model on the same machine used for the GFRP case yielded comparable results between experiments and FEM, especially in admittance results (**Figure 5.5**). It can be noticed that the first resonance detected by FEM is 260 kHz; this resonance is present in the experimental results but very damped. The second peak $\approx$640 kHz had a good agreement; finally, the free PWAS resonance frequency is shown at $\approx$890 kHz.

5.3. GUIDED SH WAVE PROPAGATION IN COMPOSITES

A set of experiments were conducted for testing the excitation and reception of SH waves in polymer composites. The idea is very similar to the experimental setup discussed in Chapter 3 (SH - Coupled PWAS); however, these experiments were not complete combinations of pitch catch experiments between SH-PWAS and regular extensional-type PWAS transducers due to the limited availability of transducers and materials. We compared experimental group velocities of guided waves with results from predictive tools, such as DISPERSE and our developed STMM. Finally we constructed a FEM models for simulating the wave propagation in 2-D in polymer composite materials. The predicted wave group velocities of guided wave propagation only in GFRP plate were covered in Chapter 4. The case of CFRP was not covered. For completeness, we recall in **Figure 5.6** the plots of **Figure 4.19**.

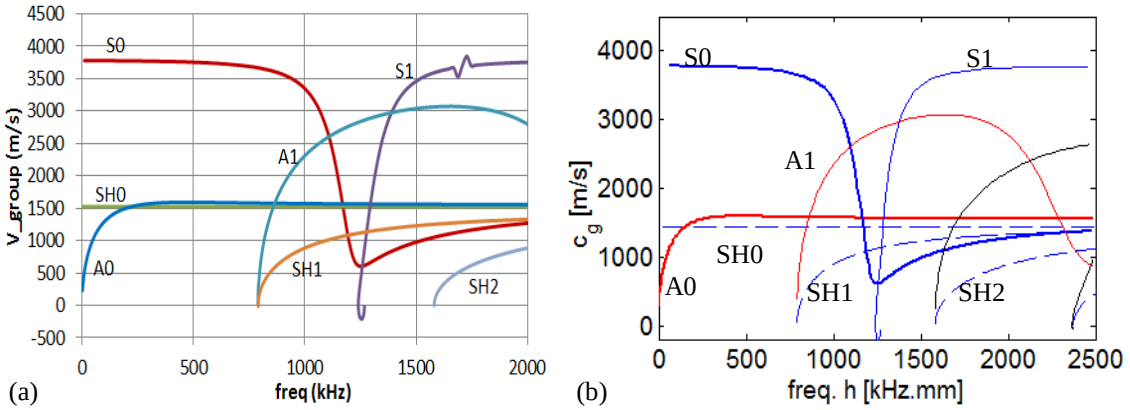

Figure 5.6. Group velocities of ultrasonic guided waves in 1-mm woven GFRP plate, (a) DISPERSE, (b) STMM.

Figure 5.6 shows the comparison between DISPERSE and our STMM predictive tool for calculated group velocities up to 2000 kHz. However, the experimental studies were done up to 300 kHz. Moreover, at this moment, we only predict wave propagation group velocities on CFRP plate by DISPERSE, because our STMM tool is under development. The predictions of both materials are shown in **Figure 5.7**.

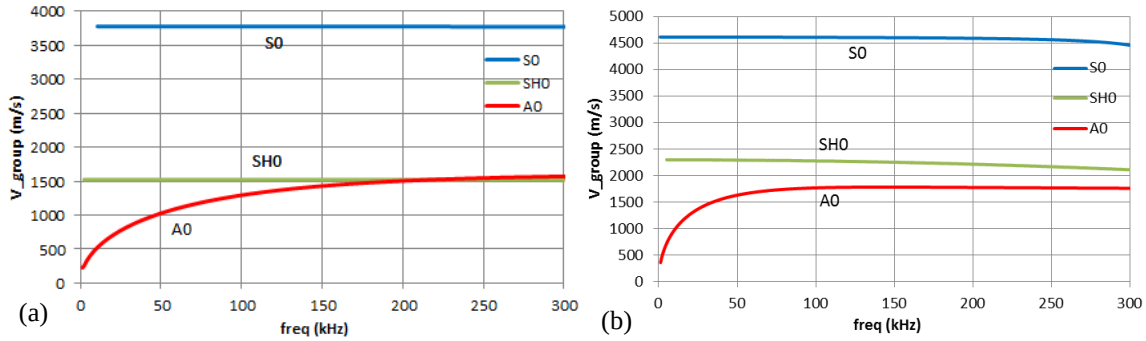

Figure 5.7. Group velocity dispersion curves for (a) 1-mm woven GFRP, (b) 2-mm $[0/45/45/0]_s$ CFRP

Now we discuss the experimental setup for each case and compare the experimental results with the predicted data, especially for our focus, SH waves.

5.3.1. Experimental Study for GFRP

The schematic setup (**Figure 5.8**) shows two installed SH-PWAS (#7 and #8) and two regular PWAS (#1 and #2). The distance between PWAS transducers is 120 mm. Pitch catch experiments were conducted by exciting PWAS transducers in turns with 3-count tone burst signals with 10V amplitude and sweep the center frequency up to 300 kHz.

Experiment-1 was done between the two SH-PWAS transducers, #7 and #8, by exciting SH-PWAS7 and receiving at SH-PWAS8; three types of waves were picked at the receiver SH-PWAS8, symmetric S0, antisymmetric A0 and SH0 (**Figure 5.10**a).

In experiment-2, the excitation was done by SH-PWAS7 and reception by PWAS1; we can see from **Figure 5.10**c that PWAS1 picked up SH0 waves as well as the expected S0 and A0. This interesting feature was also observed in isotropic aluminum plate. In experiment-3, the excitation was done by the regular PWAS1; the receiver SH-PWAS7 picked up SH waves. PWAS1 is supposed to excite only Lamb-type waves; however, SH0 waves were picked up by SH-PWAS7. Experiment-3 was exactly identical to experiment-2 (**Figure 5.10**c).

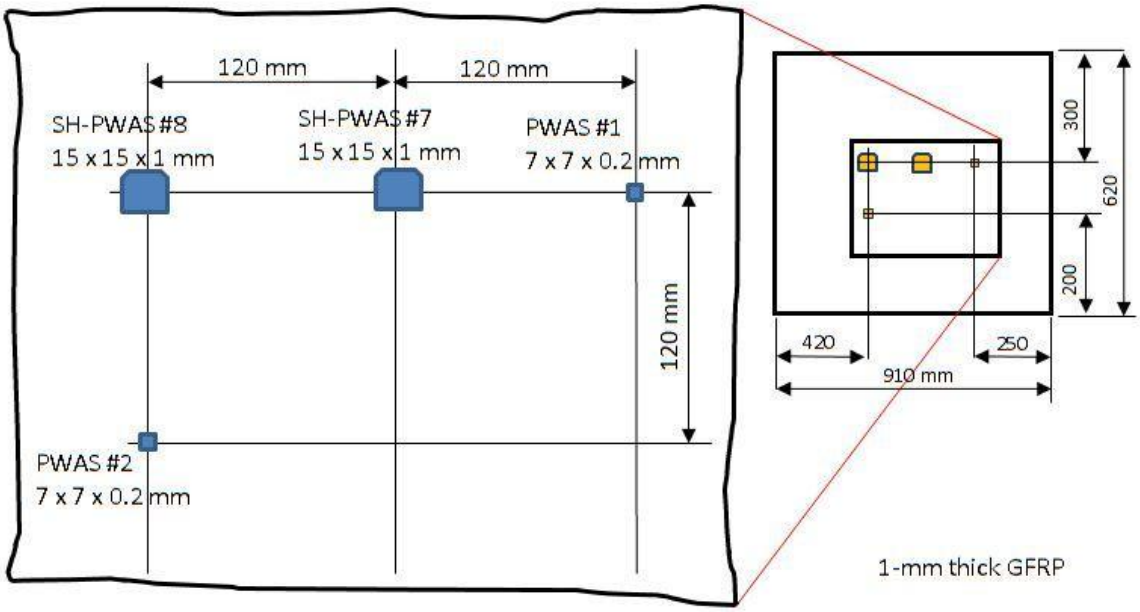

Figure 5.8. Schematic of transducers positions for SH-PWAS experiments on woven GFRP plate

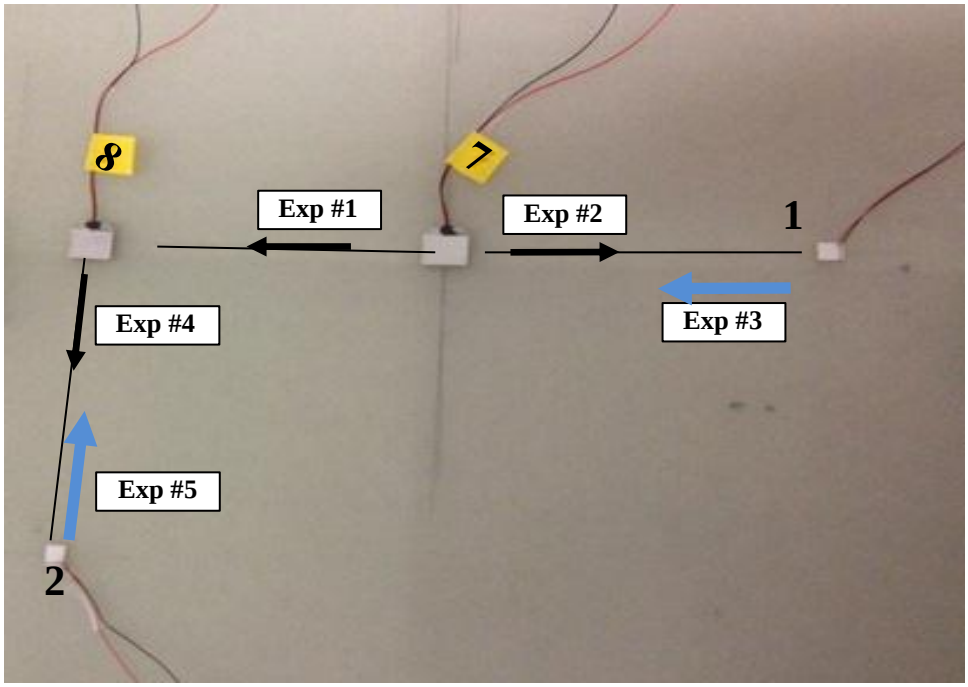

Figure 5.9. Experiments numbering and directions of pitch catch experiments between various SH-PWAS and PWAS on GFRP

Finally, experiment-4, where SH-PWAS8 was excited and the received signals were picked up by regular PWAS2. In this case, only S0 and A0 waves were picked up. This observation leads to the conclusion that SH-PWAS only excites SH waves perpendicular to its poling direction. This observation is analogous to the case performed on aluminum plate (**Figure 3.28**c) in which we showed that SH waves cannot be excited if the poling directions of two SH-PWAS were perpendicular to each other. Experiment-5 (the reverse situation of experiment-4) showed identical results (**Figure 5.10**b).

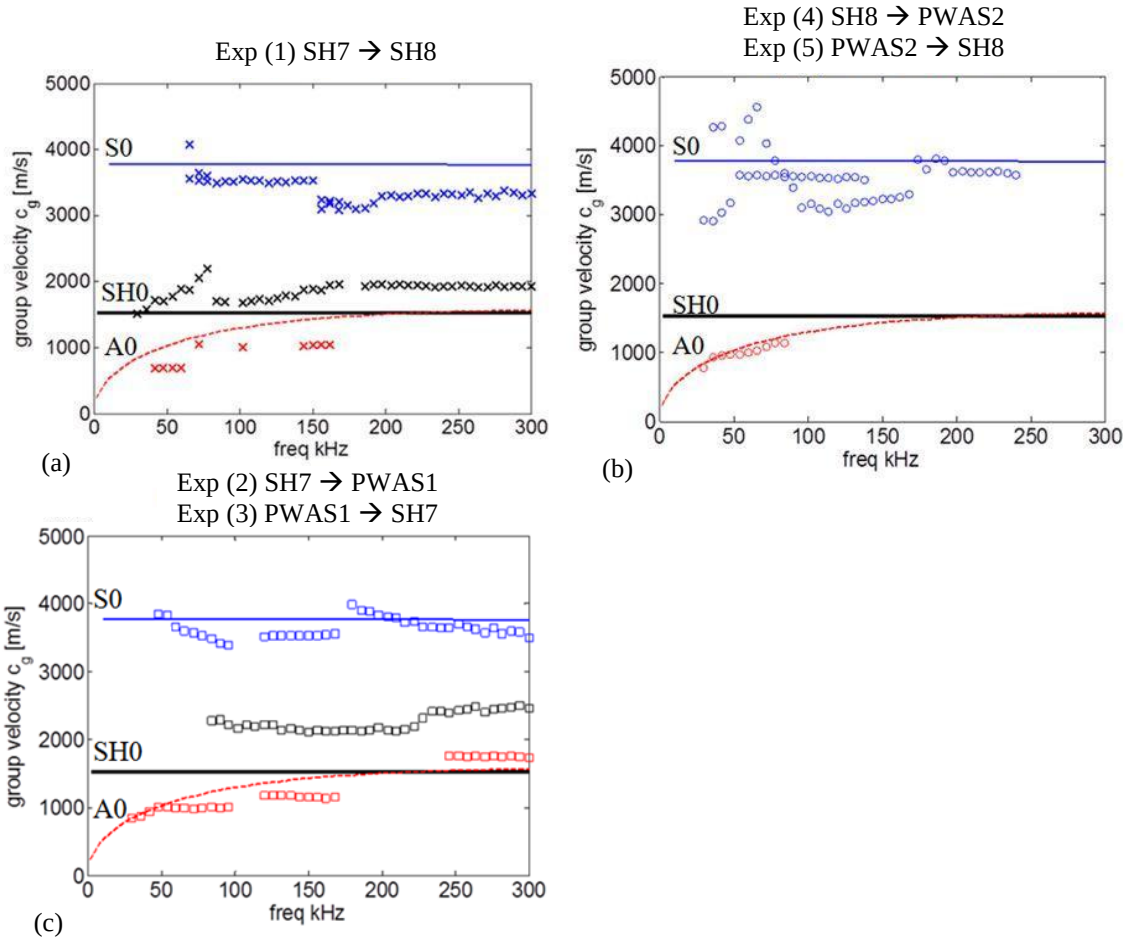

Figure 5.10. Dispersion group velocity curves for received wave signals (SH-PWAS experiment on GFRP): (a) SH7→SH8, (b) SH8→PWAS2, (c) SH7→PWAS1

5.3.2. Experimental Study for CFRP

Similar setup was established for experimental study of SH waves on 2-mm thick CFRP composite plate; a schematic is shown in **Figure 5.11**. And set of five experiments were performed.

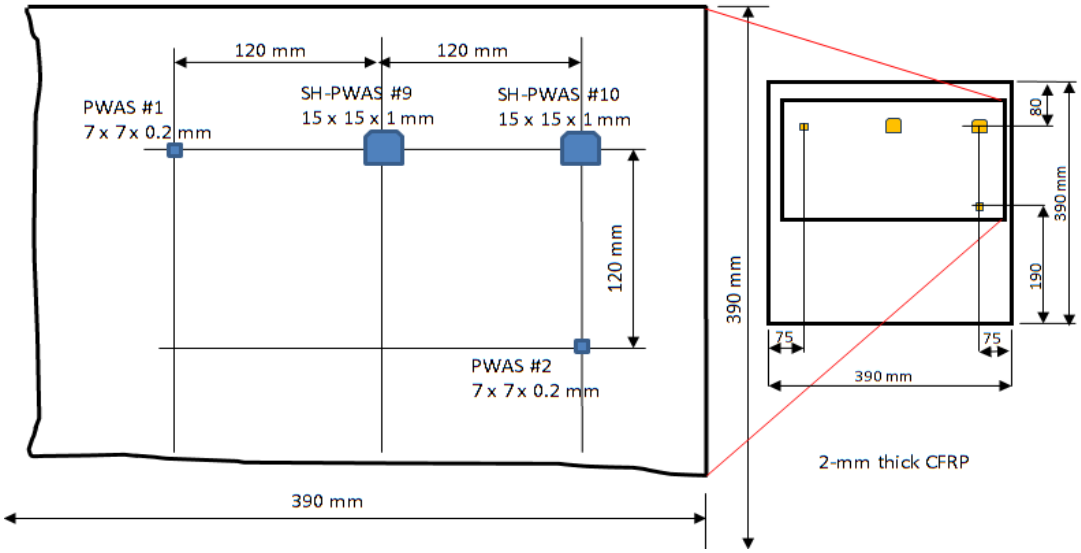

Figure 5.11. Schematic of transducers positions for SH-PWAS experiments on 8-ply CFRP plate

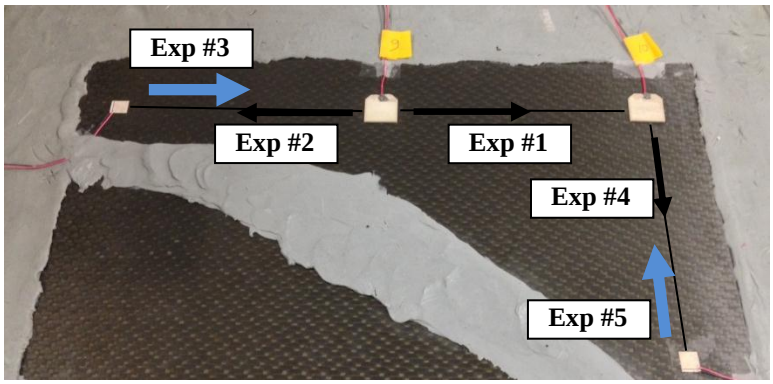

Figure 5.12. Experiments numbering and directions of pitch catch experiments between various SH-PWAS and PWAS on CFRP

The summary of experiments numbering is shown in **Figure 5.12**. The results are reported in **Figure 5.13**. An observation was noticed in experiment-1 of exciting the SH-

PWAS9 and receiving the signals by SH-PWAS10: it was noticed that the two wave packets captured by SH-PWAS10 had speeds that looked shifted compared to analytical predictions (**Figure 5.13**a). Recalling the material property updating we used earlier at the beginning of the chapter; we run the analytical predictions based on the manufacturer given properties; the new comparison of results is plotted in **Figure 5.13**b. This can be the reason of the shifted experimental results. However this will affect other experiments. We keep at this moment the reduced material properties that Gresil and Giurgiutiu (2013) suggested.

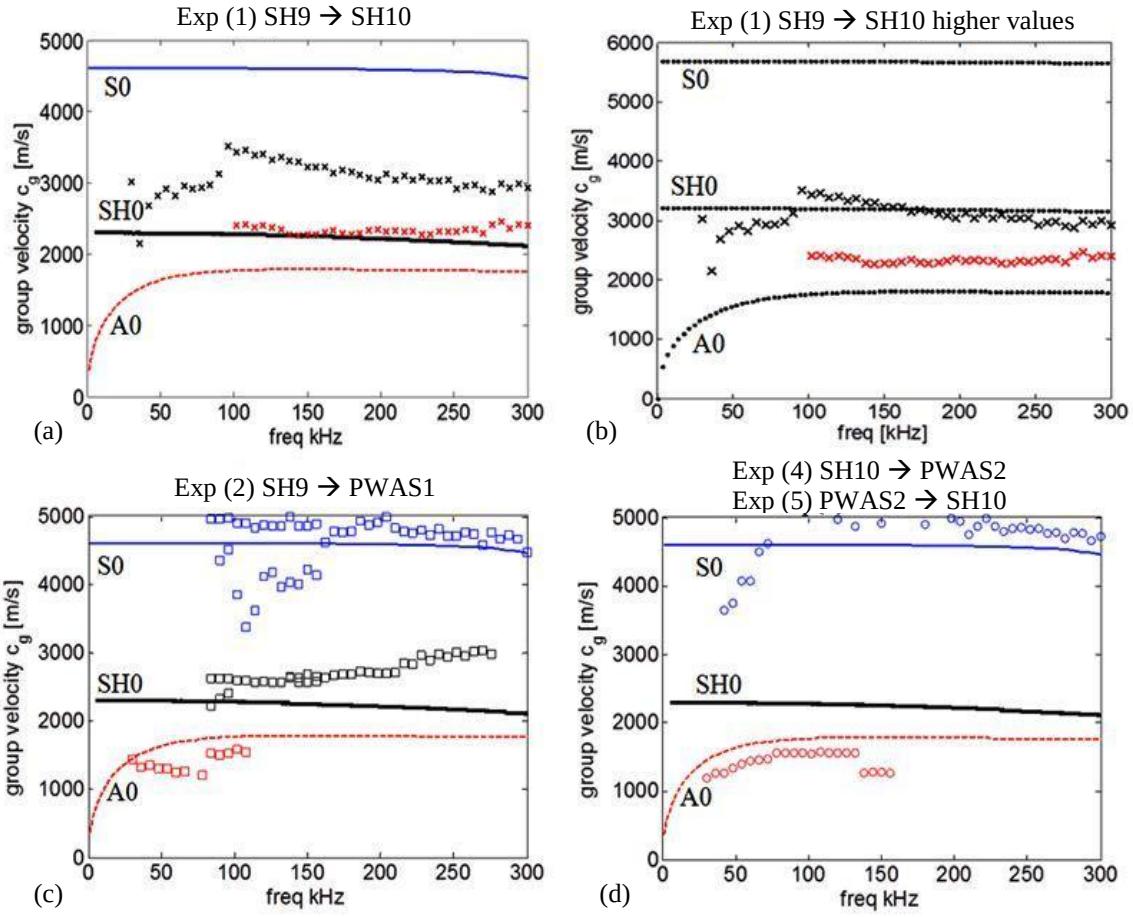

Figure 5.13. Group velocity curves for CFRP experiments: (a) SH→SH, (b) modified SH→SH, (c) SH9→PWAS1, (d) SH10→PWAS2.

Experiment-2 (where SH-PWAS9 was excited and the receiver was PWAS1) showed similar results obtained on GFRP plate by capturing the three waves S0, A0 and SH0. Experimental-3 (the reverse situation of experiment-2) showed identical results (**Figure 5.13**c)

In experiment-4, we excite the SH-PWAS10 which is installed such that poling direction is parallel to the line connecting SH-PWAS10 and receiver PWAS2; in this situation, PWAS2 did not capture SH waves, but only received A0 and S0 modes. Experiment-5 was identical to experiment-4 (**Figure 5.13**d).

5.3.3. FEM Case Studies for GFRP

The dimensions of the plate used for FEM for wave propagation were 450 mm x 450 mm and 1-mm thick GFRP, the actual material consists of 6 identical woven layers. We modeled the whole 1-mm thickness as one woven layer. The setup for simulating experiment-2 and 3 was shown in **Figure 4.21**. Here, we show the FEM mesh and geometry for experiment-1 setup (**Figure 5.14**), where wave propagation between two SH-PWAS transducers was studied. The two SH-PWAS were modeled by coupled field elements; this allowed us to apply excitation voltage as input for the model, and receive the signal at the receiver SH-PWAS as actual voltage.

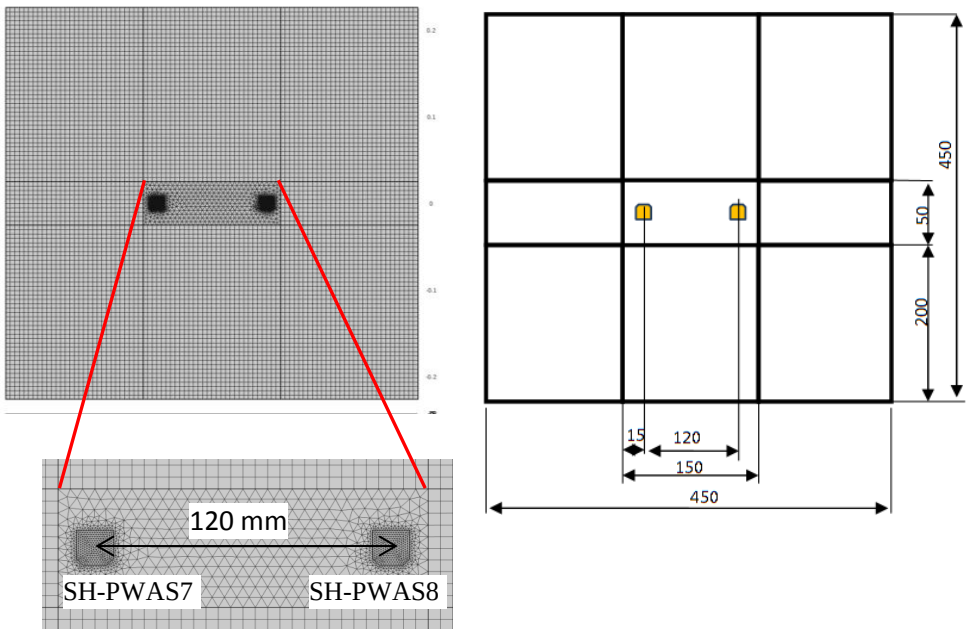

Figure 5.14. FEM schematic for guided wave propagation between SH-PWAS7 and SH-PWAS8

The excitation signal was 3-count tone burst with 10V signal amplitude and center frequency 60 kHz. The reason for selecting this relatively low frequency was to satisfy accuracy and convergence requirements, beside the available computational resources. For convergence, the required time step should be $\leq (1/30 f_c)$. For our 60 kHz situation, the maximum possible time step is $0.55\,\mu s$. We used $0.5\,\mu s$ time step and total simulation time $500\,\mu s$. This case study was the first model we ran, as a proof of concept, so we used rough mesh size and did not satisfy wavelength requirements. In this case study, more concern was towards SH waves. Referring to dispersion group velocity curves (**Figure 5.7**a), the speed of SH0 was 1500 m/s. For 60 kHz excitation signal, the corresponding wavelength is 25 mm.

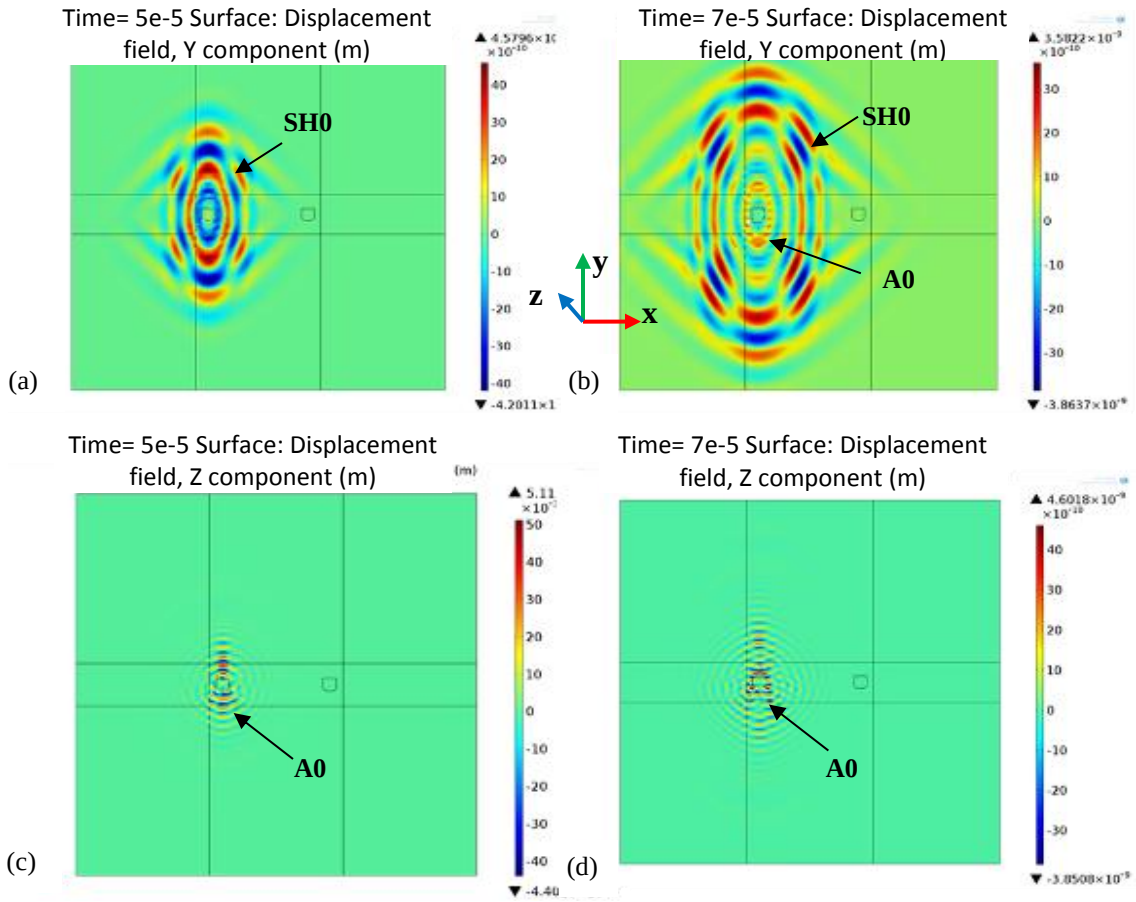

Figure 5.15. 2-D simulation results for wave propagation in 1-mm thick woven GFRP plate, particle displacement inplane Y direction: (a) at 50 μs ,(b) at 70 μs . Out of plane Z particle displacement: (c) at 50 μs ,(d) at 70 μs .

Mesh size used was 5 mm for the plate with 2 elements per thickness (i.e. 0.5 mm). Piezoelectric element mesh size was 1 mm with 2 elements per thickness (i.e. 0.5 mm). The simulation was done on 3.4 GHz intel i7 processor with 8-core PC with 16 GB RAM; the simulation took $\approx$ 2 hours.

Referring to the coordinate system shown in **Figure 5.15**, the SH waves are the waves associated with particle oscillation in y-direction which is parallel to SH-PWAS poling direction. While, the wave propagation direction of SH waves is *x* direction. **Figure 5.15**a,b show the y-displacement of the particle oscillation. SH0 can be noticed

having a speed between S0 and A0. Only those mode patterns appear on y-displacement solution. When plotting the out of plane z-displacement of particle oscillation, we can see only A0 mode because of its dominant energy is in the out of plane direction (**Figure 5.15**c,d). We report in **Figure 5.16** the comparison between the voltage signal picked by the receiver SH-PWAS8 and the calculated output signal from FEM.

As we can see from **Figure 5.16**, the FEM predicted SH0 and A0 modes. A0 mode from FEM is comparable to experimental results. The S0 mode was observed experimentally, but the FEM did not pick it up.

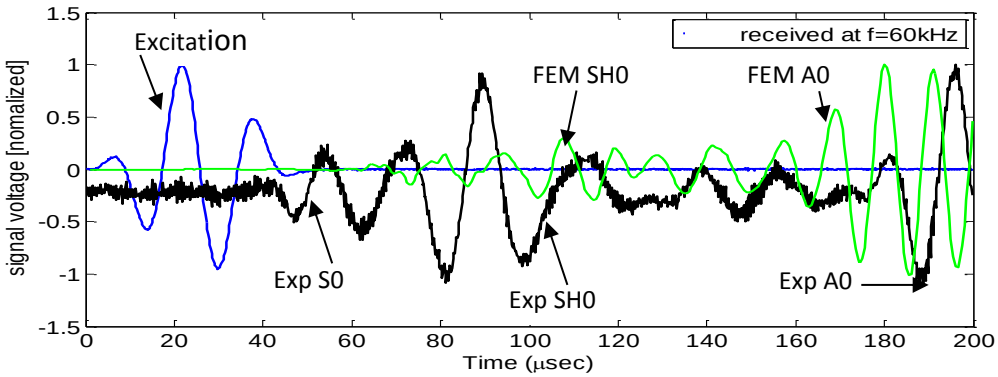

Figure 5.16. FEM vs. experimental results for guided wave propagation in 1-mm thick woven GFRP (SH-PWAS to SH-PWAS).

The second case study was exciting the regular extensional-mode PWAS with the received signal being picked up by SH-PWAS. As discussed in the experimental section, we did not expect that regular extensional-mode PWAS could excite SH waves. Observing SH waves when the regular PWAS was used for excitation could be reasoned by finite dimensional differences between the two transducers: the regular PWAS and the SH-PWAS. For completeness, we report the results for the FEM that simulates wave propagation between PWAS and SH-PWAS7.

For getting accurate results, it is required for each mode that the number of elements per wavelength is ≥ 10. Recalling **Figure 4.20**, the speeds for S0, SH0, and A0 at 48 kHz excitation are $\approx$3800m/s, 1500m/s, and 1000 m/s respectively; this corresponds to wavelengths $\approx$ 80, 31, and 21 mm respectively. The critical mode is A0, which enforces the 2-mm mesh size requirement. But we used 3-mm mesh size because of computational resources available, and we would expect that the results for 2-D solution for A0 mode will not look very smooth, as shown in **Figure 5.17**. For convergence, the required time step should be $\leq (1/30 f_c)$ which in our 48 kHz case should be 0.7 µs ; we used 0.5 µs time step and 200 µs total simulation time.

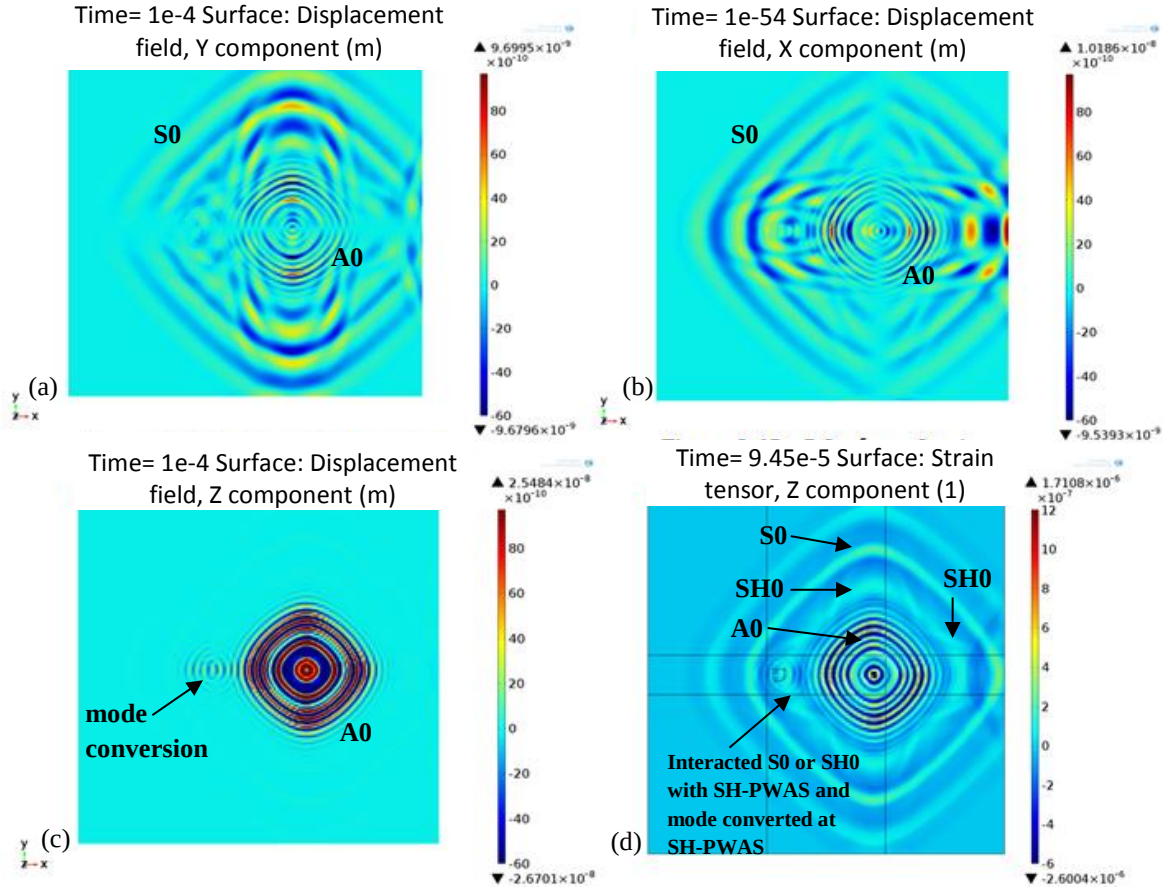

Figure 5.17. 2-D simulation results for wave propagation in1-mm thick woven GFRP plate at, (a) particle displacement inplane Y direction, (b) inplane X direction, (c) out of plane Z direction, (d) out of plane strain tensor

The simulation was done on dual 2.8 GHz XEON 2ML2 processor, and used up to 96 GB of RAM; the simulation took 9 hours. The 2-D simulations allowed us to see the wave propagation patterns; **Figure 5.17**a,b show the symmetric S0 and antisymmetric A0 modes very clearly (A0 mode is the mode with lower wavelength because of its lower wave propagation speed.) The fact that both S0 and A0 have inplane components, allowed the simulation to capture both S0 and A0 for inplane displacement plots. However, the out of plane (the Z component) of the symmetric S0 mode is very weak, as we can see from **Figure 5.17**c, where S0 mode almost does not exist.

Figure 5.17c shows the A0 mode out of plane displacement very clearly at 100 μs. And a small excitation can be seen around the receiver SH-PWAS, which is just a receiver PWAS and not used as excitation source; this can be explained by the active/passive behavior of PWAS transducers. While A0 mode excited by PWAS1 did not yet arrive at SH-PWAS, the other faster modes (e.g. S0 and SH0) had already arrived and interacted with the transducer, mode converted as A0, and the SH-PWAS appeared as if it was exciting A0 mode towards PWAS1.

Figure 5.17d shows the out of plane component of the strain tensor; we selected this variable for discussion; because it was found the best one showing most of the interesting modes and mode conversion phenomenon. Finally, the fact that the GFRP plate was woven showed that the waves are not propagating in circles, but rather in diamond-shaped, because the material stiffness properties are identical in 0º and 90º directions, but the material is less stiff in 45º directions.

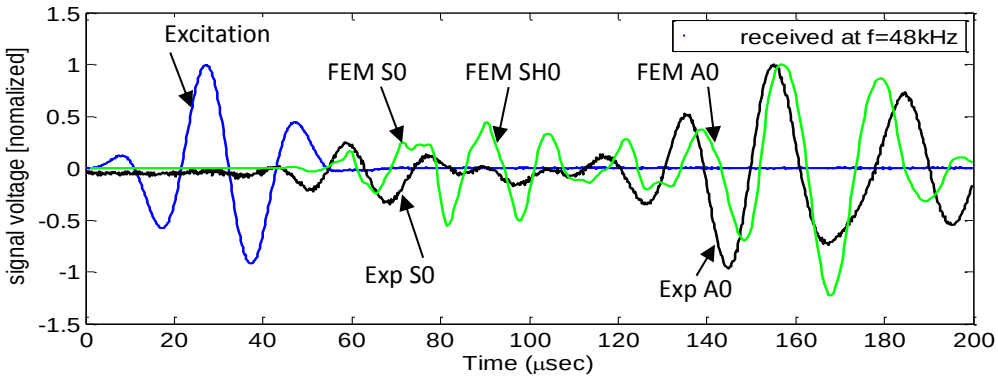

Figure 5.18. FEM vs. experimental results for guided wave propagation in 1-mm thick woven GFRP

As we can see from **Figure 5.18**, the FEM predicted S0, SH0 and A0 modes. A0 mode had good agreement with experimental results, S0 mode predicted by FEM and measured experimentally were fairly close; while SH0 at this particular frequency was not very clear experimentally.

5.3.4. FEM Case Study for CFRP

The dimensions of the plate used for FEM for wave propagation in CFRP were originally 450 mm x 450 mm and 2-mm thick. That was modified a little to save in computation resources and time. As shown in **Figure 5.19,** the geometry of the plate was no longer a square of length 450 mm, but was reconstructed to 570 mm x 450 mm; such that the distance between the two SH-PWAS is still 120 mm; afterwards the geometry was sliced in two; imposing symmetry conditions; simulations were done only on half the model. In the post processing stage in COMSOL Multiphysics, it is possible to request doubling the solved domain for the case of symmetry in the solution.

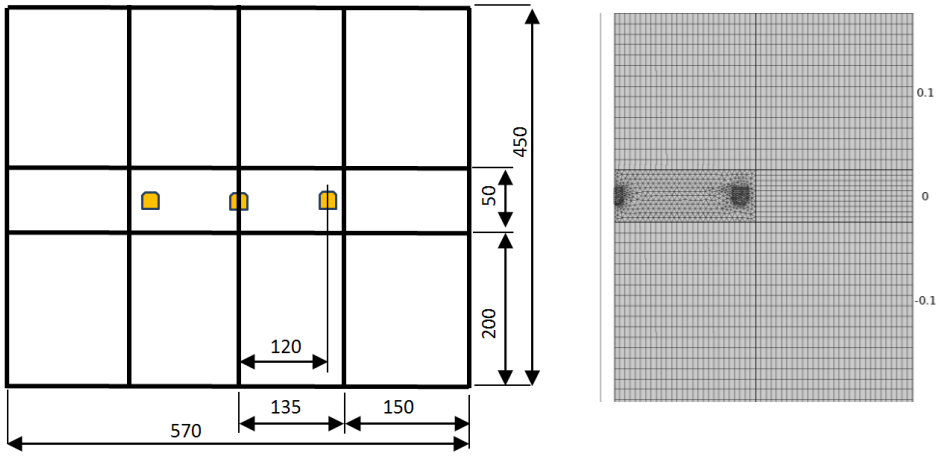

Figure 5.19. FEM geometry for guided wave propagation between SH-PWAS9 and SH-PWAS10 on CFRP plate

The CFRP plate is 2-mm thick 8 layer laminate; we used 8 elements per the thickness to get one element per layer. The excitation signal was 3-count tone burst with 10V signal amplitude and center frequency 48 kHz. Time step was $0.5\,\mu s$ and the total simulation time was $200\,\mu s$. The used mesh size was 5-mm for the plate lateral dimensions and 1 element per layer (i.e. mesh size of 0.25 mm); the PWAS was meshed by 2-mm in-plane squares with 2 elements per the 1-mm thickness. The simulations wavelength requirements were not satisfied. We expected not a very accurate solution. The simulation time was ≈ 6 hours.

The results shown in **Figure 5.20** describes the SH wave propagation with two simulation time captures (**Figure 5.20**a, b). Also shown is the out of plane A0 mode that the SH-PWAS excites along with SH waves.

Figure 5.20c shows that before A0 mode reached the right and the left SH-PWAS transducers, a small excitation can be seen around the two receiver SH-PWAS, which are just receiver PWAS transducers and not used as excitation sources. This can be explained

by the active/passive behavior of PWAS transducers. While A0 mode (excited by the middle SH-PWAS) did not yet arrive at the two SH-PWAS transducers, the other faster modes (e.g. S0 and SH0) had already arrived and interacted with both transducers, mode converted as A0, and the two SH-PWAS transducers appeared as if they were exciting A0 mode towards the middle PWAS.

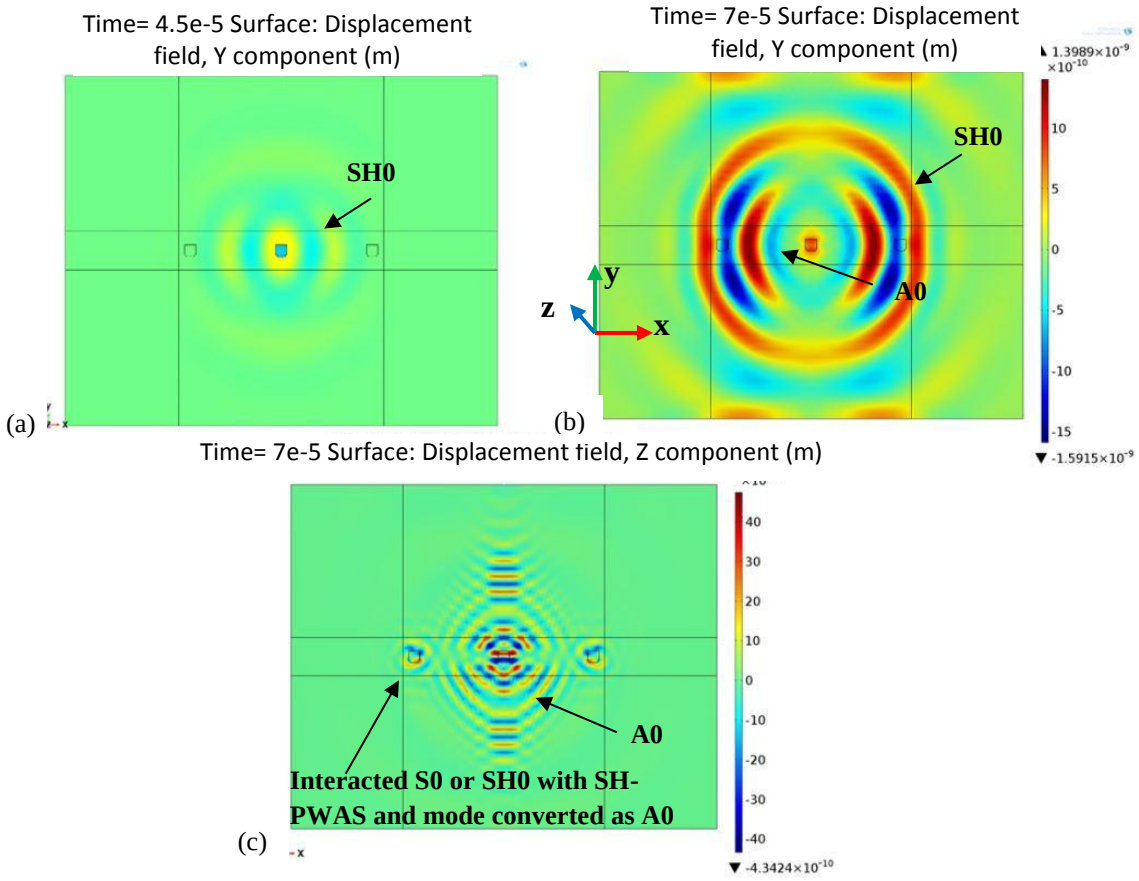

Figure 5.20. 2-D simulation results for wave propagation in 2-mm thick CFRP plate, particle displacement inplane Y direction: (a) at 45 μs ,(b) at 70 μs .(c) Out of plane Z particle displacement at 70 μs .

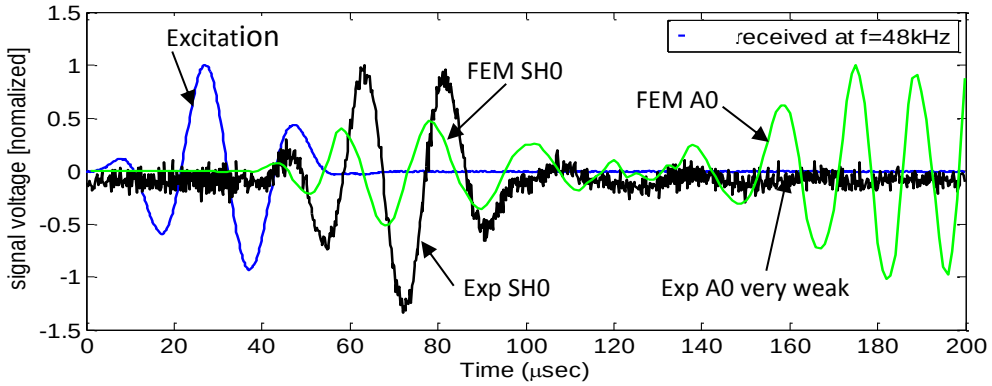

Figure 5.21. FEM vs. experimental results for guided wave propagation in 2-mm thick CFRP

As we can see from **Figure 5.21**, the FEM predicted SH0 and had good agreement with experimental results. The FEM also predicted A0 as a strong received signal, while the experimental result was very weak and noisy.

5.4. SUMMARY AND CONCLUSIONS

SH-PWAS was studied for E/M impedance method and wave propagation of SH waves in two composite plates, one was a cross ply GFRP laminate and the other was a quasi-isotropic CFRP laminate. It was shown that the impedance analysis is suitable for capturing local effects at the plates at frequencies ≈400 kHz. To capture the whole plate resonances, relatively smaller frequencies of excitation need to be used. Experimental admittance results were comparable to FEM results obtained using coupled field piezoelectric elements bonded to composite layers.

Wave propagation method showed that the SH-PWAS can excite SH waves as well as S0, A0, providing that the receiver PWAS is in a position such that the wave propagation direction between SH-PWAS and the receiver PWAS is perpendicular to

SH-PWAS poling direction. If we excite SH-PWAS and receive the signal along a direction parallel to the poling direction, only A0 and S0 waves were captured. These phenomena were observed in both GFRP cross ply laminate and CFRP quasi-isotropic laminate.

2-D FEM wave propagation simulation showed the wave propagation patterns of SH waves. The mesh size used was not satisfying the accuracy conditions of wavelength and mesh size because of our limited computational resources; nevertheless, the overall wave propagation showed consistent results with our expectations. The received signals predicted by FEM were compared with experimentally measured voltage signals. For the experiment between two SH-PWAS in GFRP, there was a little shift between received SH0 waves, but a good match for A0 mode. Predictive models of transmitted waves from a regular PWAS showed three waves: A0, S0 and SH0; however the experimental results did not show a strong SH0 signal.

Moreover, for CFRP simulations, there was a good match between SH0 mode predicted by FEM and measured experimentally. On the other hand, A0 was captured by FEM, but it was not detected experimentally.

SH-PWAS is a good transducer for generating SH waves in composite materials, and it is way less expensive than EMAT transducers; this makes it a potential candidate for composites SHM.

CHAPTER 6: GUIDED WAVE DAMAGE DETECTION IN AN AEROSPACE PANEL

The objective of this chapter is to test and to apply the basic theory that was covered in previous chapters on a realistic complex structure for detecting simulated damages. Of course, this will require more advanced system with some damage detection algorithms. We used a realistic aging aircraft specimen that was fabricated at Sandia National Lab with simulated aging-like induced damage. We presented the SHM system we used; it was developed by Metis Design (www.metisdesign.com). Brief description of sensors installation and system operation was addressed. Finally we proposed the tests that we will perform.

6.1. MATERIALS

The aging aircraft specimen was fabricated at Sandia National Lab with simulated aging-like induced damage (cracks and corrosion). It is made of 1-mm (0.040″) 2024-T3 Al-clad sheets assembled with 4.2-mm (0.166″) diameter countersunk rivets, with a U-shaped (BAC 1498-152 stringer), as shown in **Figure 6.1**.

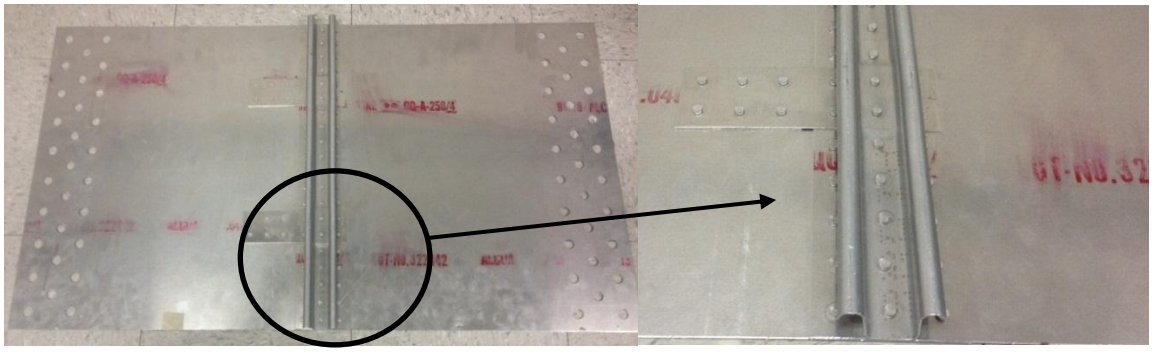

Figure 6.1. Image of the 2024-T3 Al plate under test

This plate was used before for testing certain simulated damages that were included in the blue print (**Figure 6.2**) developed at Sandia National Laboratory. The detailed experimental setup and results were reported in Giurgiutiu et al. (2002).

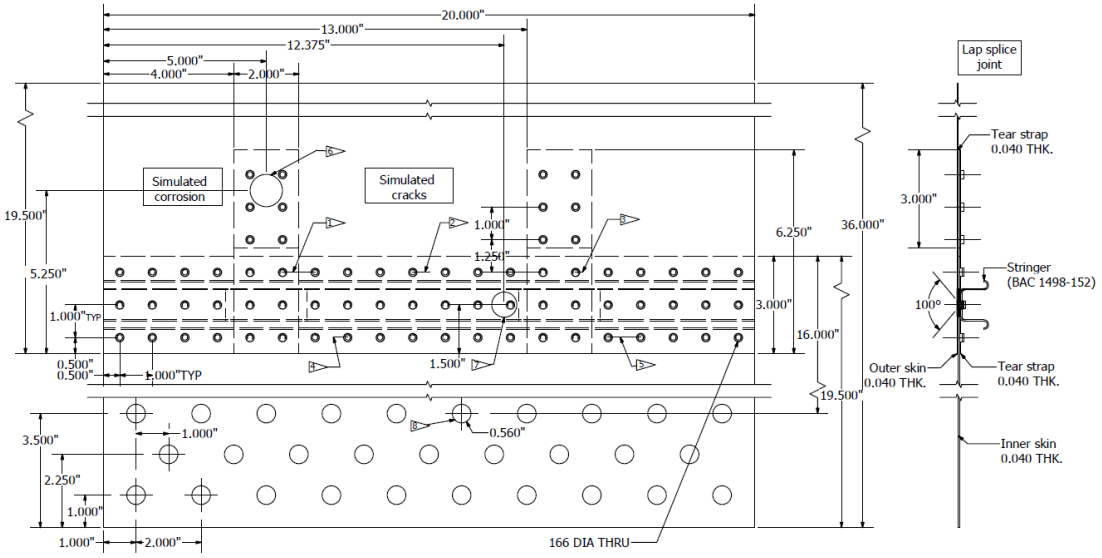

Figure 6.2. Blue print of the experimental panel developed at Sandia National Lab.

6.2. EXPERIMENTAL SET UP FOR MD7 ANALOG SENSOR-ASSEMBLE SYSTEM

The hardware is developed by Metis Design (www.metisdesign.com) and it includes (1) piezoelectric-based damage localization sensors (MD7 VectorLocator™), (2) distributed digitization hardware (MD7 IntelliConnector™), and (3) a data accumulation

hub (MD7 HubTouch™). These items are shown in **Figure 6.3, Figure 6.4**, and described briefly here after.

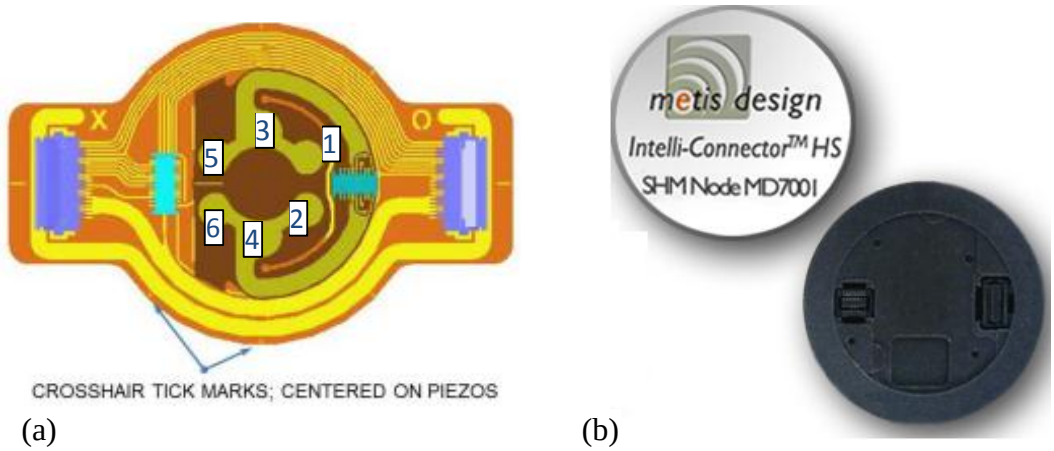

(a) (b)

Figure 6.3. (a) MD7 VectorLocator™, (b) MD7 IntelliConnector™. Source: Metis Design

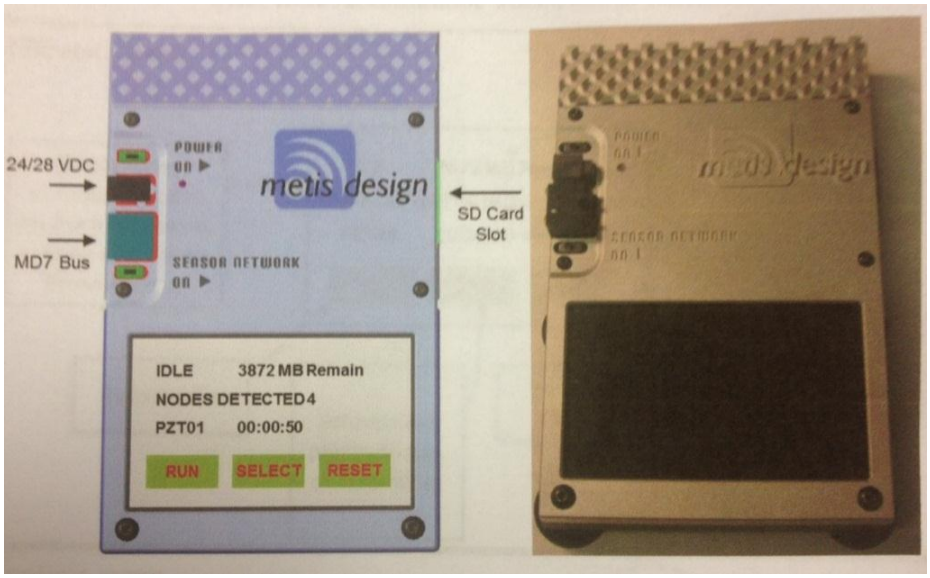

Figure 6.4. MD7 Data Accumulator hub, HubTouch™, source: Metis Design manual

As we can see from **Figure 6.3**(a), the VectorLocator™ consists of a central actuating disk with multiple sensing disks. The actuating and the sensing component

consist of seven piezoelectric wafers that are integrated into a custom flex-circuit assembly that connects to the IntelliConnectors™ shown in **Figure 6.3**(b).

For the bonding of the flex-circuit to the aluminum plate, we used Vishay Micro-Measurements AE-10 adhesive; dead weights of 10 N were used, and the adhesive was left to cure for 24 hours in 25 C room.

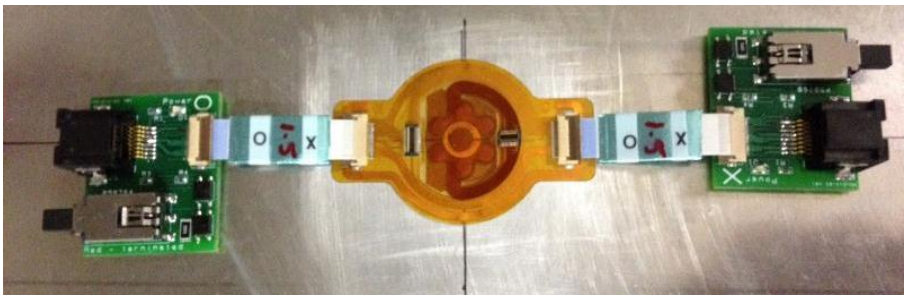

Figure 6.5. Sensors node VectorLocator™ after bonding. Connectors are used to connect different sensors node together or to the data accumulator hub.

The IntelliConnector™ is a digital sensor infrastructure; a direct replacement of traditional instrumentation such as oscilloscopes and function generators. This device greatly reduces unnecessary cable weight by allowing data to be carried over a serial sensor-bus and increases signal fidelity by digitizing at the point-of-measurement to eliminate EMI. The IntelliConnectors™ excite analog sensors mated through micro-connectors and digitize their response (Kessler et al., 2011). The complete setup is shown in **Figure 6.6**.

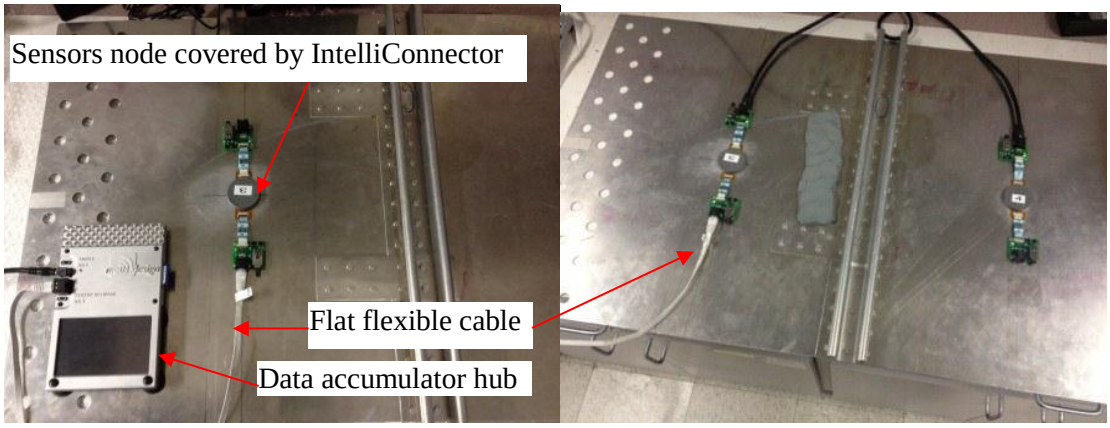

Figure 6.6. Complete setup of the MD7 SHM system

6.3. OPERATION OF MD7 SYSTEM

After the experimental setup, and powering up the system, the data accumulator hub will automatically detect the number of sensor nodes connected to the system. A "profile" needs to be loaded to the data accumulator hub; this profile contains the required parameters to perform the pitch catch, the example profile we used is shown in **Figure 6.7**. The main parameters of concern are:

- excitation waveform type: tone burst, # number of Hanning cycles
- Actuator start frequency kHz
- Frequency step size (kHz)
- Actuation amplitude Vpp

```
//-------------------------------------------------------------------------------------------------------------
//
// Filename:  PC001.GW
//
// Profile Version: 4.5
//
// This file is used to set the run-time parameters for the MD7 Hub Touch system.
//
// Do not modify the format or the spacing - Parameter values only.
//-------------------------------------------------------------------------------------------------------------

      Parameter Description                                  Valid Values
5.5   Waveform type, #of cycles of hanning window            3.5-5.5 in increments of 0.5.
50    Actuator start frequency (kHz)                         Range 30-100 kHz in 1 kHz steps, 100-500 kHz in 5kHz steps
30    Number of frequency steps                              0 = No stepping, one freq. only. Max = 100
10    Frequency step size (kHz)                              1 kHz (30-100 kHz) & 5 kHz (100-500 kHz)
20    Actuator amplitude (Vpp)                               1.25 - 20V in 1.25V increments
6     Number of sensor channels to aquire on                 0-6. 0 is actuator only. 1-6 are act+sensor
200   Data collection time (us)                              100-999 us.
50    Pulse-echo gain. Gain for act., listening for echo     1-500 (real gain)
50    Pitch-catch gain. Gain for sensor only, listening      1-500 (real gain)
64    Number of averages.                                    1 (no averages), 2-1024 (in powers of 2)
0     Pause time between averaged actuations (ms)            0-300 ms (in addition to 20 ms default)
1     Number of complete tests.                              1-999
0.10  Pause time between complete test sets (minutes)        0.10 - 1440.0
0     Flag to allow warmup                                   0: No Warmup, will Write SD; 1: Allow warmup, no SD write
```

Figure 6.7. Profile of a measurement, to be uploaded to the memory card before test

6.4. ANALYZING EXPERIMENTAL MEASUREMENTS BY METIS DESIGN SHM SOFTWARE

6.4.1. CAD Modeling

For pursuing analysis on the part, a CAD model needs to be created and meshed in the regular FEM manner. Besides, the plate layout file needs to be created, which defines plate limits, i.e. length and width. One point to consider here, that the CAD file needs to be created in inches, however the layout in meters and there is a conversion file to be supplied in the working directory, inside mesh folder. **Figure 6.8** shows the CAD model.

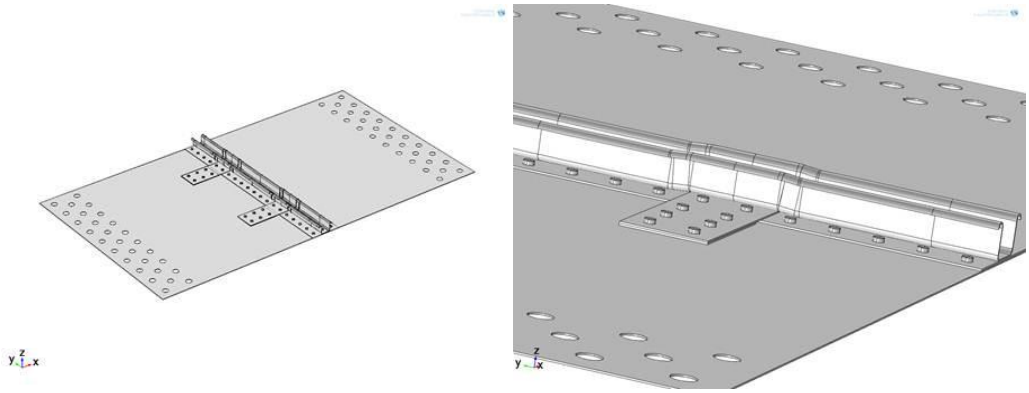

Figure 6.8. CAD Model on COMSOL for possible separate FEM later.

6.4.2. FEM Meshing

The CAD file is then imported into a finite element modeling software package for automatic meshing, typically ANSYS is the software that the Metis Design uses with the help of ANSYS script to perform meshing directly.

Typical exported mesh files are (1) the nodes list which specifies the node number and its coordinates, (2) the elements list, which specifies the element number and its connectivity with nodes (**Figure 6.9**).

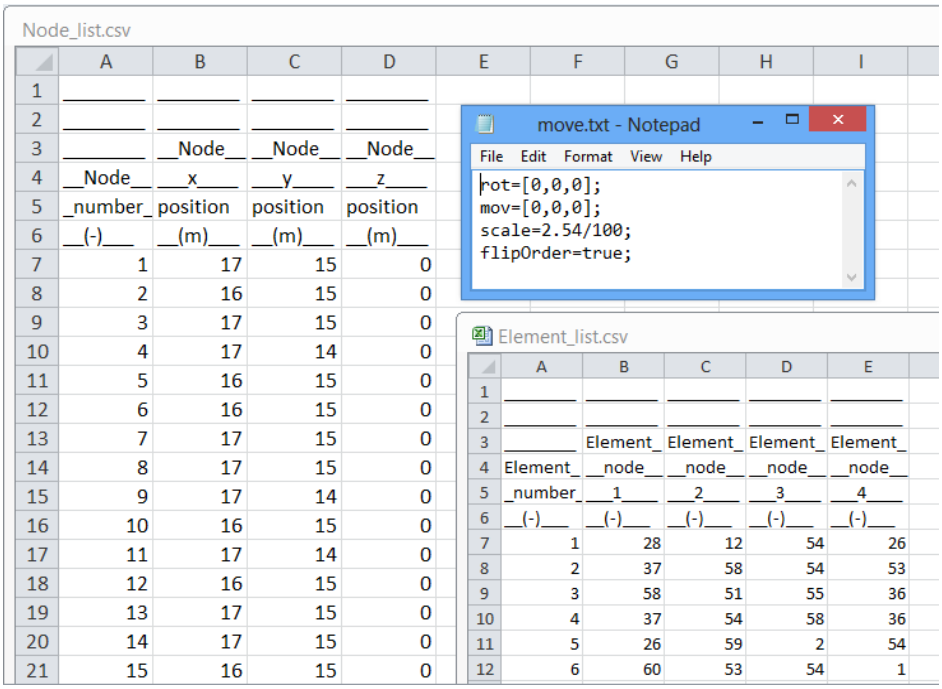

	A	B	C	D
1				
2				
3		__Node__	__Node__	__Node__
4	__Node__	___x____	___y____	___z____
5	_number_	position	position	position
6	__(-)___	__(m)___	__(m)___	__(m)___
7	1	17	15	0
8	2	16	15	0
9	3	17	15	0
10	4	17	14	0
11	5	16	15	0
12	6	16	15	0
13	7	17	15	0
14	8	17	15	0
15	9	17	14	0
16	10	16	15	0
17	11	17	14	0
18	12	16	15	0
19	13	17	15	0
20	14	17	15	0
21	15	16	15	0

	A	B	C	D	E
1					
2					
3		Element_	Element_	Element_	Element_
4	Element_	__node__	__node__	__node__	__node__
5	_number_	___1____	___2____	___3____	___4____
6	__(-)___	__(-)___	__(-)___	__(-)___	__(-)___
7	1	28	12	54	26
8	2	37	58	54	53
9	3	58	51	55	36
10	4	37	54	58	36
11	5	26	59	2	54
12	6	60	53	54	1

Figure 6.9. Exported mesh files and move.txt file for relative position, rotation and unit conversion

Once the mesh files are generated, it is ready to use the Metis Design software package for SHM, the starting windows is shown in **Figure 6.10**.

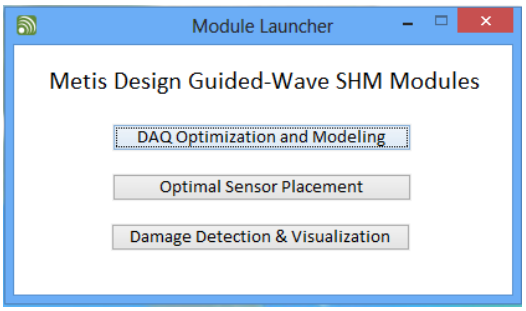

Figure 6.10. Module launcher for Metis Design software package

Our main focus here is not about DAQ optimization and modeling, neither the optimal sensor placement. But in general, the purpose of the DAQ optimization module is to import preliminary data from small set of sensors and the measured pitch-catch data for example; for the goal of optimizing the full scale testing. Also it aims to estimate statistical model parameters for sensors, e.g. the frequency at which the signals are having the maximum average, the global maxima, and the global standard deviations. This is used to calculate the frequency at which the signal to noise ratio (SNR) is the maximum.

Optimal sensor placement module:

The purpose of this module is to determine the optimal arrangement of specified number of sensors, given the statistical signal model parameters from previous module. This module exports to the layout file that is needed for the damage detection module. However at this stage, we designed our layout ourselves.

6.4.3. Damage Detection and Visualization

We installed two nodes of sensors, node 3 and node 4, the layout file provided is

ID	x	y	orient	mirrored	Transducer Functionality							Side				
3	0.6604	0.254	0	0	1	1	0	1	0	1	1	1	1	-3.14159	3.141593	1
4	0.254	0.254	180	0	1	1	1	1	1	1	1	1	1	-3.14159	3.141593	1

Figure 6.11. Layout of the sensor nodes

The working directory contains the following files

- **Mesh**
  - Node_list.csv – *Structure mesh node list*
  - Element_list.csv – *Structures mesh element list*
  - move.txt – *Settings to move and scale mesh after import (optional)*
  - Prior_probability.csv – *Nodal prior probabilities of damage (optional)*
- **Data**
  - **Dataset 1** – *User defined name*
    - **Run001** – *Contains acquired data from structure*
    - **Run002**
    - **Run003**
  - **Dataset 2**
    - …
- layout.csv – *Defines the sensor node layout on the structure (may be generated using Optimal Sensor Placement Module)*

Figure 6.12. Required files in the working directory of the software.

The file we meshed and imported in the damage detection and visualization module is shown in **Figure 6.13**.

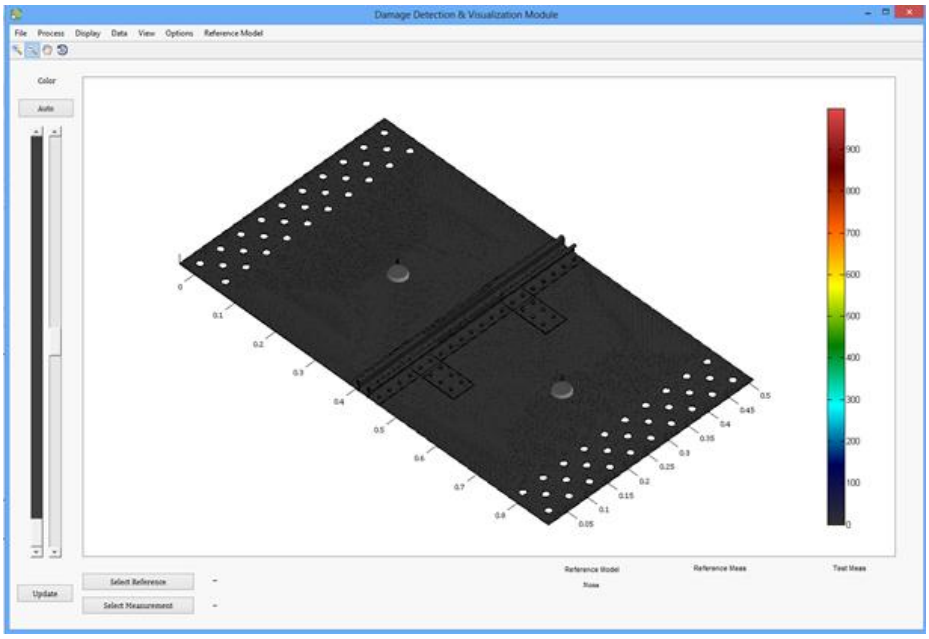

Figure 6.13. Damage detection and visualization module, after importing our test structure.

6.5. PROPOSED WORK

The SHM system developed by Metis Design is based on the baseline measurements concept. This means that when we installed the sensors nodes and run the pitch catch experiments between basically the 12 sensors within the two nodes, we have a baseline measurement Run001. Whatever damages that were induced in the plate (e.g. corrosion, slit cracks), this is the baseline measurement. We propose inducing some simulated damages, either by using the strong magnet attached to the plate with two magnets from both sides of the plate, or cover a part of the plate by clay as a wave absorption domain. After that we run another measurement run and save it as Run002. As shown in **Figure 6.13**, it is required to load reference measurement, then another measurement that is after inducing damage. As an illustration for the method, we installed a chunk of clay as shown in **Figure 6.6**, and the resulted output analysis is shown in **Figure 6.14**.

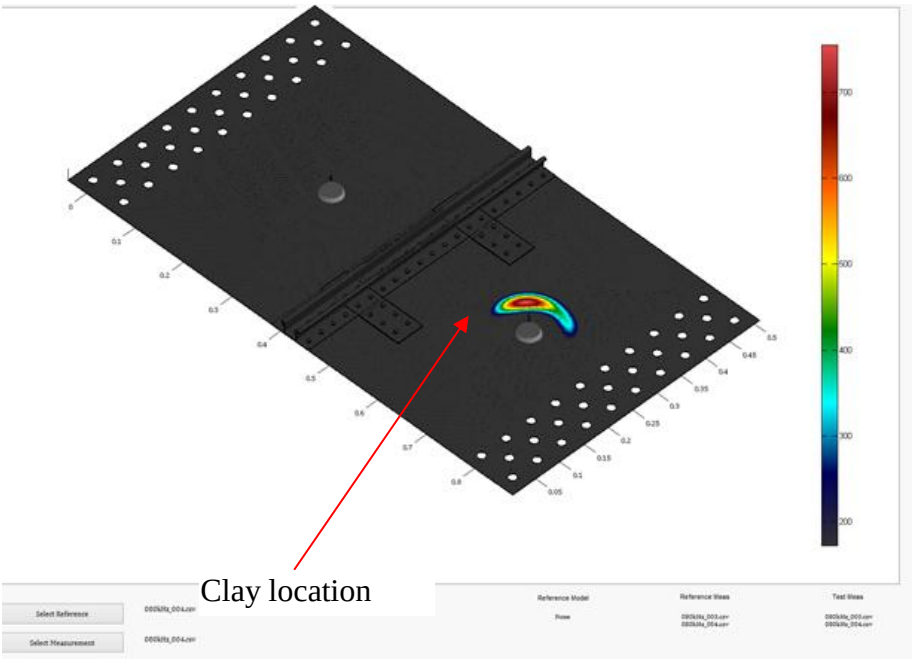

Figure 6.14. Preliminary result based on a baseline measurement and a measurement after inducing the clay on the plate at 80 kHz

6.6. SUMMARY AND CONCLUSIONS

The MD7 guided-wave SHM system developed by Metis Design was studied and tested, the steps included, sensor installation, operation and performing pitch catch measurements, CAD modeling, FEM meshing, exporting mesh to the software, and analysis in the damage detection and visualization module.

We conclude that the system is applicable on the plate under test, and further experiments to be conducted by inducing other forms of damages and test the system if it can detect these damages. Careful selection of frequency of excitation is an important parameter to be considered.

CHAPTER 7: SHM OF VARIABLE STIFFNESS CFRP PLATE

In this Chapter, we study the wave propagation in a CFRP plate with variable fiber orientations along plate width and length at every layer. This type of structure was studied by Tatting and Gurdal (2003); Blom (2010). The objectives here are: (1) to find experimentally the dispersion wave propagation speeds and (2) to discuss the challenges for getting accurate results. The methods involved for finding wave propagation speeds in this study are time of flight (TOF) with using Hilbert envelops over the signals, and short time Fourier transform (STFT). We installed eight PWAS transducers on the plate and performed pitch catch experiments between different transducers to investigate wave propagation along different fiber orientation angles, (keeping in mind that the fiber orientation is not homogenous at every x and y position.) This fiber orientation pattern leads to varying the plate stiffness as function of x, and y dimensions. Hence we refer to this plate as variable stiffness (VS) plate.

7.1. MATERIALS

The plate we used is a 140x 390 mm CFRP plate with a variable thickness that is ranging from 2.9 mm at edges to 3.4 mm in the middle. This plate was fabricated and studied by Tatting and Gurdal (2003). **Figure 7.1** shows the plate during fabrication stage.

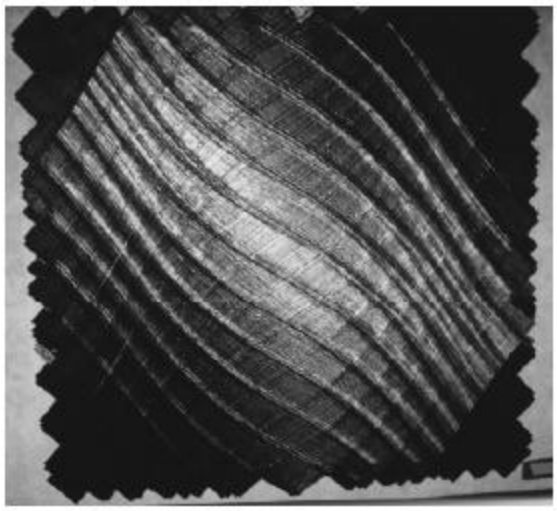

Figure 7.1. Fabricated CFRP panel with variable fiber orientation (Tatting and Gurdal, 2003)

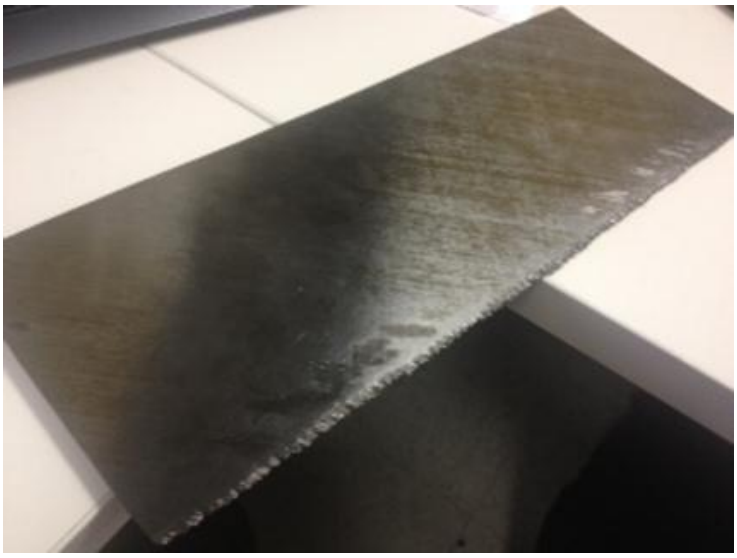

Figure 7.2. The part provided for performing wave propagation tests on

The final fabricated plate with PWAS transducers installed on it is shown in **Figure 7.3.**

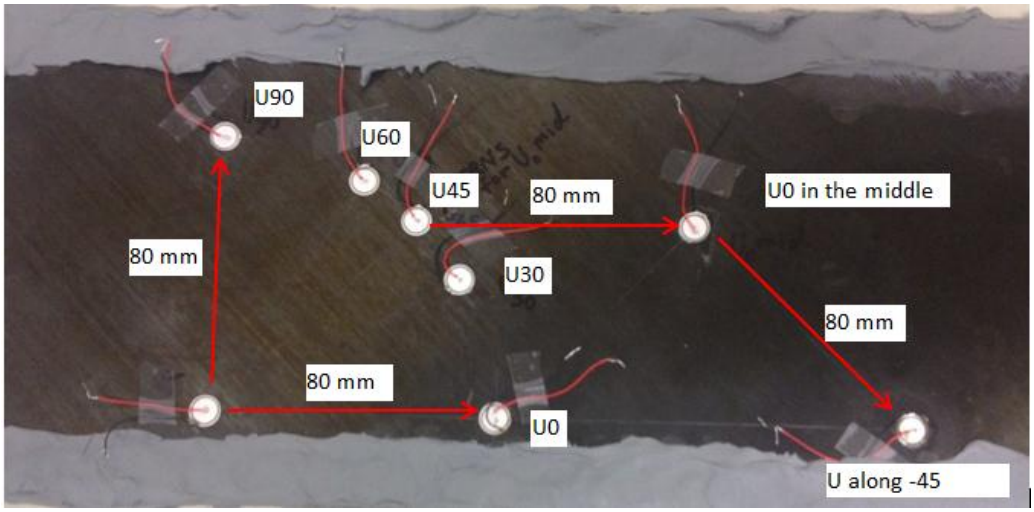

Figure 7.3. The VS CFRP plate with PWAS transducers installed and clay around boundaries

7.2. WAVE PROPAGATION EXPERIMENTS

The PWAS transducers were installed such that wave propagation along different angles can be studied, U0, U30, U45, U60, and U90. Also another test was performed between two PWAS transducers at the middle of the plate, and two PWAS with wave propagation along negative 45 deg. direction. All pitch catch experiments were performed between transducers 80 mm apart. The excitation used was 3-count tone burst with 10 V amplitude and frequency sweep up to 300 kHz. The challenge on this plate is that it is relatively small, and lots of reflections existed, hence we used the clay to damp these reflections as much as possible. The results of wave propagation are shown in the next few figures, in **Figure 7.4**.

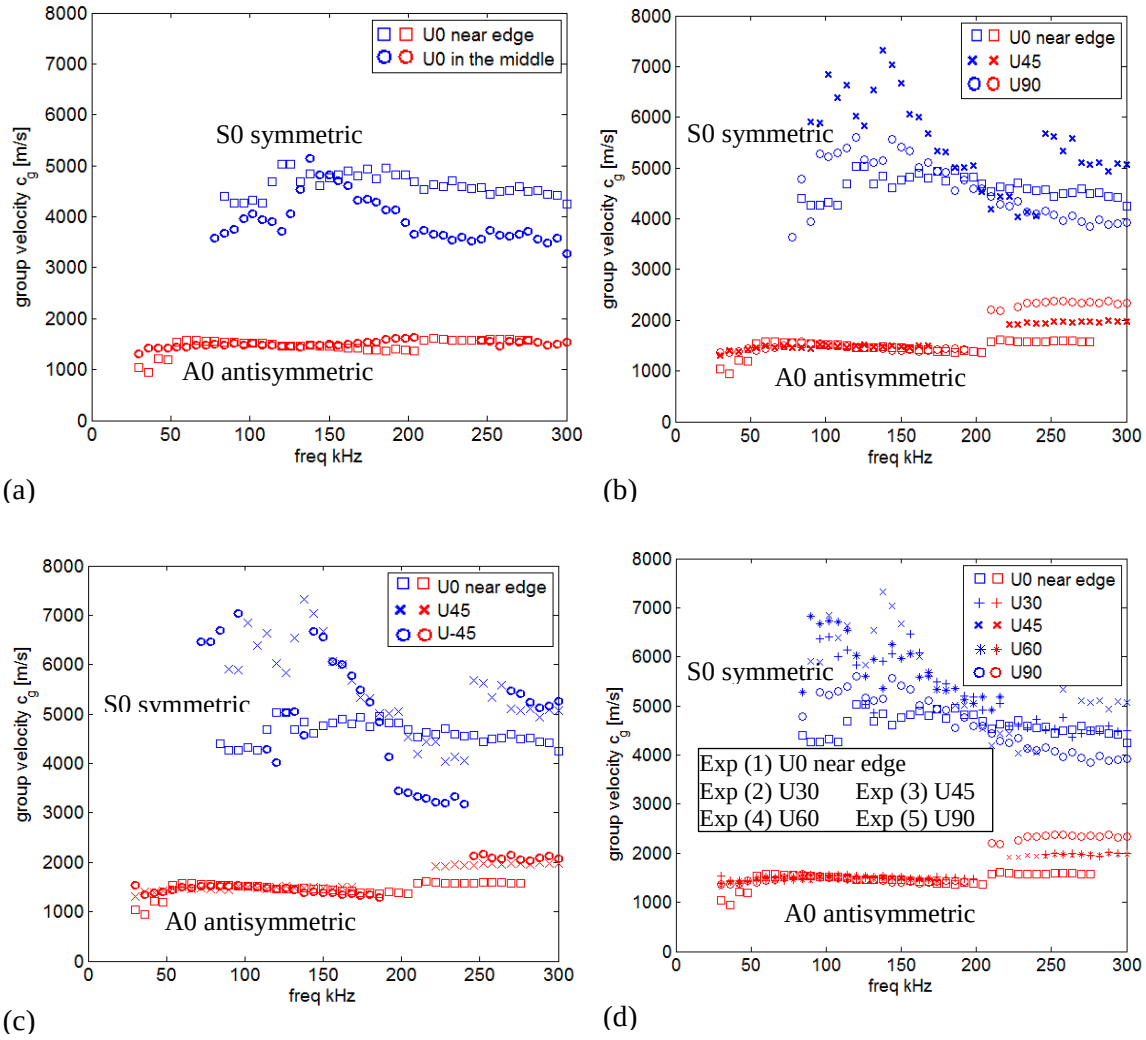

Figure 7.4. Experimental results of dispersion wave propagation group velocities for CFRP VS plate

As we can see from **Figure 7.4**a, the wave propagation along the same direction U0 but at two different locations of the plate are not the same; A0 is almost a constant and is having a speed around 1500 m/s, while S0 showed some differences. **Figure 7.4**b,c show that the wave propagation speeds along 45 deg. and -45 deg. directions were the maximum, probably because of the maximum stiffness at this part was along the 45 deg. directions.

7.3. SHORT TIME FOURIER TRANSFORM

The method we followed for analyzing pitch catch experiments was the time of flight (TOF) between the excitation signal and received signals; Hilbert envelops were used for better estimating the received modes. Another method that can give an overall picture is the short time Fourier transform (STFT), at which fast Fourier transform (FFT) is applied on intervals of time; when stacking these results together, it will lead to a time-frequency domain plot in which we can see the maxima and the minima of a signal. **Figure 7.5** shows an example signal for wave propagation along U0 direction at 66 kHz excitation. And **Figure 7.6** shows the resulting STFT.

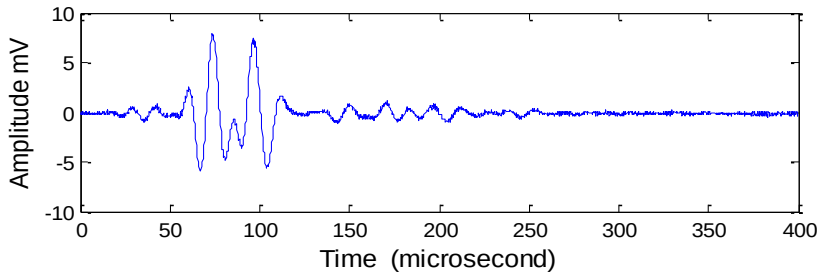

Figure 7.5. Time domain signal at excitation signal of 66 kHz along U0 direction

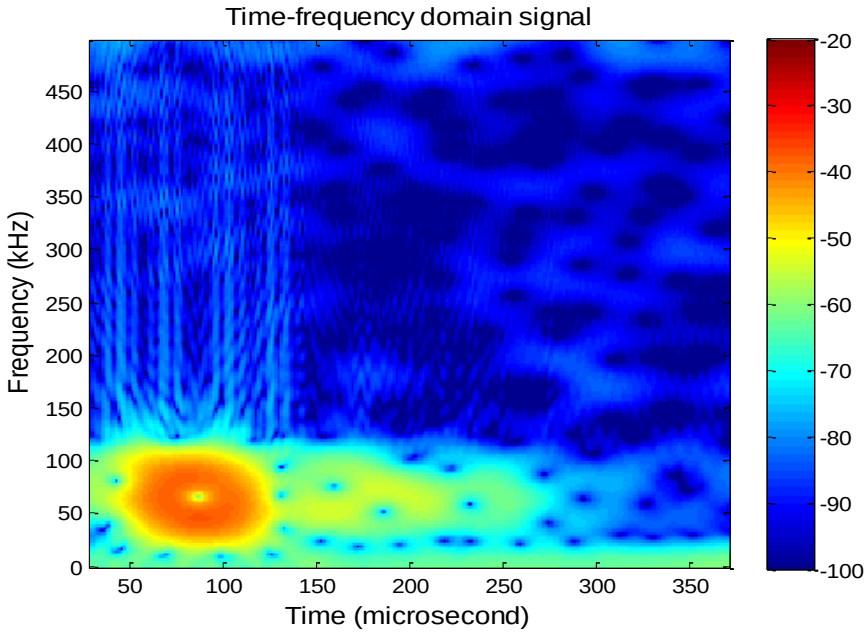

Figure 7.6. Short time Fourier transform of the time signal at 66 kHz along U0

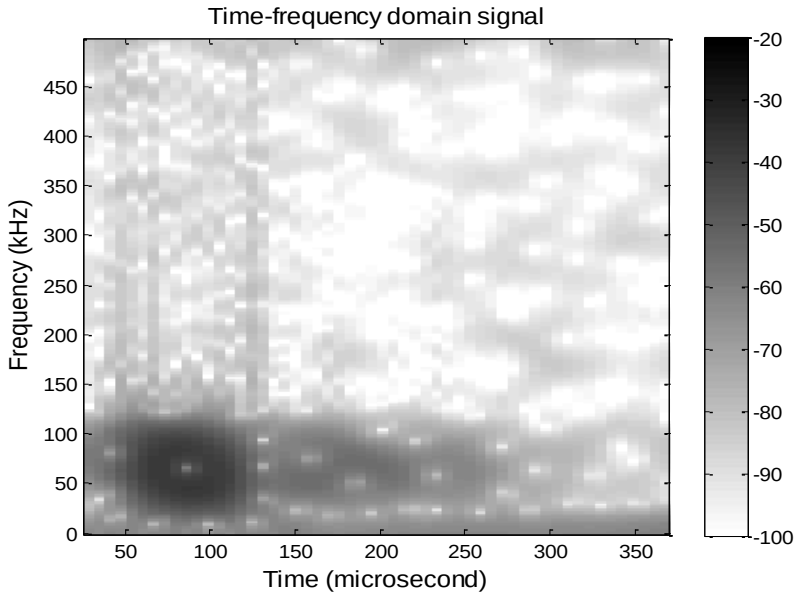

Figure 7.7. Black and White version of **Figure 7.6** for printing purposes

The analysis was performed for all the received signals along U0, at frequency sweep from 12kHz to 300 kHz. The overlapped STFT results are shown in **Figure 7.8**, **Figure 7.9**.

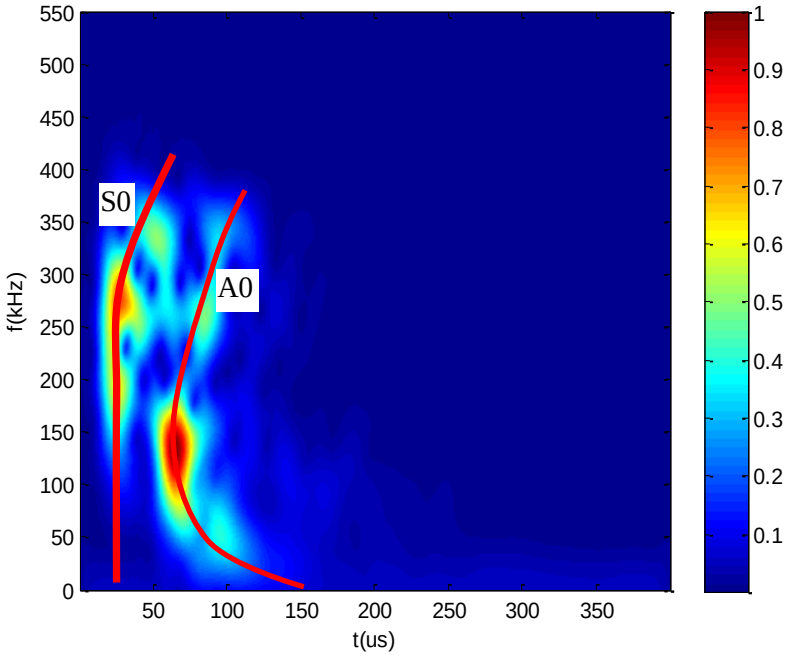

Figure 7.8. STFT of all the received signals from 12 kHz to 300 kHz

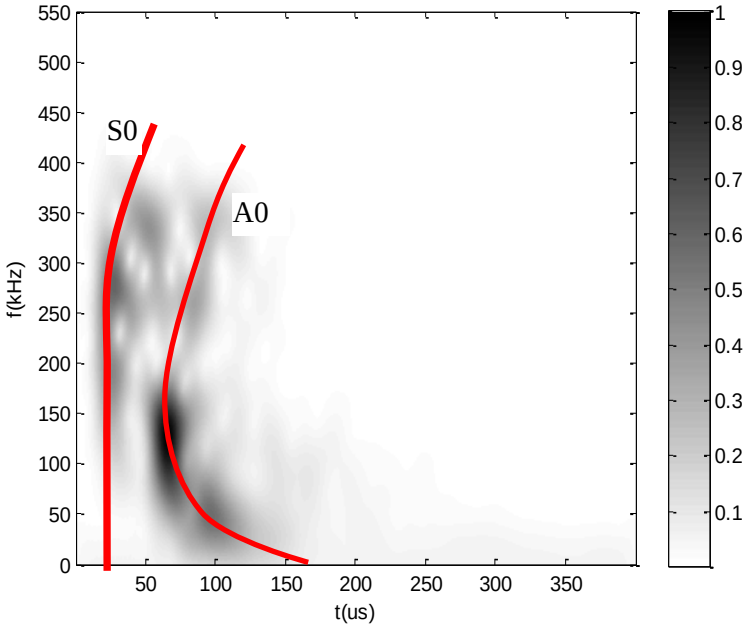

Figure 7.9. Black and white version of **Figure 7.8** for printing purposes.

7.4. SUMMARY AND CONCLUSIONS

Wave propagation experiments were performed on a VS CFRP plate. Beside the scattering due to experimental errors, etc., the results showed that A0 mode is the mode preferred to be used in SHM analysis, as its speed is almost constant with frequencies and different locations of the plate. We conclude that solely experimental results for wave propagation are not enough to find wave propagation speeds for SHM applications. Predictive tools in terms of analytical or FEM are needed to better analyze such complex structures.

CHAPTER 8: CONCLUSIONS AND FUTURE WORK

This dissertation has addressed analytical and numerical predictive models for ultrasonics transduction in metallic and composite structures using piezoelectric wafer active sensors (PWAS) for structural health monitoring (SHM). The key themes for this dissertation are power and energy; ultrasonic shear horizontal waves; wave propagation in composites.

The dissertation started with a background of ultrasonic guided waves in plates, PWAS as an active/passive transducer, and various ways in which PWAS are used for SHM applications. A predictive model of power and energy transduction between PWAS and the structure has been developed based on exact Lamb wave solution. The aim was optimizing guided wave mode tuning, PWAS electromechanical (E/M) impedance, and PWAS size for having power-efficient SHM systems. The power and energy models were applicable on multimodal Lamb wave situations that exist at high frequency ultrasonics and/or relatively thick structures. Experimental validation was conducted using scanning laser Doppler vibrometer (SLDV).

The dissertation continued with investigating the excitation and reception of shear horizontal (SH) guided waves in plates. A special type of PWAS was used, which is poled in the thickness-shear direction (d_{35} mode), we called it SH-PWAS. The E/M impedance of the free and the bonded SH-PWAS transducer have been developed analytically and by finite element modeling (FEM). The predictive models of the E/M

impedance have been validated experimentally. Next, wave propagation experimental and FEM studies were conducted between different combinations of SH-PWAS and regular inplane PWAS transducers. The excitability of SH waves and the directivity of the SH-PWAS were investigated. Finally, we presented simulations of our developed analytical models of SH waves' power and energy, along with a MATLAB graphical user interface (GUI) for the analysis of SH-waves including: dispersion phase and group velocities, mode shapes, and wave energy.

In order to investigate SH waves excitation and reception in composites; we needed a stable robust method for determining dispersion curves in composites. The transfer matrix method (TMM) has been used to calculate dispersion curves of guided waves in composites. TMM suffers numerical instability at high frequency-thickness values, especially in multilayered composites. A method of using stiffness matrix method (SMM) was investigated to overcome instability. A combined stiffness transfer matrix method (STMM) was proposed to obtain correct and stable results over the entire domain of interest. STMM procedure was coded in a MATLAB graphical user interface that also allows displaying modeshapes at any selected root of interest. This was followed by a comparative study between commonly used methods for the calculation of ultrasonic guided waves in composites, e.g. global matrix method (GMM), semi–analytical finite element (SAFE).

Furthermore, the dissertation presented three SHM applications: (1) using the SH-PWAS for case studies on composites, (2) testing of SHM industrial system for damage detection in an aluminum aerospace-like structure panel, and (3) measuring dispersion wave propagation speeds in a variable stiffness CFRP plate.

8.1. RESEARCH CONCLUSIONS

8.1.1. Power and Energy

Exact Lamb wave theory was used to model the power and energy transduction between PWAS transducer and hosted structures. The model was developed based on the normal mode expansion (NME) theory and straight-crested harmonic waves. The pin-force model was used to simulate perfect bonding between the PWAS and the structure. The model is applicable on multi-modal situations, for example, a half-inch thick steel plate, where three symmetric and three antisymmetric modes exist within the 500 kHz excitation window. Modal participation factors were developed to predict how much each mode contributes to the final power.

It was noticed that the transmitter reactive power (i.e., the power that depends on the capacitive behavior of the PWAS) was directly proportional to the transmitter admittance. The power transducted by the PWAS has an extra component, which is the transmitter active power, i.e., the power converted into the ultrasonic waves. A remarkable variation of active power with frequency was observed, and we noticed that the active power was not monotonic with frequency, but manifested peaks and valleys. As a result, the ratio between the reactive and active powers was not constant, but presented the peaks and valleys. The increase and decrease of active power with frequency corresponds to the PWAS tuning of various ultrasonic waves traveling into the structure. The developed model for Lamb waves case was compared with the axial and flexural waves, that approximate Lamb waves at relatively low frequencies and the two simulations showed good agreement. Next, a parametric study was performed to optimize the transducer size and excitation frequency to guarantee maximum energy transfer

between the source and the examined structure. Finally, an experimental study was performed using the scanning laser vibrometer to compare the out-of-plane structural oscillation at receiver PWAS transducers bonded on aluminum plates with analytical predictions, as well as the received voltage through the piezoelectric effects. The results have shown good agreement.

8.1.2. Shear Horizontal Coupled PWAS

The shear-horizontal piezoelectric wafer active sensor (SH-PWAS) was presented as a candidate for SHM compared to other-state-of-the-art transducers. Characterization of the SH-PWAS includes the analytical development of the free transducer (in d_{35} mode). We developed the E/M impedance and admittance of the free transducer based on the constant electric field assumption and based on the constant electric displacement assumption. The analytical model with the constant electric field assumption is more representative of the experimental case and FEM. The first resonance frequency of the free transducer is 900 kHz. We also extended the analytical development to the constrained SH-PWAS case, where the transducer is bonded to structures in the form of beams. The interaction between the SH-PWAS and the structure was studied. The analytical model was compared with experimental results and finite element analysis. It was shown that the analytical model predicts well the finite element and experimental results in the situation where the transducer – to – structure mass ratio is < 5%. It was also shown that the SH-PWAS has directivity effects, where an axial-flexural response is obtained when the transducer poling direction is parallel to the beam length. When the transducer poling direction is perpendicular to the beam length, the SH response is obtained.

The study then discussed the excitation and reception of SH waves using the SH-PWAS. Excitation of SH waves was analyzed by finite element simulations and experiments. SH0 non-dispersive waves were captured in aluminum plates. Multiple experiments were performed to show the SH waves excitation and receiving capabilities of both SH-PWAS and regular inplane PWAS transducers. It was shown that positioning and orientation of the SH-PWAS affects the generation of SH waves: (1) SH-PWAS excites SH waves in the direction perpendicular to its poling direction; (2) Regular inplane PWAS can sense SH waves; (3) SH-PWAS transducers can sense A0 and S0 Lamb waves. Directivity analysis showed that excited SH wave amplitude gradually decreases as the measuring direction deviates from the maximum received amplitude direction. Finally, we presented simulations of our developed wave power and energy analytical models along with a MATLAB graphical user interface (GUI) for the analysis of SH-waves including dispersion phase and group velocities, mode shapes, and wave energy.

8.1.3. Guided Wave Propagation in Composites

Different algorithms for calculating dispersion wave speeds in composites were reviewed. This work focused on the transfer matrix method (TMM) and the efforts for generating a stable robust algorithm. A combined stiffness transfer matrix method (STMM) was proposed to obtain correct and stable results over the entire domain of interest. STMM procedure was coded in a MATLAB graphical user interface that also allows displaying modeshapes at any selected root of interest. This was followed by a comparative study between commonly used methods for the calculation of ultrasonic

guided waves in composites, e.g. global matrix method (GMM), semi–analytical finite element (SAFE). Case studies were presented for an isotropic plate; a unidirectional fiber composite layer with fibers along 0º or 90º degrees w.r.t wave propagation direction; a unidirectional fiber composite layer with arbitrary fiber angles; multilayered unidirectional composite with fibers along 0º direction; and cross-ply composites. For each of the preceding cases, we obtained phase velocities, group velocities, and wavenumber-frequency domain solutions. Some observations we noticed include: as fibers angle increase from 0º towards 90º with respect to wave propagation direction, the phase and group velocities reduce; because for the fibers along 90º the material is in the most compliant case along wave propagation direction. Another observation regarding the equivalent matrix method (EMM) is that: the case of cross ply of $[0/90]_s$, i.e. 0/90/90/0 shows slight different results than the simple 0/90 case. The EMM predicted the exact same result for both cases because it just averages the properties of the 0-direction fibers and 90-direction fibers; hence the EMM does not account the difference between the 2-layer 0/90 and the 4-layer [0/90]s cases.

Afterwards, a comparable study was established between the STMM results and results from commercially available software, e.g. DISPERSE software based on GMM, and GUIGUW software based on SAFE. This was followed by experimental and FEM studies on a glass fiber reinforced polymer (GFRP) woven composite. PWAS transducers were used for pitch catch experiments using tone burst excitation signals. Experimental dispersion group velocities showed good agreement with the theory. COMSOL Multiphysics finite element model was constructed using coupled-field elements for the PWAS; this allowed simulation of the input excitation and output response in voltage

directly. FEM showed the propagation pattern of guided waves in composites. For the specific case of a woven GFRP composite, the wave propagation along 0 and 90 degrees was similar, but was different along 45 degrees, which resulted in diamond pattern instead of the conventional propagation in circles obtained for isotropic materials.

8.1.4. SH-PWAS for Exciting SH Waves in Composites

SH-PWAS was studied for the E/M impedance method and wave propagation of SH waves in two composite plates, one was cross ply GFRP woven composite and the other was quasi-isotropic [0/45/45/0] carbon fiber reinforced polymer (CFRP) composite with woven prepreg. Admittance experimental results were comparable to FEM built using coupled field piezoelectric elements bonded to composite layers. Wave propagation method showed that the SH-PWAS can excite SH waves as well as S0, A0, providing that the receiver PWAS is in a position such that the wave propagation direction between SH-PWAS and the receiver PWAS is perpendicular to SH-PWAS poling direction. If we excite SH-PWAS and receive the signal along a direction parallel to the poling direction, only A0 and S0 waves were captured. FEM models showed well the wave propagation pattern in woven GFRP plate and quasi-isotropic CFRP composite plate, however, lack of accuracy existed in the received signals due to limited computational resources.

8.1.5. Guided Wave Damage Detection in an Aerospace-Like

The MD7 guided-wave SHM system developed by Metis Design was studied and tested. It is concluded that the system is applicable on the plate under test. Careful selection of frequency of excitation is an important parameter to be considered.

8.1.6. SHM of Variable Stiffness CFRP Plate

Wave propagation experiments were performed on a VS CFRP plate. Besides the scattering due to experimental errors, the experimentally-measured wave speeds of the S0 mode were more scattered than A0 mode. We concluded that A0 mode is the more preferred mode to be used in SHM analysis; its speed was almost constant with frequencies and different locations of the plate. A general conclusion is that solely experimental results for wave propagation are not enough to find wave propagation speeds for SHM applications. Predictive tools in terms of analytical or FEM are needed to better analyze such complex structures.

8.2. MAJOR CONTRIBUTIONS

The dissertation has contributed to the fundamental studies of using ultrasonics in SHM. The list of the major contributions includes

1. Development of the analytical models of ultrasonic waves power and energy based on the exact Lamb wave modes.
2. Predicting the power partitioning between multimodal Lamb waves (three symmetric and three antisymmetric modes) for a thick structure application.

3. Characterization of the SH-PWAS as a candidate for exciting SH waves in SHM applications, including:
    a) Modeling the E/M impedance of a bonded SH-PWAS to the structure analytically for the first time.
    b) Performing a comprehensive experimental and FEM studies to investigate excitation and reception of SH waves and the directivity of the SH-PWAS.
4. The development of a MATLAB-based graphical user interface (GUI) for SH waves analysis, including: dispersion curves, modeshapes and wave energy.
5. A novel approach (STMM) was proposed for obtaining a stable and correct solution of dispersion curves in composites over the entire solving domain.
6. The development a MATLAB-based GUI for a quicker and easier analysis of the dispersion curves in composites, including:
    a) Loading the unstable results of the transfer matrix method (TMM).
    b) Displaying the complete stable stiffness transfer matrix method (STMM).
    c) Calculating displacements and stresses modeshapes at any given root on the dispersion curves.
7. Performing comprehensive pitch catch experiments and FEM between SH-PWAS and regular in-plane PWAS for investigating SH wave excitation and reception in composites.

8.3. RECOMMENDATION FOR FUTURE WORK

The dissertation has addressed analytical and numerical models to advance fundamental understanding of using ultrasonics for SHM of metallic and composite materials. The recommended future work includes:

1. Extending power and energy transduction models for situations of bonded PWAS on composite materials.
2. Performing more experimental studies to validate power and energy models; power need to be a parameter in the measurements.
3. Performing scanning laser vibrometer measurements to capture the shear horizontal response of the SH-PWAS.
4. Continue developing the stiffness transfer matrix method (STMM) and predict dispersion curves for more complex composite layups.
5. Performing more experiments of the wave propagation in composites and investigating types of damages, SH-PWAS is capable to detect.

REFERENCES

APC International Ltd, *Physical and Piezoelectric Properties of APC Materials.* [Online] Available at: http://www.americanpiezo.com

Aldrin, J.; Knopp, J.; Judd, D.; Mandeville, J.; Lindgren, E. (2006) Spiral Creeping Waves in Ultrasonic Angled-Beam Shear Wave Inspection of Fastener Holes in Multilayer Structures, AIP Conf. Proc. *820*, pp. 187-194.

Aldrin, J.; Kropas-Hughes, C.V.; Knopp, J.; Mandeville, J.; Judd, D.; Lindgren, E. (2006) Advanced echo-dynamic measures for the characterisation of multiple ultrasonic signals in aircraft structures. *Insight: Non-Destructive Testing & Condition Monitoring, 48*(3), pp. 144-148.

Alleyne, D.; Cawley, P. (1992) The Interaction of Lamb Waves With Defects. *IEEE Trans. Ultrason. Ferroelectr. Freq. Control, 39*(3), pp. 381-396.

Auld, B. (1990) *Acoustic Fields and waves in solids.* New York: John Wiley & Son.

Baillargeon, P.B. (2003) *Active Vibration Suppression of Smart Structures Using Piezoelectric Shear Actuators,* University of Maine Electronic Dissertation.

Banerjee, S.; Ricci, F.; Monaco, E.; Mal, A. (2008) A wave propagation and vibration-based approach for damage identification in structural components. *Journal of Sound and Vibration, 322*(1-2), pp. 167-183.

Bartoli, I.; Marzani, A.; Lanza di Scalea, F.; Viola, E. (2006)Modeling Wave Propagation in Damped Waveguides of Arbitrary Cross-section. *J. Sound & Vibration, 295*, pp. 685-707.

Benjeddou, A.; Trindade, M.A.; Ohayon, R. (1997) A Unified Beam Finite Element Model for Extension and Shear Piezoelectric Actuation Mechanisms. *J. Intelligent Mat. Syst. Struct., 8*(12), pp. 1012-1025.

Blom, A. (2010) *Structural performance of fiber-placed, variable-stiffness composite conical and cylindrical shells,* Ph. D. Thesis, Delft University of Technology.

Bocchini, P.; Marzani, A.; Viola, E. (2011) Graphical User Interface for Guided Acoustic Waves. *Journal of Comput. Civ. Eng., 25*(3), pp. 202-201.

Centolanza, L.R.; Smith, E.C.; Munsky, B. (2002) Induced-shear piezoelectric actuators for rotor blade trailing edge flaps. *J. Smart Mater. Struct, 11,* pp. 24-35.

Chang, F. (1998) Smart layer: built-in diagnostics for composite structures. *Proc. of the 4th European Conference on Smart Materials and Structures.*

Cheng, C.; Chen, S.; Zhang, Z.; Lin, Y. (2007) Analysis and experiment for the deflection of a shear-mode PZT actuator. *Smart Mater. Struct., 16,* pp. 230-36.

Chinthalapudi, A.; Hassan, H. (2005) *Investigation of Methods to Detect Defects in Thin Layered Materials,* Karlskrona, Master's Degree Thesis, Blekinge Institute of Technology, Sweden.

Delsanto, P.P.; Schechter, R.S.; Mignogna, R.B. (1997) Connection machine simulation of ultrasonic wave propagation in materials III: The three-dimensional case. *Wave Motion, 26*(4), pp. 329-339.

Ferroperm Piezoceramics, [Online] Available at: www.ferroperm-piezo.com/

Flynn, E.; Todd, M.; Kessler, S.; Dunn, C. (2011) Identifying Scatter Targets in 2D Space using In Situ Phased-Arrays for Guided Wave Structural Health Monitoring. *The 8th Int. Workshop on Structural Health Monitoring* Stanford, CA.

Fortunko, C.M.; King, R.B.; Tan, M. (1982) Nondestructive Evaluation of Planar Defects in Plates Using Low-Frequency Shear Horizontal Waves. *J. Applied Physics,* 53, pp. 3450-3458.

Gao, H.; Ali, S.; Lopez, B. (2010) Inspection of Austenitic Weld with EMAT, *Review of Progress in Quantitative Nondestructive Evaluation 29B*, pp. 1175-1181.

Gavric, L. (1995) Computation of Propagative Waves in Free Rail Using a Finite Element Technique. *Journal of Sound and Vibration, 185*(3), pp. 531-543.

Giurgiutiu, V. (2005) Tuned Lamb wave excitation and detection with piezoelectric wafer active sensors for structural health monitoring. *J.Intell. Mat. Syst. Struct., 16,* pp. 291-305.

Giurgiutiu, V. (2008) *Structural Health Monitoring with Piezoelectric Wafer Active Sensors.* Amsterdam: Elsevier Academic Press.

Giurgiutiu, V.; Santoni, G. (2011) Structural Health Monitoring of Composite Structures with Piezoelectric-Wafer Active Sensors. *AIAA Journal , 49*(3), pp. 565-581.

Giurgiutiu, V.; Zagrai, A. (2000) Characterization of piezoelectric wafer active sensors. *J.Intell. Mater. Sys. Struct., 11*, pp. 959-976.

Giurgiutiu, V.; Zagrai, A.; Bao, J. (2002) Piezoelectric wafer embedded active sensors for aging aircraft structural health monitoring. *Structural Health Monitoring, 1*, pp. 41-61.

Glazounov, A.; Zhang, Q. (1998) Piezoelectric actuator generating torsional displacement from piezoelectric d15 shear response. *J. Applied Physics Letters, 72*, pp. 2526-28.

Glushkov, E.; Glushkova, N.; Eremin, A. (2011) Forced wave propagation and energy distribution in anisotropic laminate composites. *Journal Acoust. Soc. America, 129*(5), pp. 2923-2934.

Glushkov, E.; Glushkova, N.; Kvasha, O.; Seemann, W. (2007) Integral equation based modeling of the interaction between piezoelectric patch actuators and an elastic substrate. *Smart Materials and Structures, 16*(3), pp. 650-664.

Glushkov, E.; Glushkova, N.; Seemann, W.; Kvasha, O. (2006) Elastic wave excitation in a layer by piezoceramic patch actuators. *Acoustical Physics, 52*(4), pp. 398-407.

Graff, K. (1991) *Wave motion in elastic solids.* New York: Dover Publications Inc.

Gresil, M.; Giurgiutiu, V. (2013) Guided wave propagation in carbon composite laminate using piezoelectric wafer active sensors. *SPIE NDE proc.,* March 10-14, San Diego, CA, pp. 869577-1:15.

Gresil, M.; Yu, L.; Giurgiutiu, V.; Sutton, M. (2012) Predictive modeling of electromechanical impedance spectroscopy for composite materials. *Structural Health Monitoring, 11*(6), pp. 671-683.

Haskell, N. (1953) The dispersion of surface waves on multi-layered media. *Bulletin of the Seismological Society of America, 43*(1), pp. 17-34.

Hayashi, T.; Song, W.-J.; Rose, J. L. (2003) Guided wave dispersion curves for a bar with an arbitrary cross-section, a rod and rail example. *Ultrasonics, 41*, pp. 175-183.

Heeg, J. (1993) *Analytical and experimental investigation of flutter suppression by piezoelectric actuation*, NASA Technical paper 3241 Langley Research Center, , Hampton, Virginia.

Ji, W.; Shen, L.-j. (2005) Exact thickness-shear resonance frequency of electroded piezoelectric crystal plates. *J. Zhejiang Univ. Sci, 6A*(9), pp. 980-985.

Jones, R. (1999) *Mechanics of composite materials.* London: Taylor & Francis.

Kamal, A.; Lin, B.; Giurgiutiu, V. (2013) Energy and power modeling of multi mode lamb waves propagating in structure bonded with piezoelectric wafer active sensors. *AIP Conf. Proc, 1511,* Denver, CO, pp. 183-190.

Kamal, A.; Lin, B.; Giurgiutiu, V. (2013) Predictive modeling of PWAS-coupled shear horizontal waves. *SPIE NDE pro,* March 10-14, San Diego, CA., pp. (86950F-1:15).

Kamas, T.; Lin, B.; Giurgiutiu, V. (2013) Analytical modeling of PWAS in-plane and out-of-plane electromechanicalimpedance spectroscopy (EMIS). *SPIE NDE proc.* March 10-14, San Diego, CA, pp. 869227-1:13.

Kessler, S.; Flynn, E.; Dunn, C.; Todd, M. (2011) A Structural Health Monitoring Software Tool for Optimization, Diagnostics and Prognostics. *3rd Annual Conference of the Prognostics and Health Management Society,* 25-29 Sept. 2011, Montreal, Quebec.

Knopoff, L., 1964. A matrix method for elastic wave problems. *Bulletin of the Seismological Society of America,* Volume 54, pp. 431-438.

Koh, Y.; Chiu, W.; Rajic, N. (2002) Effects of local stiffness changes and delamination on Lamb wave transmission using surface-mounted piezoelectric transducers. *Composite Structures, 57,* pp. 437-443.

Kural, A.; Pullin, R; Featherston, C; Pager, C; Holford, K. (2011) Wireless power transmission using ultrasonic guided waves. *Journal of Physics,* Conference Series *305*(012088), pp. 1-11.

Le Crom, B.; Castaings, M. (2010) Shear horizontal guided wave modes to infer the shear stiffness of adhesive bond layers. *J. Acoust. Society of America., 127*(4), pp. 2220-2230.

Lee, B.C.; Staszewski, W.J. (2003) Modelling of Lamb waves for damage detection in metallic structures: Part I. Wave propagation. *Smart Mat. Str., 12*, pp. 804-814.

Lee, J.; Kim, Y.; Cho, S.; (2009) Beam-focused shear-horizontal wave generation in a plate by a circular magnetostrictive patch transducer employing a planar solenoid array. *J. Smart Mater. Struct, 18*, pp. 015009.

Li, F.; Murayama, H.; Kageyama, K. (2009) Guided Wave and Damage Detection in Composite Laminates Using Different Fiber Optic Sensors. *Sensors, 9*(5), pp. 4005-4021.

Lin, B.; Giurgiutiu, V. (2012) Power and Energy Transduction Analysis of Piezoelectric Wafer Active Sensors for Structural Health Monitoring. S*tructural Health Monitoring – An International Journal, 11*(1), pp. 109-121.

Lin, B.; Giurgiutiu, V.; Kamal, A. (2012) The Use of Exact Lamb Waves Modes for Modelling the Power and Energy Transduction of Structurally- Bonded Piezoelectric Wafer Active Sensors. *SPIE NDE proc.* March 11-15, San Diego, CA., pp. 83450A-1:12.

Lowe, M. (1995) Matrix techniques for modeling ultrasonic waves in multilayered media, *Ultrasonics Ferroelectrics and Frequency Control, IEEE Transactions, 42*(4), pp. 525-542.

Milyutin, E.; Gentil, S.; Muralt, P. (2008) Shear mode bulk acoustic wave resonator based on c-axis oriented AIN thin film. *J. Applied Physics, 104*, pp. 084508.

Milyutin, E.; Muralt, P. (2011) Electro-mechanical coupling in shear-mode FBAR with piezoelectric modulated thin film. *Ultrasonics Ferroelectrics and Frequency Control, IEEE Transactions, 58*, pp. 685-688.

Monnier, T. (2006) Lamb Waves-based Impact Damage Monitoring of a Stiffened Aircraft Panel using Piezoelectric Transducers. *J. Int. Mat. Sys. and Structures, 17*, pp. 411-421.

Moser, F.; Jacobs, L.J.; Qu, J. (1999) Modeling elastic wave propagation in waveguides with the finite element method. *NDT & E International, 32*(4), pp. 225-234.

Mueller, V.; Zhang, Q. (1998) Shear response of lead zirconate titanate piezoceramics. *J. Applied Physics, 83*, pp. 3754.

Nadella, K.; Cesnik, C. (2012) Numerical simulation of wave propagation in composite plates. *SPIE NDE proc.* March, San Diego, CA, 8348, 83480L.

Nadella, K.; Cesnik, C. (2012) Simulation of Guided Wave Propagation in Isotropic and Composite Structures using LISA, *53rd AIAA/ASME/ASCE/AHS/ASC Structures, Structural Dynamics and Materials Conference*.

Nayfeh, A. (1995) *Wave Propagation in Layered Anisotropic Media.* New York: Elsevier.

Park, G.; Rosing, T.; Todd, M.D.; Farrar, C.R.; Hodgkiss, W. (2007) *Energy Harvesting for Structural Health Monitoring Sensor Networks,* LA 14314-M8 Los Alamos National Laboratory Report.

Pavlakovic, B.; Lowe, M. (2003). *DISPERSE Manual,* London: Imperial College.

Pollock, P.; Yu, L; Sutton, M.A; Guo, S.; Majumdar, P.; Gresil, M. (2012) Full-Field Measurements for Determining Orthotropic Elastic Parameters of Woven Glass-Epoxy Composites Using Off-Axis Tensile Specimens. *Experimental Techniques.*

Rokhlin, S.; Chimenti, D.; Nagy, P. (2011) *Physical Ultrasonics of Composites,* Oxford University Press.

Rose, J.(1999) *Ultrasonic Waves in Solid Media.* New York, Cambridge University Press.

Rose, J.; Pelts, S.; Li, J. (2000) Quantitative Guided Wave NDE. *15th World Conference on Non-Destructive Testing* Rome, Italy.

Ruzzene, M.; Jeong, S.M.; Michaels, T.E.; Michaels, J.E.; Mi, B. (2005) Simulation and measurement of ultrasonic waves in elastic plates using laser vibrometry, Green Bay, Wisconsin, *AIP Conf. Proc.,* 24, pp. 172-179.

Santoni, G. (2010) *Fundamental Studies in the Lamb-Wave Interaction Between Piezoelectric Wafer Active Sensor and Host Structure During Structural Health Monitoring,* Dissertation, University of South Carolina.

Santoni, G.; Chrysochoidis, N.A.; Giurgiutiu, V.; Saravanos, D.A. (2007) Analytical and Experimental Evaluation of Piezoelectric Wafer Active Sensors Performances for Lamb Waves based Structural Health Monitoring in Composite Laminates. *SPIE NDE proc.* March 19-22, San Diego, CA, pp. 6532-22.

Schmidt, H.; Jensen, F.B. (1985) A full wave solution for propagation in multilayered viscoelastic media with application to Gaussian beam reflection at fluid-solid interfaces. *Journal Acoust. Soc. America, 77*(3), pp. 813-825.

Sherrit, S.; Djrbashian, A.; Bradford, S. (2013) Analysis of the impedance resonance of piezoelectric multi-fiber composite stacks. *SPIE NDE proc.* March 10-14, San Diego, CA, pp. 868904-1:12.

Sohoni, V. (1995) *A new smooth step function for ADAMS mscsoftware.* [Online] Available at: http://webcache.googleusercontent.com/search?q=cache:fZ-a--O62ksJ:web.mscsoftware.com/support/library/conf/adams/na/1995/UC950030.PDF+&cd=1&hl=en&ct=clnk&gl=us [Accessed June 2014].

Sorohan, S.; Constantin, N.; Gavan, M.; Anghel, V. (2011) Extraction of dispersion curves for waves propagating in free complex waveguides by standard finite element codes. *Ultrasonics, 51*, pp. 503-515.

STEMiNC, *Steiner & Martins, Inc.* [Online] Available at: http://www.steminc.com/

Sun, C.; Zhang, X. (1995) Use of thickness-shear mode in adaptive sandwich structures. *J. Smart Mater Struct, 4*, pp. 202-206.

Su, Z.; Yang, C.; Pan, N.; Ye, L.; Zhou, L. (2007) Assessment of delamination in composite beams using shear horizontal (SH) wave mode. *Composites Science and Technology, 67*(2), pp. 244-251.

Su, Z.; Ye, L.; Lu, Y. (2006) Guided Lamb waves for identification of damage in composite structures: A review. *J. of Sound and Vibration, 295*(3-5), pp. 753-780.

Tatting, B.; Gurdal, Z. (2003) *Automated finite element analysis of elastically-tailored plates,* Technical Report, NASA/CR-2003-212679.

Thomson, W. (1950) Transmission of elastic waves through a stratified solid medium. *journal of Applied Physics, 21*, pp. 89-93.

Viktorov, I. (1967) *Rayleigh and Lamb waves - physical theory and applications.* New York: Plenum Press.

Wang, L.; Rokhlin, S. (2001) Stable reformulation of transfer matrix method for wave propagation in layered anisotropic media. *J. Ultrasonics, 39*, pp. 407–418.

Wilcox, P.; Lowe, M.; Cawley, P. (2001) Mode and Transducer Selection for Long Range Lamb Wave Inspection. *Journal of Intelligent Material Systems and Structures, 12*, pp. 553-565.

Yanagitani, T. (2011) Shear Mode Piezoelectric Thin Film Resonators. In: *Acoustic Waves – From Microdevices to Helioseismology*, M. G. Beghi, ed. InTech, Japan pp. 501-520.

Zhou, W.; Li, H.; Yuan, F. (2013) Guided wave generation, sensing, and damage detection using in-plane shear piezoelectric wafer. *SPIE NDE proc.* March 10-14, San Diego, CA , pp. 869225-1:12.